Nonlinear Earthquake Response of Concrete Gravity Dams

by

Luis M. Vargas-Loli

Gregory Fenves

Department of Civil Engineering
The University of Texas at Austin
Austin, Texas

December 1987

NONLINEAR EARTHQUAKE RESPONSE OF CONCRETE GRAVITY DAMS

by

Luis M. Vargas-Loli

Gregory Fenves

Department of Civil Engineering
The University of Texas at Austin
Austin, Texas

December 1987

i. a

Abstract

A numerical procedure for computing the nonlinear transient response of coupled fluid-structure systems is developed. The study concentrates on two types of nonlinear behavior in concrete dams: water cavitation and tensile cracking of concrete. The fluid is considered compressible and inviscid, undergoing small amplitude motion. The computational procedure employs a mixed pressure-displacement finite element formulation for the fluid and a displacement formulation for the structure. The formulation for the fluid includes the effects of cavitation through a bilinear equation of state. Upon discretization, the coupled nonlinear equations of motion are symmetric and are solved by a fully implicit time integration method.

The effect of water cavitation on the earthquake response of concrete gravity dams when subjected to representative ground motions is investigated. Assuming the material in the dam is linear elastic, the response results show that water cavitation has little influence on maximum displacements and stresses in the dam. However, peak accelerations at the dam crest may increase by a factor of two. This may have an important consequence by amplifying the response of stiff appurtenant equipment attached to the dam crest. The effect of reservoir bottom materials, modeled by an approximate absorbing boundary, reduces the hydrodynamic pressures on the dam, hence reducing the magnitude of displacements and stresses.

The second nonlinear effect studied involves the tensile cracking of mass concrete. The crack band model with a smeared crack representation is used to model mass concrete. Microcrack initiation is determined by a strain criterion and

strain-softening behavior defines the formation of a crack surface in conjunction with an energy release requirement. Criteria for crack closure and reopening of cracks are established based on experimental results. The cracking model is incorporated into the finite element displacement formulation for the dam.

The response of a typical concrete dam with empty and full reservoir subjected to various ground motion records is examined. The response results demonstrate that concrete tensile cracking has an important effect on the displacement and stress responses of gravity dams. The vibrational period increases as the dam becomes more flexible. Large compressive stresses normal to the cracked surfaces develop due to cracking, but they are still small compared with the concrete compressive strength. With a full reservoir, cracking starts in the dam at the heel and extends along the base of the dam. At a later time in response history, the cracking at the base stabilizes but extensive cracking develops in the upper part of the dam propagating completely across the cross section. The extensive cracking could result in severe damage of the dam and possible release of water in the reservoir.

Acknowledgments

Table of Contents

List of Tables

List of Figures

Chapter 1

Introduction

The computation of the dynamic response of fluid-structure systems has received considerable attention in the past decade. An important fluid-structure interaction problem is determining the earthquake response of a concrete dam impounding a large reservoir of water. Although dynamic analyses assuming linear behavior provide important information regarding the characteristics of earthquake response, a precise evaluation of the dam performance is not possible because the material behavior, particularly the strength, is not represented. Because of the catastrophic consequences of a dam failure, engineers require reliable analytical procedures to predict the conditions under which a dam may fail. A realistic dynamic analysis of a concrete dam should include the effects of significant nonlinearities in the response to earthquake ground motion. Experimental and analytical studies have identified several sources of nonlinear behavior in dam-water systems, such as the formation and collapse of gaseous regions in the impounded water due to cavitation, tensile cracking of concrete in the dam; and opening, closing and slippage of joints between monolith blocks [14,18,30]. Recognizing the importance of nonlinear behavior in assessing dam safety, this investigation presents a numerical procedure for computing the nonlinear dynamic response of fluid-structure systems, with particular emphasis on concrete gravity dams in which water cavitation and concrete tensile cracking in the dam are considered. Even though the motivation is to compute the earthquake response of dams, the numerical procedure is applicable to other fluid-structure sys-

1

tems in which the fluid is inviscid and undergoes small amplitude motion.

1.1 Review of Literature

1.1.1 Fluid-Structure Interaction

Researchers have developed several methods of analysis for fluid-structure systems. The available methods use a finite element idealization of the structure with displacements as the response quantity, but they differ in the formulation for the fluid. Saini, et al [40], and Zienkiewicz, et al [47], used hydrodynamic pressure as the unknown variable in a finite element discretization of the fluid domain. However, the unsymmetrical equations of motion of the coupled fluid-structure system require special time integration methods for transient analysis [35,49]. Another approach is to represent the fluid response in terms of a potential function for displacement or velocity [27,48]. Again the coupled equations of motion are unsymmetric, but the irrotationality condition on fluid motion is automatically satisfied, as with the pressure formulation. A third major formulation uses displacements of the fluid as the response quantity. This method was used early by Chopra, et al [13], and substantial contributions have been made by Bathe and Hahn [5], Olson and Bathe [32], Hamdi, et al [19] and Wilson and Khalveti [46].

The major advantages of the displacement formulation are that the fluid elements can be coupled to the structure elements using standard finite element assembly procedures and the equations of motion are symmetric. The disadvantage of the displacement formulation, compared to the scalar formulations, is the large number of displacement components, particularly for three-dimensional fluid domains. Also, because the displacement formulation gives excessively stiff elements, reduced integration is often employed. However, reduced integration is related to a differ-

ent differential operator for the fluid motion [32], and it also introduces spurious vibration modes associated with the vorticity of the fluid.

Another major approach for computing the response of fluids involves a combination of the formulations described above. Liu and Chang [24] developed a mixed solution procedure in which the pressure is approximated in a different manner than the fluid velocity. The transient analysis procedure explicitly solves for the pressure, which is then used in an implicit solution for the velocity. In another mixed approach, Olson and Bathe [33] used pressure and velocity potential as the unknown functions for the fluid to overcome shortcomings in the displacement formulation for certain classes of fluid-structure systems. Although the choice of these scalar functions reduces the number of unknowns and results in symmetric equations of motion, special interface elements must be developed to couple the fluid and structure domains. In a different application, Taylor and Zienkiewicz [44] presented a mixed formulation for viscous fluid flow. The work combined independent approximation of the velocity, pressure and deviatoric stress (due to viscosity), and it demonstrated an improved representation of nonlinear material models.

As mentioned earlier, however, the nonlinear behavior of the fluid may be important in the dynamic response of fluid-structure systems. Fluids can not develop an absolute pressure less than the vapor pressure of the fluid. If the fluid pressure reaches the vapor pressure, dissolved gasses form vapor pockets due to cavitation of the fluid. The effects of cavitation have been investigated in the context of earthquake response of concrete gravity dams. Clough and Chang [14] modeled dam-water interaction including cavitation by two methods: an added mass approximation and a finite element pressure formulation, in which water compressibility was neglected in both cases. Their results, interpreted in terms of separation and impact of the reservoir on the dam, demonstrated that impact of the fluid due to collapse of cavitated

regions near the dam face can increase tensile stresses in the upper part of the dam by 20-40%. A more accurate representation of cavitation requires consideration of fluid compressibility, such as the bilinear fluid model proposed by Bleich and Sandler [10]. This fluid model was used in a recent study of concrete dams by Zienkiewicz, et al [48], in which the authors concluded that cavitation does not significantly alter the maximum stresses in the dam. The evidence regarding the importance of cavitation on the earthquake response of concrete gravity dams is still inconclusive from these limited studies. Furthermore, there has been no investigation of cavitation effects on concrete arch dams, where dam-water interaction effects are more important than for gravity dams [16].

1.1.2 Tensile Cracking in Concrete

Analytical methods for the modeling of tensile cracking in concrete have been the subject of intense research. Studies have been mainly devoted to applications for reinforced concrete in which two major approaches have been employed. Ngo and Scordelis [28] studied the static behavior of reinforced concrete members including tensile cracking using finite elements with the locations of the cracks predefined. The cracks were modeled by the separation of nodes between elements, a technique called the discrete crack approach. This idea was later generalized by Nilson [29] who modeled cracking allowing automatic determination of crack locations. The discrete crack approach, however, has a severe computational disadvantage because the topology of the finite element mesh must be redefined at every load stage. To remedy this problem, Rashid [37] proposed a model in which the cracks were assumed uniformly distributed over a finite element, in a concept known as the smeared crack approach. The smeared crack approach has been used extensively along with a maximum tensile strength criterion for determining crack initiation. Nevertheless, the smeared crack

approach has been criticized [6,7], because after crack initiation the force required to propagate the crack depends on the size of the finite element. To overcome this problem, Bažant and Cedolin [7] introduced the blunt crack band model, which used fracture mechanics concepts, to modify the smeared crack approach. Tensile cracking was recognized as a fracture process and the energy required to form a surface crack (fracture energy) was used as an additional material parameter. Bažant and Oh [8] presented a comprehensive study on the accuracy and generality of the crack band theory, a method following the blunt crack approach, to predict tensile cracking behavior of plain concrete.

An early application of these models to concrete dams was conducted by Pal [34], who used a smeared crack approach. The Koyna dam was analyzed neglecting dam-water interaction, and the nonlinear compressive and tensile behavior of concrete was accounted for by adjusting an equivalent uniaxial stress-strain constitutive relationship according to the current state of stress. The response results show that tensile cracks formed near the change in downstream slope, in the upper part of the dam, but the cracking did not extend through the cross section. The findings in this study must be taken cautiously since the fracture energy was not properly considered in the model. In another investigation, Chapuis, et al [12], used local singular finite elements to obtain stress intensity factors to determine fracture conditions. The Pine Flat dam was exposed to an artificially generated earthquake with a 0.1g peak acceleration. Dam-water interaction was taken into account by performing linear analyses to obtain the stress history at the locations at which cracking was likely to occur. The response results indicate that cracking at the heel of the dam (upstream face) is not critical. In the upper part of the dam, at the change in slope, cracking propagates from the upstream face over various elements and turns into the body of the dam, stopping without reaching the downstream face. The

upper portion of the dam appeared to remain stable.

Mlakar [26] studied the response of three dams of different heights, sub-jected to the horizontal and vertical components of the Parkfield ground motion. The dam-water interaction was approximated by means of added masses attached to the dam, corresponding to hydrodynamic pressures in the fundamental mode as obtained from a linear analysis. In the shorter dam, it was found that extensive cracking occurs around the dam heel immediately after crack initiation. In the other two cases with taller dams, cracking started at the heel and was followed by the initiation of new cracks in the upper portion of the dam. In certain cases, cracks propagated through the cross section nearly instantaneously after crack initiation, although no indication of the crack orientations was provided. The constitutive model employed in these studies does not seem to account for proper release of fracture energy. In addition, the added mass approach for the fluid-structure interaction can only represent the general characteristics of the interaction at the fundamental frequency, disregarding effects of compressibility and the contribution of higher vibration modes.

The discrete crack approach has also been used to model tensile cracking in concrete gravity dams. Skrikerud and Bachmann [41] developed a computational procedure that takes into account the initiation, extension, closure and reopening of discrete cracks. Dam-water interaction was not considered. Each crack was mon-itored and the topology of the finite element mesh redefined based on the state of cracking. Analysis of the Koyna dam indicates that the upper part of the dam would separate completely as the cracking extends through the cross section due to a sim-ulated earthquake with a $0.5g$ peak acceleration. The response was also dependent on the mesh refinement and orientation.

The significance of tensile cracking of mass concrete on the earthquake

response of gravity dams is still not well understood based on these few investigations. The models employed have several limitations making it difficult to draw conclusive and reliable predictions about the safety of gravity dams.

1.2 Objectives and Organization of Report

The objective of this study is to develop a numerical procedure to compute the nonlinear dynamic response of concrete dams during earthquakes. The model includes dam-water interaction with water compressibility, cavitation of the water, tensile cracking of concrete in the dam, and the approximate effects of the elastic materials that may be deposited at the reservoir bottom. The procedure employs a mixed pressure-displacement finite element formulation for the fluid, where the fluid pressure and displacement are approximated independently, and a displacement formulation for the structure. This approach, which parallels the work in Ref. [44], retains the ease of coupling the fluid elements with the structure elements, but avoids the need for reduced integration and allows easy incorporation of the bilinear fluid model to include the effects of cavitation. Tensile cracking of concrete is considered using the crack band theory with a smeared crack representation. Considerations for dynamic loads, such as closure and reopening of cracks, are established based on experimental results.

In Chapter 2 the numerical technique for computing the nonlinear transient response of fluid-structure systems is developed. The coupled governing equations are discretized, and the equations of motion are shown to be symmetric. A fully implicit and an implicit-explicit time integration methods are used to solve the equations of motion. Chapter 3 examines several fluid elements based on the mixed pressure-displacement finite element formulation introduced in Chapter 2. Through eigenvalue analyses and the patch test, the suitability of the elements is evaluated.

Also, the details for the numerical integration of the element matrices are given as well as the algorithm for the fluid state determination when cavitation is allowed. An application of the numerical procedure is presented in Chapter 4, in which the earthquake response of typical gravity dams including cavitation is examined.

Chapter 5 discusses the inclusion of concrete tensile cracking as the predominant material nonlinearity in concrete dams, and describes the crack band theory with modifications for computing dynamic response. The cracking model is incorporated in the procedure developed in Chapter 2 and the algorithm for the state determination is detailed. In Chapter 6, the nonlinear response of a typical dam-water system, including concrete cracking, to representative ground motions is assessed. The ground motions are scaled to quantify the amount of cracking, and empty and full reservoir conditions are considered. Chapter 7 presents the conclusions of this investigation and recommendations for further study.

Chapter 2

Analytical Procedure for Dynamic Response of Fluid-Structure Systems

2.1 Introduction

An analytical procedure for computing the nonlinear transient response of coupled fluid-structure systems is developed in this chapter. A mixed pressure-displacement finite element formulation is used for the fluid and a standard displacement formulation for the structure. In addition to the interaction between the fluid and the structure, the method includes an approximate model of interaction between the fluid and the elastic materials that may deposit at the bottom of the reservoir. The resulting equations of motion for the coupled system are symmetric. A fully implicit and implicit-explicit time integration schemes are employed to solve the equations of motion.

2.2 System Considered

The system under consideration, which is shown in Fig. 2.1, consists of a structure domain, Ω_S, and a fluid domain, Ω_F, with a common interface, Γ_{SF}. The normal, n, to the boundary of the fluid points out of the fluid domain. A time dependent displacement, u_g, such as due to an earthquake ground motion, may be specified along a portion of the fluid reservoir bottom, Γ_{FU}, in which materials such as sediments may exist, and structure boundary, Γ_{SU}. The free surface of the fluid is represented by the boundary Γ_{FP}. For very large, or infinite, fluid domains, it is necessary to truncate the domain at a boundary, $\Gamma_{FP'}$, to give a numerical problem

of tractable size. The boundary condition on the truncated boundary must represent the radiation of energy out of the fluid domain.

2.3 Equations of Motion for the Fluid

2.3.1 Governing Equations

An inviscid fluid undergoing small amplitude, irrotational motion satisfies the momentum balance equation,

$$\rho_0 \dot{\mathbf{v}}^t + \nabla p = \mathbf{0} \qquad (2.1)$$

the continuity equation,

$$\frac{\dot{\rho}}{\rho_0} + \nabla^T \mathbf{v}^t = 0 \qquad (2.2)$$

and an equation of state,

$$p = f(\rho) \qquad (2.3)$$

for homentropic flow [3,23]. In Eqs. 2.1 to 2.3, $\mathbf{v}^t = \mathbf{v}^t(\mathbf{x}, t)$ is the velocity of the fluid particle at position $\mathbf{x}$ and time t with respect to a fixed frame of reference; $p = p(\mathbf{x}, t)$ and $\rho = \rho(\mathbf{x}, t)$ are the change in pressure and density from the reference values p_0 and ρ_0, respectively; and $f(\rho)$ is a function that is described later in this section. The total fluid velocity, $\mathbf{v}^t$, can be expressed in terms of the relative velocity, $\mathbf{v}$, as

$$\mathbf{v}^t = \mathbf{v} + \mathbf{v}_g \qquad (2.4)$$

in which $\mathbf{v}_g$ is a specified ground velocity.

The reference (or hydrostatic) pressure can be obtained from the reference density, ρ_0, by solution of

$$\nabla p_0 = \rho_0 \mathbf{g} \qquad (2.5)$$

where $\mathbf{g}$ is the acceleration due to gravity.

2.3.2 Boundary and Initial Conditions

In addition to Eqs. 2.1 to 2.3, boundary conditions must be specified at the fluid boundaries. The derivations of the boundary conditions are presented in Appendix A. The boundary condition at the free surface is

$$\dot{p} = -\rho_0(\mathbf{n}^T\mathbf{g})\mathbf{n}^T\mathbf{v}^t \quad \text{on} \ \Gamma_{FP} \tag{2.6}$$

where a linear surface wave may develop. At the fluid-reservoir bottom boundary the condition is

$$p = \rho_r c_r \mathbf{n}^T \mathbf{v} \quad \text{on} \ \Gamma_{FU} \tag{2.7}$$

where ρ_r and c_r are the density and the velocity of pressure waves in the reservoir bottom materials, respectively; $\mathbf{v}$ is the interaction velocity, between the fluid and the materials at the bottom of the reservoir. The condition at the truncated boundary is

$$p = \rho_0 c_0 \mathbf{n}^T \mathbf{v}^t \quad \text{on} \ \Gamma_{FP'} \tag{2.8}$$

in which c_0 is the velocity of pressure waves in the fluid. Finally, at the fluid-structure interface the boundary condition is,

$$p = p_b \quad \text{on} \ \Gamma_{SF} \tag{2.9}$$

where p_b is the, yet unknown, hydrodynamic pressure at the fluid-structure interface.

At rest initial conditions for the fluid are assumed; that is,

$$\mathbf{v}^t = \mathbf{0}, \ p = 0, \ \text{and} \ \rho = 0 \quad \text{at} \ t = 0 \tag{2.10}$$

2.3.3 Governing Equations in Terms of Displacements

Anticipating that the equations of motion for the structure, formulated in terms of displacements, will be coupled with the equations for the fluid, the small

amplitude fluid motion may be represented by the total fluid displacement, $\mathbf{u}^t$, where $\mathbf{v}^t = \dot{\mathbf{u}}^t$ and $\mathbf{v}_g = \dot{\mathbf{u}}_g$. The total fluid displacement can be expressed as

$$\mathbf{u}^t = \mathbf{u} + \mathbf{u}_g \qquad (2.11)$$

where $\mathbf{u}$ is the displacement of the fluid with respect to the specified motion, $\mathbf{u}_g$, at the base of the fluid-structure system. Observe also that this representation of the fluid displacement yields, $\mathbf{v} = \dot{\mathbf{u}}$. Substitution of Eq. 2.11 into Eq. 2.1 gives the momentum balance equation in terms of relative fluid displacement

$$\rho_0 \ddot{\mathbf{u}} + \nabla p + \rho_0 \ddot{\mathbf{u}}_g = \mathbf{0} \qquad (2.12)$$

Integration of Eq. 2.2 over time with the initial conditions, Eq. 2.10, gives the change in density of the fluid,

$$\rho = -\rho_0 \nabla^T \mathbf{u} \qquad (2.13)$$

because $\nabla^T \mathbf{u}_g = 0$ when the boundaries Γ_{FU} and Γ_{SU} move in a rigid manner. In terms of the fluid displacement, the boundary conditions in Eqs. 2.6-2.9 are,

$$p = -\rho_0 (\mathbf{n}^T \mathbf{g}) \mathbf{n}^T (\mathbf{u} + \mathbf{u}_g) \quad \text{on} \quad \Gamma_{FP} \qquad (2.14)$$

$$p = \rho_r c_r \mathbf{n}^T \dot{\mathbf{u}} \quad \text{on} \quad \Gamma_{FU} \qquad (2.15)$$

$$p = \rho_0 c_0 \mathbf{n}^T (\dot{\mathbf{u}} + \dot{\mathbf{u}}_g) \quad \text{on} \quad \Gamma_{FP'} \qquad (2.16)$$

$$p = p_b \quad \text{on} \quad \Gamma_{SF} \qquad (2.17)$$

In Eq. 2.15, $\rho_r c_r$ can be alternatively expressed as [15],

$$\rho_r c_r = \rho_0 c_0 \frac{1 + \alpha_r}{1 - \alpha_r} \qquad (2.18)$$

where α_r is the wave reflection coefficient, which is defined as the amplitude of the reflected hydrodynamic pressure waves due to a unit vertically propagating pressure

wave incident on the reservoir bottom. It is believed [15] that values of the wave reflection coefficient, α_r, may range between 1 and 0. For rigid reservoir bottom materials, $\alpha_r = 1$, and for very soft reservoir bottom materials, $\alpha_r = 0$, meaning full absorption of vertically incident pressure waves.

2.3.4 Equation of State Including Cavitation

The equation of state for an ideal, barotropic fluid gives the hydrodynamic pressure as a unique function of the change in density, ρ (see Eq. 2.3). The equation of state is [3]

$$p = c_0^2 \rho \tag{2.19}$$

However, fluids can not develop an absolute pressure less than the vapor pressure of the fluid. When the absolute pressure, $p + p_0$, equals the vapor pressure, p_v (measured with respect to the atmospheric pressure), dissolved gasses in the fluid form a cavitated region. With continued expansion of the cavitated region, the density decreases at the roughly constant vapor pressure. The gaseous, or cavitated, region is maintained until external forces increase the density of the fluid enough to collapse the cavitated region.

To model the effects of cavitation, Bleich and Sandler [10] proposed a continuum model of the fluid in which the fluid is linearly compressible if the absolute pressure is greater than the vapor pressure. However, if the pressure drops below p_v, the gaseous, cavitated region is represented as a fluid with a velocity of wave propagation near zero. This model results in a bilinear equation of state, where the velocity of wave propagation depends on the density [10],

$$p = c_0^2 \rho, \qquad \text{for} \quad \rho \geq \frac{p_v - p_0}{c_0^2} \tag{2.20}$$

$$p = (\beta_0 c_0)^2 \rho + (1 - \beta_0^2)(p_v - p_0), \quad \text{for} \quad \rho \le \frac{p_v - p_0}{c_0^2} \tag{2.21}$$

The constant β_0 represents the resistance of the cavitated region to expansion. The constant is normally assumed zero, but Bleich and Sandler state that it should be nonzero if the cavitated region is in contact with the fluid-structure interface [10]. The bilinear equation of state is depicted in Fig. 2.2.

2.3.5 Weak Form of Governing Equations

The finite element discretization of the fluid can be obtained from the weak form of the governing equations. The weak form of the momentum balance equation, Eq. 2.12, is

$$\int_{\Omega_F} \delta \mathbf{u}^T (\rho_0 \ddot{\mathbf{u}} + \nabla p + \rho_0 \ddot{\mathbf{u}}_g) \, d\Omega = 0 \tag{2.22}$$

where $\delta \mathbf{u}$ is an arbitrary displacement field. Use of the divergence theorem on the second term in the integrand of Eq. 2.22, with the boundary conditions, Eqs. 2.14-2.17, gives,

$$\int_{\Omega_F} \delta \mathbf{u}^T \rho_0 \ddot{\mathbf{u}} \, d\Omega + \int_{\Gamma_{FU}} \delta \mathbf{u}^T \mathbf{n} \rho_r c_r \mathbf{n}^T \dot{\mathbf{u}} \, d\Gamma + \int_{\Gamma_{FP'}} \delta \mathbf{u}^T \mathbf{n} \rho_0 c_0 \mathbf{n}^T (\dot{\mathbf{u}} + \dot{\mathbf{u}}_g) \, d\Gamma$$

$$- \int_{\Gamma_{FP}} \delta \mathbf{u}^T \mathbf{n} \rho_0 (\mathbf{n}^T \mathbf{g}) \mathbf{n}^T (\mathbf{u} + \mathbf{u}_g) \, d\Gamma - \int_{\Omega_F} \nabla^T \delta \mathbf{u} \, p \, d\Omega$$

$$+ \int_{\Gamma_{SF}} \delta \mathbf{u}^T \mathbf{n} \, p_b \, d\Gamma + \int_{\Omega_F} \delta \mathbf{u}^T \rho_0 \ddot{\mathbf{u}}_g \, d\Omega = 0 \tag{2.23}$$

In a displacement finite element formulation, the equation of state is satisfied point-by-point in the fluid domain by substituting Eqs. 2.20-2.21 into Eq. 2.23 and relating density to displacements by the continuity equation, Eq. 2.13. The present mixed formulation satisfies the equation of state in the "weak," or average sense. The weak form of the equation of state is obtained by expressing the density

in terms of the pressure, from Eqs. 2.20-2.21, multiplying by an arbitrary pressure field, δp, and integrating over the domain of the fluid, Ω_F,

$$\int_{\Omega_F} \delta p \left(\frac{p}{c^2 \rho_0} - \frac{\rho^u}{\rho_0} - \frac{\rho}{\rho_0} \right) d\Omega = 0 \qquad (2.24)$$

where

$$c = c_0, \quad \rho^u = 0, \quad \text{for} \quad \rho \geq \frac{p_v - p_0}{c_0^2} \qquad (2.25)$$

$$c = \beta_0 c_0, \quad \rho^u = \frac{(1 - \beta_0^2)(p_v - p_0)}{(\beta_0 c_0)^2}, \quad \text{for} \quad \rho \leq \frac{p_v - p_0}{c_0^2} \qquad (2.26)$$

Substitution of the continuity equation, Eq. 2.13, into Eq. 2.24 gives the weak form of the equation of state used in the present formulation

$$\int_{\Omega_F} \delta p \left(\frac{p}{c^2 \rho_0} - \frac{\rho^u}{\rho_0} + \nabla^T \mathbf{u} \right) d\Omega = 0 \qquad (2.27)$$

The mixed finite element formulation of the fluid domain is based on the weak form of the governing equations, Eqs. 2.23 and 2.27. The evaluation of the integrals in Eqs. 2.23 and 2.27 require that the functions $\mathbf{u}$ and $\delta\mathbf{u}$ be piecewise continuous; however, p and δp may be discontinuous functions because their derivatives do not appear in the integrands.

2.3.6 Finite Element Discretization

In the present formulation, different or mixed finite element approximations for the displacement and pressure are adopted. In each element, the displacements are given by

$$\mathbf{u} = \mathbf{N}_I^F \mathbf{u}_I \qquad (2.28)$$

$$\delta\mathbf{u} = \mathbf{N}_I^F \delta\mathbf{u}_I \qquad (2.29)$$

where $\mathbf{N}_I^F$ are specified, piecewise continuous, shape functions for node I, $\mathbf{u}_I$ and $\delta\mathbf{u}_I$ are vectors of displacements at node I, and repeated subscripts indicate summation

over the nodes of an element. Independent of the displacements, the pressure field in an element is approximated by

$$p = R_I p_I \tag{2.30}$$

$$\delta p = R_I \delta p_I \tag{2.31}$$

where R_I is a specified pressure function, corresponding to pressure parameter p_I, that is continuous over the element but may be discontinuous across element boundaries. The pressure parameters, p_I, are not necessarily associated with nodes because of the relaxed continuity requirements for the pressure function in the weak forms. The criteria for selecting the displacement and pressure shape functions will be established in Chapter 3.

Working first with the weak form of the equation of state, Eq. 2.27 is divided into integrals over element subdomains, Ω_{F_e}. Substitution of Eqs. 2.28-2.31 into Eq. 2.27, then gives

$$\int_{\Omega_{F_e}} \delta p_L \left(R_L \frac{1}{c^2 \rho_0} R_K p_K - R_L \frac{\rho^u}{\rho_0} + R_L B_J^F u_J \right) d\Omega = 0 \tag{2.32}$$

where $B_I^F = \nabla^T N_I^F$. For arbitrary δp_L, the solution of Eq. 2.32 for the pressure parameters in an element is

$$p_K = -(h_{LK})^{-1} g_{LJ} u_J + (h_{LK})^{-1} p_L^u \tag{2.33}$$

where

$$h_{LK} = \int_{\Omega_{F_e}} R_L \frac{1}{c^2 \rho_0} R_K \, d\Omega \tag{2.34}$$

$$g_{LJ} = \int_{\Omega_{F_e}} R_L B_J^F \, d\Omega \tag{2.35}$$

$$p_L^u = \int_{\Omega_{F_e}} R_L \frac{\rho^u}{\rho_0} \, d\Omega \tag{2.36}$$

Returning to the weak form of the momentum balance equation, the substitution of Eqs. 2.28-2.31 into Eq. 2.23, with the integration performed over the element subdomains, for arbitrary δu_I, gives

$$\sum_e \left\{ m_{IJ}^F \ddot{u}_J + (c_{IJ}^{F'} + c_{IJ}^{F''}) \dot{u}_J + (k_f)_{IJ}^F u_J - g_{KI}^T p_K + p_I^F \right.$$

$$\left. + m_{IJ}^F r_J \ddot{u}_g + c_{IJ}^{F'} r_J \dot{u}_g + (k_f)_{IJ}^F r_J u_g \right\} = 0 \qquad (2.37)$$

where the summation indicates assembly over the elements in the fluid domain, and

$$m_{IJ}^F = \int_{\Omega_{F_e}} (N_I^F)^T \rho_0 N_J^F \, d\Omega \qquad (2.38)$$

$$c_{IJ}^{F'} = \int_{\Gamma_{FP'_e}} (N_I^F)^T n \rho_0 c_0 n^T N_J^F \, d\Gamma \qquad (2.39)$$

$$c_{IJ}^{F''} = \int_{\Gamma_{FU_e}} (N_I^F)^T n \rho_r c_r n^T N_J^F \, d\Gamma \qquad (2.40)$$

$$(k_f)_{IJ}^F = - \int_{\Gamma_{FP_e}} (N_I^F)^T n \rho_0 (n^T g) n^T N_J^F \, d\Gamma \qquad (2.41)$$

$$p_I^F = \int_{\Gamma_{SF_e}} (N_I^F)^T n \, p_b \, d\Gamma \qquad (2.42)$$

The terms that are proportional to the ground motion in Eq. 2.37 result from the fact that $u_g = N_J r_J u_g$ for the matrix r_J representing rigid-body motion of the element.

Substitution of Eq. 2.33 into Eq. 2.37 at the element level and assembly of the element contributions gives the equations of motion for the fluid

$$M^F \ddot{U}^F + C^F \dot{U}^F + K_f^F U + F^F = -M^F R^F \ddot{u}_g - C^{F'} R^F \dot{u}_g - K_f^F R^F u_g - P^F \qquad (2.43)$$

where $C^F = C^{F'} + C^{F''}$, and M^F, $C^{F'}$, $C^{F''}$, K_f^F and P_F are assembled from the element matrices defined in Eqs. 2.38-2.42. The matrix R^F represents rigid-body motion of the discretized fluid domain. The vector of nonlinear restoring forces, F^F, is assembled from

$$f_I^F = -g_{KI}^T p_K \qquad (2.44)$$

which upon substitution of Eq. 2.33 yields

$$\mathbf{f}_I^F = (\mathbf{k}_T)_{IJ}^F \mathbf{u}_J - \mathbf{g}_{KI}^T (h_{LK})^{-1} p_L^u \qquad (2.45)$$

where

$$(\mathbf{k}_T)_{IJ}^F = \mathbf{g}_{KI}^T (h_{LK})^{-1} \mathbf{g}_{LJ} \qquad (2.46)$$

is the tangent stiffness matrix for the fluid element.

In Eq. 2.43, the velocity dependent damping force and dynamic force proportional to the ground velocity develop because of the radiation condition at the truncated and absorptive boundaries. Because of the assumption of inviscid fluid there is no internal damping, so a finite fluid domain with rigid boundaries will have no damping. Also note that ground displacement components tangential to the free surface and the absorptive boundary, and ground velocity components tangential to the truncated or absorptive boundaries do not introduce forces on the right hand side of Eq. 2.43; the terms are retained for the case of general ground motion.

2.3.7 Irrotationality Condition

The motion of the fluid is irrotational if the initial conditions are irrotational. This is shown by taking the curl of Eq. 2.1 to find that $curl\ \ddot{\mathbf{v}}^t = 0$, which upon double integration with respect to time, and recognizing that $curl\ \mathbf{u}_g = 0$, gives the irrotationality condition in terms of fluid displacement: $curl\ \mathbf{u} = 0$. However, because of errors introduced by discretization and time integration of the equations of motion, vorticity can develop in the numerical solution. The condition of irrotational motion can be satisfied numerically by augmenting the weak form of the momentum balance equation, Eq. 2.22, with a penalty constraint [19,46]

$$\int_{\Omega_F} \delta \mathbf{u}^T (\rho_0 \ddot{\mathbf{u}} + \nabla p + \rho_0 \ddot{\mathbf{u}}_g)\, d\Omega + \alpha \int_{\Omega_F} \delta \omega^T \omega\, d\Omega = 0 \qquad (2.47)$$

where $\omega = curl\ \mathbf{u}$ and α is a penalty parameter.

In the finite element discretization,

$$\omega = \mathbf{W}_I^F \mathbf{u}_I \tag{2.48}$$

$$\delta\omega = \mathbf{W}_I^F \delta\mathbf{u}_I \tag{2.49}$$

where $\mathbf{W}_I^F = curl\ \mathbf{N}_I^F$. Substituting Eqs. 2.48-2.49 into the weak form, Eq. 2.47, adds a stiffness term to the equations of motion for the fluid, Eq. 2.43,

$$\mathbf{M}^F\ddot{\mathbf{U}}^F + \mathbf{C}^F\dot{\mathbf{U}}^F + \mathbf{K}^F\mathbf{U} + \mathbf{F}^F = -\mathbf{M}^F\mathbf{R}^F\ddot{\mathbf{u}}_g - \mathbf{C}^{F'}\mathbf{R}^F\dot{\mathbf{u}}_g - \mathbf{K}_f^F\mathbf{R}^F\mathbf{u}_g - \mathbf{P}^F \tag{2.50}$$

where $\mathbf{K}^F = \mathbf{K}_f^F + \mathbf{K}_w^F$, and $\mathbf{K}_w^F$ is assembled from

$$(\mathbf{k}_w^F)_{IJ} = \alpha \int_{\Omega_{F_e}} (\mathbf{W}_I^F)^T \mathbf{W}_J^F\ d\Omega \tag{2.51}$$

The penalty parameter, α, must be large enough to enforce the irrotationality constraint, and Eq. 2.51 must be evaluated numerically with reduced integration to prevent locking of the elements [46]. Selection of α is discussed in Chapter 3.

2.4 Equations of Motion for the Structure

Using standard procedures for the finite element discretization of the structural domain, Ω_S, the equations of motion for the structure subjected to ground motion are

$$\mathbf{M}^S\ddot{\mathbf{U}}^S + \mathbf{C}^S\dot{\mathbf{U}}^S + \mathbf{F}^S = -\mathbf{M}^S\mathbf{R}^S\ddot{\mathbf{u}}_g + \mathbf{P}^S \tag{2.52}$$

where $\mathbf{U}^S$ is the vector of displacements of the nodes with respect to the motion, $\mathbf{u}_g$, of boundary, Γ_{SU}; $\mathbf{M}^S$ and $\mathbf{C}^S$ are the mass and damping matrices of the structure, respectively; and $\mathbf{F}^S$ is the vector of restoring forces. For a linear, elastic structure, $\mathbf{F}^S = \mathbf{K}^S\mathbf{U}^S$, where $\mathbf{K}^S$ is the stiffness matrix of the structure. The vector $\mathbf{P}^S$ is

assembled from the vector, $\mathbf{p}_I^S$, of forces on the elements due to the pressure, p_b, at the fluid-structure interface,

$$\mathbf{p}_I^S = \int_{\Gamma_{SF_e}} (\mathbf{N}_I^S)^T \mathbf{n}\ p_b\ d\Gamma \tag{2.53}$$

in which $\mathbf{N}_I^S$ is the shape function for node I of the structure.

2.5 Coupling of Fluid and Structure

The fluid and structure are coupled by the compatibility requirement that the normal displacements at the interface, Γ_{SF}, are equal. To enforce compatibility, the equations of motion for the fluid domain, Eq. 2.50, are partitioned into displacement components normal to Γ_{SF}, denoted by subscript B, and all other components, denoted by subscript F. Thus, Eq. 2.50 for the fluid becomes,

$$\begin{bmatrix} \mathbf{M}_{FF}^F & \mathbf{M}_{FB}^F \\ \mathbf{M}_{BF}^F & \mathbf{M}_{BB}^F \end{bmatrix} \left\{ \begin{array}{c} \ddot{\mathbf{U}}_F \\ \ddot{\mathbf{U}}_B \end{array} \right\} + \begin{bmatrix} \mathbf{C}_{FF}^F & \mathbf{0} \\ \mathbf{0} & \mathbf{0} \end{bmatrix} \left\{ \begin{array}{c} \dot{\mathbf{U}}_F \\ \dot{\mathbf{U}}_B \end{array} \right\} + \begin{bmatrix} \mathbf{K}_{FF}^F & \mathbf{K}_{FB}^F \\ \mathbf{K}_{BF}^F & \mathbf{K}_{BB}^F \end{bmatrix} \left\{ \begin{array}{c} \mathbf{U}_F \\ \mathbf{U}_B \end{array} \right\}$$

$$+ \left\{ \begin{array}{c} \mathbf{F}_F^F \\ \mathbf{F}_B^F \end{array} \right\} = - \begin{bmatrix} \mathbf{M}_{FF}^F & \mathbf{M}_{FB}^F \\ \mathbf{M}_{BF}^F & \mathbf{M}_{BB}^F \end{bmatrix} \left\{ \begin{array}{c} \mathbf{R}_F \\ \mathbf{R}_B \end{array} \right\} \ddot{u}_g - \begin{bmatrix} \mathbf{C}_{FF}^{F'} & \mathbf{0} \\ \mathbf{0} & \mathbf{0} \end{bmatrix} \left\{ \begin{array}{c} \mathbf{R}_F \\ \mathbf{R}_B \end{array} \right\} \dot{u}_g$$

$$- \begin{bmatrix} (\mathbf{K}_f^F)_{FF} & (\mathbf{K}_f^F)_{FB} \\ (\mathbf{K}_f^F)_{BF} & \mathbf{0} \end{bmatrix} \left\{ \begin{array}{c} \mathbf{R}_F \\ \mathbf{R}_B \end{array} \right\} u_g - \left\{ \begin{array}{c} \mathbf{0} \\ \mathbf{P}_B^F \end{array} \right\} \tag{2.54}$$

Eq. 2.52 for the structure is partitioned into displacement components normal to Γ_{SF}, denoted also by subscript B, and all other components, denoted by subscript S,

$$\begin{bmatrix} \mathbf{M}_{BB}^S & \mathbf{M}_{BS}^S \\ \mathbf{M}_{SB}^S & \mathbf{M}_{SS}^S \end{bmatrix} \left\{ \begin{array}{c} \ddot{\mathbf{U}}_B \\ \ddot{\mathbf{U}}_S \end{array} \right\} + \begin{bmatrix} \mathbf{C}_{BB}^S & \mathbf{C}_{BS}^S \\ \mathbf{C}_{SB}^S & \mathbf{C}_{SS}^S \end{bmatrix} \left\{ \begin{array}{c} \dot{\mathbf{U}}_B \\ \dot{\mathbf{U}}_S \end{array} \right\} + \left\{ \begin{array}{c} \mathbf{F}_B^S \\ \mathbf{F}_S^S \end{array} \right\} =$$

$$- \begin{bmatrix} \mathbf{M}_{BB}^S & \mathbf{M}_{BS}^S \\ \mathbf{M}_{SB}^S & \mathbf{M}_{SS}^S \end{bmatrix} \left\{ \begin{array}{c} \mathbf{R}_B \\ \mathbf{R}^S \end{array} \right\} \ddot{u}_g + \left\{ \begin{array}{c} \mathbf{P}_B^S \\ \mathbf{0} \end{array} \right\} \tag{2.55}$$

The partitioned equations of motion, Eqs. 2.54 and 2.55, include transformation of the displacements at the fluid-structure interface into components normal and tangential to the interface. The normal components are placed in partition B,

and the tangential components are placed in partitions F or S. Each interface node then has $2n-1$ degrees-of-freedom, where n is the number of spatial dimensions. The transformations are carried out using standard procedures, one node at a time, at the element level and are presented in Appendix B. Fig. 2.3 shows the partitioning of the displacement components for the two domains and fluid-structure interface.

For compatibility of the normal displacements along the interface, the shape functions $\mathbf{N}_I^S$ for the structure elements and $\mathbf{N}_I^F$ for the fluid elements must be identical for common nodes on the interface. Consequently, the forces due to hydrodynamic pressure at the interface are automatically in equilibrium, $\mathbf{P}_B^F = \mathbf{P}_B^S$, according to Eqs. 2.42 and 2.53.

Using the compatibility conditions and the resulting equilibrium of forces at the interface, the combination of partitioned Eqs. 2.54 and 2.55, a direct assembly operation, gives the coupled equations of motion for the fluid-structure system,

$$
\begin{bmatrix} \mathbf{M}_{FF}^F & \mathbf{M}_{FB}^F & \mathbf{0} \\ \mathbf{M}_{BF}^F & \mathbf{M}_{BB}^F + \mathbf{M}_{BB}^S & \mathbf{M}_{BS}^S \\ \mathbf{0} & \mathbf{M}_{SB}^S & \mathbf{M}_{SS}^S \end{bmatrix} \begin{Bmatrix} \ddot{\mathbf{U}}_F \\ \ddot{\mathbf{U}}_B \\ \ddot{\mathbf{U}}_S \end{Bmatrix} + \begin{bmatrix} \mathbf{C}_{FF}^F & \mathbf{0} & \mathbf{0} \\ \mathbf{0} & \mathbf{C}_{BB}^S & \mathbf{C}_{BS}^S \\ \mathbf{0} & \mathbf{C}_{SB}^S & \mathbf{C}_{SS}^S \end{bmatrix} \begin{Bmatrix} \dot{\mathbf{U}}_F \\ \dot{\mathbf{U}}_B \\ \dot{\mathbf{U}}_S \end{Bmatrix} +
$$

$$
\begin{bmatrix} \mathbf{K}_{FF}^F & \mathbf{K}_{FB}^F & \mathbf{0} \\ \mathbf{K}_{BF}^F & \mathbf{K}_{BB}^F & \mathbf{0} \\ \mathbf{0} & \mathbf{0} & \mathbf{0} \end{bmatrix} \begin{Bmatrix} \mathbf{U}_F \\ \mathbf{U}_B \\ \mathbf{U}_S \end{Bmatrix} + \begin{Bmatrix} \mathbf{F}_F^F \\ \mathbf{F}_B^F + \mathbf{F}_B^S \\ \mathbf{F}_S^S \end{Bmatrix} = - \begin{bmatrix} \mathbf{M}_{FF}^F & \mathbf{M}_{FB}^F & \mathbf{0} \\ \mathbf{M}_{BF}^F & \mathbf{M}_{BB}^F + \mathbf{M}_{BB}^S & \mathbf{M}_{BS}^S \\ \mathbf{0} & \mathbf{M}_{SB}^S & \mathbf{M}_{SS}^S \end{bmatrix}
$$

$$
\begin{Bmatrix} \mathbf{R}_F \\ \mathbf{R}_B \\ \mathbf{R}^S \end{Bmatrix} \ddot{u}_g - \begin{bmatrix} \mathbf{C}_{FF}^{F'} & \mathbf{0} & \mathbf{0} \\ \mathbf{0} & \mathbf{0} & \mathbf{0} \\ \mathbf{0} & \mathbf{0} & \mathbf{0} \end{bmatrix} \begin{Bmatrix} \mathbf{R}_F \\ \mathbf{R}_B \\ \mathbf{R}^S \end{Bmatrix} \dot{u}_g - \begin{bmatrix} (\mathbf{K}_f^F)_{FF} & (\mathbf{K}_f^F)_{FB} & \mathbf{0} \\ (\mathbf{K}_f^F)_{BF} & \mathbf{0} & \mathbf{0} \\ \mathbf{0} & \mathbf{0} & \mathbf{0} \end{bmatrix} \begin{Bmatrix} \mathbf{R}_F \\ \mathbf{R}_B \\ \mathbf{R}^S \end{Bmatrix} u_g
$$

$$(2.56)$$

When needed, the pressure in a fluid element is computed from $p = R_K p_K$, where p_K is given by Eq. 2.33, in which h_{LK} and p_K^u are determined from the density, $\rho = -\rho_0 \mathbf{B}_I^F \mathbf{u}_I$ (from Eq. 2.13).

The coupling of the response of the fluid and structural domains is represented very directly by the symmetric equations of motion in Eq. 2.56. The mass and

stiffness contributions of the fluid and structure are simply added at the common normal degrees-of-freedom along the interface. It is not necessary to compute integrals over the interface to represent the coupling. The bandwidth of the matrices is typical of standard displacement elements, with the exception of the normal degrees-of-freedom on the interface which can be handled effectively by profile storage of the matrices.

2.6 Solution of Coupled Equations of Motion

For convenience in describing the solution of the equations of motion for the fluid-structure system, Eq. 2.56 can be expressed as

$$\mathbf{M}\ddot{\mathbf{X}} + \mathbf{C}\dot{\mathbf{X}} + \mathbf{K}\mathbf{X} + \mathbf{F} = -\mathbf{M}\mathbf{R}\ddot{u}_g - \mathbf{C}_F\mathbf{R}\dot{u}_g - \mathbf{K}_F\mathbf{R}u_g \qquad (2.57)$$

where $\mathbf{X} = [\mathbf{U}_F^T \ \mathbf{U}_B^T \ \mathbf{U}_S^T]$, and the definitions of $\mathbf{M}$, $\mathbf{C}$, $\mathbf{C}_F$, $\mathbf{K}$, $\mathbf{K}_F$, $\mathbf{F}$ and $\mathbf{R}$ follow from the corresponding terms in Eq. 2.56. Because the restoring force, $\mathbf{F}$, is a nonlinear function of $\mathbf{X}$, Eq. 2.57 must be solved in the time domain. The present study applies two methods of time integration to the solution of Eq. 2.57; a fully implicit method and an implicit-explicit procedure. Both time integration schemes follow the description in Ref. [21].

2.6.1 Fully Implicit Method

If the solution at time step t_n is known, $\mathbf{X}_n = \mathbf{X}(t_n)$, $\dot{\mathbf{X}}_n = \dot{\mathbf{X}}(t_n)$ and $\ddot{\mathbf{X}}_n = \ddot{\mathbf{X}}(t_n)$, the solution at time step $t_{n+1} = t_n + \Delta t$ is sought,

$$\mathbf{M}\ddot{\mathbf{X}}_{n+1} + \mathbf{C}\dot{\mathbf{X}}_{n+1} + \mathbf{K}\mathbf{X}_{n+1} + \mathbf{F}_{n+1} = -\mathbf{M}\mathbf{R}\ddot{u}_{g(n+1)} - \mathbf{C}_F\mathbf{R}\dot{u}_{g(n+1)} - \mathbf{K}_F\mathbf{R}u_{g(n+1)}$$

$$(2.58)$$

where

$$\mathbf{X}_{n+1} = \tilde{\mathbf{X}}_{n+1} + (\Delta t)^2\beta\ddot{\mathbf{X}}_{n+1} \qquad (2.59)$$

$$\dot{X}_{n+1} = \tilde{\dot{X}}_{n+1} + (\Delta t)\gamma\ddot{X}_{n+1} \qquad (2.60)$$

in which

$$\tilde{X}_{n+1} = X_n + \Delta t\dot{X}_n + \frac{(\Delta t)^2}{2}(1 - 2\beta)\ddot{X}_n \qquad (2.61)$$

$$\tilde{\dot{X}} = \dot{X}_n + \Delta t(1 - \gamma)\ddot{X}_n \qquad (2.62)$$

In Eqs. 2.59-2.62, Δt is a specified time step, and β, γ are parameters of the time integration procedure. In the procedure, Eq. 2.58 is expressed as an equivalent static problem in terms of X_{n+1} by substitution of Eqs. 2.59-2.62. Because the restoring force, F_{n+1}, is a nonlinear function of X_{n+1}, the equivalent static problem can be solved by a Newton-Raphson procedure that iterates until convergence is achieved. The algorithm, described in [21], applied to Eq. 2.58 is as follows:

1. $X_n, \dot{X}_n, \ddot{X}_n$ are known; set iteration counter, $i = 0$.

2. Predict response at t_{n+1};

$$X^i_{n+1} = \tilde{X}_{n+1} \qquad (2.63)$$

$$\dot{X}^i_{n+1} = \tilde{\dot{X}}_{n+1} \qquad (2.64)$$

$$\ddot{X}^i_{n+1} = 0 \qquad (2.65)$$

3. Form vector of unbalanced forces;

$$\Delta F = -MR\ddot{u}_{g(n+1)} - C_F R\dot{u}_{g(n+1)} - K_F Ru_{g(n+1)}$$
$$- M\ddot{X}^i_{n+1} - C\dot{X}^i_{n+1} - KX^i_{n+1} - F^i_{n+1} \qquad (2.66)$$

where F^i_{n+1} is assembled from the element contributions as follows,

(a) *Fluid Elements*. For each fluid element the resisting forces are calculated from Eq. 2.44. Chapter 3, presents a detailed procedure for the state determination of the fluid.

(b) *Structural Elements.* The resisting forces for the structural elements are evaluated using standard procedures. Chapter 5 presents a detailed treatment of nonlinear models for the structure, particularly the effects of tensile cracking in concrete.

4. Obtain the equivalent dynamic stiffness matrix

$$K^* = \frac{1}{(\Delta t)^2 \beta} M + \frac{\gamma}{\Delta t \beta} C + K + K_T^F + K_T^S \tag{2.67}$$

where K_T^F, as defined in Eq. 2.46, and K_T^S, the tangent stiffness matrices for the fluid and structure, are assembled from the element contributions, which are conveniently computed in Step 3.

5. Solve for the incremental displacements

$$K^* \Delta X = \Delta F \tag{2.68}$$

6. Update the response

$$X_{n+1}^{i+1} = X_{n+1}^i + \Delta X \tag{2.69}$$

$$\ddot{X}_{n+1}^{i+1} = \frac{1}{(\Delta t)^2 \beta}(X_{n+1}^{i+1} - \tilde{X}_{n+1}) \tag{2.70}$$

$$\dot{X}_{n+1}^{i+1} = \dot{\tilde{X}}_{n+1} + \Delta t\, \gamma\, \ddot{X}_{n+1}^{i+1} \tag{2.71}$$

7. Check if the unbalanced force and incremental displacements are within acceptable tolerances. If so, the last iterate gives the solution for X_{n+1}, $\dot{X}_{n+1}$ and $\ddot{X}_{n+1}$. If not, increment the iteration counter, $i \leftarrow i + 1$, and go to step 3.

To start the time integration, at rest initial conditions are assumed, so $X_0 = 0$, $\dot{X}_0 = 0$; $\ddot{X}_0$ can be obtained by solution of Eq. 2.57 at time zero.

2.6.2 Implicit-Explicit Method

The fully implicit method requires the assembly and factorization of the tangent stiffness matrices for the fluid and the structure at every iteration in every time step. Although, as it will be shown through example, equilibrium convergence in a time step is rapid, it is possible to avoid the assembly and factorization of $\mathbf{K}^*$ by evaluating the nonlinear restoring force explicitly. There is no advantage in evaluating the nonlinear restoring force in the fluid explicitly because of the near incompressible behavior of the fluid. However, when nonlinear models for the structure are included (Chapter 5) there may be computational advantage in evaluating $\mathbf{F}^S$ explicitly. The implicit-explicit algorithm is nearly identical to the fully implicit algorithm described above, with two exceptions [21]:

1. In Step 3, the unbalanced force is computed based on an explicit evaluation of the restoring force in the structure using the predicted displacements;

$$\Delta \mathbf{F} = -\mathbf{M}\mathbf{R}\ddot{\mathbf{u}}_{g(n+1)} - \mathbf{C}_F\mathbf{R}\dot{\mathbf{u}}_{g(n+1)} - \mathbf{K}_F\mathbf{R}\mathbf{u}_{g(n+1)} - \mathbf{M}\ddot{\mathbf{X}}^i_{n+1}$$

$$- \mathbf{C}\dot{\mathbf{X}}^i_{n+1} - \mathbf{K}\mathbf{X}^i_{n+1} - \left\{ \begin{array}{c} \mathbf{F}^F_F \\ \mathbf{F}^F_B \\ 0 \end{array} \right\}^i_{n+1} - \left\{ \begin{array}{c} 0 \\ \mathbf{F}^S_B \\ \mathbf{F}^S_S \end{array} \right\}_{n+1} \qquad (2.72)$$

where the fluid restoring force is evaluated as before, but the structure restoring force, $\mathbf{F}_S$, is evaluated at the displacements $\tilde{\mathbf{X}}_{n+1}$, which do not change during a time step.

2. The effective dynamic stiffness matrix is

$$\mathbf{K}^* = \frac{1}{(\Delta t)^2 \beta}\mathbf{M} + \frac{\gamma}{\Delta t \beta}\mathbf{C} + \mathbf{K} + \mathbf{K}^F_T \qquad (2.73)$$

in which the structure elements do not contribute to the tangent stiffness matrix.

2.7 Application to One-Dimensional Systems

To demonstrate the numerical procedure developed in the previous sections, the transient response of an idealized fluid-structure system is computed. The structure is represented by a single degree-of-freedom oscillator, and the fluid is modeled as a one-dimensional domain. For the one-dimensional domain, there are no surface waves and the motion is irrotational by definition. The fluid is discretized using two-node elements with constant pressure over the element and linearly varying displacement. For this case, the displacement and mixed formulations give the same element stiffness matrix.

2.7.1 Response to Pressure Pulse

The system considered is shown in Fig. 2.4, where a 5 ft. long fluid domain is discretized by forty elements. A constant pressure pulse is applied at the far end of the fluid. The structure has a mass of 10 lb-sec^2/ft and stiffness of 10^4 K/ft . For the fluid, $\rho_0 = 1$ lb-sec^2/ft^4 and $c_0 = 5000$ ft/sec . This problem was considered in Ref. [24] and is included here for comparison.

The response of the system is computed for two cases, a linear fluid ($\beta_0 = 1$) and a fluid that cavitates ($\beta_0 = 0$) when the dynamic pressure is less than zero (assume $p_0 = p_v = 0$). The equations of motion were solved using the fully implicit time integration method with $\beta = 0.25$ and $\gamma = 0.5$. Based on accuracy considerations a time step of $\Delta t = 2 \times 10^{-5}$ seconds was used. The response of the system is shown in Fig. 2.5, where normalized pressure, $p/\bar{p}_0$, in the fluid at the structure interface and displacement, $uk/\bar{p}_0$, of the structure are plotted with respect to time, tc_0/L. For the linearly compressible fluid, the response results represent the pressure peaks and arrival time well, and they are in close agreement with the results in Ref.[24].

Cavitation, of course, limits the minimum pressure of the fluid, as clearly shown in Fig. 2.5. In addition, cavitation limits the magnitude of the subsequent maximum pressure peaks. However, for this system and loading, cavitation has a negligible effect on the displacement of the structure. Even with the bilinear model for the cavitating fluid, convergence of the solution procedure was very rapid, in at most two cycles of iteration in a time step.

2.7.2 Response to Ground Motion

The idealized one-dimensional fluid-structure system shown in Fig. 2.6, has a radiating boundary at the end of the 900 ft long fluid domain, which was discretized by twenty elements. The structure has a mass of 58.7 $K\text{-sec}^2/\text{ft}$, natural vibration frequency of 30 rad/sec, yield strength and yield displacement of 1320 kips and 0.30 in, respectively. For the fluid, $\rho_0 = 1.94$ $\text{lb-sec}^2/\text{ft}^4$ and $c_0 = 4720$ ft/sec. The ground motion is idealized by a sinusoidal ground acceleration with a peak value of 0.31g and an excitation frequency equal to 0.70 times the natural vibration frequency of the structure. Artificial damping is included in the fluid to eliminate high-frequency noise from the numerical solution. Numerical experiments demonstrate that the response is not sensitive to the small amount of artifical damping.

Several cases of the fluid-structure system were considered. First, a linear fluid and a cavitating fluid [with $p_0 = 40$ psi, and $p_v = 0$] were considered. In combination, a linear structure and a nonlinear structure, modeled as an elasto-plastic spring, were also considered. The yield strength of the spring was chosen to be two-thirds of the maximum force developed in the linear structure (without the fluid) due to the ground motion. A time step of $\Delta t = 0.01$ sec was adequate for a linear system or one nonlinear component. For an elasto-plastic structure and

bilinear fluid, a time step of 0.005 sec was necessary for an accurate solution. Again, the convergence of the procedure was very rapid, never requiring more than three iterations.

The response of the linear model of the structure is shown in Fig. 2.7, where the pressure in the fluid at the interface and displacement of the structure relative to the ground motion are plotted with respect to time. The fluid near the interface cavitates when the motion of the structure in the downstream direction attempts to generate a negative pressure. As the structure reverses direction, the cavitated region collapses, producing larger peak pressures at higher frequencies than if a linear fluid is assumed. The cutoff in negative pressure results in larger displacements in the downstream direction. The maximum displacement in the upstream direction is generally reduced (except for the second cycle) by the increased resisting pressure associated with the collapse of the cavitated region near the structure. Including the effects of cavitation increases the maximum displacement (and hence force) in the structure by 18%.

The response of the elasto-plastic model of the structure is shown in Fig. 2.8. The pressure variation for a linear fluid and elasto-plastic structure are very similar to the case of a completely linear system. The displacement of the structure, however, shows a residual displacement in the upstream direction due to yielding of the spring in that direction. When cavitation is included, the effect on pressure is very similar to the previous cases of a linear structure. However, cavitation changes the cycle at which first yield occurs (in the downstream direction) and increases the ductility demand from 1.34 to 1.53. Because of the cutoff in pressure, cavitation reduces the residual drift of the structure by approximately one-third.
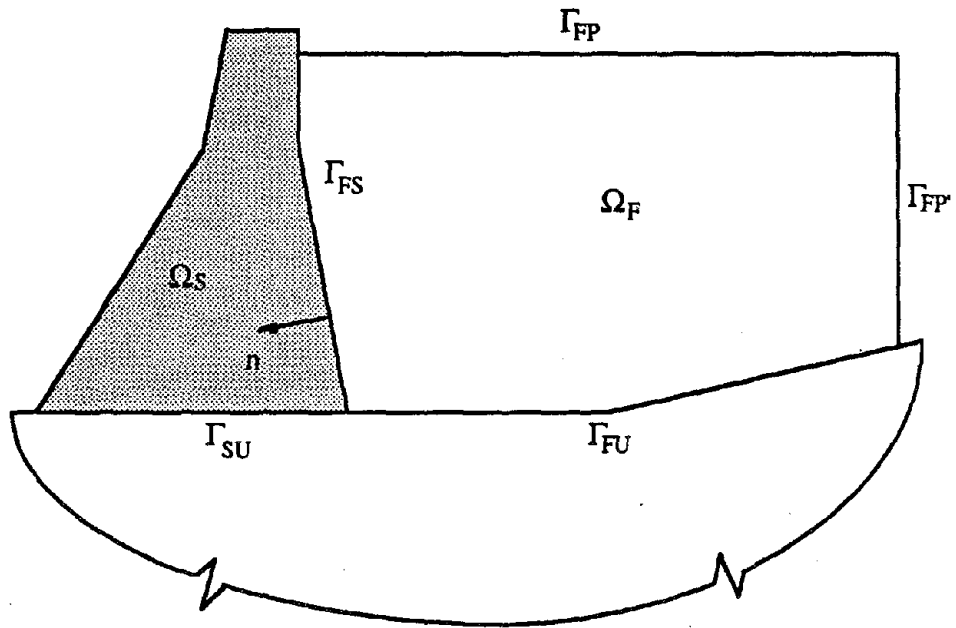
Fig. 2.1 Fluid-structure system.
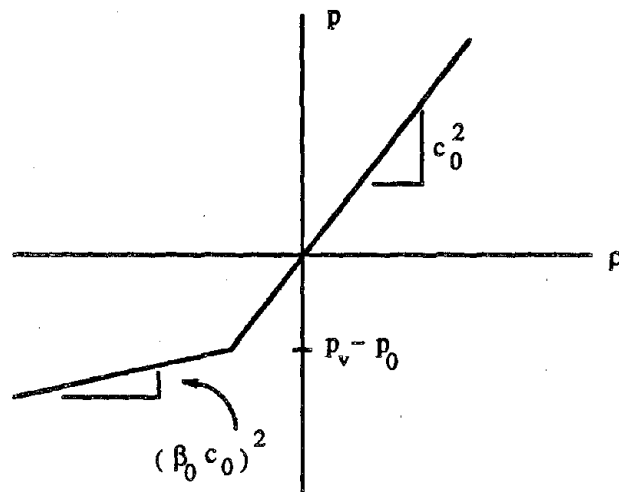
Fig. 2.2 Equation of state of fluid including
effects of cavitation (Ref. 10).
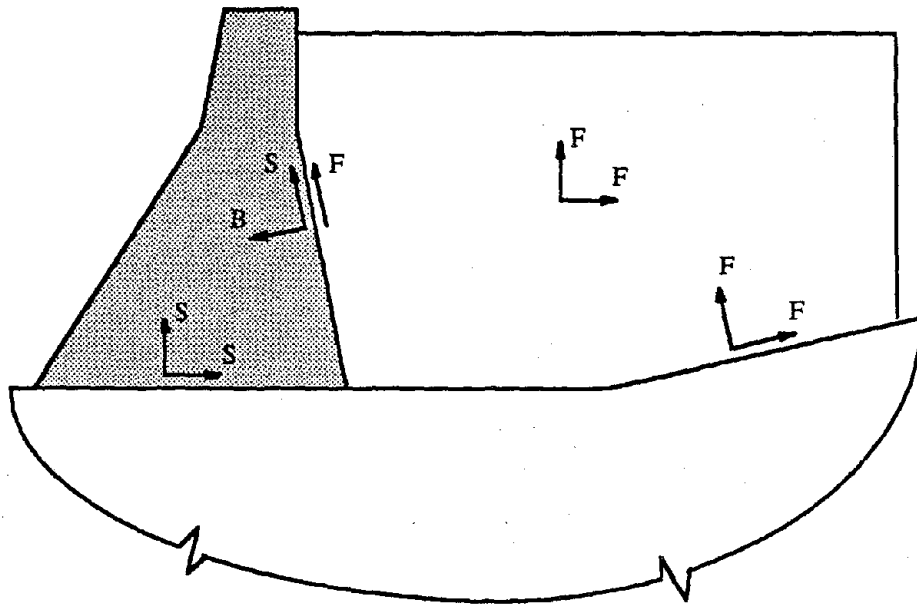
Fig. 2.3 Degrees of freedom in partitioned equations of
motion for fluid-structure system.
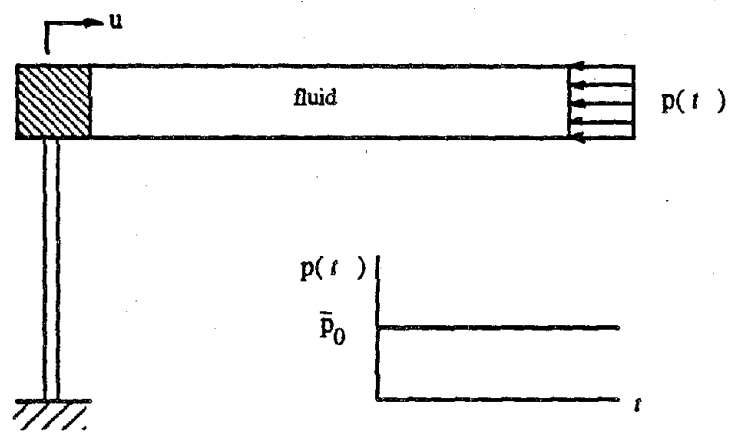
Fig. 2.4 One-dimensional fluid-structure system
subjected to pressure pulse.
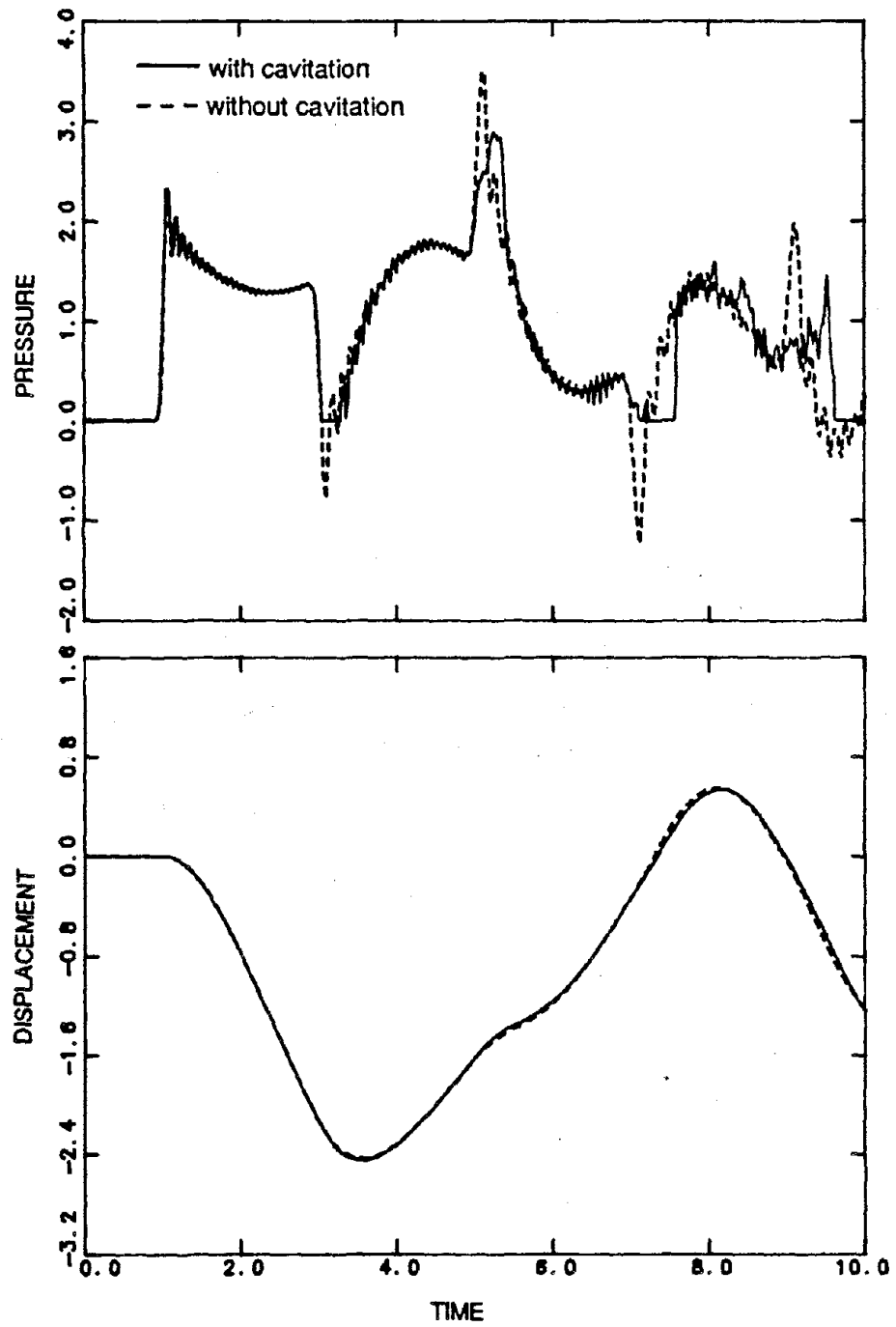
Fig. 2.5 Response of one-dimensional system to pressure pulse.
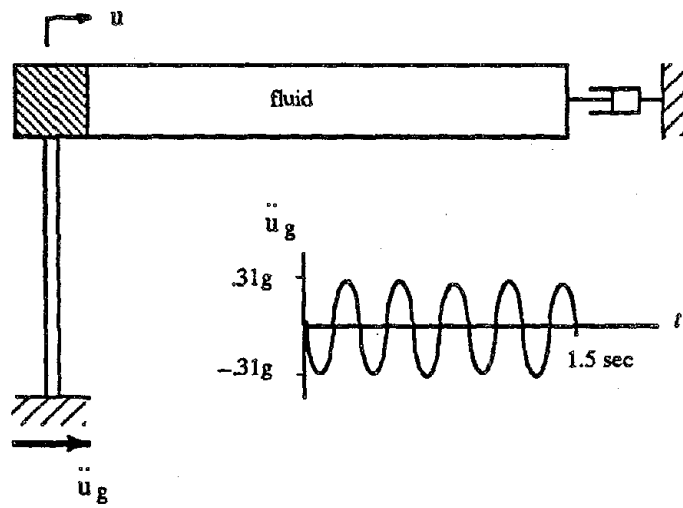
Fig. 2.6 One-dimensional fluid-structure system
subjected to ground motion
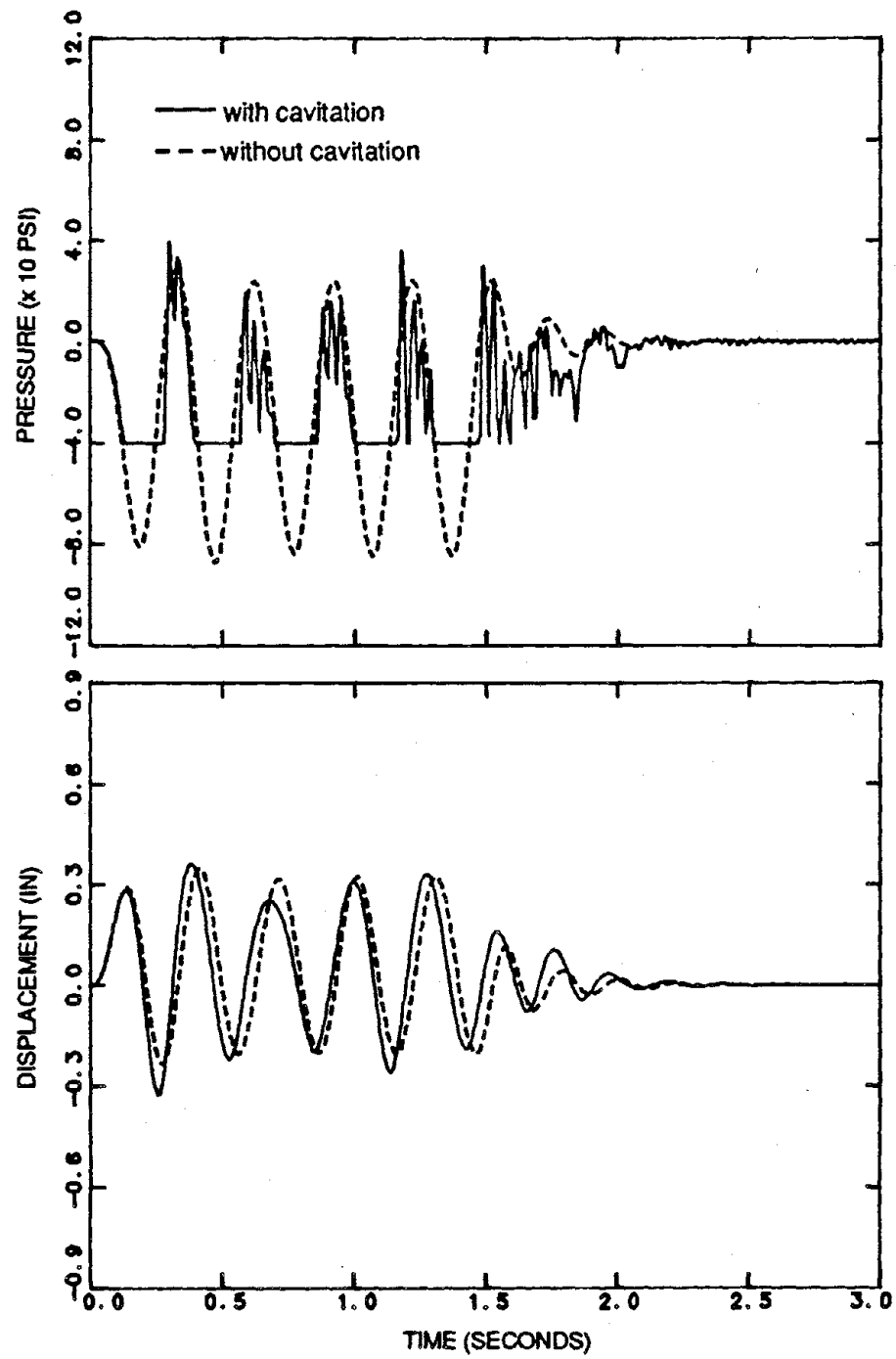
Fig. 2.7 Response of one-dimensional system to ground motion, linear structure.
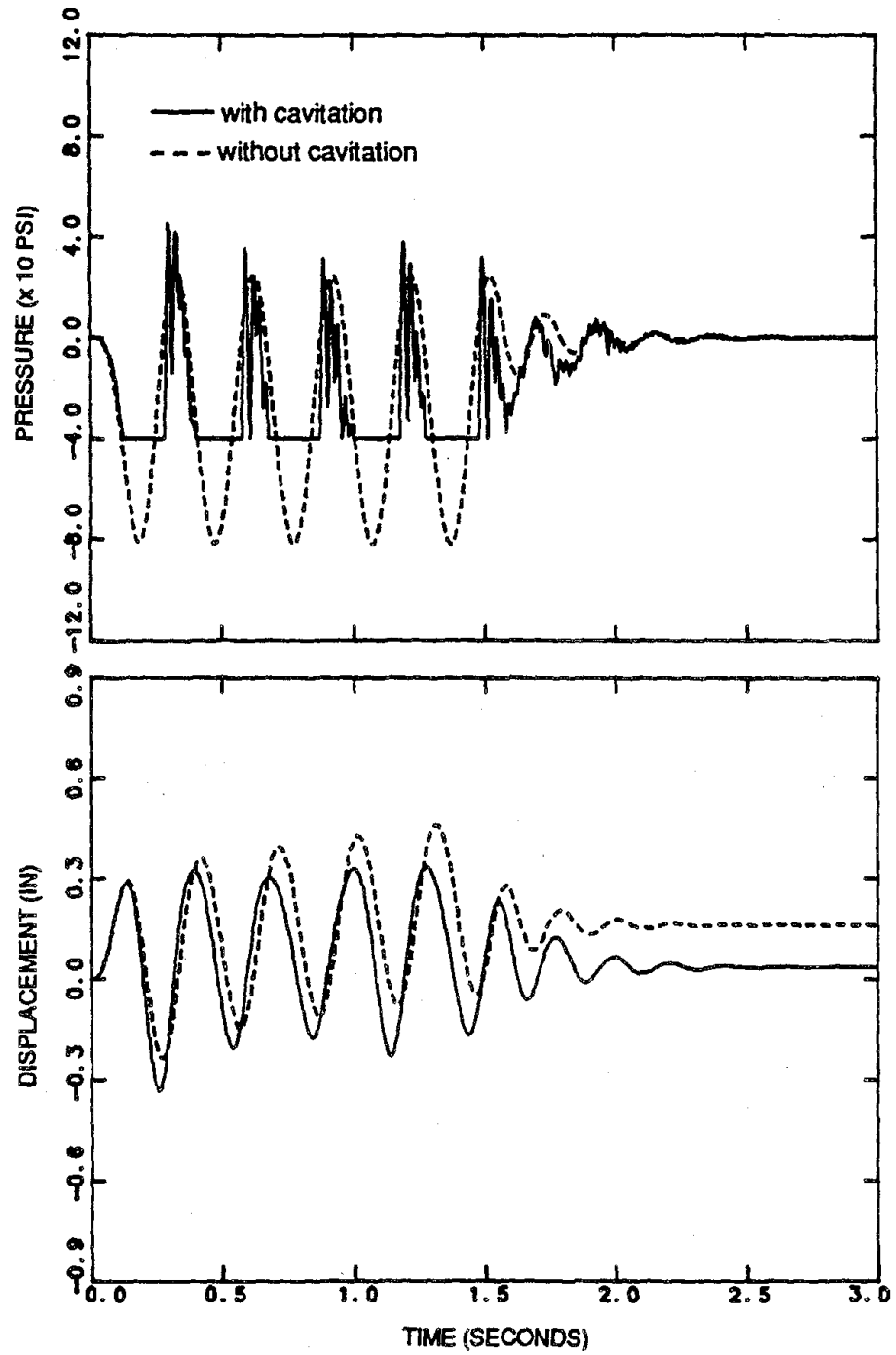
Fig. 2.8 Response of one-dimensional system to ground motion, elasto-plastic structure.

Chapter 3

Finite Elements for Fluid Domain

3.1 Introduction

A family of fluid elements based on the mixed pressure-displacement finite element formulation, introduced in Chapter 2, is thoroughly examined in this chapter. The study is restricted to two-dimensional domains, although the formulation can be extended to three-dimensional domains. Mixed quadrilateral isoparametric finite elements for the fluid domain are presented with constant or linear pressure variation and linear or quadratic displacement variation. The displacements are associated with nodal points in the element, i.e 4, 8, or 9-nodes, but the pressure parameters are not necessarily related to nodes. The satisfaction of the irrotationality condition on fluid motion introduces a constraint which is enforced by a penalty function, as described in Section 2.3.7.

One of the requirements for completeness in a finite element solution is that the element represent rigid body displacements of the domain. For two-dimensional solid domains, rigid body motion consists of two translations and one rotational component. For the case of inviscid fluid, however, the rigid body motion requirement is broader because of the absence of shear stress resistance. A fluid finite element must be able to represent fluid flow, in which the translational and rotational components are already considered. This necessary distinction aids the interpretation of some results presented in this chapter.

Selection of the shape functions for displacement and pressure in the mixed formulation requires care in order to obtain a convergent element for the fluid domain.

37

The weak forms of the governing equations for the fluid, Eqs. 2.23 and 2.27, show that interelement continuity of the pressure is not required because pressure derivatives do not appear in the integrands. Thus, a variety of shape functions for the pressure are admissible. In this study the pressure variation in the fluid elements is represented by polynomial functions. It is possible to express the pressure functions in terms of global coordinates of the domain, or natural coordinates of the element, as used for displacement shape functions. The number of terms in the pressure functions must be sufficient to avoid rank deficiency of the fluid stiffness matrix, Eq. 2.46. Also, careful selection of the pressure functions is necessary to avoid overconstraining or locking of the solution[11,20,44]. These considerations are addressed in Section 3.3.

The need to satisfy the irrotationality condition on fluid motion requires the use of a penalty function. The element stiffness matrix, the fluid stiffness plus the penalty matrix, must possess sufficient rank to avoid singularity of the global fluid stiffness matrix. Therefore, an eigenvalue analysis is used to verify that the number of pressure functions and the integration order of the irrotational matrix provide a non-singular stiffness matrix for an assemblage of fluid elements. Furthermore, a patch test is carried out to verify that the requirements for convergent fluid elements are satisfied.

3.2 Displacement Approximation

Standard shape functions are used for the displacements, N_I^F, Eq. 2.28, for node I. Namely [4,51],

$$4 - \text{node element}: \quad N_I^F = \tfrac{1}{4}(1 + s_I s)(1 + t_I t), \quad \text{for} \quad I = 1, 2, 3, 4$$

$$8 - \text{node element}: \quad N_I^F = \tfrac{1}{4}(1 + s_I s)(1 + t_I t)(s_I s + t_I t - 1), \quad \text{for} \quad I = 1, 2, 3, 4$$

$$N_I^F = \tfrac{1}{2}(1 - s^2)(1 - t_I t), \quad \text{for} \quad I = 5, 7$$

$$N_I^F = \tfrac{1}{2}(1 - t^2)(1 + s_I s), \quad \text{for} \quad I = 6, 8$$

$$9 - \text{node element}: \quad N_I^F = \tfrac{1}{4}(s^2 + s_I s)(t^2 + t_I t), \quad \text{for} \quad I = 1, 2, 3, 4$$

$$N_I^F = \tfrac{1}{2}(1 - s^2)(t^2 + t_I t), \quad \text{for} \quad I = 5, 7$$

$$N_I^F = \tfrac{1}{2}(1 - t^2)(s^2 + s_I s), \quad \text{for} \quad I = 6, 8$$

$$N_I^F = (1 - s^2)(1 - t^2) \quad \text{for} \quad I = 9$$

$$(3.1)$$

where s and t are the natural coordinates for the element as shown in Fig. 3.1, and the s_I and t_I are values of s and t at node I.

3.3 Pressure Approximation

Because of the assumption that the fluid is inviscid, the fluid finite element must only represent, through its stiffness matrix, those resisting forces associated with compressional (volumetric) deformation. The pressure functions, R_I, Eq. 2.30, which have a primary importance in establishing the fluid element stiffness matrix, k_{IJ}^F, Eq. 2.46, must meet certain requirements to interpolate properly the pressure within an element and provide a convergent element. Specifically, the pressure functions must be invariant under coordinate transformation and linearly independent, to guarantee the existence and uniqueness of the inverse of matrix h_{LK}, Eq. 2.34. The rank of h_{LK}, defined as the number of linearly independent rows and columns

in a matrix [42], is obviously the same as the number of independent pressure functions. The minimum number of the R_I functions is determined by the rank of h_{LK} (and h_{LK}^{-1}) needed to avoid singularity of the element stiffness matrix, including the irrotationality constraint and surface waves contributions. Further, as reported in Ref. [44], for two-dimensional problems the number of terms used for the pressure functions can be, at the most, the number of new nodes added by each element in a finite element mesh without overconstraining the solution. Thus, for the 4-node element one pressure function suffices, while for the 8 and 9-node elements three and four pressure functions can be used, respectively. This requirement is later verified in the eigenvalue analysis and patch test described in Section 3.6.

For two-dimensional problems it has been shown that using complete polynomials in global coordinates of the domain provides better results than polynomials in natural coordinates of the element [44,50]. Based on these findings, global coordinates are used in this study. The vector of pressure functions for each element is then given by

$$4 - \text{node element;} \quad \mathbf{R} = \lfloor\, 1 \,\rfloor$$

$$8 - \text{node element;} \quad \mathbf{R} = \lfloor\, 1 \quad x \quad y \,\rfloor \qquad (3.2)$$

$$9 - \text{node element;} \quad \mathbf{R} = \lfloor\, 1 \quad x \quad y \quad xy \,\rfloor$$

where x and y are the global coordinates of the domain. The isoparametric formulation can be used to express the global coordinates in an element as $x = N_I^F X_I$ and $y = N_I^F Y_I$, where X_I and Y_I are the coordinates of the node I.

The matrix $\mathbf{g}_{LJ}$, Eq. 2.35, is a function of both R_I and N_I, and its rank is the minimum of either the number of pressure functions or the order of k_{IJ}^F minus the number of modes that produce fluid flow [44]. The fluid element stiffness matrix, k_{IJ}^F, should have only non-zero eigenvalues associated with volumetric change. This can also be stated as having k_{IJ}^F with a rank equal to the number of constraints

imposed on the element and is the same as the number of pressure functions.

To illustrate this, Figs. 3.2-3.4 show the mode shapes associated with the non-zero eigenvalues of the elements (related to compressional deformation) and the ranks of h_{LK}, g_{LJ} and k_{IJ}^F for rectangular finite elements of 4, 8 and 9-nodes, respectively. The element considered has an aspect ratio of 1.5 and unit thickness. The eigenvalues, result from solving $k^F x = \lambda_i x$, are scaled with respect to the fluid bulk modulus, $\rho_0 c_0^2$, such that $\bar{\lambda}_i = \lambda_i / \rho_0 c_0^2$. It is clearly noticed that when fluid flow is prevented, by imposing displacement boundary contraints, the matrix k_{IJ}^F is rank deficient, justifying the need of the irrotationality constraint and surface waves conditions to avoid singularity of the global fluid stiffness matrix. Remedies to this shortcoming will be presented in Section 3.6.

3.4 Numerical Integration of Fluid Element Matrices

Standard Gaussian quadrature is used to integrate numerically the fluid element matrices. The number of integration points required to integrate a polynomial function is determined by the order of the polynomial. If n integration points are used, then a polynomial of order $2n - 1$ can be exactly integrated [17]. The integration is performed by mapping the finite element domain, Ω_{Fe}, from global coordinates (x, y) to natural coordinates (s, t). In the following subsections the numerical integration of the fluid element matrices is presented.

As opposed to the displacement finite element formulation for the fluid domain [46], it is important to point out that the numerical evaluation of the tangent stiffness matrix for the fluid, k_{IJ}^F, through the matrices h_{LK} and g_{LJ}, does not require reduced integration to prevent overconstrained elements.

3.4.1 Matrix h_{LK}

Numerically, h_{LK}, Eq. 2.34, is determined as,

$$h_{LK} = t_0 \sum_i \sum_j w_i w_j R_L(s_i, t_j) \frac{1}{c^2(s_i, t_j)\rho_0} R_K(s_i, t_j) \mid J \mid \qquad (3.3)$$

where t_0 is the thickness of the element; w_i and w_j are the weights of the integration points i and j of position (s_i, t_j) within the mapped element; and $\mid J \mid$ is the determinant of the Jacobian of the transformation from global to natural coordinates. For a linear fluid, in which $c^2 \rho_0$ is a constant function, the order of the numerical integration is only based on the degree of the pressure functions. Examining R_I, in Eq. 3.2, it is observed that for the 4-node element a 1x1 order of integration is needed, while for the 8- and 9-node elements a 2x2 order of integration suffices. For nonlinear fluid or arbitrary quadrilaterals, the order of integration adopted is the same as that for linear fluid, mentioned above.

Notice that the state of the fluid is a function of the nonlinear pressure wave velocity, c, representing cavitation. The value of c depends on the density of the fluid and is evaluated at each integration point based on the current state of the element by:

- Compute the density, ρ:

    From Eq. 2.13, $\rho(s_i, t_j) = -\rho_0 B_I^F(s_i, t_j) u_I$

- Compare $\rho(s_i, t_j)$ with $\rho_{crit} = \frac{p_v - p_0(s_i, t_j)}{c_0^2}$;

    $p_0(s_i, t_j)$ is the hydrostatic pressure at the integration point,

    From Eq. 2.25, if $\rho(s_i, t_j) \geq \rho_{crit}$ then $c(s_i, t_j) = c_0$

    From Eq. 2.26, if $\rho(s_i, t_j) < \rho_{crit}$ then $c(s_i, t_j) = \beta_0 c_0$

3.4.2 Matrix g_{LJ}

The element matrix g_{LJ}, Eq. 2.35, is independent of the state of the fluid and is computed numerically as

$$g_{LJ} = t_0 \sum_i \sum_j w_i w_j R_L(s_i, t_j) \mathbf{B}_J^F(s_i, t_j) \mid \mathbf{J} \mid \qquad (3.4)$$

The order of integration is determined by the degree of the functions R_I and the derivatives of $\mathbf{N}_I^F$, given by $\mathbf{B}_I^F$. Thus, for the 4-node element R_I is a constant function and the derivative of $\mathbf{N}_I^F$ is constant in one coordinate and linear in the other, so a 1x1 order of integration is required. Using the same reasoning, a 2x2 order of integration is needed for the 8 and 9-node elements.

3.4.3 Vector p_L^u

This vector p_L^u, Eq. 2.36, represents the unbalanced pressure in the element due to cavitation. It is a function of the state of the fluid and is evaluated numerically by

$$p_L^u = t_0 \sum_i \sum_j w_i w_j R_L(s_i, t_j) \frac{\rho^u(s_i, t_j)}{\rho_0} \mid \mathbf{J} \mid \qquad (3.5)$$

For the numerical integration of this vector, the order of the integrand depends upon the degree of R_I and the nonlinear function ρ^u. Based solely on the function R_I, the integrand has a degree of one, therefore p_L^u could be integrated with only one integration point. However, in nonlinear problems, equilibrium convergence requires a more accurate computation of the unbalanced forces than of the tangent stiffness matrix. Because the variation of the function ρ^u is not precisely known, a 2x2 numerical integration order is adopted. Furthermore, for computational efficiency p_L^u is conveniently evaluated along with the matrices h_{LK} and g_{LJ} in the same loop. Since the state of the fluid affects $\rho^u(s_i, t_j)$, due to cavitation, the following procedure is used at each integration point:

- Compute the density, ρ, as for the matrix h_{LK}

- Compare $\rho(s_i, t_j)$ with $\rho_{crit} = \frac{p_v - p_0(s_i, t_j)}{c_0^2}$;

  $p_0(s_i, t_j)$ is the hydrostatic pressure at the integration point,

  From Eq. 2.25, if $\rho(s_i, t_j) \geq \rho_{crit}$ then $\rho^u(s_i, t_j) = 0$

  From Eq. 2.26, if $\rho(s_i, t_j) < \rho_{crit}$ then $\rho^u(s_i, t_j) = \frac{1 - \beta_0^2}{\beta_0^2} \rho_{crit}$

3.4.4 Matrices $m_{IJ}^F, c_{IJ}^{F'}, c_{IJ}^{F''}$ and $(k_f)_{IJ}^F$

These matrices are similar to those extensively used in finite element displacement formulations for solids and their numerical integration is well documented in many textbooks [4,20,51]. The consistent mass matrix, m_{IJ}^F, requires 2x2 integration for a linear displacement variation and 3x3 integration for a quadratic one. The other matrices, $c_{IJ}^{F'}, c_{IJ}^{F''}$ and $(k_f)_{IJ}^F$, which are integrated over the boundaries, require second and third orders of integration depending upon whether the displacement variation is linear or quadratic.

3.4.5 Matrix $(k_w^F)_{IJ}$

As described in Section 2.3.7, the irrotational stiffness matrix, is added to the element stiffness matrix, Eq. 2.51, k_{IJ}^F, to constrain vorticity introduced by the discretization and time integration of the equations of motion for the fluid. It accomplishes this by increasing the rank of the element stiffness matrix and therefore preventing singularity of the global fluid stiffness matrix. The penalty matrix is computed as

$$(k_w^F)_{IJ} = \alpha \ t_0 \sum_i \sum_j w_i w_j (W_I^F(s_i, t_j))^T W_J^F(s_i, t_j) \mid J \mid \qquad (3.6)$$

This matrix must be evaluated numerically with reduced integration to prevent locking of the elements, that is, 1x1 or 2x2 order of integration for the 4 or 8 and 9-node

elements, respectively. A later section will establish rules for the numerical integration and selection of the penalty parameter, α.

3.5 State Determination

The tangent stiffness matrix, Eq. 2.46, and nonlinear resisting forces, Eq. 2.44, due to cavitation, are based on the current state of the fluid element. The state determination procedure for computation of those terms is as follows:

1. Compute h_{LK}, g_{LJ} and p_L^u from Eqs. 3.3- 3.5

2. Form the partitioned array:

   $[g_{LJ} \mid g_{LJ}u_J - p_L^u]$

3. Solving a linear systems of equations, compute:

   $(h_{LK})^{-1}[g_{LJ} \mid g_{LJ}u_J - p_L^u]$

   Note that the second submatrix gives the negative of the pressure parameters, p_K, Eq. 2.33. This equation solution involves 1, 3 and 4 equations for the 4, 8 and 9-node element, respectively.

4. Multiply by g_{KI}^T:

   $\left[g_{KI}^T(h_{LK})^{-1}g_{LJ} \mid g_{KI}^T(h_{LK})^{-1}g_{LJ}u_J - g_{KI}^T(h_{LK})^{-1}p_L^u\right]$

   The first submatrix is the tangent stiffness matrix, $(k_T)_{IJ}^F$, and the second the vector of nonlinear restoring forces, $f_I^F = -g_{KI}^T p_K$.

3.6 Eigenvalue Analysis, Penalty Parameter and Patch Test

An eigenvalue analysis is carried out to evaluate the selection of the pressure functions, R_I, and to verify the necessity of the rotational constraints in the fluid to avoid rank deficiency of the fluid stiffness matrix. The test example, depicted in Fig. 3.5, is a water tank with rigid walls; it has also been studied in Ref. [46].

The water has a density, $\rho_0 = 1.94$ lb-sec^2/ft^4; and pressure wave velocity, $c_0 = 4720$ ft/sec.

A parametric study for the penalty parameter is also performed. Several values for α are considered to investigate the sensitivity of the sloshing and compressional frequencies of a single fluid finite element, with 4, 8 or 9-nodes. The convergence of the first sloshing and compressive frequencies are investigated using the same example as that of the eigenvalue analysis. This section ends with a patch test for an assemblage of fluid elements to verify the requirements for a convergent element.

3.6.1 Eigenvalue Analysis

The fluid finite elements considered in the eigenvalue analysis have 4-nodes with 1 pressure function, 8-nodes with 3 pressure functions, and 9-nodes with 4 pressure functions. For single elements the number of non-zero eigenvalues representing compressional modes was discussed in Section 3.3 and is shown in Figs. 3.2-3.4. The 4-node element has one compressional mode and seven zero-energy modes, some of which correspond to vorticity and surface sloshing. When considering the rigid water tank with one 4-node finite element, as shown in Fig. 3.6(a), fluid flow constraints provide only six displacements boundary conditions; thus, one zero-eigenvalue related to rotation is left. This zero-eigenvalue vanishes when one rotational constraint is included. The addition of surface sloshing stiffness does not have any effect on the deformation of a single element. When the rigid water tank is modeled with two finite elements, Fig. 3.6(b), there are only two non-zero eigenvalues associated with compression, and ten zero-energy modes, some associated with vorticity and sloshing. After including seven displacement boundary conditions to restrain fluid flow, there

is a remainder of three zero-eigenvalues which are eliminated when two rotational constraints (one for each element) and surface sloshing are included.

As mentioned in Ref. [46], a large (high frequency) eigenvalue corresponding to a rotational constraint is associated with each integration point. This was verified using the rigid water tank, modeled with one and two finite elements. In both cases, when the irrotationality penalty matrix was fully integrated, with 2x2 integration order, the fluid stiffness matrix including the penalty matrix has only high frequency eigenvalues related to vorticity, eliminating the compressional frequencies. The elements are overconstrained by full integration of the penalty matrix and the solution locks. Therefore, a reduced integration on the irrotationality penalty matrix is required.

For the 8-node element with three pressure functions, Fig. 3.3 shows that the fluid stiffness matrix has three compressional modes and thirteen zero-energy modes. The results for the rigid water tank discretized with this type of element, in which surface sloshing and the irrotational penalty matrix computed with reduced integration are taken into account, are depicted in Fig. 3.7. In both cases, for one and two finite elements, the penalty matrix is integrated at four points, however, only three and seven rotational modes are introduced, respectively. The remaining rotational mode has been replaced by a zero-energy mode associated with shear deformation. This apparently unexpected result is readily confirmed because shear deformation is not accounted for in the weak form for momentum balance. When four pressure functions are used instead, the problem becomes overconstrained, as pointed out in Ref. [44], because more constraints are introduced than degrees of freedom for each element added to a mesh.

The same analysis is performed on the 9-node element, with four pressure

functions (Fig. 3.8). As with the 8-node element, a 2x2 reduced integration rule is used for the penalty matrix. Although, there are four high frequency eigenvalues related to rotation, one of them is in fact related to a shear deformation mode. This is the principal difference between the 8 and 9-node elements. Whereas in the 8-node element the shear mode has a zero eigenvalue, in the 9-node element the eigenvalue corresponding to shear mode is grouped with the high frequency rotational eigenvalues. As a result, shear deformation is constrained in the 9-node element.

Figs. 3.9, 3.10 and 3.11 show the first sloshing and compressional frequencies, obtained from the generalized eigenvalue problem (including mass), for the rigid water tank modeled with one and two 4, 8 and 9-node finite elements, respectively; the corresponding modes shapes are also shown. Notice in Figs. 3.9 and 3.10 that single 4-node and 8-node elements are not able to reproduce sloshing. The reason is that in a single 4-node element, there are two constraints imposed in the element, one compression and one rotation, and only two degrees of freedom. In a single 8-node element, there are seven constraints in the element, three compressions and four rotations, and seven the degrees of freedom. Thus, for both elements sloshing is not reproduced. When a reduced integration rule (one gaussian point) is used for the irrotational penalty matrix in the single 8-node element, see Fig. 3.10, a sloshing mode is produced since the number of constraints is less than the number of degrees of freedom.

The rate of convergence for the first compressional and sloshing frequencies of the water in the rigid tank are shown in Figs. 3.12 to 3.14, for the three types of elements studied, as a function of the number of elements versus percent error with respect to the exact solution. The exact solution for the first sloshing and compresional frequencies are 2.24 and 1186.30 rad/sec, respectively [46]. Observe that fast convergence is achieved for all the elements, particularly the 9-node element

(Fig. 3.14). Of special interest is the performance of the 8-node element, Fig. 3.13, when the rigid water tank is modeled with one and four elements. For both cases, sloshing can not be reproduced because of the excess of constraints imposed as compared with the number of degrees of freedom. For a large two-dimensional finite element mesh, adding a new 8-node element will add only three new nodes, that is, six new degrees of freedom. However, since seven constraints are introduced by the new element, some modes will be eliminated. This is not the case for the 4 and 9-node elements. Hence, although the 8-node element shows convergence for the sloshing and first compressional mode, it fails to reproduce some vibrational modes.

3.6.2 Penalty Parameter

The appropriate value of the penalty parameter, α, is evaluated through a study of single 4, 8 and 9-node fluid elements. The natural frequencies of a rectangular element, with the same geometry and properties as the tank problem in Fig. 3.5, without boundary restraints are computed for two values of the penalty parameter: five and fifty times the water bulk modulus, $\rho_0 c_0^2$. Tables 3.1-3.3 present the frequencies for the three types of elements. Note that the rotational modes are related to very high frequencies, an order of magnitude larger than the compressional frequencies for the larger value of α. The sloshing frequencies are not affected by the value of α whereas the compressional frequencies show a slight influence. In general, values of the penalty number over fifty times the fluid bulk modulus do not significantly change the frequencies and provide sufficient separation of compressional and rotational modes to have little effect in the dynamic response.

3.6.3   Patch Test

A patch test is conducted for both a uniform and an arbitrary mesh of 4, 8 and 9-nodes fluid finite elements to assure that the elements represent correct pressures in the patch. Fig. 3.15 shows the assemblage of elements used for the test, with the same geometry and fluid properties as the rigid water tank of Fig. 3.5. A uniform pressure is applied at the free surface and body forces are not considered. Both, the 4 and 9-node elements passed the test by representing exact pressure in the elements. The 8-node element in the uniform rectangular mesh failed the test, however, it passed it for the arbitrary mesh.

Summarizing, the 4 and 9-node elements performed well in representing the vibrational characteristics of inviscid fluid and proved to be convergent. On the other hand, it seems that the 8-node element with three pressure functions is unreliable and its further use will not be considered. A value of the penalty parameter of fifty times the fluid bulk modulus has been found adequate and will be adopted in this study.

3.7   The Mixed versus Displacement Formulation

In the mixed formulation the pressure variation is approximated by independent pressure parameters and the equation of state is satisfied in the average sense. In the displacement formulation for fluids the pressure function is evaluated by the satisfaction, point-by-point, of the equation of state, Eq. 2.20-2.21, from the displacement function. The term in the weak form of momentum balance, Eq. 2.23, that is affected by the choice of formulation is the nonlinear restoring force, that is

$$- \int_{\Omega_F} \nabla^T \delta \mathbf{u} \; p \; d\Omega \qquad (3.7)$$

In the displacement formulation, the equation of state, Eqs. 2.20-2.21, is substituted directly into the weak form of momentum balance. The density is then expressed in terms of displacements by Eq. 2.13, which upon substitution into Eq. 3.7, and considering Eqs. 2.25-2.26, gives:

$$\int_{\Omega_F} \nabla^T \delta \mathbf{u} \, (\rho_0 c^2) \, \nabla^T \mathbf{u} \, d\Omega - \int_{\Omega_F} \nabla^T \delta \mathbf{u}(\rho^u c^2) \, d\Omega \tag{3.8}$$

The substitution of displacement shape functions (Eqs. 2.28-2.29) into Eq. 3.8, with integration over the elements, for arbitrary $\delta \mathbf{u}_I$, gives the nonlinear restoring force, for the fluid elements as

$$\mathbf{f}_I^F = (\mathbf{k}_T)_{IJ}^F \mathbf{u}_J - \mathbf{f}_I^u \tag{3.9}$$

where

$$(\mathbf{k}_T)_{IJ}^F = \int_{\Omega_{F_e}} (\mathbf{B}_I^F)^T (\rho_0 c^2) \, \mathbf{B}_J^F \, d\Omega \tag{3.10}$$

is the tangent stiffness matrix for the fluid element, and

$$\mathbf{f}_I^u = \int_{\Omega_{F_e}} (\mathbf{B}_I^F)^T (\rho^u c^2) \, d\Omega \tag{3.11}$$

is the vector of unbalanced forces due to cavitation. As reported in Ref. [46], Eq. 3.10 provides a excessively stiff element and requires reduced numerical integration. In contrast, the tangent stiffness matrix, Eq. 2.46, in the mixed formulation does not require reduced integration. As demonstrated in Ref. [25], the mixed formulation and displacement formulation with reduced and selective integration give the same stiffness matrix for 4, 8 and 9-nodes elements for linear problems.

No major advantage exists between the displacement and mixed formulations when computing the tangent stiffness. In the displacement formulation, the element stiffness matrix, Eq. 3.10, must be recomputed, using reduced integration, on the matrix triple product, whenever cavitation takes place. In the mixed formulation, only h_{LK}, Eq. 2.34, needs to be recalculated since g_{LJ}, Eq. 2.35, remains

constant. However, an equation solution and matrix multiplication are required to form the element stiffness matrix, as described in Section 3.5. Although not a very common practice, if it is desired to store matrices g_{LJ} for computing the tangent stiffness in the mixed formulation, it requires less storage than $\mathbf{B}_I^F$ in the displacement formulation.

The major advantage of the mixed over the displacement formulation for the fluid is in computing the nonlinear restoring force when cavitation is permitted. In the displacement formulation, full numerical integration of the restoring forces, $\mathbf{f}_I^F$, Eq. 3.9, is required for accurate restoring forces because the formulation attempts to satisfy the equation of state throughout the element. On the other hand, in the mixed formulation, where the equation of state is satisfied in the average sense, the restoring forces $\mathbf{f}_I^F$ (Eq. 2.44 or Section 3.5) are only calculated by integration over fewer points, reducing the computational effort considerably. Considering the 9-node element, where in the displacement formulation the vector of nonlinear restoring forces is evaluated by 3x3 integration; in the mixed formulation only 2x2 integration is necessary. It can be argued that reduced integration on the restoring forces approximately produces the same averaging results as in the mixed formulation. However, in the case of nonlinear problems it has not been shown that reduced integration produces the same 'average' restoring forces as does the mixed formulation which, explicitly formulates the averaging in the weak form of the equation of state.

Table 3.1: Frequencies of a single 4-node element (rad/sec)

Mode No.	$\alpha = 5\rho_0 c_0^2$	$\alpha = 50\rho_0 c_0^2$	Mode Type
1-4	0	0	rigid body
5	2.66	2.66	sloshing
6	4.47	4.47	sloshing
7	2793.92	2793.92	compressional
8	6247.40	19756.01	rotational

Table 3.2: Frequencies of a single 8-node element (rad/sec)

Mode No.	$\alpha = 5\rho_0 c_0^2$	$\alpha = 50\rho_0 c_0^2$	Mode Type
1-6	0	0	rigid body
7	2.69	2.69	sloshing
8	4.08	4.08	sloshing
9	6.05	6.05	sloshing
10	2793.92	2793.92	compressional
11	3385.26	3386.74	compressional
12	5816.36	5880.48	compressional
13	6247.40	19756.01	rotational
14	7722.05	24153.67	rotational
15	13270.27	41940.43	rotational
16	13971.40	44181.44	rotational

Table 3.3: Frequencies of a single 9-node element (rad/sec)

Mode No.	$\alpha = 5\rho_0 c_0^2$	$\alpha = 50\rho_0 c_0^2$	Mode Type
1-7	0	0	rigid body
8	2.71	2.71	sloshing
9	3.74	3.74	sloshing
10	6.51	6.51	sloshing
11	2793.92	2793.92	compressional
12	3385.26	3386.74	compressional
13	5816.36	5880.48	compressional
14	6247.40	6247.40	compressional
15	6247.40	19756.01	rotational
16	7722.05	24153.67	rotational
17	13270.27	41940.43	rotational
18	13971.40	44181.44	rotational

a) 4-node

b) 8-node

c) 9-node
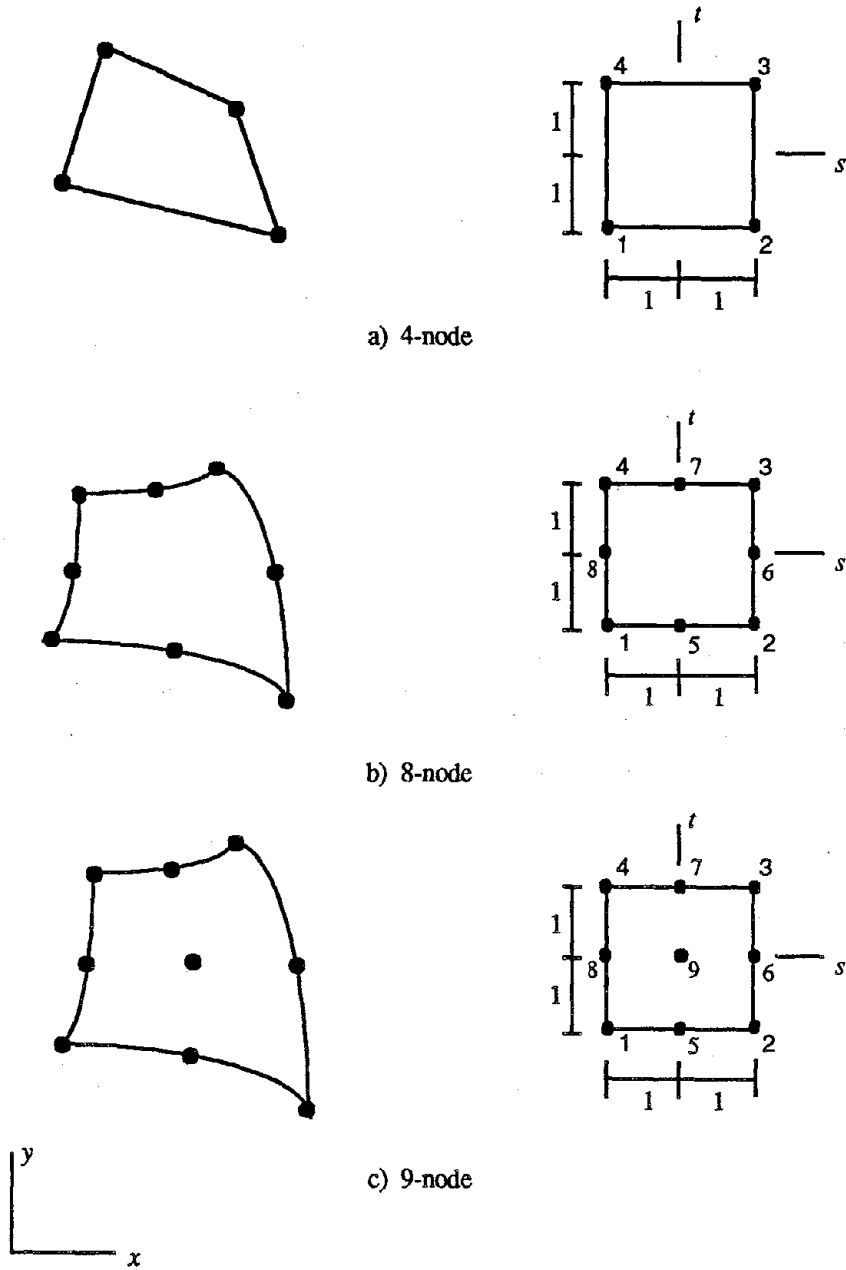
Fig. 3.1 Fluid elements
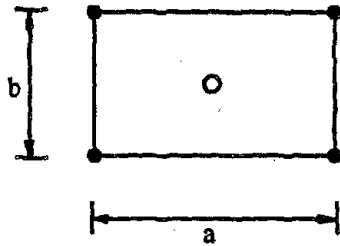
1 pressure function

$$\text{rank}(h_{LK}) = \text{rank}(g_{LJ}) = \text{rank}(k_{IJ}^{F}) = 1$$
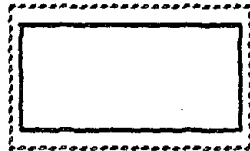
$a/b = 1.5$

$$\bar{\lambda}_1 = 2.17$$

mode shape

Fig. 3.2 Mode shapes of non-zero eigenvalues of k_{IJ}^{F} and rank of h_{LK} , g_{LJ} and k_{IJ}^{F} for the 4-node element.
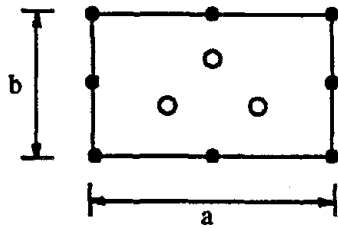
3 pressure functions

$$\text{rank}(\,h_{LK}) = \text{rank}(\,g_{LJ}\,) = \text{rank}(\,k_{IJ}^{F}\,) = 3$$

a/b = 1.5

$\overline{\lambda}_1 = 2.17$
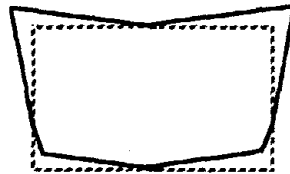
$\overline{\lambda}_3 = 6.22$

$\overline{\lambda}_2 = 3.17$

Fig. 3.3 Mode shapes of non-zero eigenvalues of k_{IJ}^{F} and rank of h_{LK}, g_{LJ} and k_{IJ}^{F} for the 8-node element.

a/b = 1.5
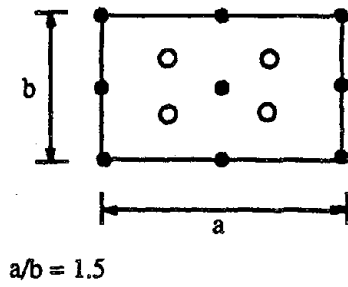
4 pressure functions

$\text{rank}(h_{LK}) = \text{rank}(g_{LJ}) = \text{rank}(k_{IJ}^F) = 4$
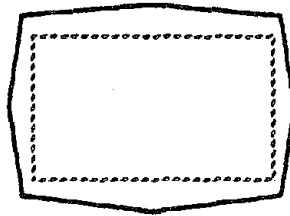
$\overline{\lambda}_1 = 2.17$

$\overline{\lambda}_3 = 3.17$
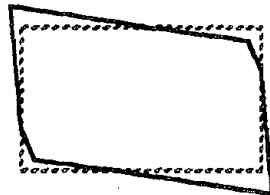
$\overline{\lambda}_2 = 2.89$

$\overline{\lambda}_4 = 6.22$

Fig. 3.4 Mode shapes of non-zero eigenvalues of k_{IJ}^F and rank of h_{LK}, g_{LJ} and k_{IJ}^F for the 9-node element.
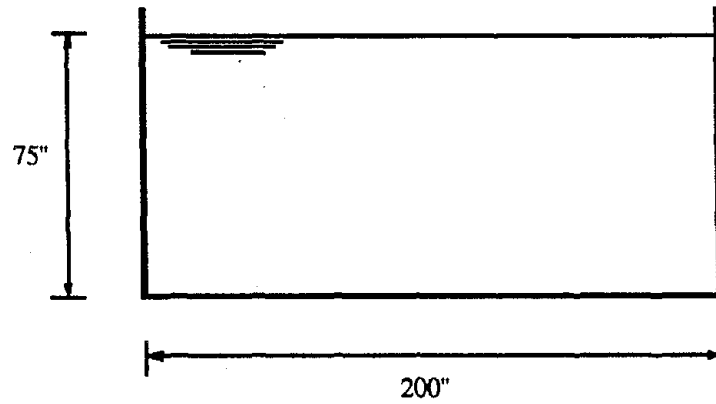
$$\rho_0 = 1.94 \text{ lb-sec}^2/\text{ft}^4$$
$$c_0 = 4720 \text{ ft/sec}$$
$$\alpha = 50 \ c_0^2 \ \rho_0$$

Fig. 3.5 Rigid water tank (Ref. 46)
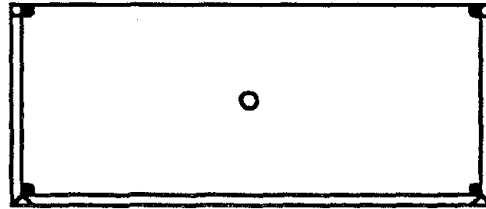
a) One element

1 compresion
1 rotation
6 boundary constraints
———
8 d.o.f
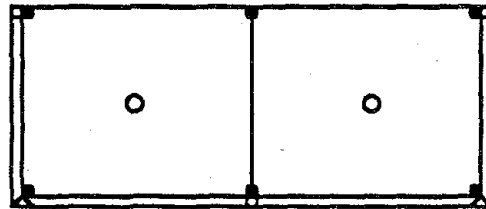
b) Two elements

1 sloshing
2 compressions
2 rotations
7 boundary constraints
———
12 d.o.f

Fig. 3.6 Eigenvalue analysis of water in rigid tank.
4-node finite elements, 1 pressure function,
1x1 integration for irrotational matrix.
$\alpha = 50 \ c_0^2 \ \rho_0$
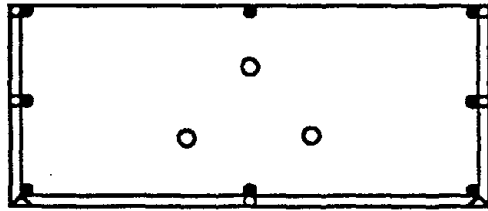
a) One element

3 compresions
3 rotations
1 shear (zero energy mode)
9 boundary constraints
———
16 d.o.f
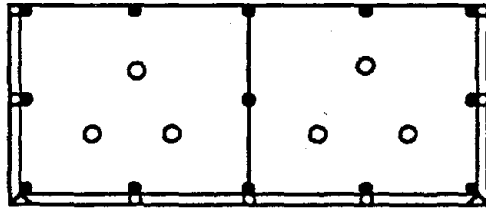
b) Two elements

1 sloshing
6 compressions
7 rotations
1 shear (zero energy mode)
11 boundary constraints
———
26 d.o.f

Fig. 3.7 Eigenvalue analysis of water in rigid tank,
8-node finite elements, 3 pressure function,
2x2 integration for irrotational matrix.
$\alpha = 50 \ c_0^2 \ \rho_0$
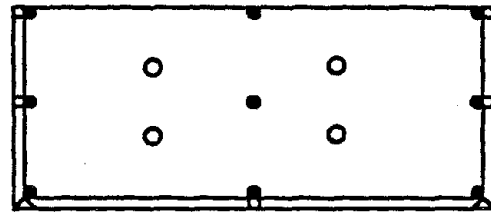
a) One element

1 sloshing
4 compressions
4 rotations
9 boundary constraints
___
18 d.o.f
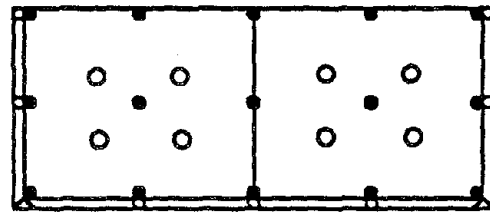
b) Two elements

3 sloshing
8 compressions
8 rotations
11 boundary constraints
___
30 d.o.f

Fig. 3.8 Eigenvalue analysis of water in rigid tank.
9-node finite elements, 4 pressure function,
2x2 integration for irrotational matrix.

$$\alpha = 50 \ c_0^2 \ \rho_0$$

sloshing mode   compressive mode

no sloshing   ω = 1307.7 rad/sec

a) One element

ω = 2.6 rad/sec   ω = 1307.7 rad/sec

b) Two elements
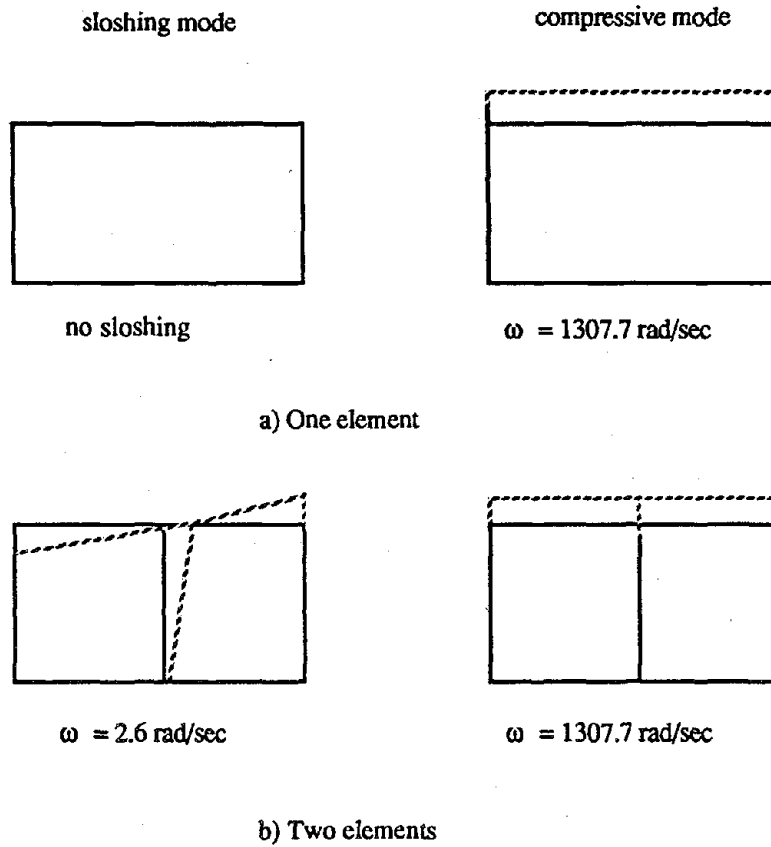
Fig. 3.9 First sloshing and compressional frequencies
and modes shapes for water in rigid tank
with 4-node elements.

sloshing mode   compressive mode

no sloshing* $\omega = 1191.6$ rad/sec

a) One element

$\omega = 2.27$ rad/sec $\omega = 1191.6$ rad/sec

b) Two elements
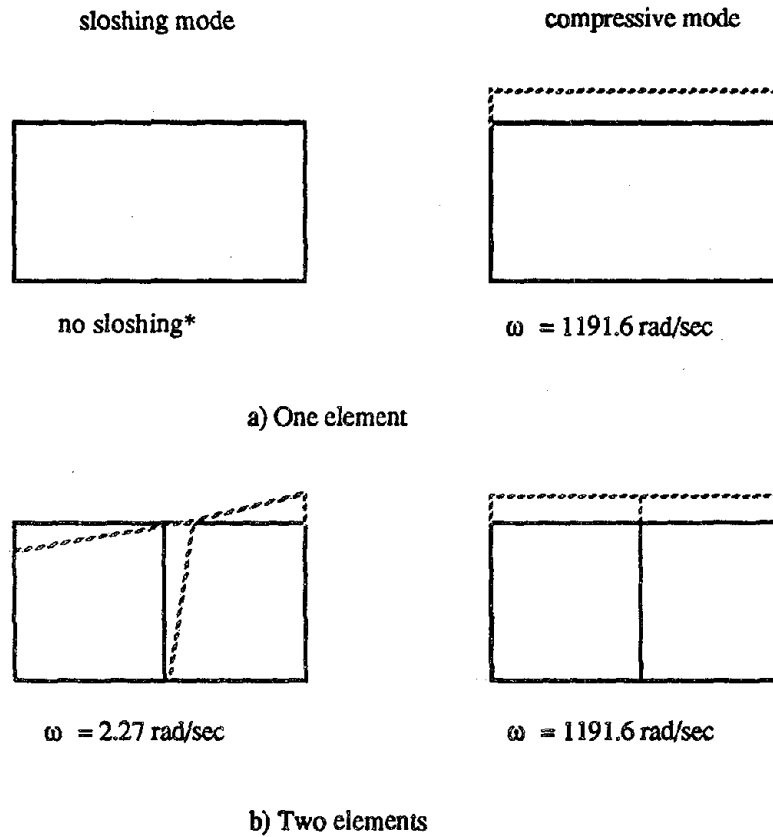
* $\omega = 2.48$ rad/sec, when penalty matrix
   integrated at one point.

Fig. 3.10 First sloshing and compressional frequencies
           and modes shapes for water in rigid tank
           with 8-node elements.

sloshing mode   compressive mode

ω = 2.24 rad/sec   ω = 1191.6 rad/sec

a) One element

ω = 2.24 rad/sec   ω = 1191.6 rad/sec

b) Two elements
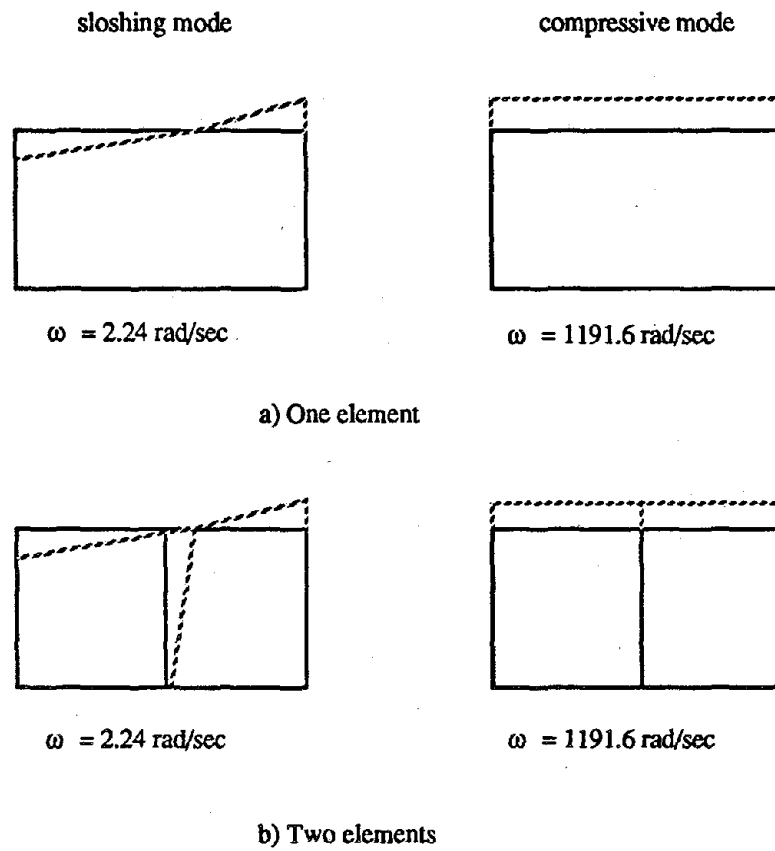
Fig. 3.11 First sloshing and compressional frequencies
and modes shapes for water in rigid tank
with 9-node elements.
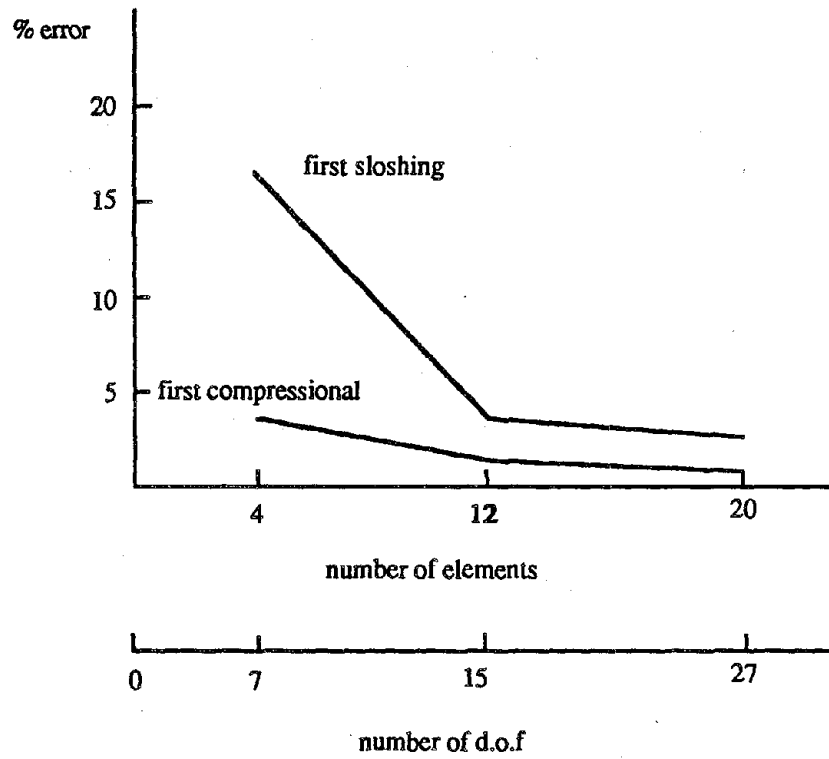
Fig. 3.12 Convergence of first compressional and
sloshing frequencies for water in rigid
tank with 4-node finite elements.
$\alpha = 50\ c_0^2\ \rho_0$

Fig. 3.13 Convergence of first compressional and
sloshing frequencies for water in rigid
tank with 8-node finite elements.
$\alpha = 50 \ c_0^2 \ \rho_0$

% error

1

first sloshing

0.5

first compressional

1   2   4

number of elements

0   9   19   35

number of d.o.f
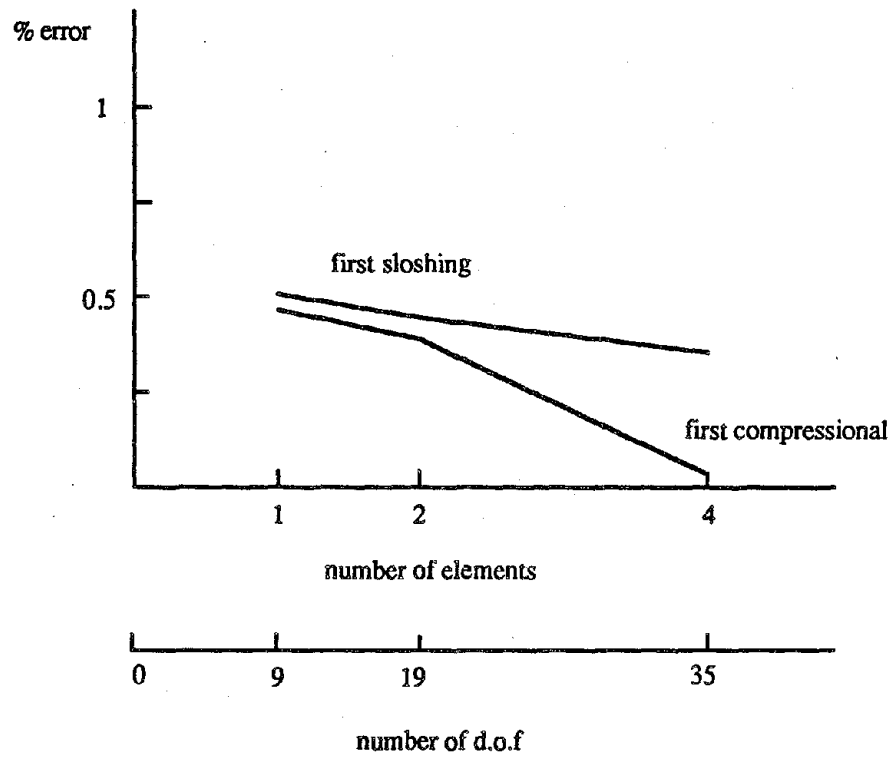
Fig. 3.14 Convergence of first compressional and
sloshing frequencies for water in rigid
tank with 9-node finite elements.

$$\alpha = 50 \ c_0^2 \ \rho_0$$

a) Uniform mesh

12"

24"
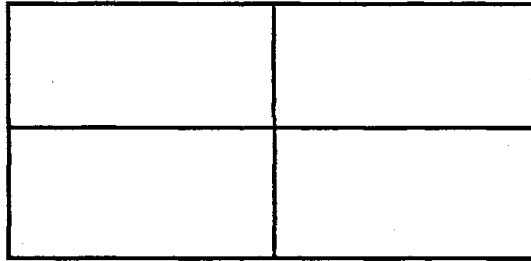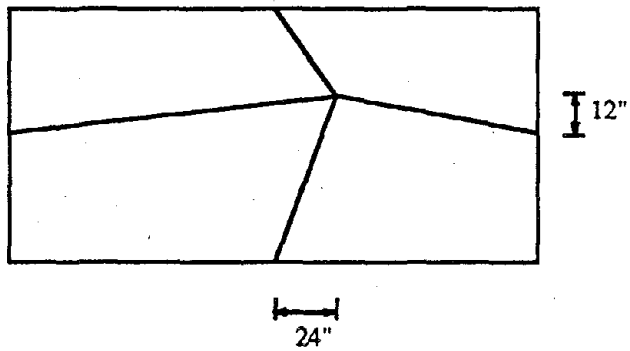
b) Arbitrary mesh

Fig. 3.15 Element array for a pressure patch test
of rigid water tank. 4-node, 8-node and
9-node elements.

Page Intentionally Left Blank

Chapter 4

Earthquake Response of Gravity Dams with Fluid Cavitation

4.1 Introduction

Early studies on the effects of water cavitation on concrete dams were based on simplified models such as a rigid dam with incompressible fluid. The ground acceleration needed to produce water cavitation in dam-water systems was found to be inversely proportional to the square root of the dam height [14]. Also, for a rigid dam cavitation can be only initiated at depths greater than 33 ft. below the reservoir free surface. These criteria, however, do not apply to flexible dams impounding compressive fluid, in which the acceleration along the height of the dam depends on the vibrational characteristics at the dam-water system.

In this chapter, the numerical procedure described in Chapters 2 and 3 is applied to two-dimensional models of concrete gravity dams impounding a reservoir of compressible fluid allowing cavitation. First, parameters regarding the finite element modeling of the fluid are evaluated. Secondly, typical concrete gravity dams are studied to assess the significance of cavitation on the earthquake response to horizontal and vertical ground motion. Finally, the effects of reservoir bottom materials, which partially absorb incident hydrodynamic pressure waves, on cavitation are analyzed.

4.2 Modeling of Fluid Domain

Several parameters involved in the finite element modeling of the fluid domain are investigated. The major factors considered in the discretization of the fluid

are: the extent of the fluid domain, element size and element order, time step for numerical integration and artificial damping for the fluid. For this purpose, a typical concrete gravity dam-water system is selected for study. The tallest nonoverflow monolith of Pine Flat dam is used for this study, and the model is shown in Fig. 4.1. The concrete in the dam is assumed to be homogeneous and isotropic, with linear elastic behavior and properties: unit weight, 155 lb/ft^3; modulus of elasticity, 3.25 million psi; Poisson's ratio, 0.2. For the amplitude of motion expected during earthquakes, it is valid to assume that a single monolith responds in a state of plane stress independent of adjacent monoliths [15]. Energy dissipation in the dam is represented by viscous damping. The damping matrix for the dam is taken proportional to the stiffness matrix to provide 5 percent of critical damping at the fundamental frequency of the dam alone. The infinite fluid domain in the upstream direction is modeled by a finite domain with an approximate radiating condition at the upstream end, as discussed in Chapter 2. The impounded water is considered to behave bilinearly to represent the effect of cavitation. The water has a density, ρ_0, of 1.94 $lb\text{-}sec^2/ft^4$; pressure wave velocity, c_0, of 4720 ft/sec.

The S69E component of the earthquake record at Taft Lincoln School Tunnel (1952) is used for the horizontal ground motion input for the evaluation of the fluid finite element modeling. For consistency with the results in Section 4.3, the ground motion is scaled from a peak ground acceleration of $0.18g$ to $1g$.

4.2.1 Extent of Fluid Domain

The fluid domain must extend a sufficient length in the upstream direction to minimize reflections of pressure waves from the truncated boundary. To examine the required extent of the fluid domain, the water is assumed linearly compressible

(no cavitation). Two values for the aspect ratio of the fluid domain, $L/H = 2$ and 3, where L is the upstream length of fluid domain, and H is the dam height, were used in the 400 ft. gravity dam-water system. The gravity dam-water system is modeled by a 4-node coarse mesh, as depicted in Fig. 4.2, for $L/H = 3$. For $L/H = 2$, the last two columns of finite elements in the fluid are eliminated. The hydrodynamic pressure at location A, near the upstream face of the dam, and location B, 640 ft. in the upstream direction, are shown in Fig. 4.3. A good agreement is obtained for both L/H ratios at location A. However, spurious wave reflections at the truncated boundary affect the pressure response at location B, although the pressures are smaller than in location A. Therefore, a L/H ratio of 3 is adopted for all subsequent response analysis of this system.

4.2.2 Element Size

Two different mesh refinements were examined with the 400 ft. concrete gravity dam-water system. The size of the element was selected by considering the time needed for the passage of pressure waves across a finite element, the pressure wave velocity, and the time step for integration of the equations of motion. The selection of the time step is discussed in Section 4.2.4. First, a 4-node coarse mesh, Fig. 4.2, and a 4-node fine mesh, Fig. 4.4, were adopted. For the linear fluid, the dam displacement response is compared with previous results [15], using a different modeling and solution procedure. The displacement of the dam crest for the two meshes is shown in Fig. 4.5. The peak horizontal displacement, 7.44 in, differs by about 9 percent from the one in Ref. [15], 8.06 in. This difference can be attributed to the modeling and assumptions employed in this study and the one in Ref. [15], in which the fluid domain is modeled as a continuum assuming a vertical upstream face and the dam discretization is much more refined. Thus, the 4-node fine mesh is

considered satisfactory for investigating the effects of cavitation.

4.2.3   Element Order

The response of the 400 ft. gravity dam-water system is compared for both the 4-node fine mesh for the fluid, Fig. 4.4, and the coarse mesh of Fig. 4.2 using 9-node elements. For the linear fluid, Fig. 4.6 shows that the response at the dam crest represents the peak displacements better with the 9-node element mesh, when compared to the results in Ref. [15]. However, the number of degrees-of-freedom in the coarse 9-node mesh is nearly twice as much as for the 4-node element mesh, increasing the computational effort considerably, particularly for nonlinear response with cavitation. Because of the involved computation of the 9-node elements and the good performance of the 4-node fine mesh, the later is adopted for modeling the fluid in the cavitation study.

4.2.4   Time Step for Numerical Integration

The time step in the numerical integration of the equations of motion, Section 2.6, is an important parameter in determining the accuracy of the solution. Even though the fully implicit numerical integration procedure is unconditionally stable for the case of linear fluid, a time step small enough to obtain an accurate solution and to allow the passage of waves through the finite elements is necessary.

The relationship between the size of the finite element and the time step is given by [4]

$$a = \Delta t \ c_0 \qquad (4.1)$$

where a is the size of the smallest finite element that lies in the direction of the wave propagation and Δt is the time step of integration. More crucial, however, is the

time step when cavitation in the fluid is allowed and the response is nonlinear. In this study, numerical experiments showed that stability of the nonlinear solution is not difficult to achieve if artificial damping for the fluid is included. For the linear case, the time step value was governed by the traveling of waves over an element, generally 0.02 or 0.01 seconds. Accuracy determined the time step for the nonlinear cases, usually half the time step used for the linear problem.

4.2.5 Artificial Damping in Fluid

One of the characteristics of the fully implicit numerical integration procedure described in Section 2.6, is the lack of numerical damping. This damping is sometimes a desirable property because it reduces high frequency noise that might disturb the solution, particulary in the presense of response nonlinearities. The formation and subsequent collapse of the cavities in the fluid induce high frequency pressure pulses which may distort and sometimes destabilize the numerical solution.

In order to minimize this shortcoming, a small amount of artificial damping in the fluid is introduced. The additional damping is considered proportional to the stiffness of the fluid, and is evaluated at the first natural frequency of the impounded water. Amounts ranging from 0.05 to 0.75% of critical damping were investigated using the 400 ft. concrete gravity dam-water system with fine 4-node mesh, Fig. 4.4. Fig. 4.7 shows the effect of artificial fluid damping on the displacement of the dam crest, assuming a linear fluid. A value of 0.10% of artificial damping closely approximates the peak displacements, whereas a damping of 0.75% reduces the displacement amplitude considerably. Numerical experiments showed that when the dam-water system is subjected to the first 9 seconds of the Taft ground motion, scaled to $1g$ peak ground acceleration, and then allowed to vibrate freely, the solu-

tion is unstable when cavitation is permitted and the artificial damping ratio is less than 0.10% with $\Delta t = 0.01$ seconds and also $\Delta t = 0.005$ seconds. Consequently, an artificial damping ratio of 0.10% is used in the response analyses presented in this chapter.

4.3 Response of Gravity Dam-Water System

4.3.1 Gravity Dam-Water System and Ground Motion

The geometry of a monolith of the Pine Flat dam is taken as a typical example to study the significance of water cavitation on the earthquake response of gravity dams. Two concrete gravity dam-water systems with dam heights of 400 ft., Fig. 4.4, and 600 ft., Fig. 4.8, are considered. The aspect ratio for the fluid domain is $L/H = 3$. The material properties and model of the concrete dam are the same as those used in Section 4.2. Energy dissipation in the dam is represented by viscous damping with a ratio of 5% at the fundamental frequency of the dam alone and with a stiffness proportional damping matrix. Further, the dam is assumed to behave linear elastically and in plane state of stress. The finite element mesh for the dam monolith is composed of 4-node nonconforming plane stress elements [43]. Concrete cracking, the major source of nonlinearity in the dam, is not included in this chapter, but it is incorporated in Chapters 5 and 6.

The vapor pressure of the water, measured with respect to the atmospheric pressure, is $p_v = -15$ psi, and the coefficient of resistance of a cavitated region to expansion, β_0, is 0.01. The fluid penalty parameter considered is fifty times the water bulk modulus, $\rho_0 c_0^2$, as determined in Chapter 3. An artificial damping of 0.10% is added to the fluid domain to stabilize the solution in presense of the highly nonlinear response of a cavitating fluid.

Two ground motions were selected for the evaluation of cavitation effects: the 1952 Kern County earthquake recorded at the Taft Lincoln School Tunnel, and the 1971 San Fernando earthquake recorded at the abutment of Pacoima Dam, a concrete arch dam. The S69E component of the Taft ground motion, which has a broad spectrum, was scaled from $0.18g$ to a peak horizontal ground acceleration of $1g$, because large accelerations are needed to induce cavitation. The vertical component of the Taft ground motion was also considered, scaled by the same factor as the horizontal component. The S16E component of Pacoima earthquake, which has a narrow band spectrum, with a peak ground acceleration of $1.17g$ was taken unscaled. The vertical component of Pacoima ground motion was considered as well.

4.3.2 Effects of Cavitation on the Response of Gravity Dams

The response of the 400 ft. concrete gravity dam-water system, Fig. 4.4, due to the S69E component of the Taft ground motion is shown in Figs. 4.9-4.10. A time step of 0.02 and 0.01 seconds was found adequate for accurate response of the system with linear and cavitating fluid, respectively. The hydrodynamic pressures in fluid elements A, B and C (see Fig. 4.4) are shown in Fig. 4.9; the horizontal and vertical displacements of the dam crest are shown in Fig. 4.10. The displacement in the upstream direction is positive and in the downstream direction negative.

A comparison of the responses for linear and cavitating fluid clearly shows the inability of water to sustain a pressure less than the vapor pressure if cavitation is permitted. Cavitation is initiated when the dam is displaced in the upstream direction and is accelerating downstream; a half-cycle later, as the velocity of the dam is decreasing from its maximum value, the cavitated regions in the fluid collapse and produce large pressure peaks of short duration. The large pressure pulses induced

by the first collapse of the cavitated region subsequently produce a large amount of additional cavitation that is not indicated by the hydrodynamic pressure on a linear fluid. Although there is a large amount of cavitation in the water, the effect on maximum displacement is very small, as shown in Fig. 4.10.

Of interest, however, is the acceleration response of the dam crest, relative to the ground motion, in which cavitation has a major effect. Fig. 4.11 shows that for the linear fluid the maximum acceleration at the dam crest is $2.5g$, whereas for the cavitating fluid this peak acceleration more than doubles to $5.5g$. Comparing Fig. 4.11 with 4.9 for the cavitating fluid, the peak acceleration occurs at the same time (at about 8.2 seconds) as the high pressure pulse impinges on the dam, an expected result since the acceleration is proportional to the hydrodynamic pressure gradient at the upstream face of the dam. Even though the amplified accelerations are of high frequency, they may be of considerable importance for the design of secondary equipment and appurtenances needed for the dam functionality.

As with displacements, the effect of cavitation on maximum principal stresses in the dam is minor. The maximum principal stresses at six different locations in the dam are shown in Table 4.1. The maximum stresses occur mostly near the geometric transition between the vertical and the sloping faces, upstream and downstream, which acts as a stress concentration. Most importantly, the stress magnitudes exceed the concrete tensile strength, indicating that at amplitudes of ground motion that induce cavitation, tensile cracking of concrete will be important, and most likely a dominant nonlinear response effect. Models to represent the inability of concrete to transmit significant tensile stresses and subsequent tensile cracking will be examined in Chapter 5 and 6.

The wave propagation phenomenon explained in Ref. [48] in regards to the

cavity movement within the fluid domain is clearly confirmed in Fig. 4.12, where cavitation zones at different times during the response are depicted. Note how the formation of cavities evolve with time and they propagate in the upstream direction where lower pressure in the fluid exists. A summary of the fluid elements that cavitate during the ground motion are shown in Fig. 4.13, where intensity of the shading is proportional to the number of cavitation events in the elements during the response to the ground motion. High cavitation is defined when an element undergoes cavitation more than 150 times; intermediate cavitation in between 100 and 150; low between 50 and 100; and minimal for an element cavitating less than 50 times. Note that cavitation decreases with depth and in the upstream direction because the hydrostatic pressure increases with depth and linear analysis [15] shows that hydrodynamic pressure decreases exponentially upstream.

The response of the concrete gravity dam-water system of 400 ft., Fig. 4.4, when subjected to the S16E component of Pacoima ground motion is depicted in Figs. 4.14-4.15. The hydrodynamic pressure at three different fluid elements, A, B and C, Fig. 4.4, are shown now in Fig. 4.14; the horizontal and vertical displacement of the dam crest can be seen in Fig. 4.15. The observations on the effects of cavitation, are the same as noted for the dam subjected to the Taft ground motion. However, less cavitation takes place as shown in Fig. 4.16. Table 4.2 the maximum stresses in the dam at various locations.

Because for rigid dams, the required acceleration to produce cavitation decreases with height, a taller dam is analyzed to evaluate the effect of dam height on cavitation. A 600 ft. concrete gravity dam-water system, depicted in Fig. 4.8, is subjected to the Taft and Pacoima ground motions. The dam geometry is obtained by uniformly scaling the geometry of the 400 ft. dam. The time steps for this case were the same as for the 400 ft. gravity dam-water system. The response for the

scaled horizontal component of the Taft earthquake is shown in Figs. 4.17-4.18. It is observed that less cavitation takes place. This behavior, which contradicts the conclusion for rigid dams, is explained by the reduction of dynamic amplification of the fundamental mode on the 600 ft. dam for the particular Taft ground motion. Fig. 4.19 depicts the cavitation pattern in the water and Table 4.3 lists the maximum stresses at selected locations in the dam. When the 600 ft. height system is subjected to the Pacoima earthquake, no cavitation takes place in any of the fluid elements; therefore its response is not shown. Tables 4.2-4.3 show the maximum stresses at six differents locations in the dam. The comments made for the magnitude of the stresses in the 400 ft. dam are the same here.

4.3.3   Significance of Vertical Ground Motion on the Response of Gravity Dams

The displacement response of the 400 ft. concrete gravity dam-water system due to the vertical component of Taft ground motion is shown in Fig. 4.20. The vertical ground motion is scaled by the same factor as used previously for the horizontal ground motion. In this case, no cavitation occurs; however, a comparison with the displacement response due to S69E component of Taft, Fig. 4.10, indicates the response to the horizontal and vertical components are nearly in phase, particularly between the seventh to the tenth second. This observation is confirmed when the dam-water system is subjected to both components simultaneously, in which the effect of the vertical component is very large, Figs. 4.21-4.22, producing considerable amount of cavitation and large differences in the displacement response. Fig. 4.23 depicts the cavitation pattern in the water. Table 4.4 shows that unlike the case of horizontal ground motion, maximum stresses increase significantly, as much as 29%, as the water cavitates. Hence, it appears that vertical ground motion is of great

importance to the dam response when cavitation is included.

The 600 ft. concrete gravity dam-water system is also subjected to the scaled vertical component of the Taft earthquake. The displacement response for vertical ground motion only is shown in Fig. 4.24 and as in the case of the 400 ft. dam, no cavitation takes place. Figs. 4.25-4.26 show the response for the vertical and S69E components simultaneously. A small difference is found with the response of the S69E component alone, Figs. 4.17-4.18, although a little more cavitation occurs (see Fig. 4.25). The cavitation pattern in the water is depicted in Fig. 4.27, in which little difference is observed with respect to Fig. 4.23. The maximum stress change, including cavitation, is around 7%, as can be noted from Table 4.5.

For linear fluid, it has been reported [15] that when rigid reservoir bottom materials are assumed, the significance of the dam response to vertical ground motion is overestimated. Therefore, a realistic model must account for the presence of sediments in the reservoir bottom. This issue is studied in the next section.

4.4 Effects of Reservoir Bottom Absorption

The presence of sediment materials at the reservoir bottom allows a partial absorption of incident hydrodynamic pressure waves. The effect of reservoir bottom materials is approximately modeled by the boundary condition of Eq. 2.15. The magnitude of these effects depend upon the wave reflection coefficient, α_r, which for all the previous cases was 1- rigid reservoir bottom materials. In this investigation, absorptive reservoir bottom materials are represented by wave reflection coefficients of: $\alpha_r = 0.5$ and $\alpha_r = 0$. It has been found that the response of concrete gravity dams is reduced in all cases, consistent with results in Ref. [15], as can be observed from Figs. 4.28 and 4.31. In the case of $\alpha_r = 0$, very little cavitation takes place.

When the dam-water system, $H = 400$ ft., is subjected to both the S69E and vertical components of the scaled Taft ground motion, for $\alpha_r = 0.5$; the response changes considerably compared to the response with $\alpha_r = 1$, as noted in Figs. 4.32-4.33. The presence of sediments undoubtedly affects the contribution of the earthquake vertical component to the total response. Moreover, the increase in maximum stresses due to cavitation is reduced to the same level as when horizontal motion is only considered, that is, a 3% difference.

Table 4.1: Maximum principal stresses in dam (psi). Concrete gravity dam-water system, $H = 400$ ft., due to the S69E component of Taft ground motion, scaled to $1g$ peak acceleration. Locations on dam shown below.

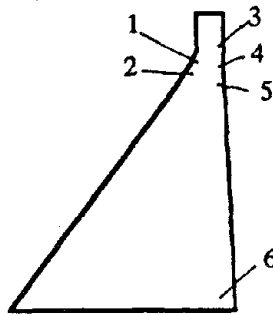| Location	Linear Fluid	Nonlinear Fluid
1	1491	1471
2	1982	1920
3	438	474
4	940	911
5	1102	1114
6	1482	1373

Table 4.2: Maximum principal stresses in dam (psi). Concrete gravity dam-water system, $H = 400$ ft., due to the S16E component of Pacoima ground motion. See Table 4.1 for locations on dam.

Location	Linear Fluid	Nonlinear Fluid
1	1848	1857
2	2530	2378
3	547	499
4	1185	950
5	1406	992
6	1558	1252

Table 4.3: Maximum principal stresses in dam (psi). Concrete gravity dam-water system, $H = 600$ ft., due to the S69E component of Taft ground motion, scaled to $1g$ peak acceleration. See Table 4.1 for locations on dam.

Location	Linear Fluid	Nonlinear Fluid
1	1741	1756
2	2289	2272
3	600	592
4	1274	1276
5	1462	1401
6	1659	1643

Table 4.4: Maximum principal stresses in dam (psi). Concrete gravity dam-water system, $H = 400$ ft., due to both the S69E and vertical components of Taft ground motion, scaled to $1g$ peak horizontal acceleration. See Table 4.1 for locations on dam.

Location	Linear Fluid	Nonlinear Fluid
1	1921	2477
2	2604	2883
3	666	775
4	1411	1176
5	1623	1312
6	1771	1472

Table 4.5: Maximum principal stresses in dam (psi). Concrete gravity dam-water system, $H = 600$ ft., due to both the S69E and vertical components of Taft ground motion, scaled to $1g$ peak horizontal acceleration. See Table 4.1 for locations on dam.

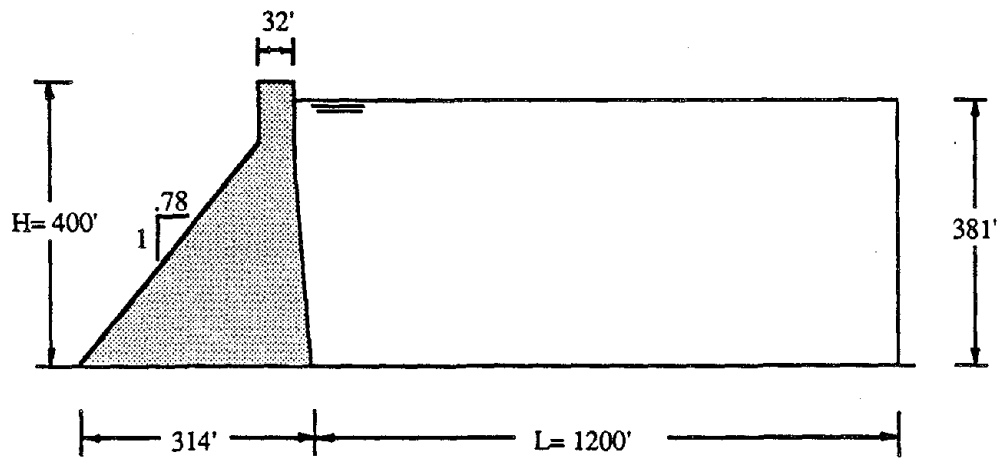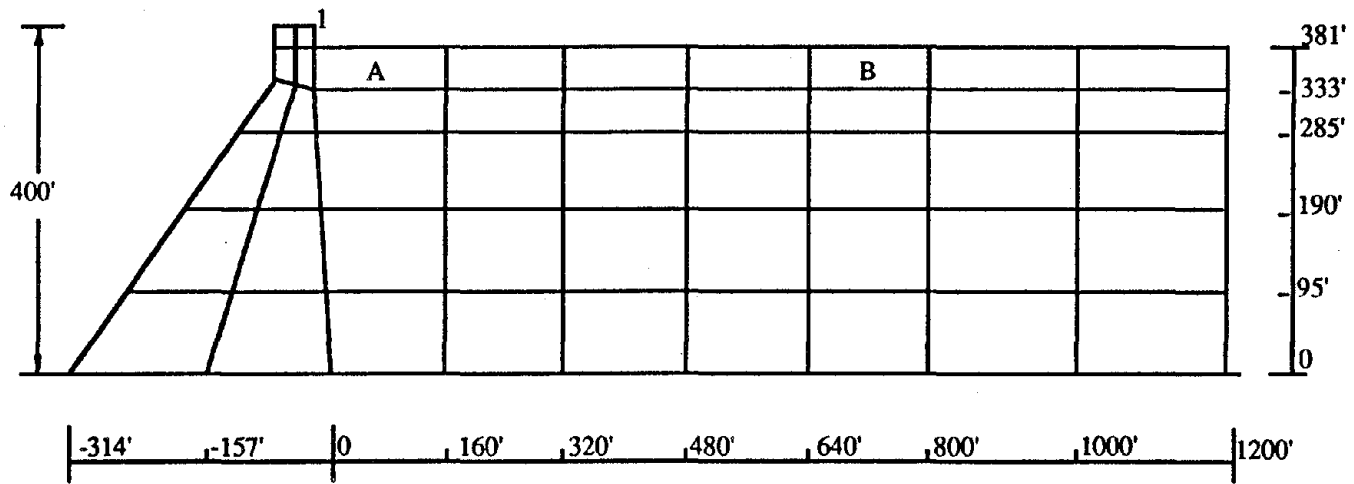| Location	Linear Fluid	Nonlinear Fluid
1	2193	1963
2	2702	2559
3	732	781
4	1558	1568
5	1799	1713
6	1993	1939

Fig. 4.1 Concrete gravity dam-water system.

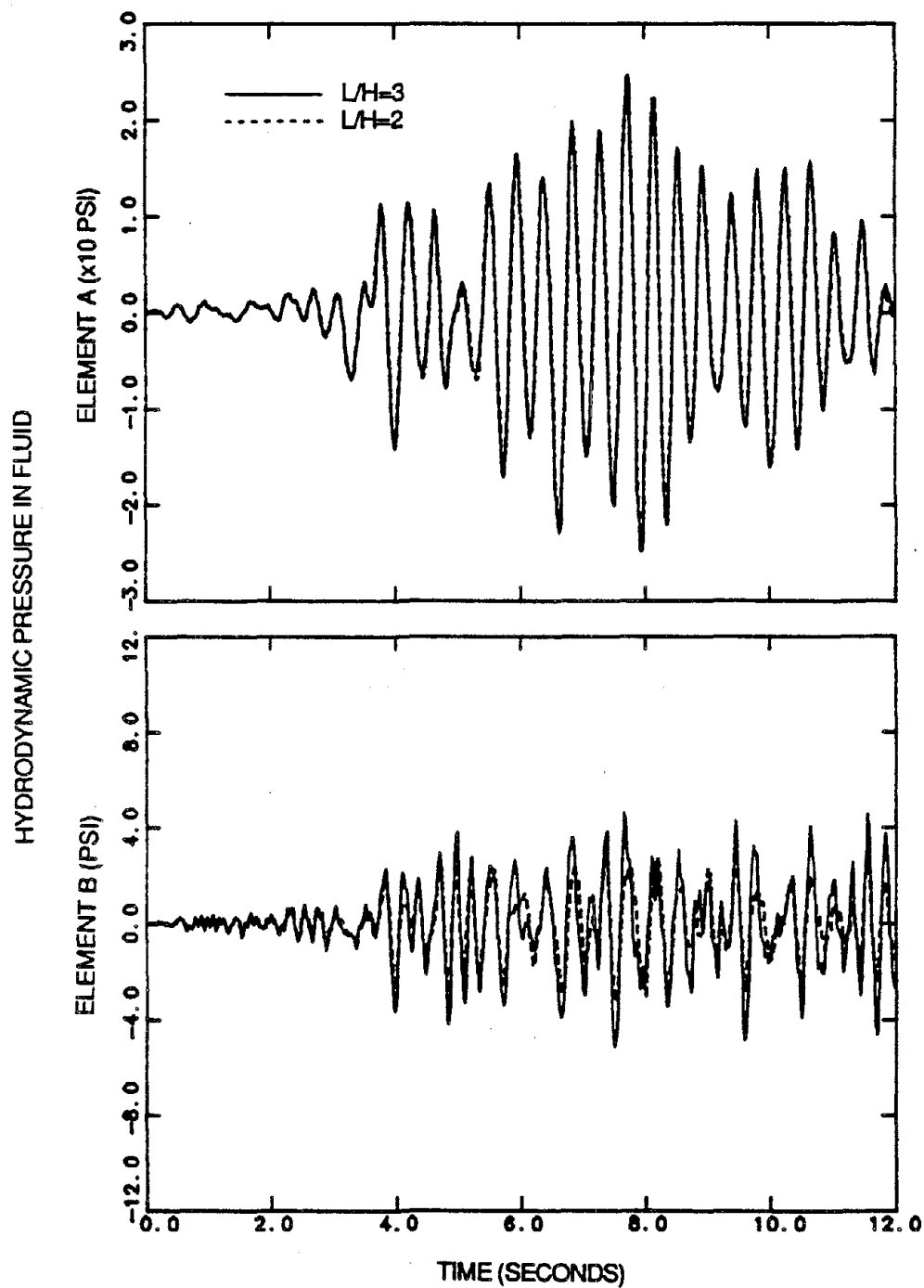Fig. 4.2 Concrete gravity dam-water system, H=400 ft.
Coarse mesh, 4-node elements.

Fig. 4.3 Effect of the extent of fluid on pressure response of the concrete
gravity dam-water system, H= 400 ft., due to the S69E component
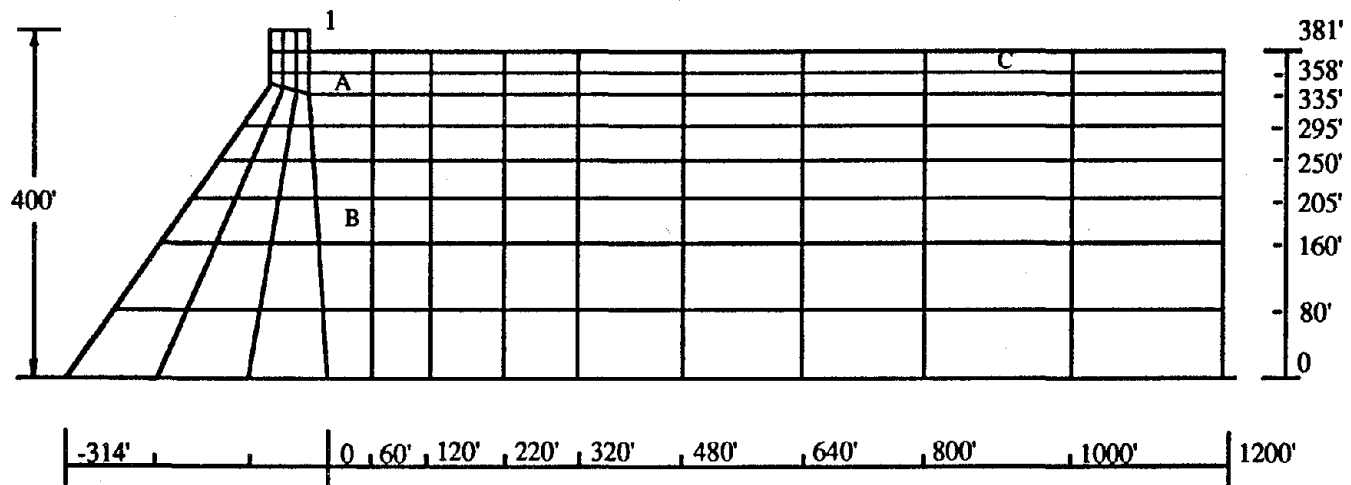of Taft ground motion, scaled to 1g peak acceleration.

Fig. 4.4 Concrete gravity dam-water system, H=400 ft.
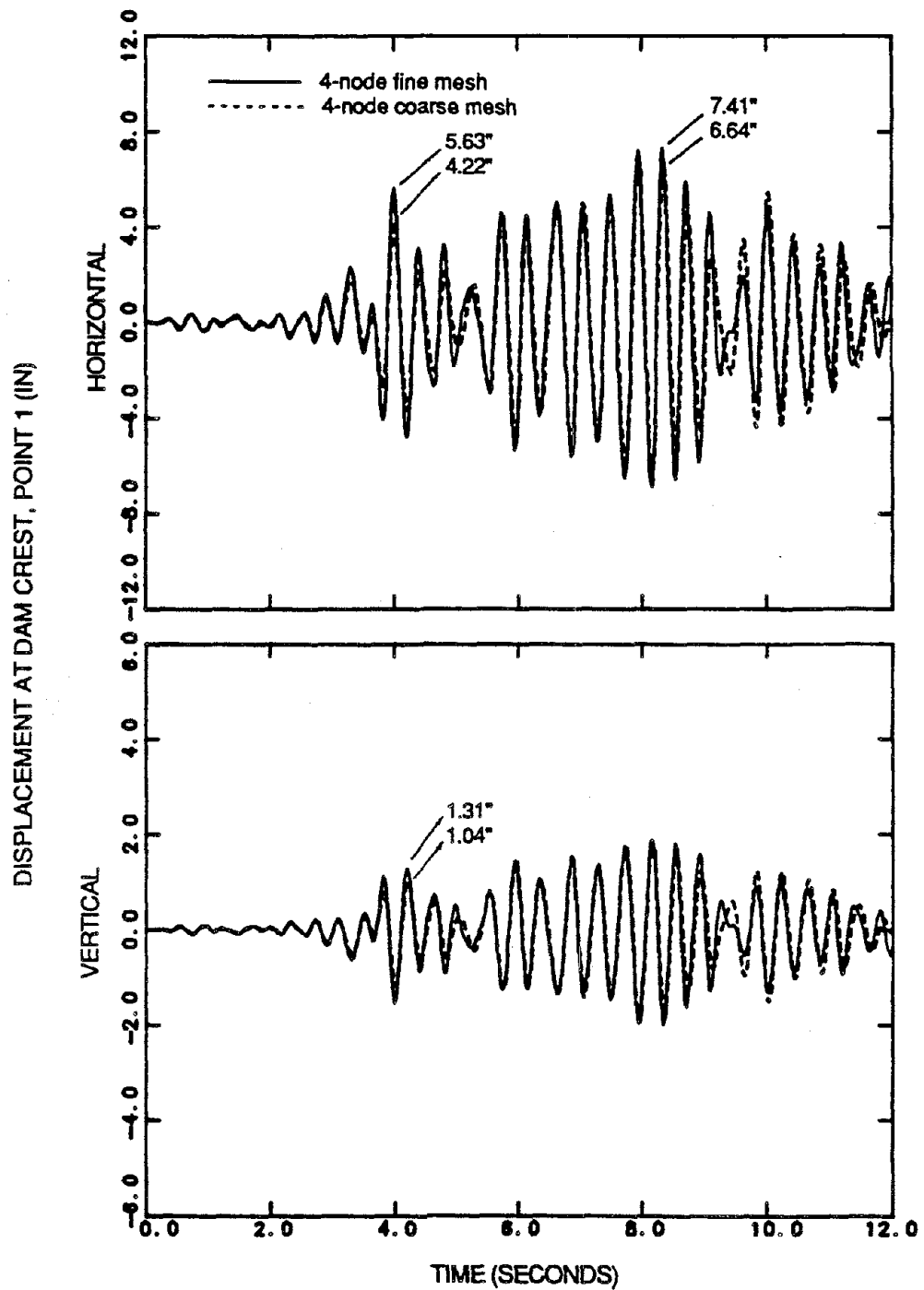Fine mesh, 4-node elements.

Fig. 4.5 Effect of element size of fluid on displacement response of the
concrete gravity dam-water system, H= 400 ft., due to the S69E
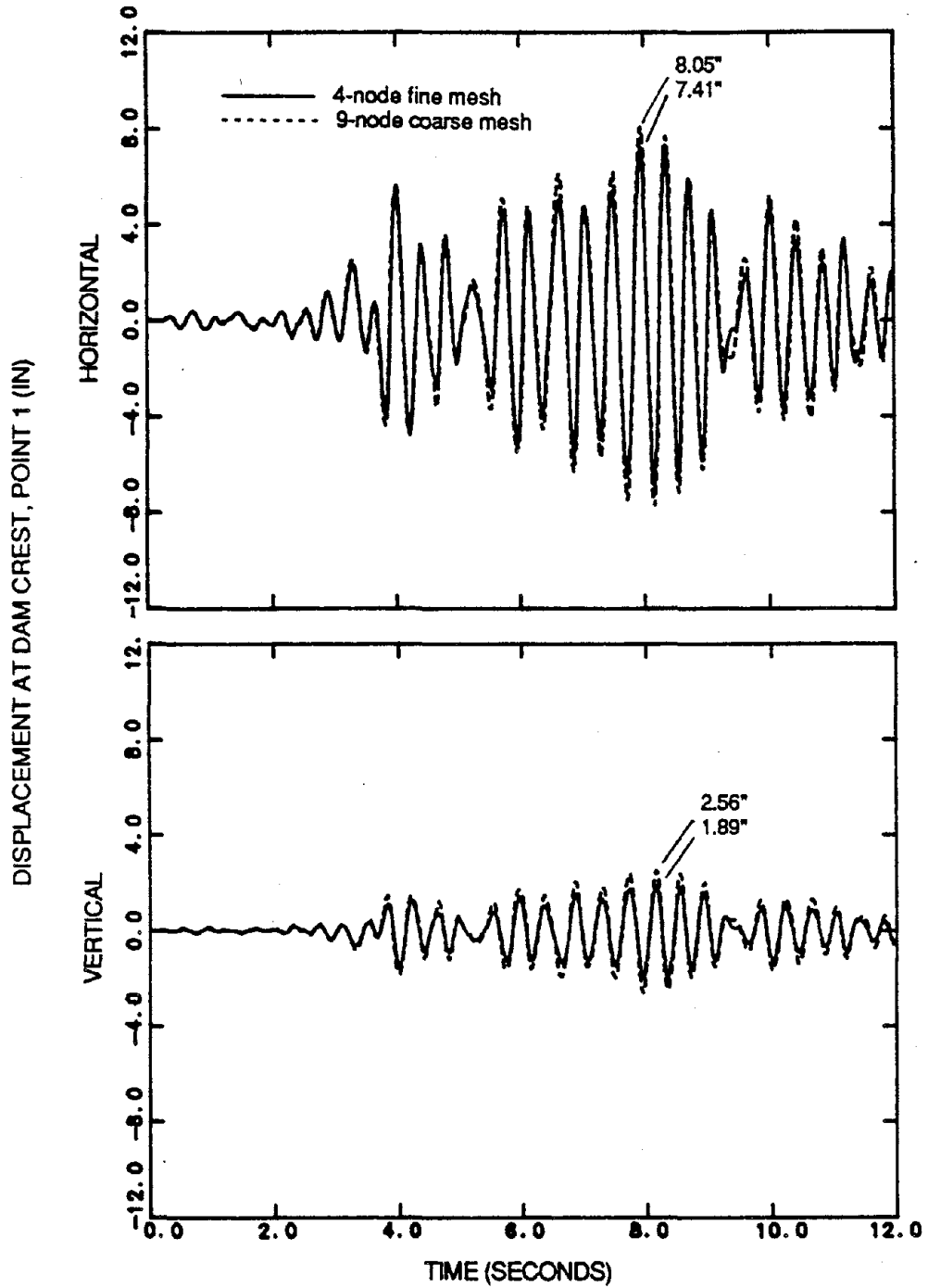component of Taft ground motion, scaled to 1g peak acceleration.

Fig. 4.6 Effect of element order of fluid on displacement response of the
concrete gravity dam-water system, H= 400 ft., due to the S69E
component of Taft ground motion, scaled to 1g peak acceleration.

Fig. 4.7 Effect of fluid artificial damping on displacement response of the concrete gravity dam-water system, H= 400 ft., due to the S69E component of Taft ground motion, scaled to 1g peak acceleration. 4-node fine mesh.
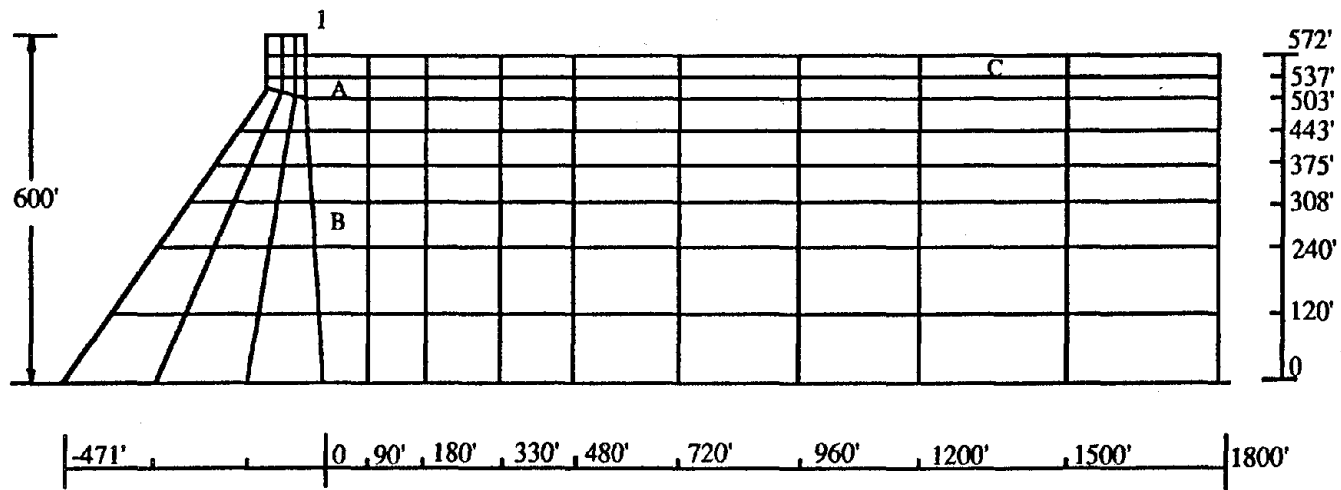
Fig. 4.8 Concrete gravity dam-water system, H=600 ft.
Fine mesh, 4-node elements.
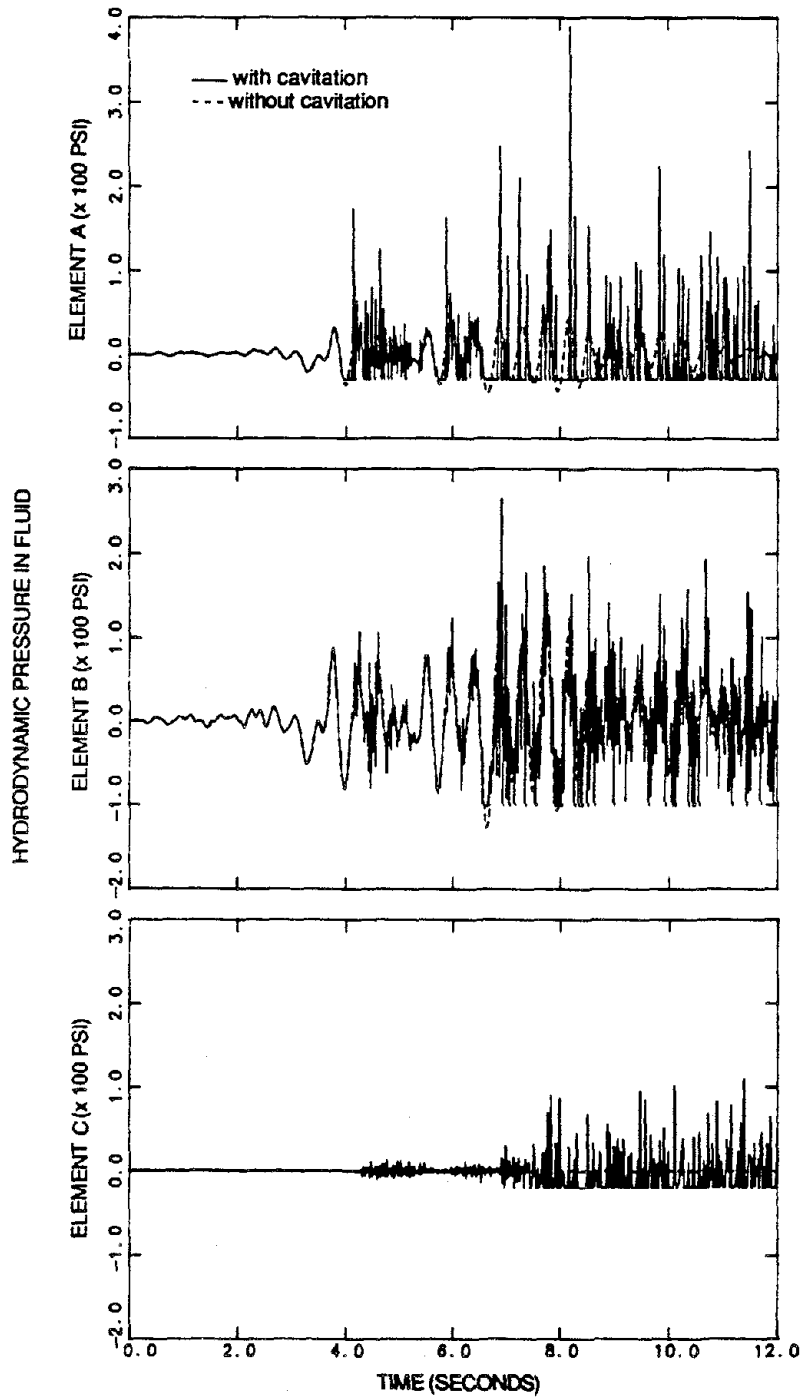
Fig. 4.9 Pressure response of the concrete gravity dam-water system,
H= 400 ft., due to the S69E component of Taft ground motion,
scaled to 1g peak acceleration.

Fig. 4.10 Displacement response of the concrete gravity dam-water system,
H= 400 ft., due to the S69E component of Taft ground motion,
scaled to 1g peak acceleration.

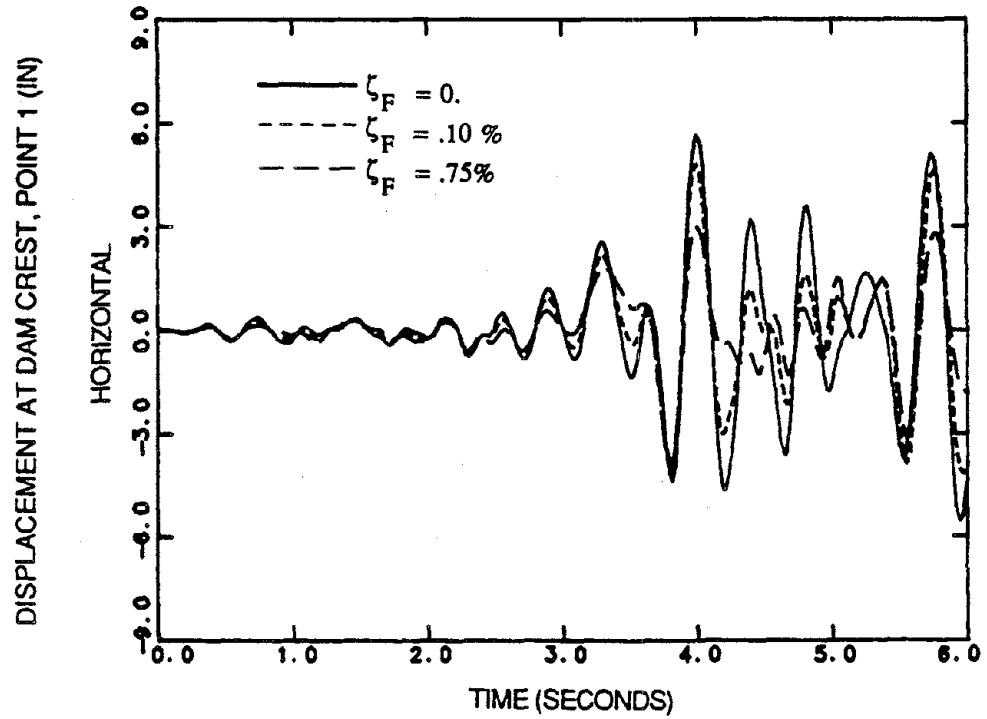Fig. 4.11 Acceleration response of the concrete gravity dam-water system, H= 400 ft., due to the S69E component of Taft ground motion, scaled to 1g peak acceleration.

a) time = 4.10 secs.

b) time = 4.20 secs.

c) time = 4.30 secs.
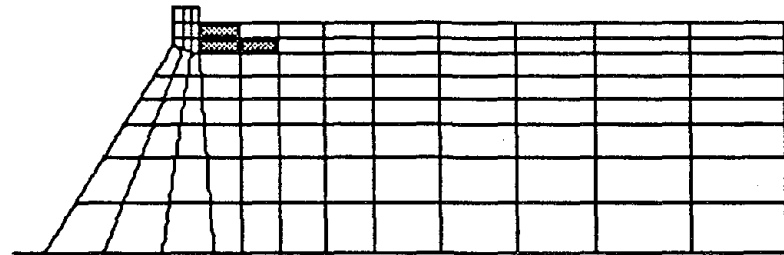
Fig. 4.12 Cavitation regions at various times after cavitation initiates.
Concrete gravity dam-water system, H= 400 ft., due to the
S69E component of Taft ground motion, scaled to 1g peak
acceleration.

d) time = 7.10 secs.
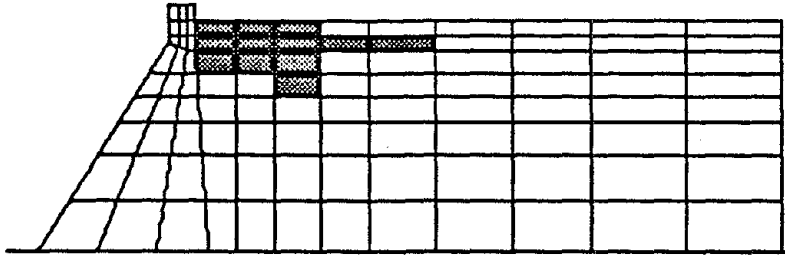
e) time = 7.20 secs.
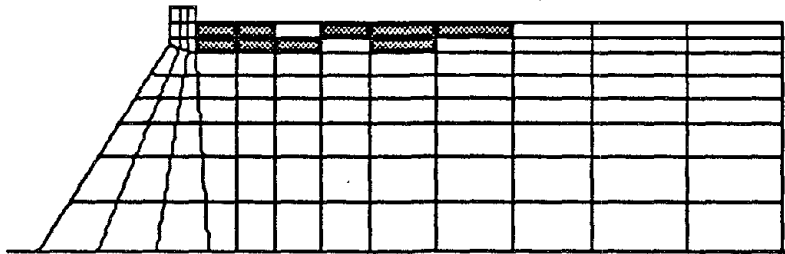
f) time = 7.30 secs.

Fig. 4.12 (continued)

high cavitation   low

intermediate   minimal
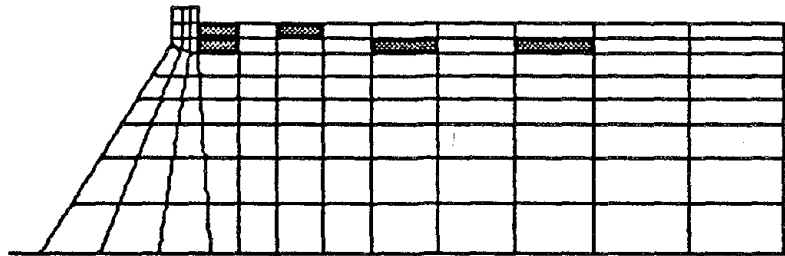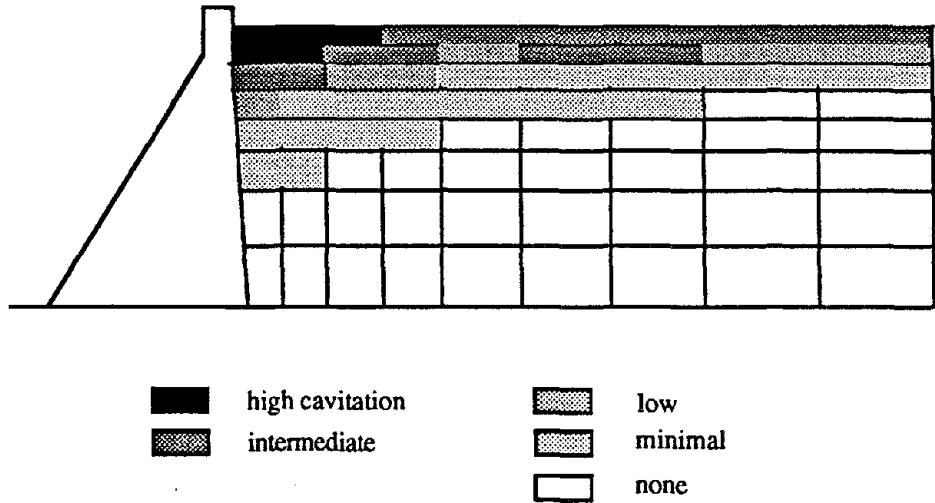
Fig. 4.13 Number of cavitation events in concrete gravity dam-water system, H= 400 ft., due to the S69E component of Taft ground motion, scaled to 1g peak acceleration.
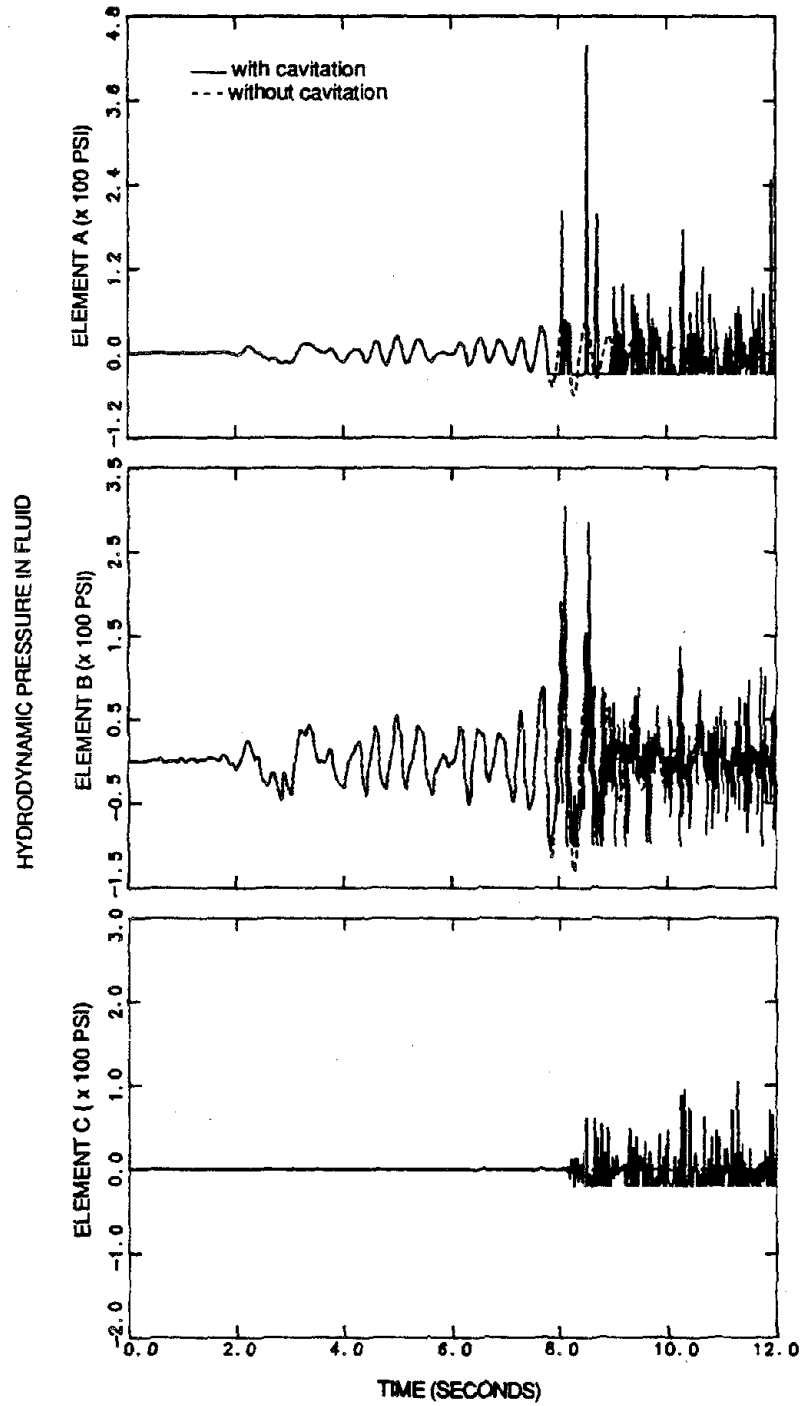
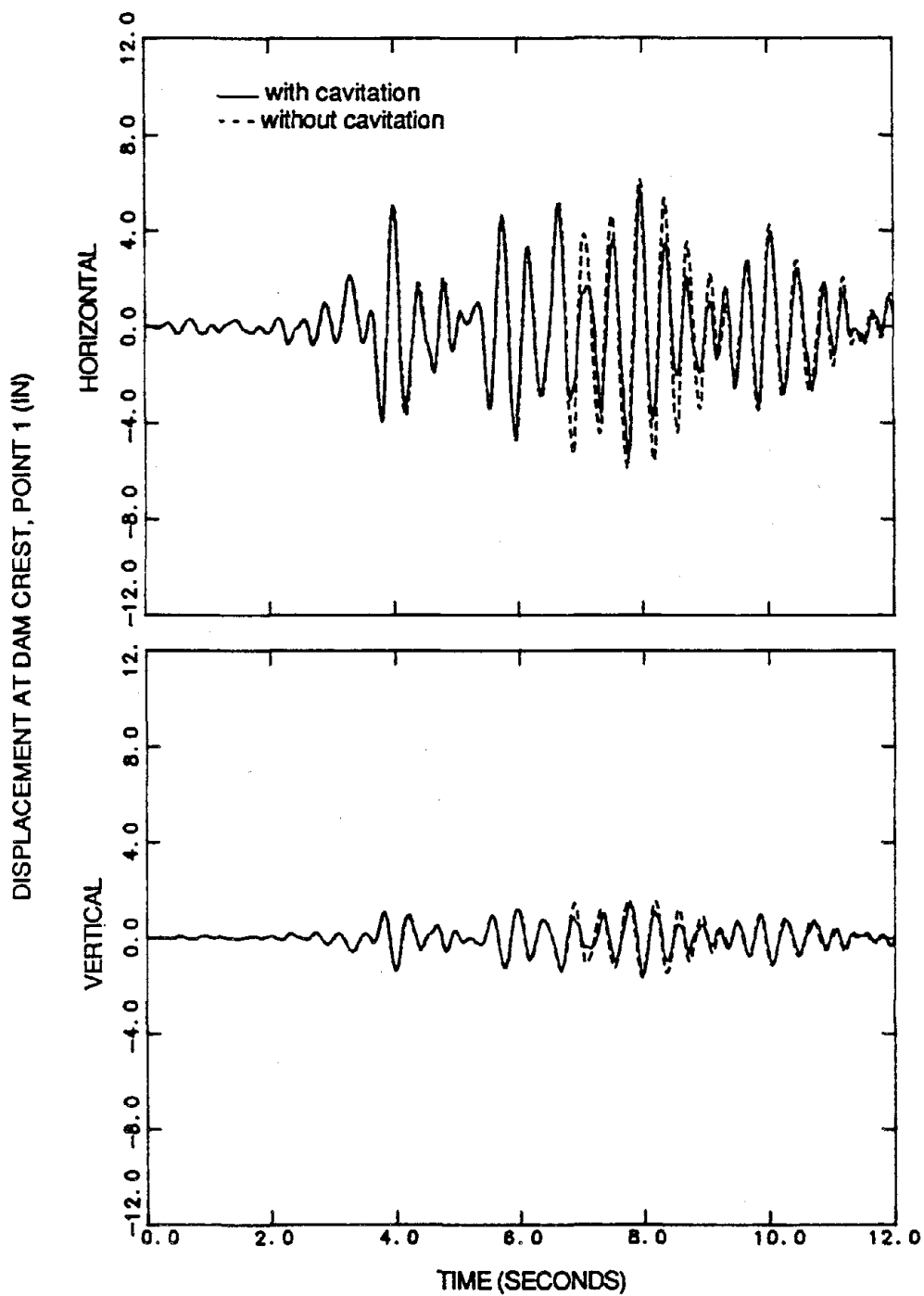Fig. 4.14 Pressure response of the concrete gravity dam-water system, H= 400 ft., due to the S16E component of Pacoima ground motion.

Fig. 4.15 Displacement response of the concrete gravity dam-water system,
H= 400 ft., due to the S16E component of Pacoima ground motion.

Fig. 4.16 Number of cavitation events in concrete gravity dam-water system,
H = 400 ft., due to the S16E component of Pacoima ground motion.

Fig. 4.17 Pressure response of the concrete gravity dam-water system,
H= 600 ft., due to the S69E component of Taft ground motion,
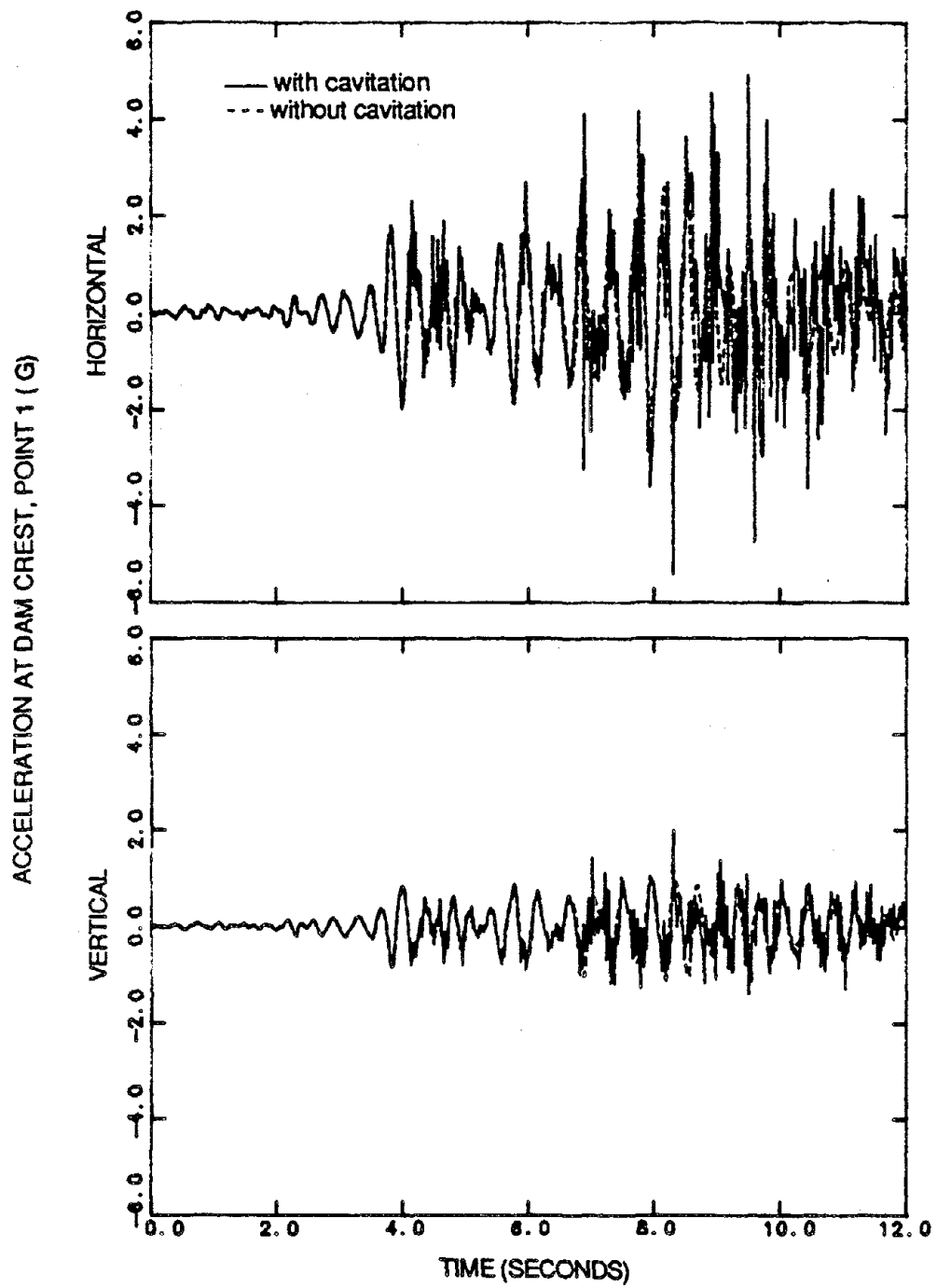scaled to 1g peak acceleration.

Fig. 4.18 Displacement response of the concrete gravity dam-water system,
H= 600 ft., due to the S69E component of Taft ground motion,
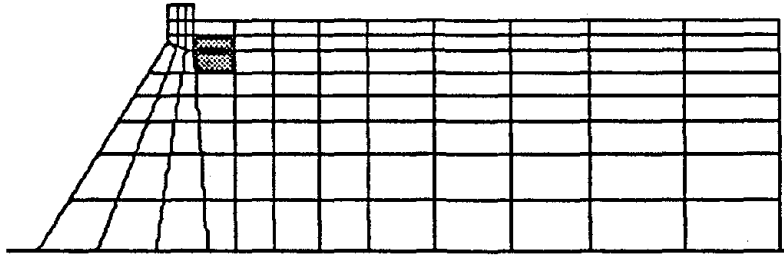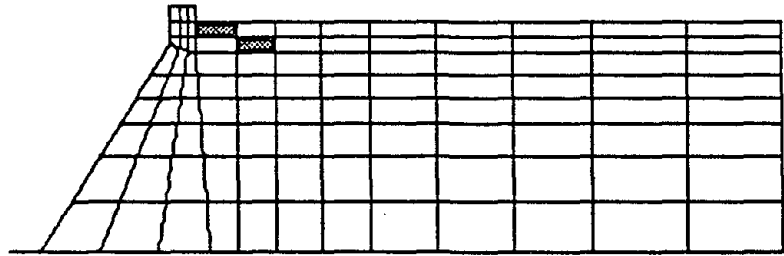scaled to 1g peak acceleration.

Fig. 4.19 Number of cavitation events in concrete gravity dam-water system,
H= 600 ft., due to the S69E component of Taft ground motion,
scaled to 1g peak acceleration.

Fig. 4.20 Displacement response of the concrete gravity dam-water system,
H= 400 ft., due to the vertical component of Taft ground motion,
scaled to 1g peak horizontal acceleration.

Fig. 4.21 Pressure response of the concrete gravity dam-water system,
H= 400 ft., due to both the S69E and vertical components of
Taft ground motion, scaled to 1g peak horizontal acceleration.

Fig. 4.22 Displacement response of the concrete gravity dam-water system,
H= 400 ft., due to both the S69E and vertical components of
Taft ground motion, scaled to 1g peak horizontal acceleration.

|		
■ high cavitation	▦ low	
▦ intermediate	▦ minimal	
	▢ none	

Fig. 4.23 Number of cavitation events in concrete gravity dam-water system, H= 400 ft., due to both the S69E and vertical components of Taft ground motion, scaled to 1g horizontal acceleration.

Fig. 4.24 Displacement response of the concrete gravity dam-water system, H= 600 ft., due to the vertical component of Taft ground motion, scaled to 1g peak horizontal acceleration.

Fig. 4.25 Pressure response of the concrete gravity dam-water system,
H= 600 ft., due to both the S69E and vertical components of
Taft ground motion, scaled to 1g peak horizontal acceleration.

Fig. 4.26 Displacement response of the concrete gravity dam-water system,
H= 600 ft., due to both the S69E and vertical components of
Taft ground motion, scaled to 1g peak horizontal acceleration.

high cavitation   low
intermediate   minimal
                   none
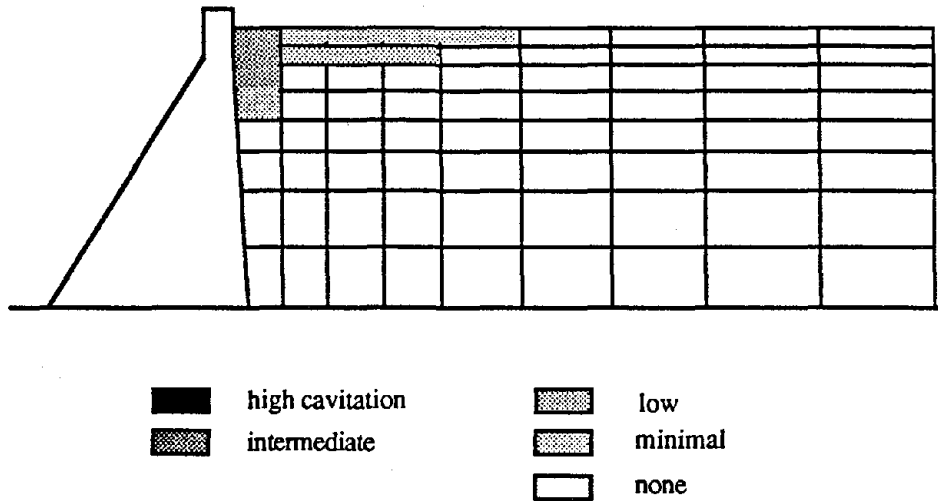
Fig. 4.27 Number of cavitation events in concrete gravity dam-water system, H= 600 ft., due to both the S69E and vertical components of Taft ground motion, scaled to 1g horizontal acceleration.
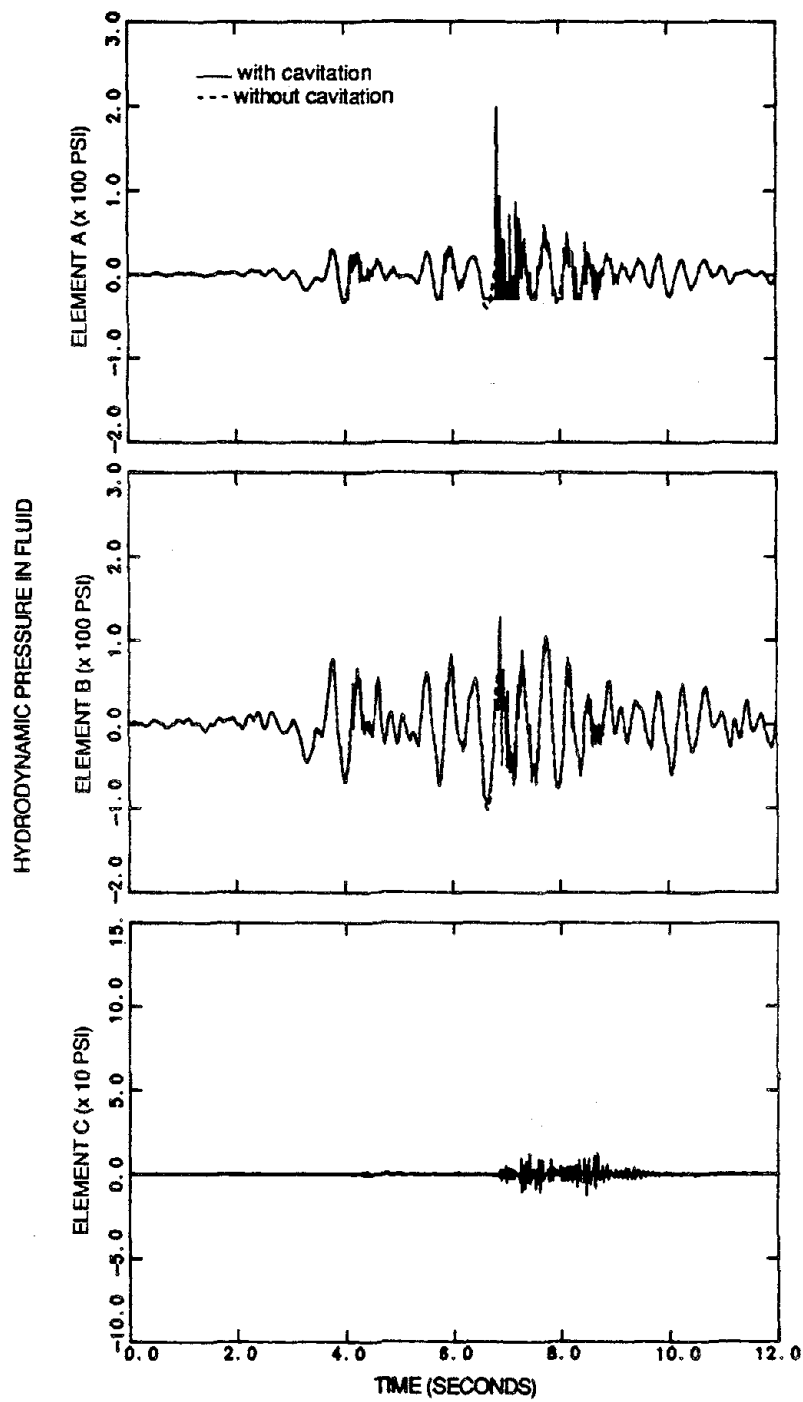
Fig. 4.28 Pressure response of the concrete gravity dam-water system,
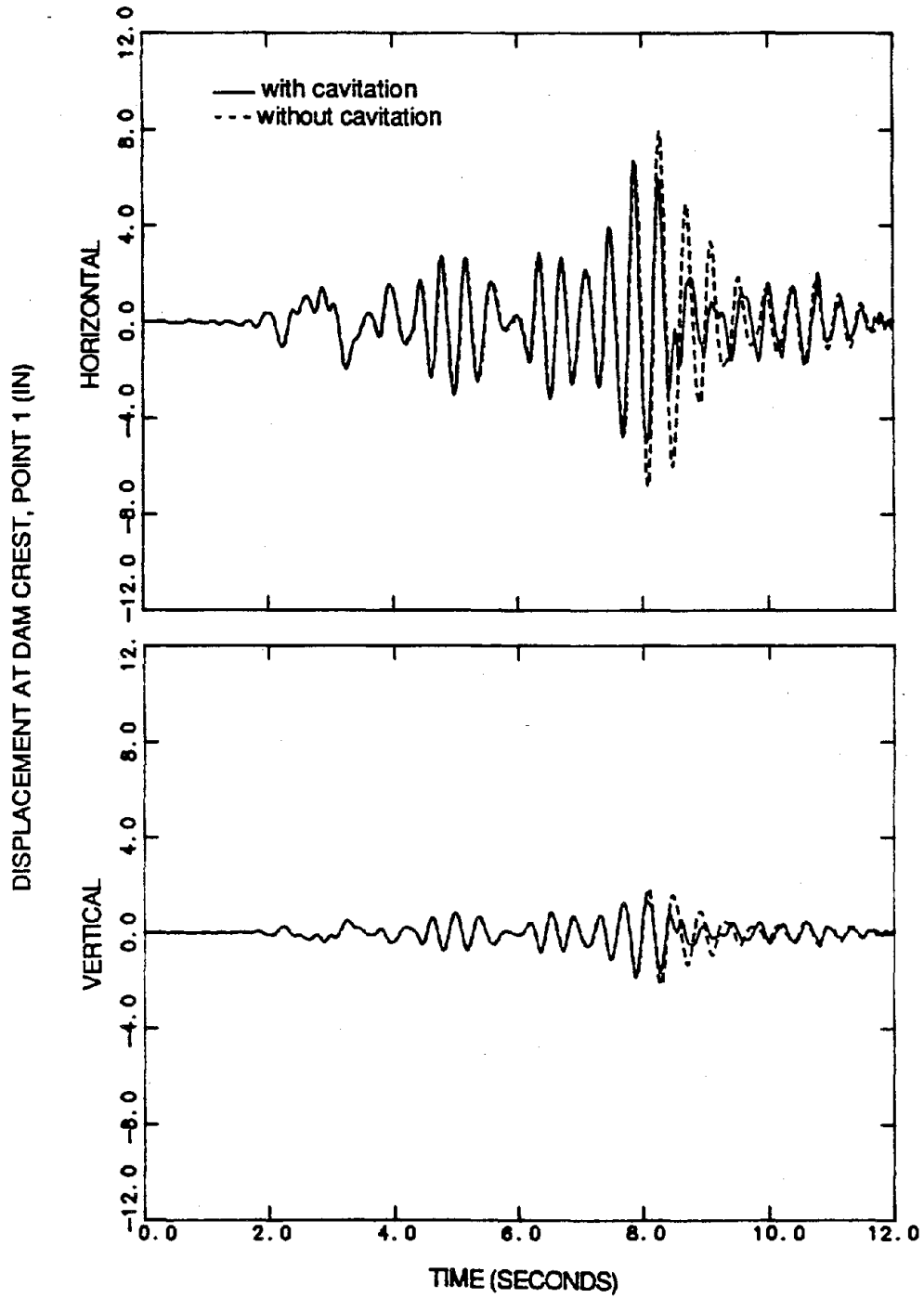H= 400 ft., due to the S69E component of Taft ground motion,
scaled to 1g peak acceleration. Absorptive reservoir bottom,
$\alpha_r = 0.5$.
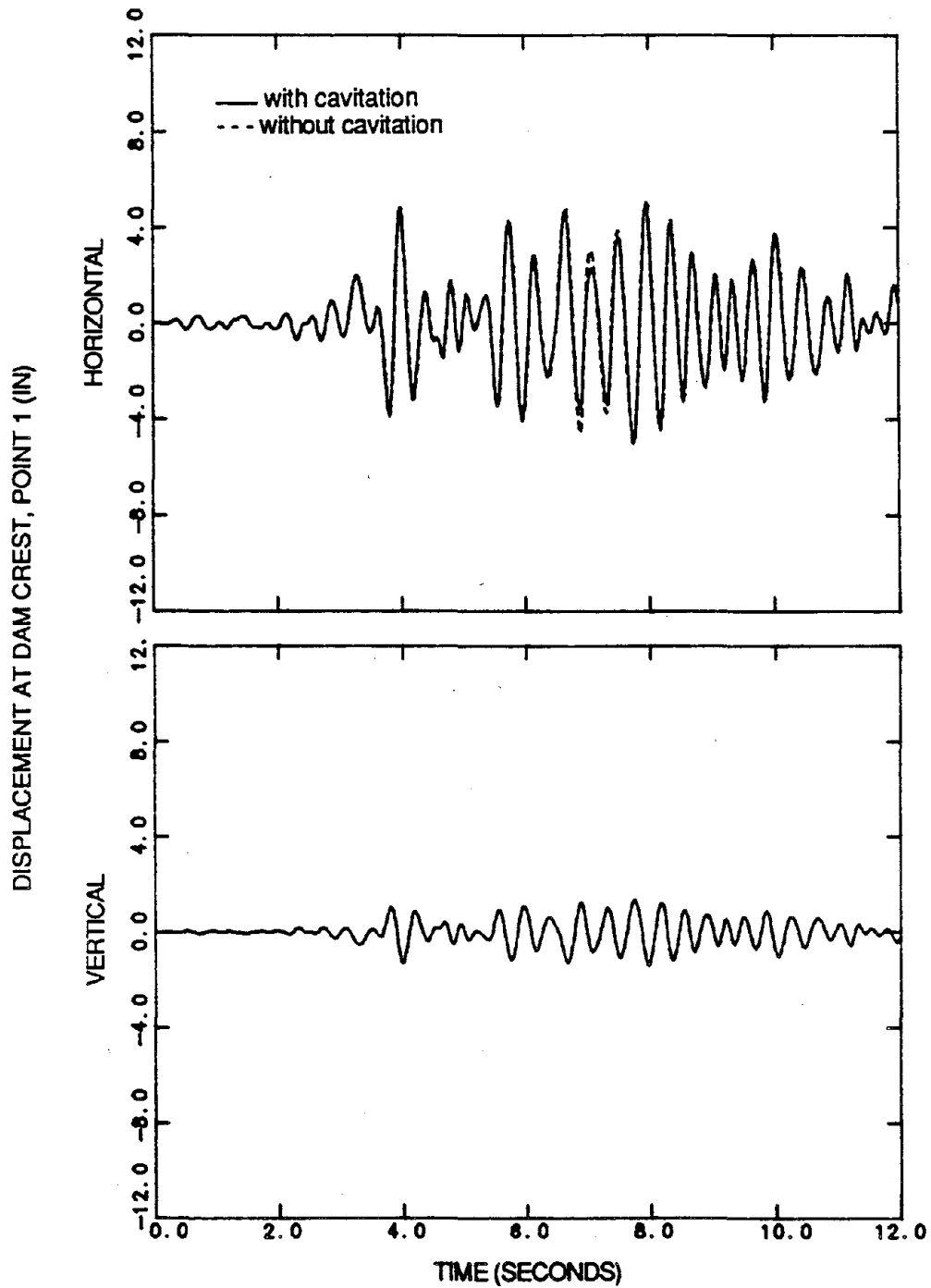
Fig. 4.29 Displacement response of the concrete gravity dam-water system,
H= 400 ft., due to the S69E component of Taft ground motion,
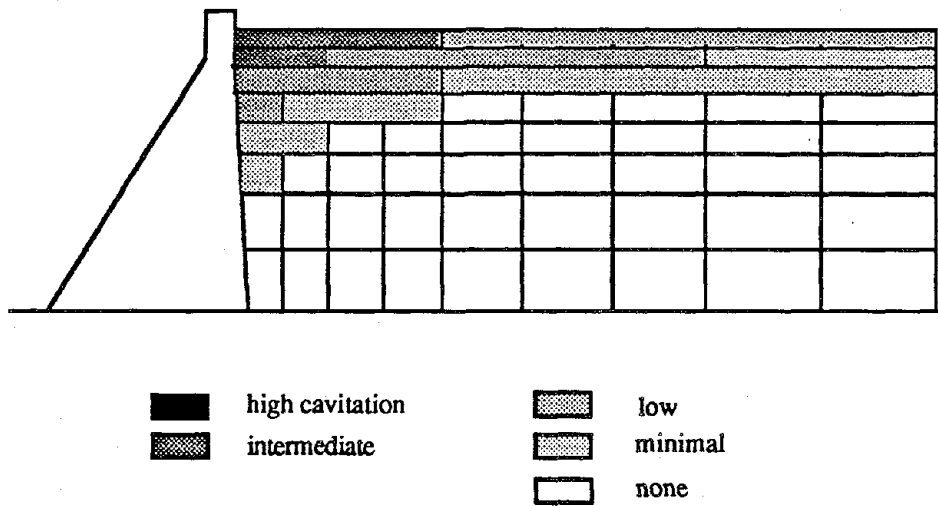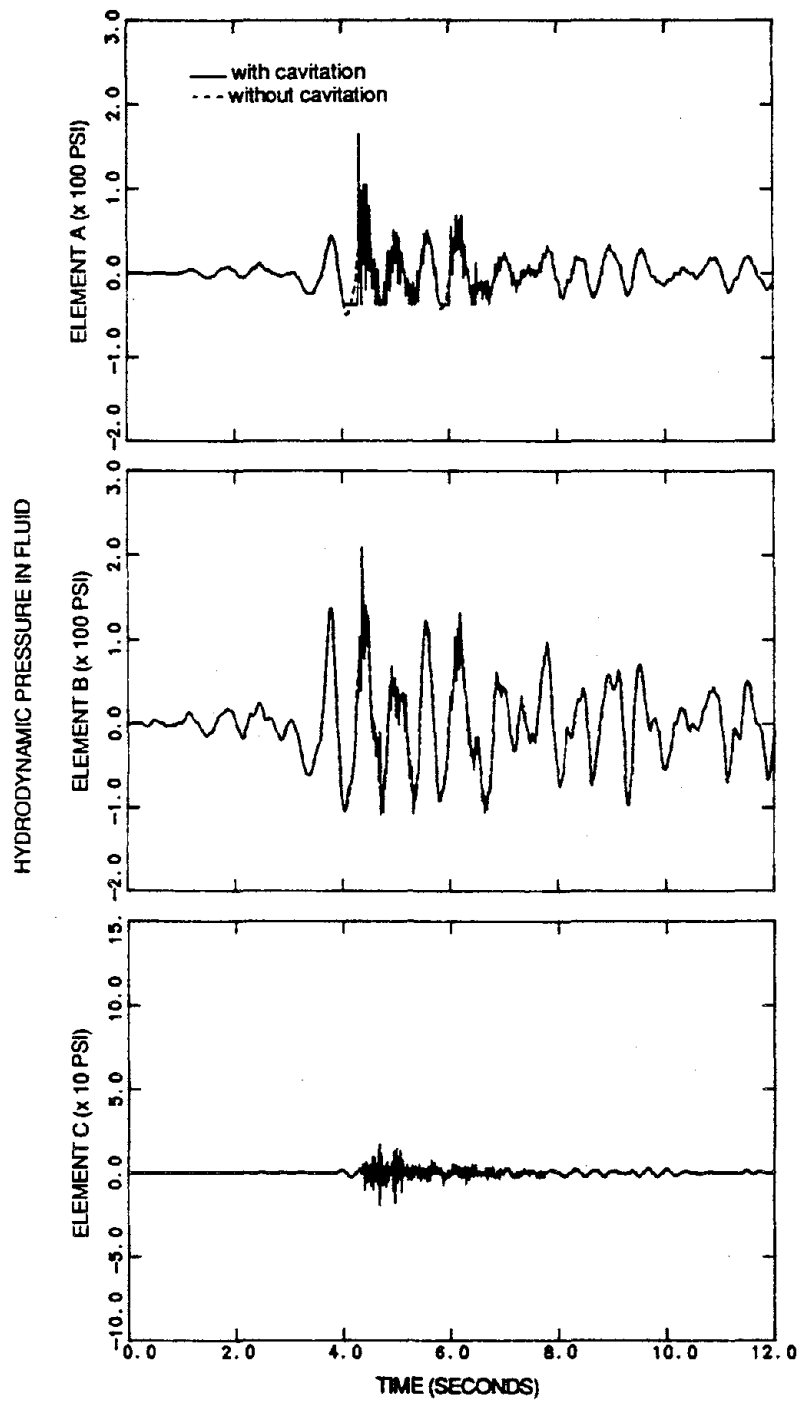scaled to 1g peak acceleration. Absorptive reservoir bottom,
$\alpha_r = 0.5$.
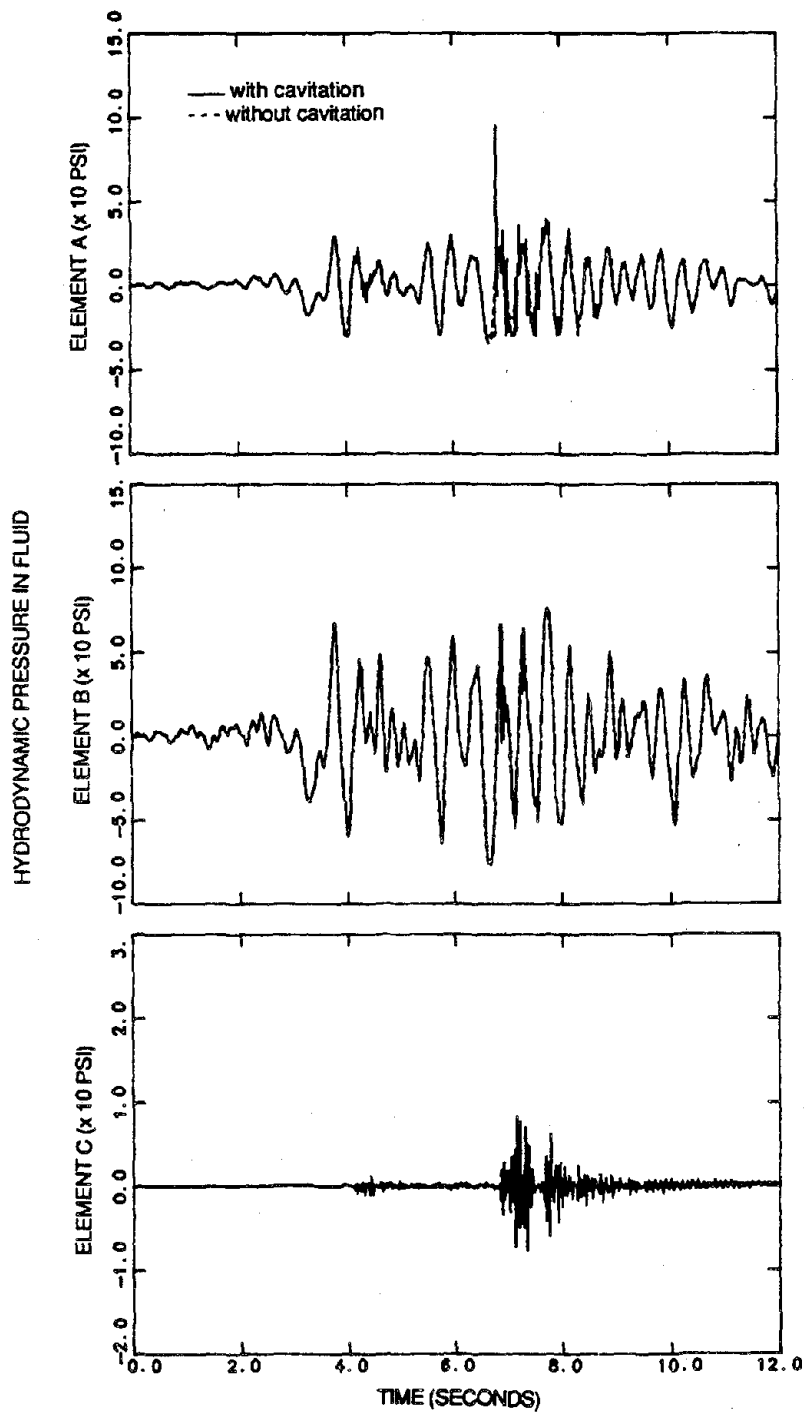
Fig. 4.30 Pressure response of the concrete gravity dam-water system,
H= 400 ft., due to the S69E component of Taft ground motion,
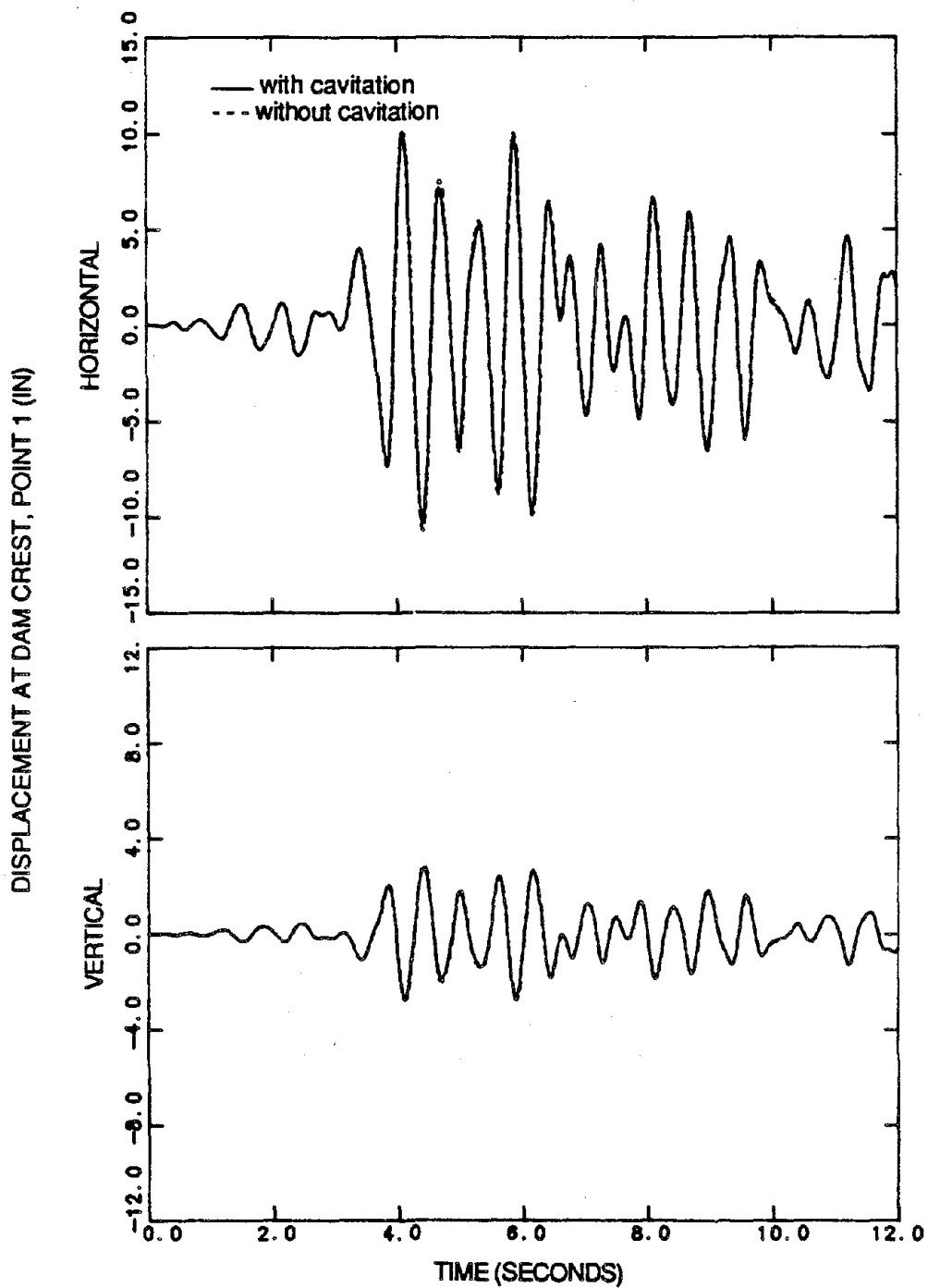scaled to 1g peak acceleration. Absorptive reservoir bottom,
$\alpha_r = 0$.
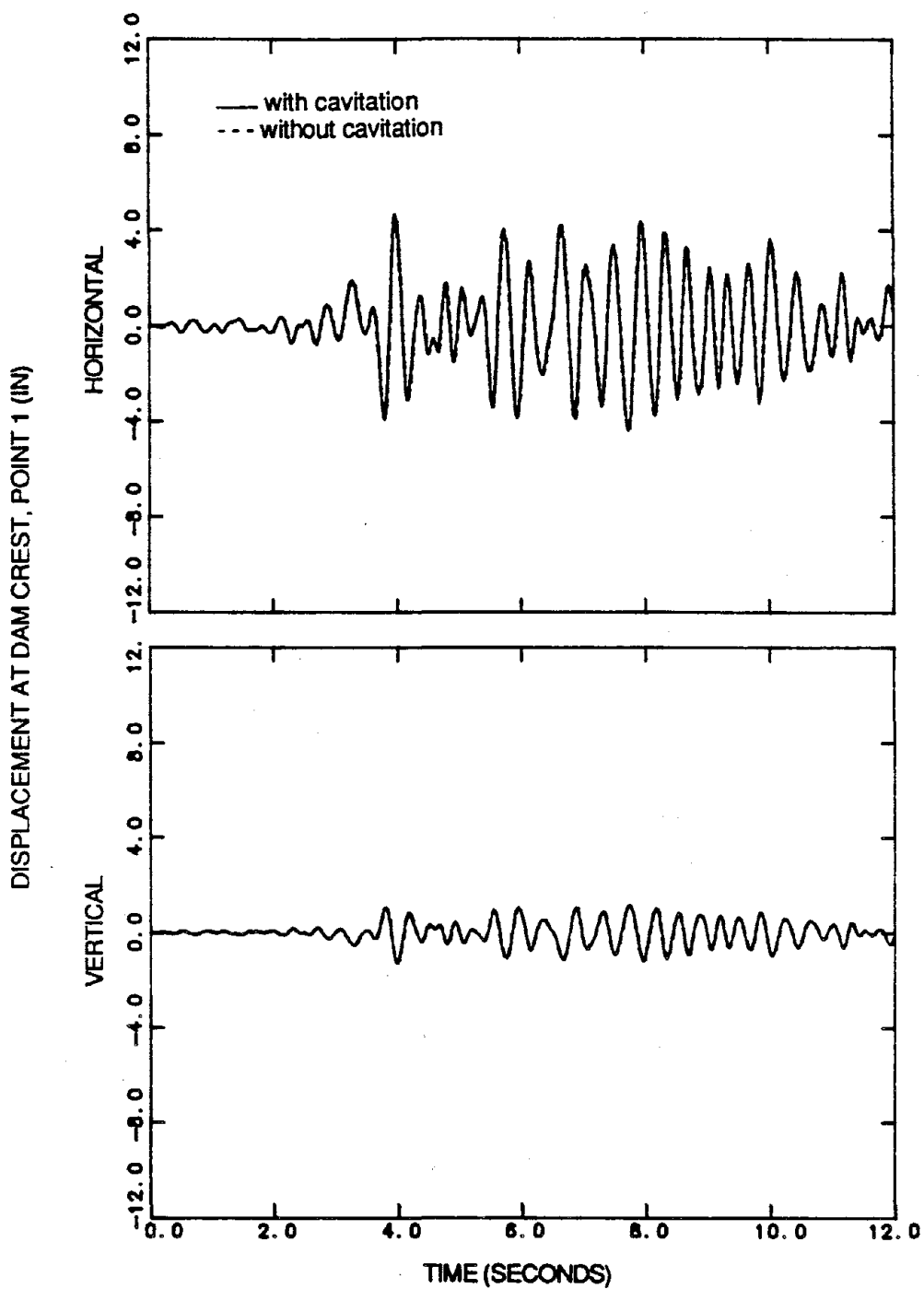
Fig. 4.31 Displacement response of the concrete gravity dam-water system,
H= 400 ft., due to the S69E component of Taft ground motion,
scaled to 1g peak acceleration. Absorptive reservoir bottom,
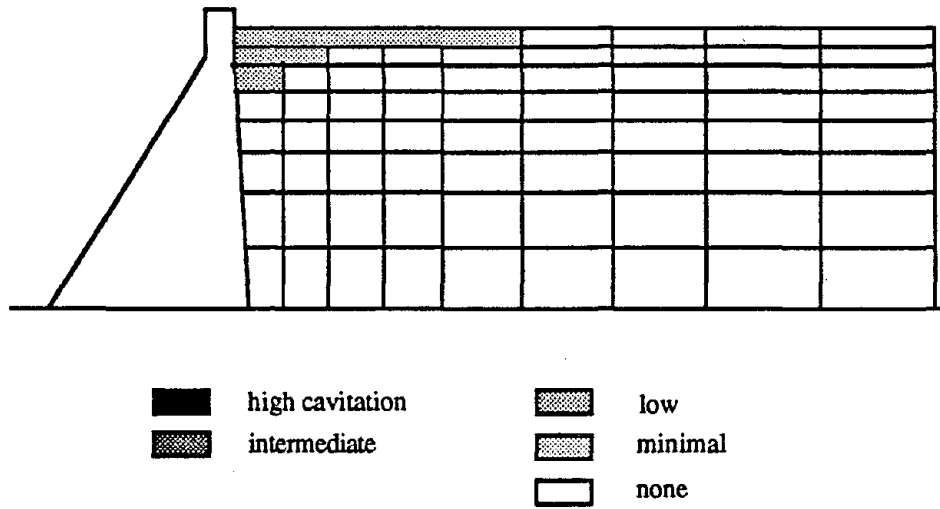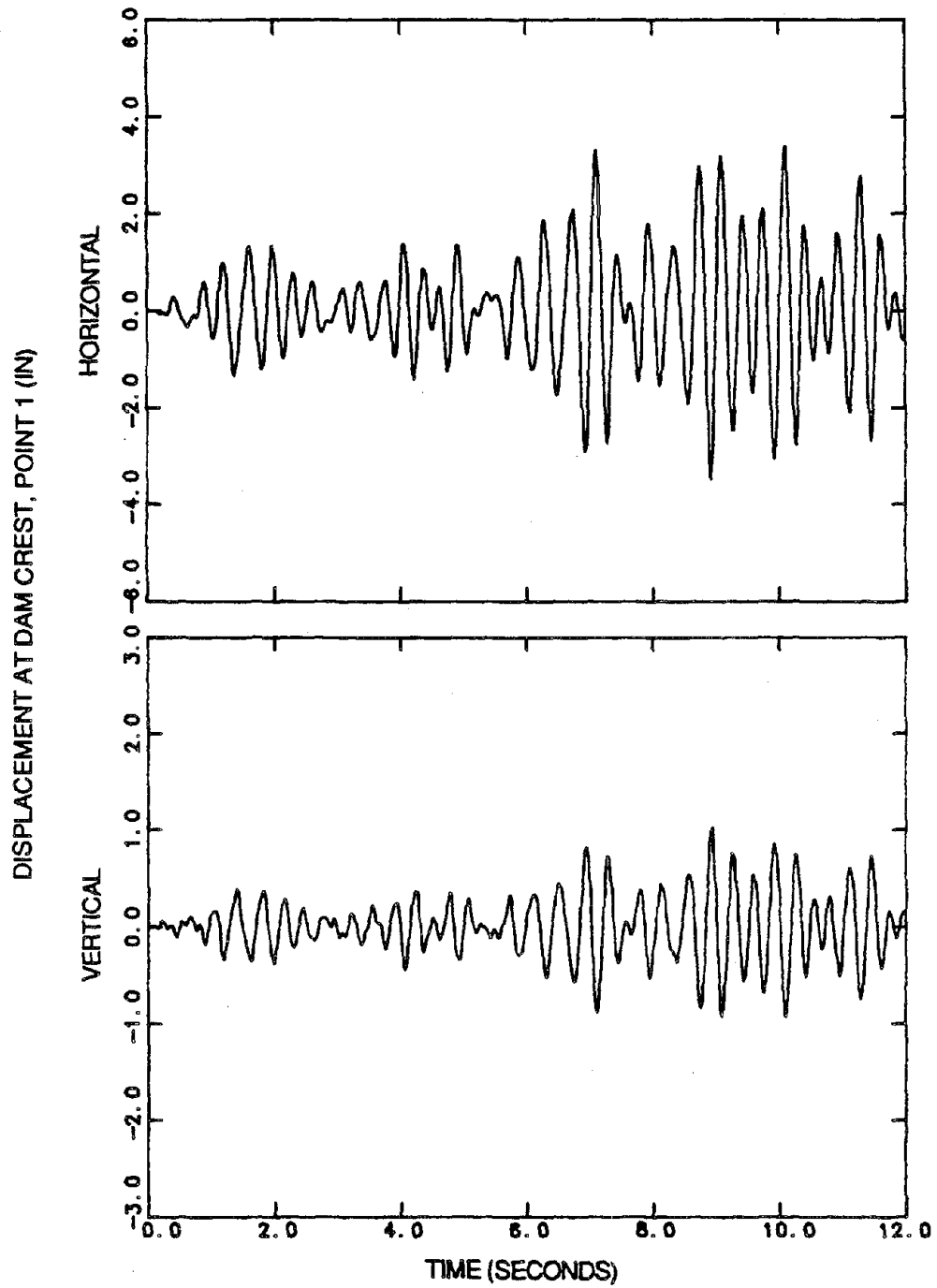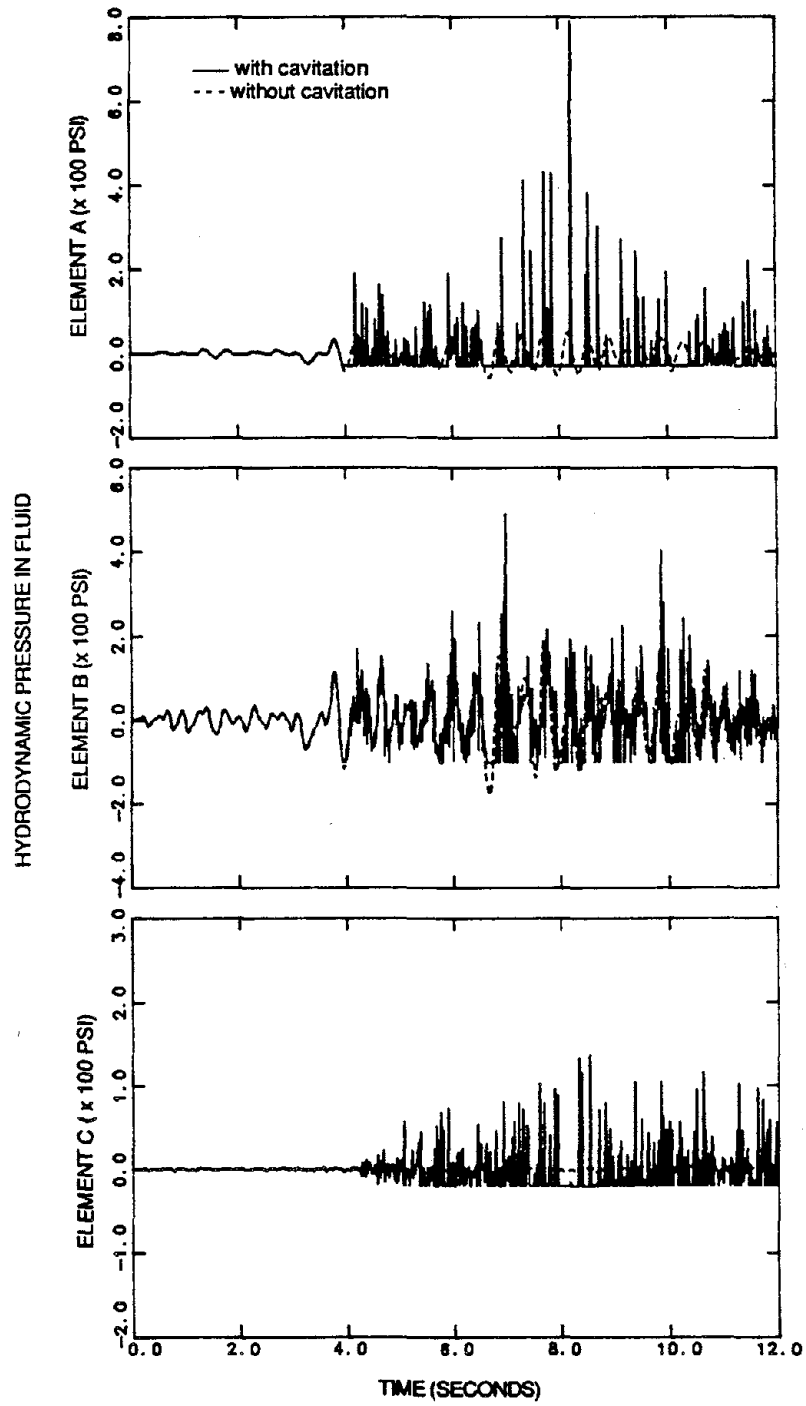$\alpha_r = 0$.
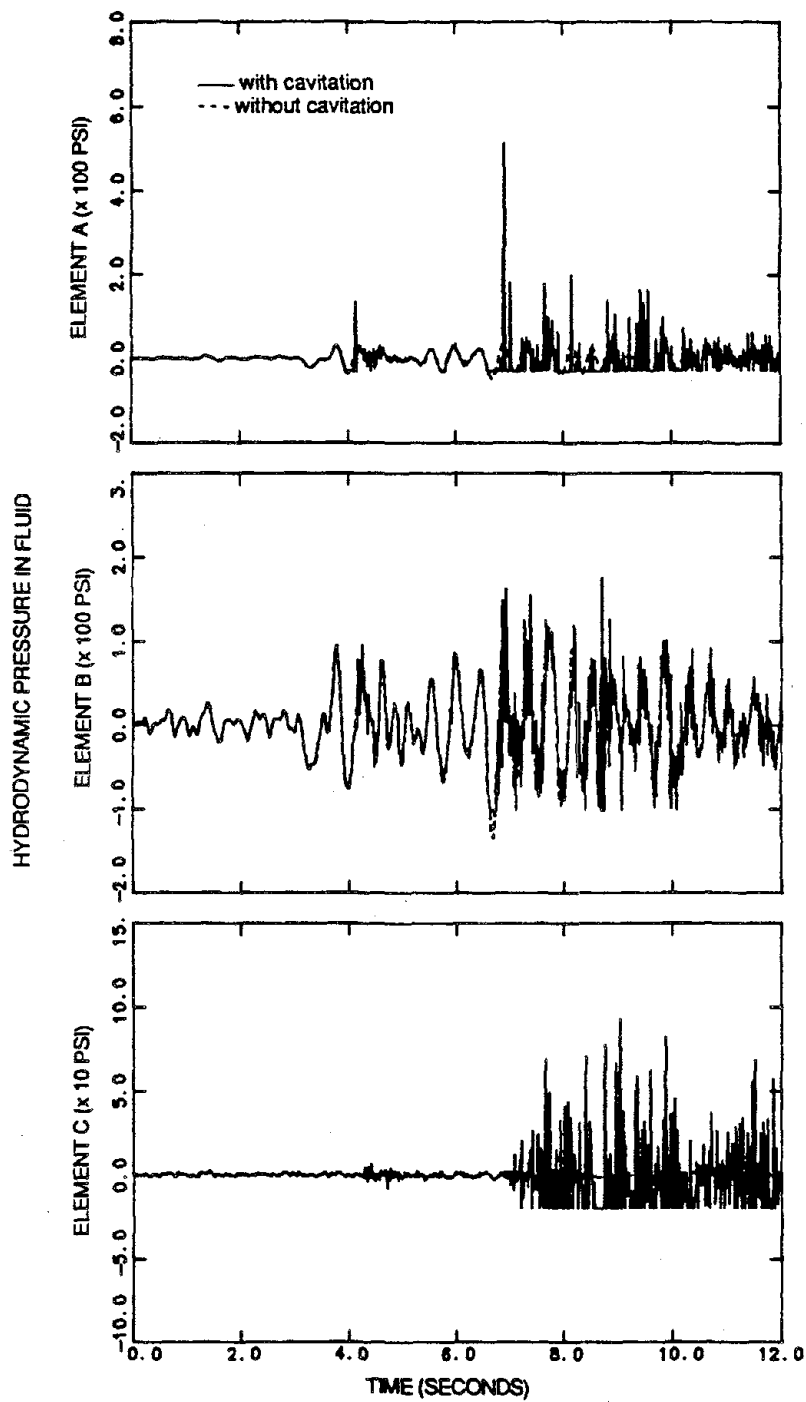
Fig. 4.32 Pressure response of the concrete gravity dam-water system, H= 400 ft., due to both the S69E and vertical components of Taft ground motion, scaled to 1g peak horizontal acceleration. Absorptive reservoir bottom, $\alpha_r = 0.5$.
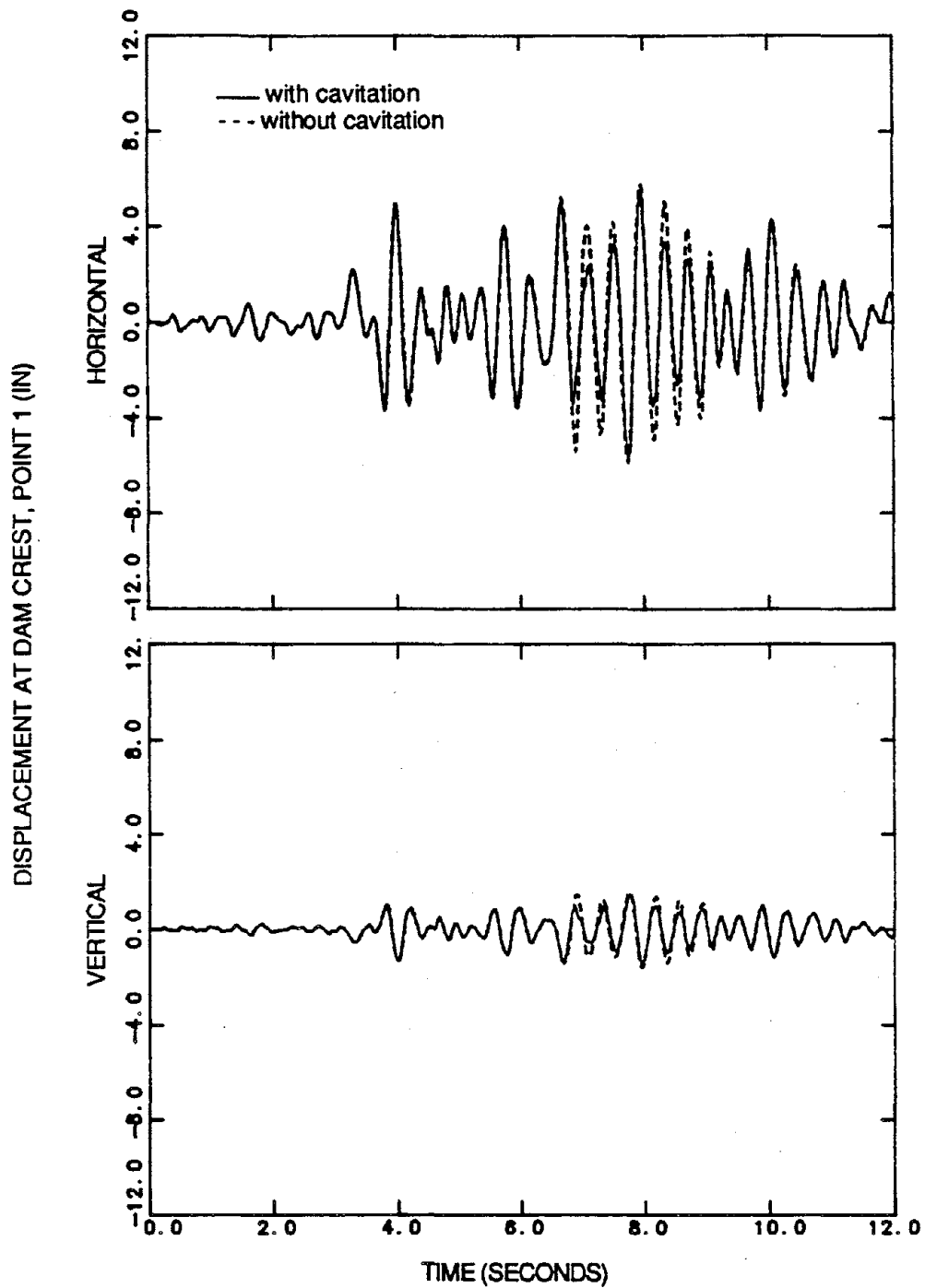
Fig. 4.33 Displacement response of the concrete gravity dam-water system,
H= 400 ft., due to both the S69E and vertical components of
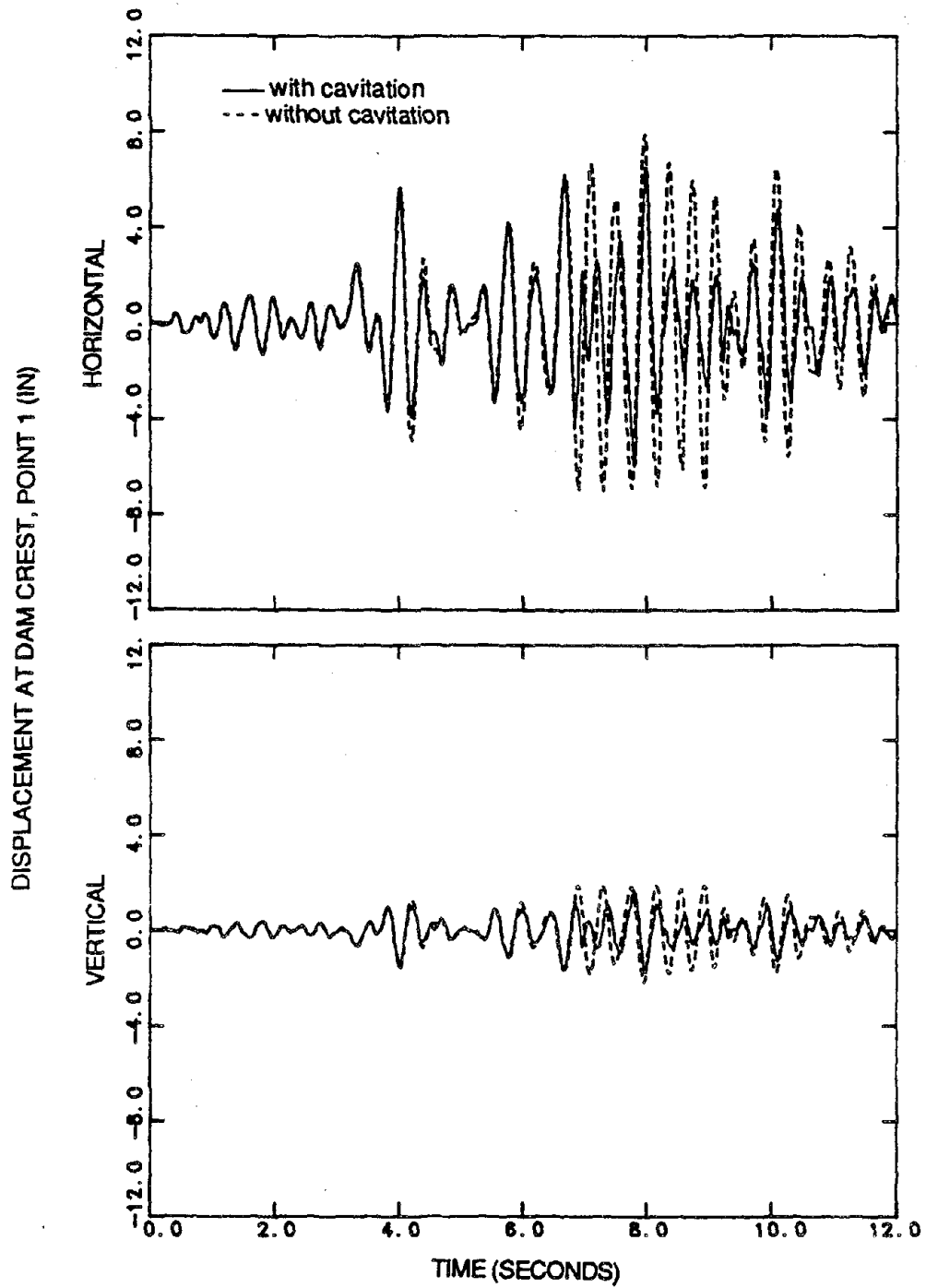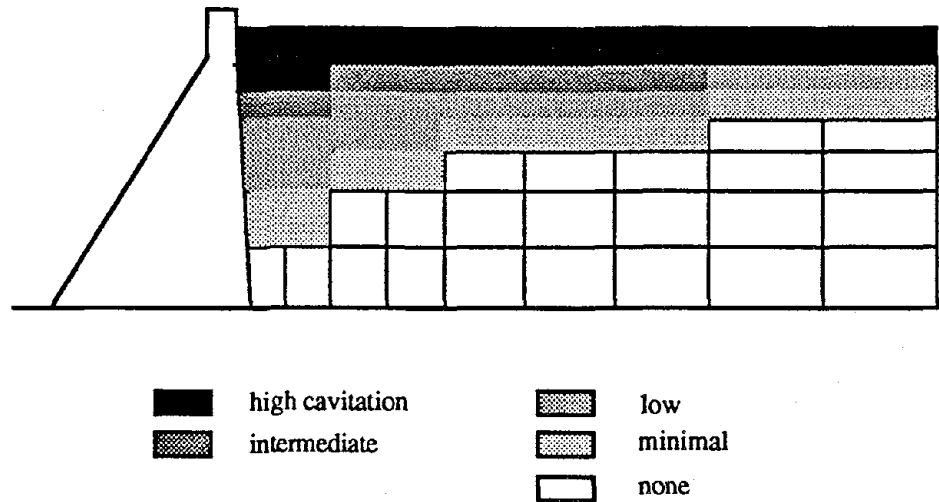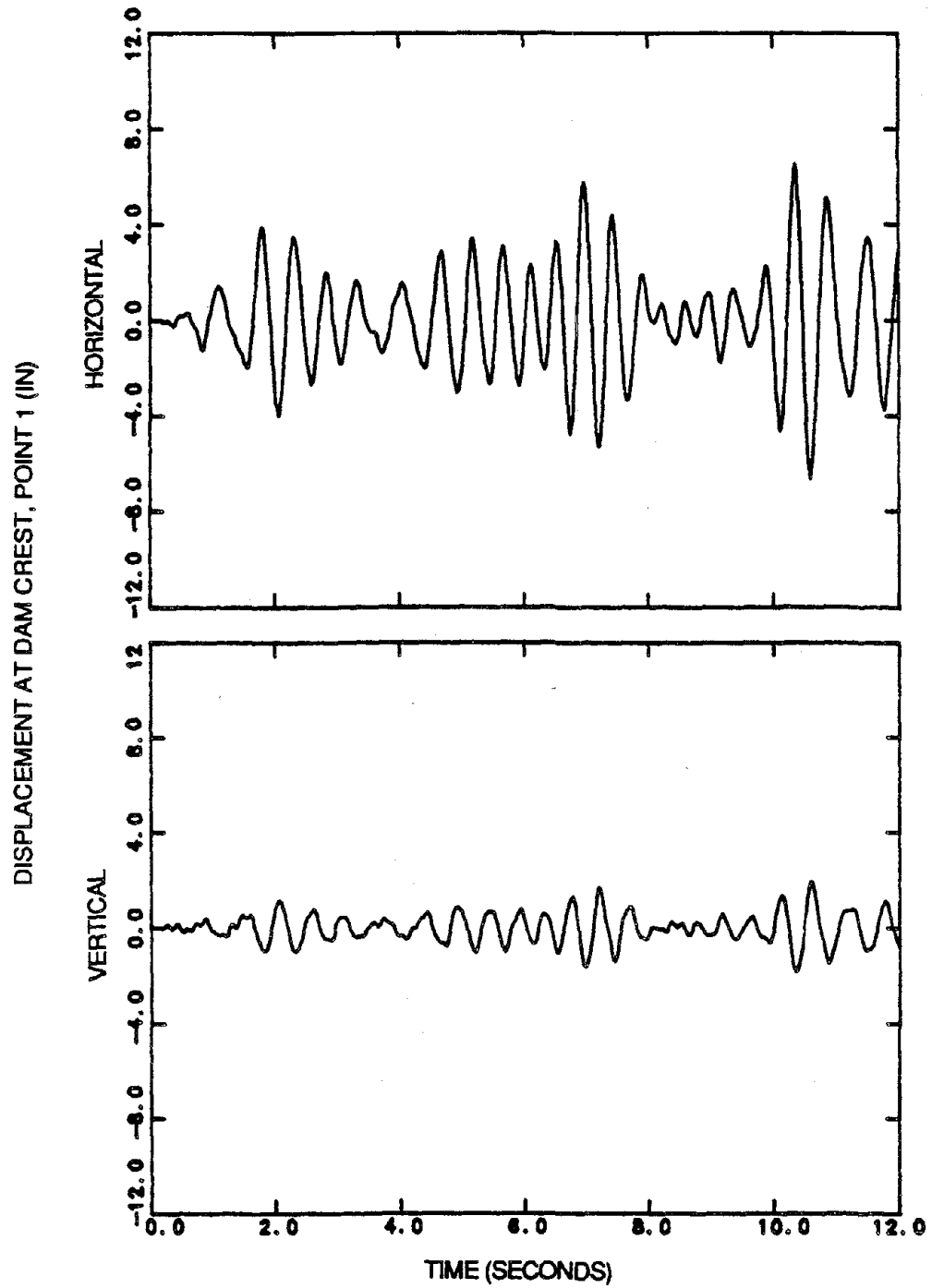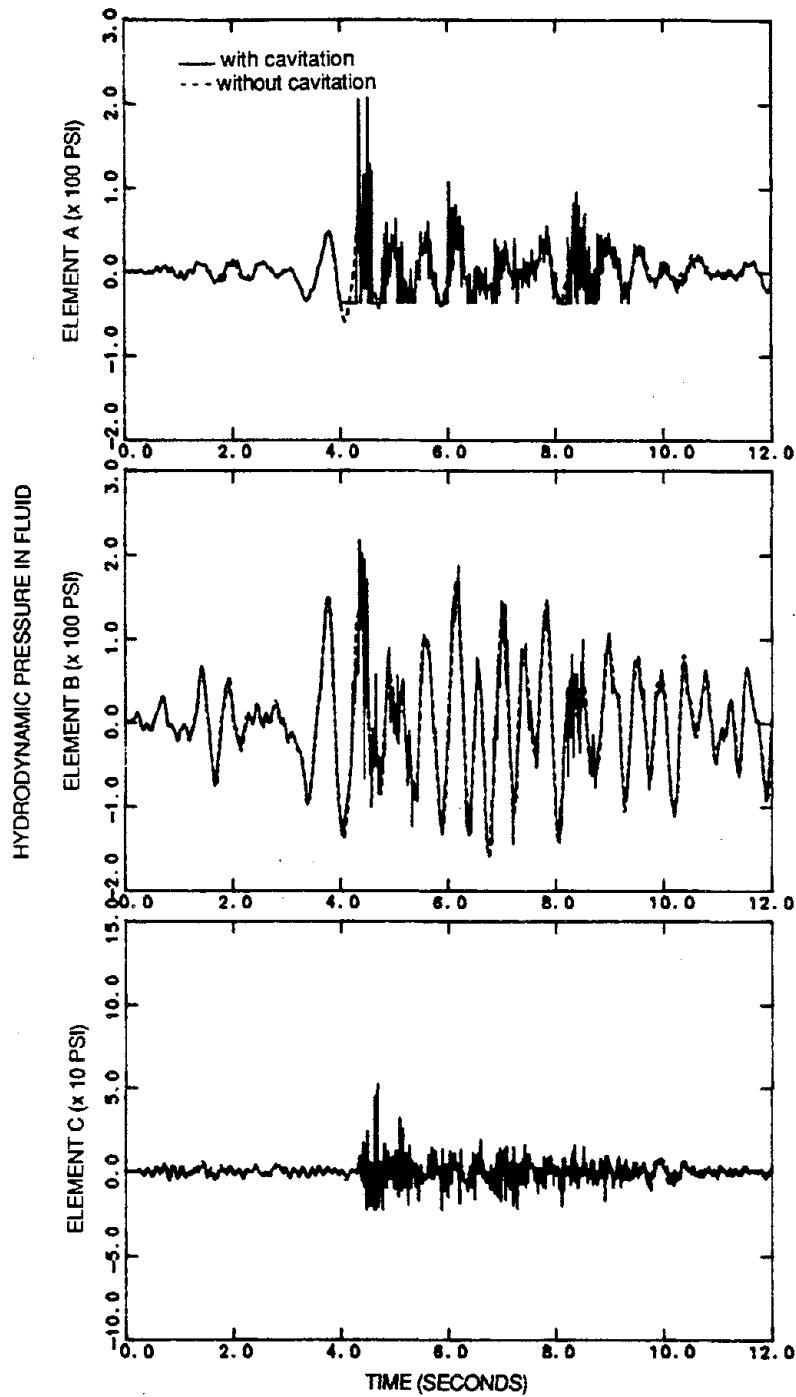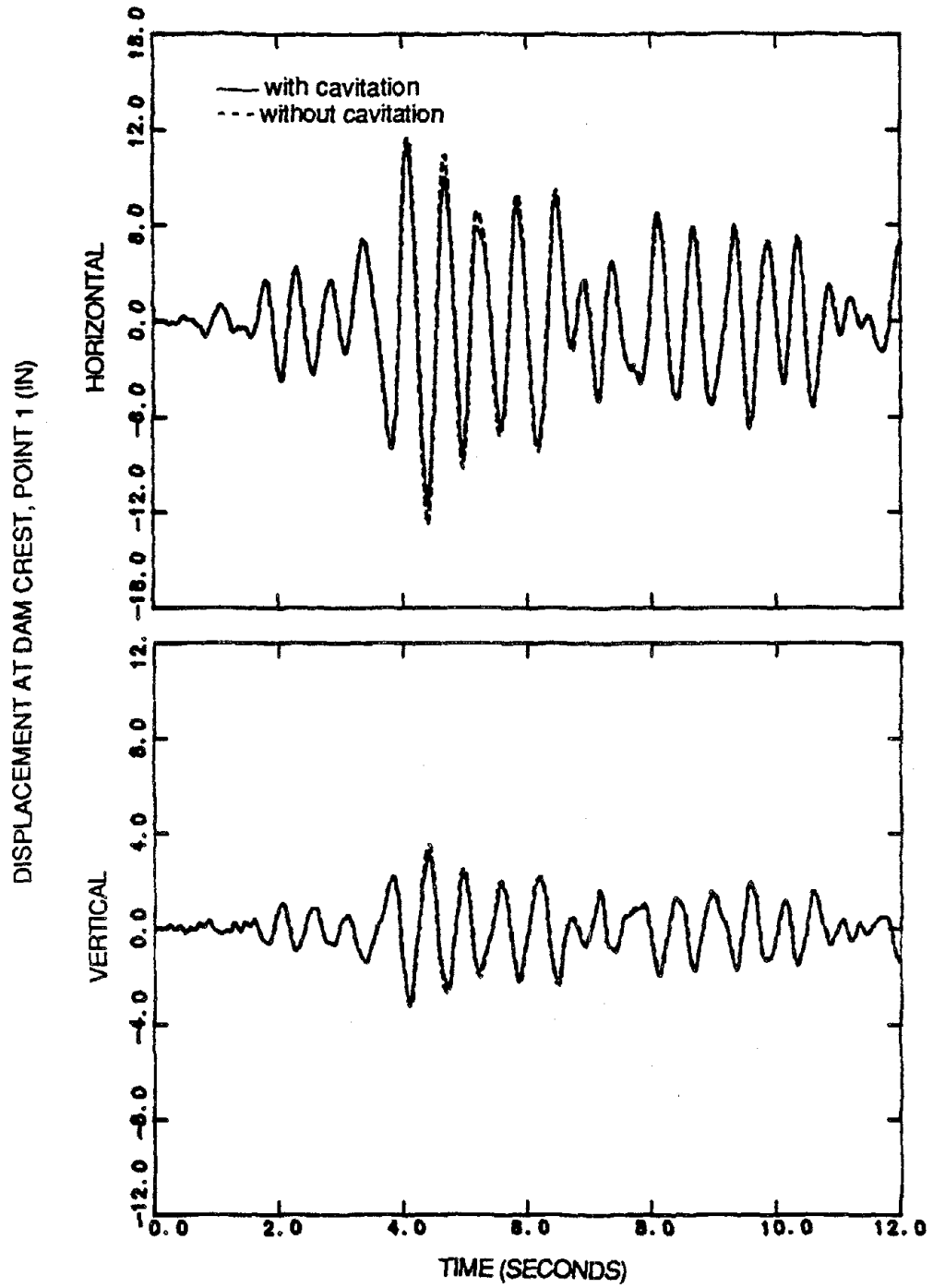Taft ground motion, scaled to 1g peak horizontal acceleration.
Absorptive reservoir bottom, $\alpha_r = 0.5$.

Page Intentionally Left Blank

Chapter 5

Tensile Crack Model for Concrete Dams

5.1 Introduction

The nonlinear behavior of mass concrete is important as the stresses approach the compressive and tensile strengths. Concrete dams resist gravity and hydrostatic loads mostly in compressive stress fields. Under current design criteria for static loads, the compressive stresses are much less than the compressive strength of concrete. For such designs, static tensile stresses either do not exist or are very small. However, the response of a concrete dam to earthquake ground motion produces large dynamic compressive and tensile stresses. Linear analyses [15] have shown that total compressive stresses rarely exceed sixty percent of the compressive strength, which is a reasonable limit value for a linear behavior of concrete in compression. Therefore, the nonlinear behavior of concrete under compressive stresses can generally be neglected in the earthquake response of dams. On the other hand, the low tensile strength of concrete will be exceeded at several locations in a concrete gravity dam during a severe earthquake [15]. In such cases, the linear response results are no longer valid since the concrete can be expected to crack under the large tensile stress. Because of the importance of tensile cracking in concrete dams, it is the only nonlinear material behavior included in this study.

Concrete cracks when the strain approaches a limit tensile strain. As the strain increases, microcracks, which are always present in concrete, coalesce to form a crack surface. In the representation presented in this chapter, microcracks are assumed to be distributed continuously within a certain width. This mode of concrete

cracking and the recognition of cracking as a fracture process is used in the so-called crack band theory. The crack band theory is developed in this chapter with modifications for computing dynamic response. The cracking model is incorporated in the analytical procedure developed in Chapter 2 which is then used to evaluate the earthquake response of a typical concrete gravity dam. The nonlinear dynamic analysis procedure requires the computation of the tangent stiffness matrix and restoring forces at every load increment, which are described along with algorithms for their evaluation.

5.2 Models for Representing Tensile Cracking in Concrete

A concrete cracking model must possess methods for crack representation, crack initiation, and criteria for crack propagation. When considering response to dynamic loads additional criteria on crack closure and reopening are necessary. Another important consideration for dynamics loads is the dependence of the concrete behavior on loading rate.

Two major approaches for crack representation have been used in the context of the finite element method: the discrete crack approach and the smeared crack approach. The discrete crack approach models tensile cracking by discrete gaps in the mesh, separating common nodal points and altering the finite element mesh when cracking occurs. Because of the computational difficulty of redefining the mesh at each load increment, a simpler crack representation has been used [37]. Instead of representing a crack as a discrete discontinuity, tensile cracks are considered continuously distributed or smeared, in the same direction over an element. Even though the smeared crack was originally developed for reinforced concrete, in which the reinforcement helps to smear cracks, it can be used for plain and mass concrete as well. The major disadvantage of the smeared crack approach is that it does not

provide information about crack width and spacing which is important in determining transfer of shear forces across the crack due to aggregate interlock. Extensive discussions of the advantages and disadvantages of both methods are summarized in Ref. [2]. Although both approaches have shortcomings, the smeared crack model is usually preferred because it can be readily incorporated into finite element analysis procedures.

Early attempts to model concrete cracking with a smeared representation were based solely on the tensile strength criterion for crack initiation [34,37]. However, when the finite element mesh is refined, the load required to extend the crack decreases as the element size is reduced [6]. This dependence of the response on element size has been criticized [6,7], because the results are unobjective with respect to the element size. A way to eliminate this dependence has been suggested [7], by considering concrete cracking as a fracture process and using fracture mechanics principles to determine crack propagation in concrete. Specifically, the energy required for crack propagation, known as fracture energy, is a characteristic property of the material, independent of the size of the finite element. The blunt crack band approach [7] introduced the fracture energy of concrete as a material parameter in conjunction with the smeared crack concept in modeling cracking of plain concrete, demostrating accuracy and objectivity with respect to the element size.

The blunt crack band method, as originally presented, provided several ways to model tensile cracking, one of which evolved into what is now known as the crack band theory [8]. Ref. [8] shows the effectiveness of the crack band theory based on experimental results on small specimens, such as the uniaxial direct test and flexural tension tests. Other researches have used similar models obtaining also accurate responses [39]. In this study, the crack band model with a smeared crack representation is used to model mass concrete. Crack initiation and formation are

determined by a strain and fracture energy criteria, respectively. The model for postcracking behavior is based on experimental evidence.

5.3 The Crack Band Theory

In the crack band theory, fracture of mass concrete is represented by progressive microcracking of the material in a zone or 'crack band'. Within the crack band, the fractured concrete behaves nonlinearly with respect to the strain accross the band, while outside the band the material is assumed to behave in a linear elastic manner. Microcracking, along with bond rupture in the concrete paste or along the aggregate-paste interface, has been identified as a strain-softening behavior, in which the stress decreases as the strain increases (Fig. 5.1). As the strain increases, the microcracks coalese to form a crack surface; in the process releasing energy due to fracture. In the crack band model, the strain softening behavior is represented by a stress-strain relationship that preserves the fracture energy of the material [8].

As mentioned earlier, the smeared crack representation avoids the need to modify the topology of the finite element mesh and can also consider the formation of cracks in any arbitrary direction. Concrete cracking is then taken into account by modifying the material stiffness relationship to recognize the increased flexibility of the element perpendicular to the crack band.

5.3.1 Crack Initiation

A maximum tensile strain criterion is adopted in the crack band model to determine crack initiation. Although not actually the case, the stress-strain relationship for tensile behavior is assumed linear up to fracture for simplicity. The

maximum tensile strain is taken as

$$\epsilon_t = \frac{f'_t}{E} \tag{5.1}$$

where f'_t and E are the concrete tensile strength and Young's modulus of elasticity, respectively. These material parameters must be modified to account for rate of loading. Typical constant increases are assumed in the current model. The tensile normal strength to the plane of cracking is affected by the stress parallel to the crack [22]. This is particularly important when high compression occurs. However, in concrete dams large compressive stresses do not occur, therefore, the effects of the biaxial stress in determining crack initiation are not considered.

In the finite element implementation, the principal strains and directions are computed at each integration point in the element if the material is currently uncracked at the load increment. If the maximum principal strain exceeds ϵ_t, then microcracks are assumed to have initiated in a direction orthogonal to the maximum strain. After crack initiates at an integration point, the crack orientation is fixed and saved for later crack monitoring. Once a crack forms, the concrete material is no longer isotropic; it becomes orthotropic with the local coordinate axes coinciding with the crack directions, as shown in Fig. 5.2. A second crack is permitted to form only in a direction orthogonal to the first crack. Consequently, only two orthogonal cracks are allowed at each integration point, with the directions fixed after the first crack forms. Cracks are allowed to close and reopen as described below.

5.3.2 Postcracking Behavior

The postcracking model of concrete used here is based on experimental evidence described in Ref. [45], where displacement-controlled direct tension tests were conducted on small cylindrical concrete specimens. The response of a direct uniaxial

monotonic tension test is depicted in Fig. 5.3(a), in which the strain-softening behavior can be clearly identified. The result of a direct cyclic uniaxial tension test is shown in Fig. 5.3(b), where it can be observed that after a maximum tensile strain is reached (point A), the stress decreases with increasing strain. This is an example of strain softening due to progressive microcracking. At point B, in Fig. 5.3(b), the strain is decreased, unloading the specimen, until the microcracks are fully closed (point C) by application of a compressive load. When the strain is increased again, reloading the specimen in tension, the crack opens to its previous value (point B) and microcracks continue to progress. Notice that when unloading takes place, the path of the stress-strain curve tends to return to the origin. Upon reloading the curve comes back to the softening behavior with the same slope of the corresponding unloading path. Fig. 5.3(b), shows that the envelope corresponding to cyclic loading is approximately the same as the curve for monotonic loading, Fig. 5.3(a).

After crack initiation, the stress normal to the crack decreases with increasing crack width. Many curves have been suggested for the softening behavior of mass concrete [39]. Fig. 5.4(a) shows the idealized stress-strain curve, based on Fig. 5.3(a), considered for this study, in which for simplicity linear softening is adopted. During cyclic loading, some cracks may start to close and others may reopen as shown in Fig. 5.3(b). To account for crack closing and reopening a criterion based on Fig. 5.3(b) is considered and its idealization is shown in Fig. 5.4(b). Observe that a completely closed crack behaves elastically, but it will reopen freely with any value of the tensile strain.

The uniaxial stress-strain relationship for mass concrete after crack initiation is then

$$\sigma = f'_t + E_t \left(\epsilon - \epsilon_t \right) \quad \text{for} \quad \epsilon_t < \epsilon < \epsilon_{max}$$

$$\sigma = 0 \qquad \text{for} \quad \epsilon > \epsilon_{max} \qquad\qquad (5.2)$$

where E_t, the softening modulus, is the slope of the softening branch (negative). The value of the softening modulus is established using fracture mechanics principles as described below.

The fracture energy, G_f, corresponding to the opening of all microcracks per unit area of crack surface can be evaluated as [8]

$$G_f = w_c \int_0^{\epsilon_f} \sigma \, d\epsilon \qquad\qquad (5.3)$$

where w_c is the width of the fracture process zone or crack band width associated with cracking; and ϵ_f is the fracture strain, the additional strain caused by the opening of the microcracks [see Fig. 5.1(b)]. The fracture energy, Eq. 5.3, can be related to the area under the complete uniaxial stress-strain diagram, W, shown in Fig. 5.1(a) (see Appendix C). For linear softening behavior, the fracture energy, G_f, is given by

$$G_f = w_c \, \frac{1}{2} \left[\frac{1}{E} - \frac{1}{E_t} \right] f_t'^2 \qquad\qquad (5.4)$$

The softening modulus, E_t, is then obtained as

$$E_t = \left[\frac{1}{E} - \frac{2G_f}{f_t'^2 w_c} \right]^{-1} \qquad\qquad (5.5)$$

The concrete crack parameters G_f, fracture energy, and w_c, crack band width, are obtained experimentally. For optimum fits from a wide range of experimental data on concrete specimens, it is suggested [8] that $w_c = 3d_a$, where d_a is the maximum aggregate size in the concrete.

Because the cracks are assumed to be smeared over an element, the finite element size, h, will be restricted to the crack band width. In the case of concrete dams, however, such a small element size is prohibitive. Consequently, larger element

sizes may be permitted provided that the fracture energy is preserved. Considering $h > w_c$ as element size, the slope of the softening branch, Eq. 5.5, is:

$$E_t = \left[\frac{1}{E} - \frac{2G_f}{f_t'^2 h}\right]^{-1} \quad \text{if} \quad h < \frac{2G_f E}{f_t'^2} \tag{5.6}$$

For values of h greater than $2G_f E/f_t'^2$, a vertical drop in the stress-strain curve must be used, as shown in Fig. 5.5(a). The fracture energy is still preserved in this case by replacing the maximum tensile strength, f_t', by a smaller equivalent strength, f_{eq} [8,9]. The equivalent strength is obtained recognizing that the area under the uniaxial stress-strain diagram, for a vertical stress drop, Fig. 5.5(a), is related to the fracture energy by the element size. That is,

$$G_f = h \frac{f_{eq}^2}{2E} \tag{5.7}$$

then solving for f_{eq}, gives

$$f_{eq} = \sqrt{\frac{2EG_f}{h}} \quad \text{if} \quad h \geq \frac{2G_f E}{f_t'^2} \tag{5.8}$$

and

$$E_t = -\infty \text{ (vertical drop)}$$

these modifications are valid for a mesh which is not too crude. Crack closing and re-opening are taken into account by the stress-strain relationship shown in Fig. 5.5(b).

5.3.3 Material Stiffness Relationship

The incremental stress-strain relationship in crack directions is given by

$$\left\{ \begin{array}{c} d\sigma_1 \\ d\sigma_2 \\ d\tau_{12} \end{array} \right\} = \mathbf{D}' \left\{ \begin{array}{c} d\epsilon_1 \\ d\epsilon_2 \\ d\gamma_{12} \end{array} \right\} \tag{5.9}$$

where $d\sigma_1$, $d\sigma_2$ and $d\tau_{12}$ are the components of the incremental stress vector, and $d\epsilon_1$, $d\epsilon_2$ and $d\gamma_{12}$ are the components of the incremental strain vector, with both stress

and strain expressed in the coordinate axes corresponding to the crack directions (Fig. 5.2). $\mathbf{D}'$ is the material stiffness matrix in local crack orientations and is given by (Appendix C):

1. Linear elastic behavior:

$$\mathbf{D}' = \begin{bmatrix} E' & \nu E' & 0 \\ \nu E' & E' & 0 \\ 0 & 0 & G \end{bmatrix} \tag{5.10}$$

where $E' = E/(1 - \nu^2)$ and ν is Poisson's ratio.

2. Strain-Softening behavior:

    (a) One crack;

$$\mathbf{D}' = \begin{bmatrix} E'_t & \nu E'_t & 0 \\ \nu E'_t & E + \nu^2 E'_t & 0 \\ 0 & 0 & \beta_g G \end{bmatrix} \tag{5.11}$$

    where $E'_t = E_t E/(E - \nu^2 E_t)$; $E_t = E_t(\epsilon_1)$.

    (b) Two cracks;

$$\mathbf{D}' = \begin{bmatrix} E_{t_1} & 0 & 0 \\ 0 & E_{t_2} & 0 \\ 0 & 0 & \beta_g G \end{bmatrix} \tag{5.12}$$

    where $E_{t_1} = E_t(\epsilon_1)$ and $E_{t_2} = E_t(\epsilon_2)$

3. Special Case (vertical stress drop):

    (a) One crack;

$$\mathbf{D}' = \begin{bmatrix} 0 & 0 & 0 \\ 0 & E & 0 \\ 0 & 0 & \beta_g G \end{bmatrix} \tag{5.13}$$

    (b) Two cracks;

$$\mathbf{D}' = \begin{bmatrix} 0 & 0 & 0 \\ 0 & 0 & 0 \\ 0 & 0 & \beta_g G \end{bmatrix} \tag{5.14}$$

To avoid numerical instabilities, a very small number is used in the diagonal positions of Eq. 5.13- 5.14 instead of zero.

Due to crack roughness and aggregate interlock, the crack surface is capable of trasmitting shear stresses. This is included in the model by a shear reduction factor, β_g, applied to the elastic shear modulus, G. Even though, the ability of the crack surface to resist shear depends upon the crack width, this relationship is still not clear and in lieu of experimental evidence, an empirical factor is assumed.

The material stiffness matrix in crack local coordinates is then transformed to global coordinates by a standard matrix transformation [51]

$$\mathbf{D}^t = \mathbf{T}^T \mathbf{D}' \mathbf{T} \tag{5.15}$$

in which

$$\mathbf{T} = \begin{bmatrix} \cos^2\theta & \sin^2\theta & \sin\theta\cos\theta \\ \sin^2\theta & \cos^2\theta & -\sin\theta\cos\theta \\ -2\sin\theta\cos\theta & 2\sin\theta\cos\theta & \cos^2\theta - \sin^2\theta \end{bmatrix} \tag{5.16}$$

where θ is the angle of crack orientation as shown in Fig. 5.2(b).

5.4 Equations of Motion for Nonlinear Structure

The coupled nonlinear equations of motion for the fluid-structure system, Eq. 2.57, are expressed in terms of dynamic displacements relative to the ground motion and the static displacements. However, because the nonlinear behavior of the structure is a function of the dynamic plus static displacements, the equations of motion for the structure, Eq. 2.52, must be modified. Hence, Eq. 2.52 can be rewritten as

$$\mathbf{M}^S \ddot{\mathbf{U}}^S + \mathbf{C}^S \dot{\mathbf{U}}^S + \mathbf{F}^S(\mathbf{U}^t) - \mathbf{F}_0^S = -\mathbf{M}^S \mathbf{R}^S \ddot{u}_g + \mathbf{P}^S \tag{5.17}$$

where $\mathbf{F}_0^S$ and $\mathbf{F}^S(\mathbf{U}^t)$ are the vectors of restoring forces in the structure due to the static and total displacements (dynamic plus static), respectively. The term, $\mathbf{F}^S(\mathbf{U}^t) - \mathbf{F}_0^S$, in Eq. 5.17, can be interpreted as the vector of restoring forces needed

to mantain equilibrium in a relative displacement configuration. The current design practice in concrete dams results in dams that do not crack under static forces. Thus, the vector of restoring forces due to static displacements, $\mathbf{F}_0^S$, is related to the static displacements, $\mathbf{U}_0^S$, by $\mathbf{F}_0^S = \mathbf{K}^S \mathbf{U}_0^S$. The coupling between fluid and structure remains without modification, except for the restoring forces in the structure as shown in Eq. 5.17.

The vector of unbalanced forces, Eq. 2.66, $\mathbf{F}_{n+1}^i$, in the numerical integration procedure is modified according to Eq. 5.17, and can be computed as:

$$\mathbf{F}_{n+1}^i = \mathbf{F}_{n+1}^{F(i)} + (\mathbf{F}_{n+1}^{S(i)}(\mathbf{X}^t) - \mathbf{F}_0^S) \tag{5.18}$$

where $\mathbf{F}_{n+1}^{F(i)}$ is the vector of restoring forces in the fluid and $\mathbf{F}_{n+1}^{S(i)}(\mathbf{X}^t)$ is the vector of restoring forces in the structure due to the current displacement $\mathbf{X}^t = \mathbf{X} + \mathbf{X}_0$. The vector of unbalanced forces, Eq. 2.66, becomes

$$\Delta \mathbf{F} = -\mathbf{M}\mathbf{R}\ddot{\mathbf{u}}_{g(n+1)} - \mathbf{C}_F \mathbf{R}\dot{\mathbf{u}}_{g(n+1)} - \mathbf{K}_F \mathbf{R}\mathbf{u}_{g(n+1)} - \mathbf{M}\ddot{\mathbf{X}}_{n+1}^i$$

$$- \mathbf{C}\dot{\mathbf{X}}_{n+1}^i - \mathbf{K}\mathbf{X}_{n+1}^i - \mathbf{F}_{n+1}^{F(i)} - (\mathbf{F}_{n+1}^{S(i)}(\mathbf{X}^t) - \mathbf{F}_0^S) \tag{5.19}$$

The evaluation of the structure tangent stiffness matrix and vector of restoring forces is presented in the next section, using the proposed model for concrete cracking.

Unlike the cavitation studies in Chapter 4, the critical damping ratio in the dam is taken proportional to the tangent stiffness matrix rather than to the linear stiffness matrix. The concrete elements that undergo cracking will experience a decrease on stiffness. Therefore, the stiffness proportional damping will decrease and the dissipation of energy will mainly come from the fracture process needed to form a surface crack. Also, the reduction in damping will ensure that viscous damping forces do not keep the crack from opening.

5.5 State Determination

The state determination involves computing restoring forces and the tangent stiffness matrix for the model of the dam. Both are functions of the incremental and current strains. The incremental strain determines the next load direction: loading, unloading or reloading. The current strain vector is used to evaluate the material stiffness matrix defined in Section 5.3.3. The algorithm to compute the structure tangent stiffness and vector of restoring forces is as follows:

1. From the incremental and relative displacements of the structure, Eqs. 2.68-2.69, the current displacements are given by

$$\mathbf{X}_{n+1}^{t(i+1)} = \mathbf{X}_{n+1}^{i+1} + \mathbf{X}_0 \qquad (5.20)$$

As explained in Section 2.6, the subscript $(n+1)$ indicates time step and the superscript $(i+1)$ the iteration.

2. Compute the incremental and current strains for the structure from

$$\Delta \epsilon^{i+1} = \mathbf{B}^S \Delta \mathbf{X}^{i+1} \qquad (5.21)$$

and

$$\epsilon_{n+1}^{i+1} = \mathbf{B}^S \mathbf{X}_{n+1}^{t(i+1)} \qquad (5.22)$$

where $\mathbf{B}^S$ is the matrix that relates the strains with the displacements through derivatives of the shape functions.

3. With the incremental and current strains, predict the vector of incremental stresses, $\Delta \sigma^{i+1}$, from

$$\Delta \sigma^{i+1} = \int_{\epsilon^i}^{\epsilon^{i+1}} \mathbf{D}^t(\epsilon) \, d\epsilon \qquad (5.23)$$

The integration is performed assuming that the direction of $d\epsilon$ is constant within iterations (i) and $(i+1)$. The tangent material stiffness matrix in global coordinates, $\mathbf{D}^t(\epsilon)$, is determined as follows:

(a) Compute the principal strains corresponding to ϵ^{i+1}: ϵ_1 and ϵ_2.

(b) Check for crack initiation;

- One crack, $\epsilon_1 > \epsilon_t$. Use Eq. 5.11 or Eq. 5.13 and save crack orientation.

- Two cracks, $\epsilon_1 > \epsilon_2 > \epsilon_t$. Use Eq. 5.12 or Eq. 5.14 and save crack orientation.

- Form the material stiffness matrix in crack directions, $\mathbf{D}'$.

(c) Crack already formed in one or two directions;

- Compute incremental strains in crack directions.

- If one crack already formed along direction-1, compute crack parameters in direction-1 according to loading (reloading) or unloading.

- Check initiation of second crack along direction-2

- If cracks already formed along directions-1 and 2, compute crack parameters in directions-1 and 2 according to loading (reloading) or unloading.

- Form the material stiffness matrix in crack directions, $\mathbf{D}'$.

(d) Transform the material stiffness matrix from local crack axes to global axes using Eq. 5.15.

4. Obtain the current stresses from

$$\sigma_{n+1}^{i+1}(\mathbf{X}^t) = \sigma_{n+1}^{i}(\mathbf{X}^t) + \Delta\sigma^{i+1} \tag{5.24}$$

5. The vector of restoring forces in the structure, $\mathbf{F}_{n+1}^{S(i+1)}$, is assembled from the element contributions, $\mathbf{f}_{n+1}^{S(i+1)}$, in which

$$\mathbf{f}_{n+1}^{S(i+1)} = \int_{\Omega_{S_e}} \mathbf{B}^S \sigma_{n+1}^{i+1}(\mathbf{X}^t)\, d\Omega \tag{5.25}$$

6. The tangent stiffness matrix is computed from the element contributions, k_{IJ}^S, where

$$k_{IJ}^S = \int_{\Omega_{S_e}} (B_I^S)^T D^t B_J^S \, d\Omega \qquad (5.26)$$

and assembled in the structure tangent stiffness matrix, K_T^S. D^t corresponds to the last increment in the integration of the incremental stresses, Eq. 5.23.

For an efficient evaluation in the computer implementation, many of the steps are performed in the same loop over the integration points of an element. The remaining part of the time integration procedure is the same as described in Section 2.6.

## 5.6 Evaluation of Crack Band Model

In order to evaluate the accuracy of the crack band theory and the need to consider fracture energy for objective results, a notched beam of plain concrete studied in Ref. [39], is analyzed using the model developed in this chapter. The finite element discretization and geometry of the beam is depicted in Fig. 5.6(a). The mesh consists of 122 nodal points and 96 isoparametric 4-node elements. The material properties are: Young modulus of elasticity, 30000 N/mm^2; Poisson ratio, 0.2; tensile strength, 3.33 N/mm^2; fracture energy, 124 N/m; and shear reduction factor of 0.001. The crack band in this case is 20 mm.

Unlike the solution strategy presented in Ref. [39], in which displacements are applied, concentrated loads are applied on two locations at the beam as shown in Fig. 5.6(a). Fig. 5.6(b) shows the experimental and numerical load-deflection curves at midspan. Because loads rather than displacements were applied, it was not possible to follow the post-peak response. The total load was applied in twenty and forty increments, and no difference in response was found. Nevertheless, notice that the numerical solution closely follows the experimental response up to the maximum

load. The maximum load attained by the beam using the maximum strength criterion without strain-softening behavior is indicated by Point A of Fig. 5.6(b). Obviously this result is unobjective. Therefore, objectivity with respect to the element size is essential to predict the behavior of concrete under tensile loads.

5.7 Summary

In this chapter the concrete models for tensile cracking have been examined. The crack band theory with a smeared crack representation has been adopted to model the tensile behavior of concrete. Extensions have been included in the model to account for dynamic loads, and has been incorporated in the numerical procedure presented in Chapter 2. The next chapter will analyze the earthquake response of representative concrete dams to assess the importance of tensile cracking.
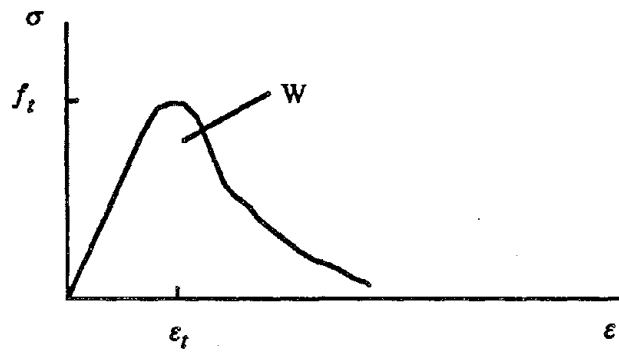
a) Stress-strain behavior
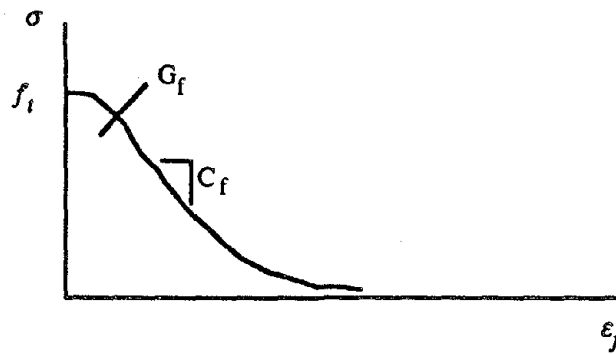
b) Strain-softening behavior

Fig. 5.1 Concrete tensile stress-strain diagram
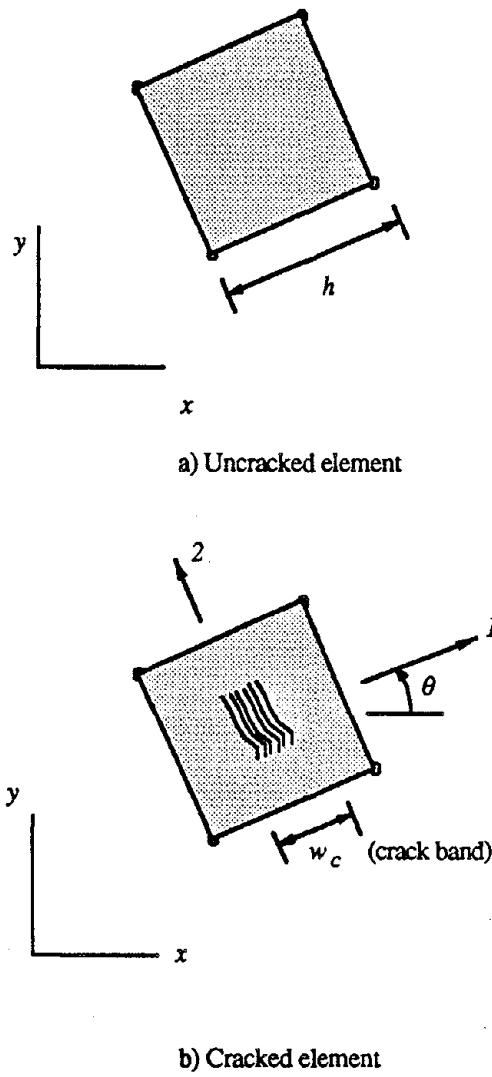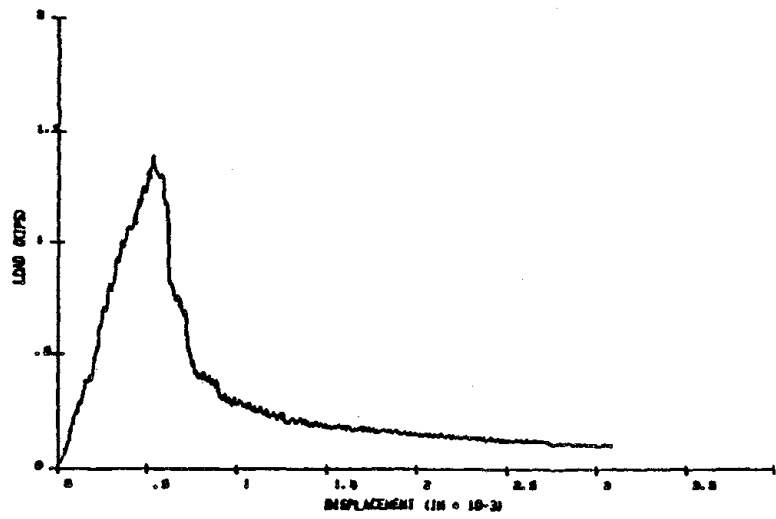
a) Uncracked element

b) Cracked element

Fig. 5.2 Coordinate axes for crack directions

a) Monotonic tension test
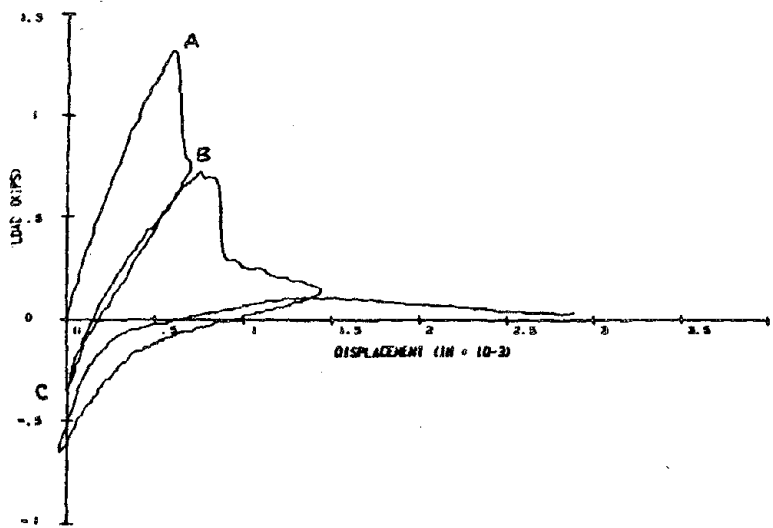
b) Cyclic tension test

Fig. 5.3 Load-displacement relationship obtained from
displacement controlled direct tension test on
concrete cylinders (Ref. 45).
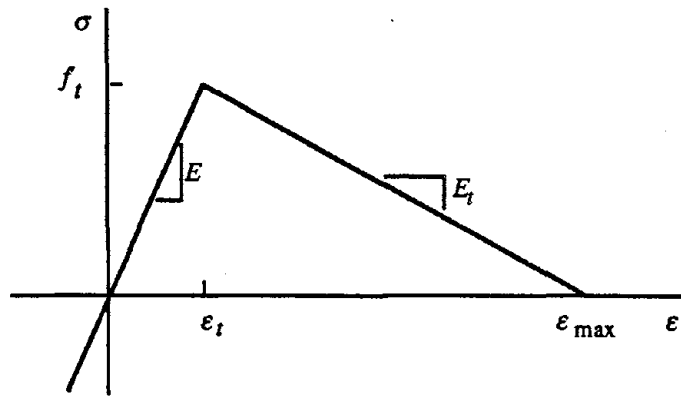
a) Linear strain-softening
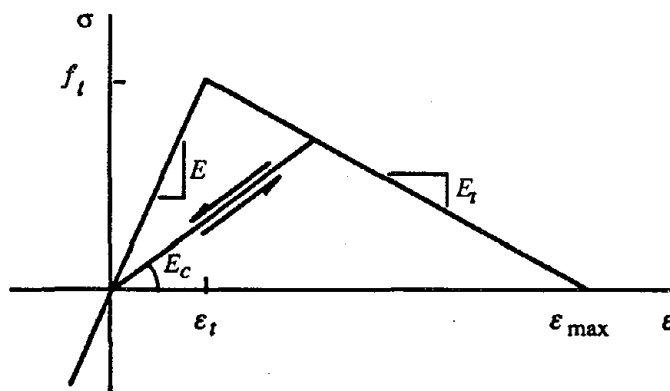
b) Unloading-reloading

Fig. 5.4 Idealized stress-strain diagram with
strain-softening.

a) Vertical stress drop behavior.

b) Unloading-reloading

Fig 5.5 Idealized stress-strain diagram with
vertical stress drop.

a) Geometry of notched beam

b) Load-deflection response

Fig. 5.6 Notched beam test case (Ref. 39)

Page Intentionally Left Blank

142

Chapter 6

Earthquake Response of Gravity Dams Including Concrete Cracking

6.1 Introduction

Previous studies on the effects of concrete tensile cracking on the response of concrete gravity dam systems have been based on simplified assumptions for the cracking 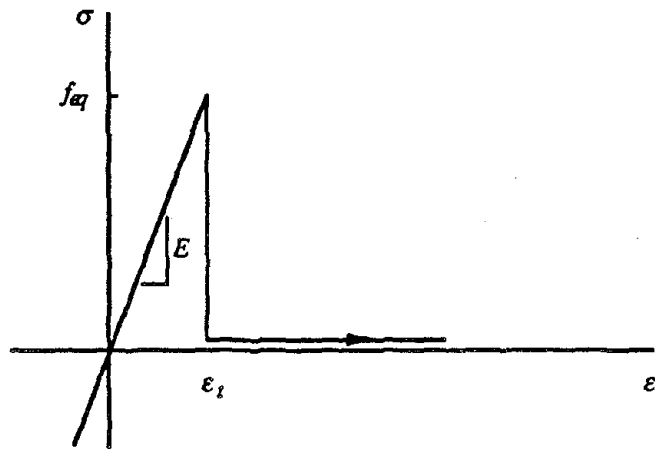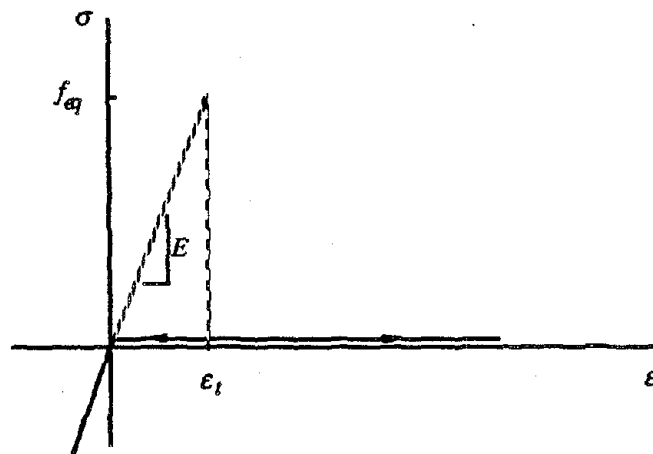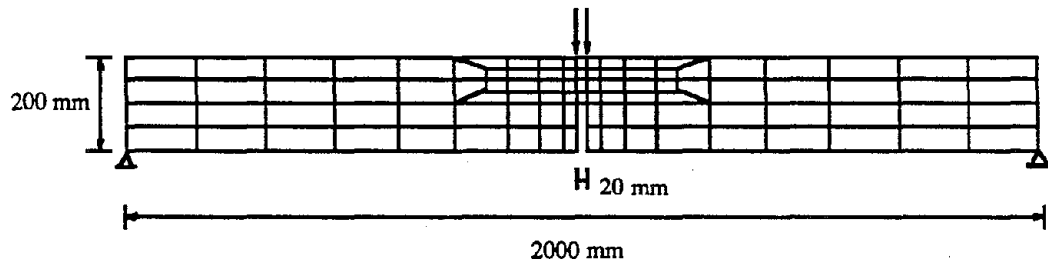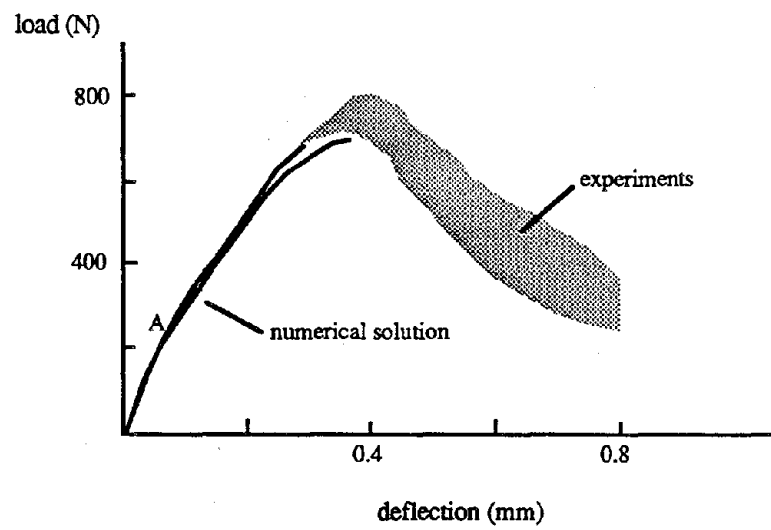model or dam-water interaction. Several studies have neglected the fluid [34,41] or used added masses in the upstream face of the dam, corresponding to hydrodynamic pressures in the fundamental vibration mode [26]. It is unrealistic to neglect water because dam-water interaction because it produces significant changes in the dynamic response, and the assumption of added masses disregards the participation of other vibrational modes and the effect of water compressibility. The tensile concrete behavior has been mainly modeled using the smeared crack approach [26,34], but the problem of objectivity with respect to the element size arises, possibly providing unreliable response results as described in Chapter 5.

In this chapter, the tensile cracking model developed in Chapter 5 is employed with the numerical procedure described in Chapter 2 to compute the earthquake response of a typical concrete gravity dam. The analysis includes the effects of dam-water interaction, with water compressibility, using the crack band model for tensile crack behavior of concrete under cyclic loads. The response of the Pine Flat dam with empty and full reservoir is examined in detail when subjected to two representative earthquake ground motions. In addition, the effects of reservoir bottom absorption and the importance of response to vertical ground motion on tensile

cracking are also studied.

6.2 Modeling of the Dam-Water System

The dam under consideration is the tallest nonoverflow monolith of the Pine Flat dam, $H = 400$ ft. The model of the dam-water system is the same as used in the cavitation studies, described in Sections 4.2 and 4.3. Since the crack band theory requires small elements to obtain objective results, a refined dam-water finite element mesh is used. The two-dimensional dam monolith is discretized by 136 4-node elements with 162 nodes and the water domain by 224 4-node constant pressure fluid elements with 255 nodes, as shown in Figs. 6.1 and 6.2. Damping in the dam is represented by a stiffness proportional damping matrix as used in Section 4.3, with a critical viscous damping ratio of 5%. Artificial damping in the fluid is not included when cavitation in the water is not permitted.

The tensile strength of concrete in the dam is taken equal to the modulus of rupture. Because there is no direct data on material properties for the Pine Flat dam, the modulus of rupture is computed for a modulus of elasticity of 3.25 million psi, which gives $f'_t = 425$ psi according to Ref. [1]. The dynamic loading on the concrete requires that the tensile strength and Young's modulus of elasticity be increased for the involved stiffness and strength due to strain rate effects. An average increase of 25% is used [36], raising the concrete modulus of elasticity and tensile strength to $E = 4.06$ million psi and $f'_t = 531$ psi, respectively. The fracture energy, G_f, is taken as 0.43 lb/in, a reasonable value for most concretes [8]. For the purpose of establishing a crack band width, a maximum aggregate size of 8 in. is adopted, which gives a crack band width of 24 in. The shear reduction factor, β_g, is taken as 0.1 [39].

Even though a refined mesh is used, the size of the elements range from 17 ft. at the crest to 32 ft. at the base (Fig. 6.1). For the crack band theory, strain softening can only be represented for elements with a maximum size of (Eq. 5.6)

$$h_{max} = \frac{2G_f E}{f_t'^2} \tag{6.1}$$

For the material properties given above, $h_{max} = 12.4$ in., which is considerably less than the size of the elements in the mesh. Therefore, the tensile strain-stress relationship with a vertical stress drop, Fig. 5.5, must be used. The equivalent tensile strength for elements larger than h_{max} is given by Eq. 5.8. As can be deduced observing Fig. 6.1, the equivalent strength decreases from the crest to the foundation level, ranging from 96 psi at the bottom elements to 130 psi at the top elements. However, these low values will cause premature cracking at the dam heel, a region of stress concentration. It then seems reasonable to scale proportionaly the tensile strength such that the largest elements, the ones next to the foundation, have an equivalent strength equal to f_t', 531 psi. The elements at the upper part of the dam then have an equivalent strength of 729 psi. The scaling still preserves the fracture energy, an essential requirement for objective results.

6.3   Response of Pine Flat Dam

As in the cavitation studies, Chapter 4, the Pine Flat dam is subjected to two ground motions: the S69E and vertical components of Taft ground motion scaled by various factors to illustrate effects of tensile cracking; and the S16E component of the Pacoima ground motion. In all the cases, a time step of 0.02 seconds is used to compute the response of the linear model of the dam, and 0.01 seconds when cracking in the dam is allowed.

6.3.1   Effects of Concrete Cracking

To examine the effects of concrete cracking on the response of Pine Flat dam, the first case analyzed is the dam with empty reservoir, that is dam-water interaction is neglected. Because of the relatively small earthquake forces on the dam without impounded water, it is necessary to scale the S69E component of Taft ground motion. With scale factors of 1, 1.5 and 2, the dam does not show any cracking. A scale factor of 2.5 ($a_g = 0.4g$) is required to induce cracking in the dam. The displacement time history at the dam crest is shown in Fig. 6.3, in which positive displacement is in the upstream direction and negative in the downstream direction. A comparison of responses for linear and nonlinear concrete shows the vibration period and crest displacements increase after cracking initiates, at a time of 5.03 seconds, when the dam is displaced in the upstream direction.

The time history of total stress at locations A and B (Fig. 6.1) in the dam is depicted in Fig. 6.4. These locations were selected because they represent points of high stress concentrations, as was shown in Section 4.3.2, with equivalent tensile strengths of 729 and 531 psi, respectively. For purpose of comparison in the stress plot, the discontinuous line shows the stress at points A and B in the horizontal direction (σ_{xx}) when the dam behaves linearly elastic. The continuous line shows the total stress in the horizontal direction up to crack initiation, beyond that time the crack orientation is known and the stress normal to the crack is plotted.

Note that at location A the stress drops to zero after the cracking releases the tensile stress. The local redistribution of stresses produces a large compressive stress at location A when the crack closes. Figs. 6.5 shows the crack pattern when cracking starts and one and one-half cycle later when the dam is displaced in the downstream direction. A continuous line indicates an open crack and a discontinuous

line a crack that was previously open but closed at this time. Cracking initiates in the downstream face at 5.03 seconds [Fig. 6.5(a)] and propagates to the upstream face [Fig. 6.5(b)]. At 5.63 seconds the cracks have propagated nearly accross the cross section, 6 out of 8 elements, at which time the numerical procedure does not converge possibly indicating failure of the dam.

The response of Pine Flat dam with full reservoir when exposed to the unscaled S69E component of Taft ground motion ($a_g = 0.18g$) is shown in Figs. 6.6-6.7. Because dam-water interaction is now included, the unscaled ground motion produces substantially larger response than for the dam with empty reservoir. In this case cracking starts at an earlier time, 3.71 seconds, in the response. There is a slight period lengthening compared to the linear model. However, the displacement at the dam crest, Fig. 6.6, increases for the two cycles after cracking initiates, but decreases afterwards. The reason for the increase in displacement is the loss of stiffness which results in a longer period, and the decrease is due to an increase in damping from release of energy due to fracture and the possible consequence of moving to a lower ordinate in the earthquake spectrum. The stress history at location A, Fig 6.7, is also affected, with an increase in stress during the first two cycles after crack initiation, followed by a reduction in total stress. The stress at location B (dam heel) drops to zero after cracking because of the release of tensile stresses. A half-cycle later, when the dam moves upstream, the cracks developed at the heel close, producing a large compressive stress compared with the linear response. This behavior is consistent with the downward vertical displacement. Figs 6.8(a) shows that cracking initiates at the heel of the dam, an expected result since at that location the concrete is in a high state of tensile stress because of the hydrodynamic forces and the low static compression produced by the hydrostatic forces. Fig. 6.8(b) depicts the crack pattern at a later time, which continues unchanged until the motion ends. Observe that the

extension of the cracking stabilizes and the dam remains intact. All tensile cracks will close under the static loads after the ground motion, and the dam remains stable.

To study the effect of more extensive cracking, the Pine Flat dam was subjected to the S69E component of Taft ground motion, scaled by factors of 1.5 and 2 ($a_g = 0.27g$ and $0.36g$, respectively). Figs. 6.9 and 6.10 show the large changes in response due to the ground motion scaled by 1.5. Clearly, tensile cracking lengthens the vibration period and increases peak displacements at the dam crest. Cracking at the dam heel also extends further accross the base, as shown in Fig. 6.11, but still remains stable.

To examine further the importance of concrete cracking, the response of the dam to Taft ground motion scaled by a factor of 2 is shown in Figs. 6.12-6.14. Cracking initiates at the heel, at a time of 3.71 seconds, when the dam is moving downstream, as in the previous cases. However, one half-cycle later, as the dam moves in the upstream direction, at a time of 4.01 seconds, cracks at the heel stabilize and close as shown in Fig. 6.14(b). At the same time, new cracks develop in the upper portion of the downstream face of the dam, propagating accross the cross section in the upstream direction, Fig. 6.14(b). When the dam is then moving back towards the downstream direction, the cracks at the foundation level reopen, at a time of 4.13 seconds [see Fig. 6.14(c)], and the cracks located in the upper portion of the dam continue to propagate due to the release of tensile stresses. Additional cracks start developing in the upstream face, until the cracking extends completely across the dam at a time of 4.19 seconds, near the change in upstream slope as shown in Fig. 6.14(d). This may indicate a complete separation of the upper part of the dam, beyond which the numerical procedure fails to converge.

To demonstrate the dependence of the nonlinear response to different

earthquakes, the response of the Pine Flat dam with full reservoir subjected to the S16E component of Pacoima ground motion ($a_g = 1.17g$) is depicted in Figs. 6.15-6.16. Cracking has little effects on the displacement response up to 3.2 seconds (see Fig. 6.15), even though cracking initiated at the heel at a time of 2.15 seconds (Fig. 6.16). The stress history in Fig. 6.16 shows a large increase in compressive stresses in the heel, but still an order of magnitude less than compressive strength of concrete. Right after 3.2 seconds, when the dam is moving in the downstream direction, extensive cracking takes place propagating from heel to toe at the foundation level until the plane of cracking completely crosses the base of the dam as shown in Fig. 6.17(b). As a result, a large rotation of the dam about the toe occurs. This can be deduced from the pronounced increase of both the negative horizontal and positive vertical displacements in Fig. 6.15. One-half cycle after, at a time of 3.71 seconds, when the dam is at the maximum upstream position, the dam rotates back closing some of the cracks at the downstream face at the base. However, extensive new cracks open in the upper part of the dam at the downstream face [Fig. 6.17(c)]. In the next half-cycle, at a time of 3.83 seconds, the cracking at the base of the dam has stabilized and the formation of new cracks in the upstream face occurs, propagating accross the upper part of the dam completely [Fig. 6.17(d)]. At this point, the numerical solution does not converge for times greater than 3.85 seconds.

As explained in Chapter 4, the Taft ground motion needed to be scaled to $1g$ peak acceleration in order to induce cavitation. In all the cases studied in this chapter, cavitation of the water never takes place. Therefore, it can be concluded that tensile concrete cracking is the predominant nonlinearity in the dam-water systems analyzed. Also, the importance of dam-water interaction has been clearly demonstrated in which the time of crack initiation, displacement and stress responses, and cracking locations are significantly different from the case of an empty reservoir.

6.3.2 Effects of Reservoir Bottom Absorption

The effects of an absorptive reservoir bottom on the response of Pine Flat dam is examined assuming a wave reflecting coefficient of $\alpha_r = 0.5$ for the reservoir bottom materials. For comparison purposes the dam-water system is analysed for the Taft ground motion. The response for a scaling factor of 1.5 is shown in Figs. 6.18-6.19, and as in the cavitation studies displacement and stress responses are reduced. Also, the cracking pattern changes. Crack initiation and propagation occur over a smaller area of the dam cross section, as can be seen from the crack patterns in Fig. 6.20.

When the dam-water system is exposed to the S69E component of Taft with a scale factor of 2, the response is reduced (Figs. 6.21-6.22) by the presence of sediment materials. Examining the crack patterns at different times, Fig. 6.23, two differences can be observed with respect to a non-absorptive reservoir bottom, Fig. 6.14. The cracking extension involves fewer elements and the crack pattern at the upper part of the dam has been shifted up. Nevertheless, the solution still fails to converge for times greater than 4.20 seconds.

Finally, the Pine Flat dam-water system is subjected to both the S69E and vertical components of Taft ground motion simultaneously, with a scale factor of 2. As concluded from the cavitation studies, in Section 4.3.3, the vertical ground motion can be only included realistically with consideration of reservoir bottom absorption. For this purpose, a value of $\alpha_r = 0.5$ is considered. The response to both components of Taft is shown in Figs. 6.24-6.25. It can be noticed that the displacement and stress time histories have not changed much compared with the response to the S69E component only and $\alpha_r = 1$ (Figs. 6.9-6.10). Furthermore, the crack patterns show less cracking, as shown in Fig. 6.26. Thus, for these cases the contribution of

the vertical ground motion to the nonlinear response of the dam is minimal when the characteristics of the reservoir bottom materials are included.
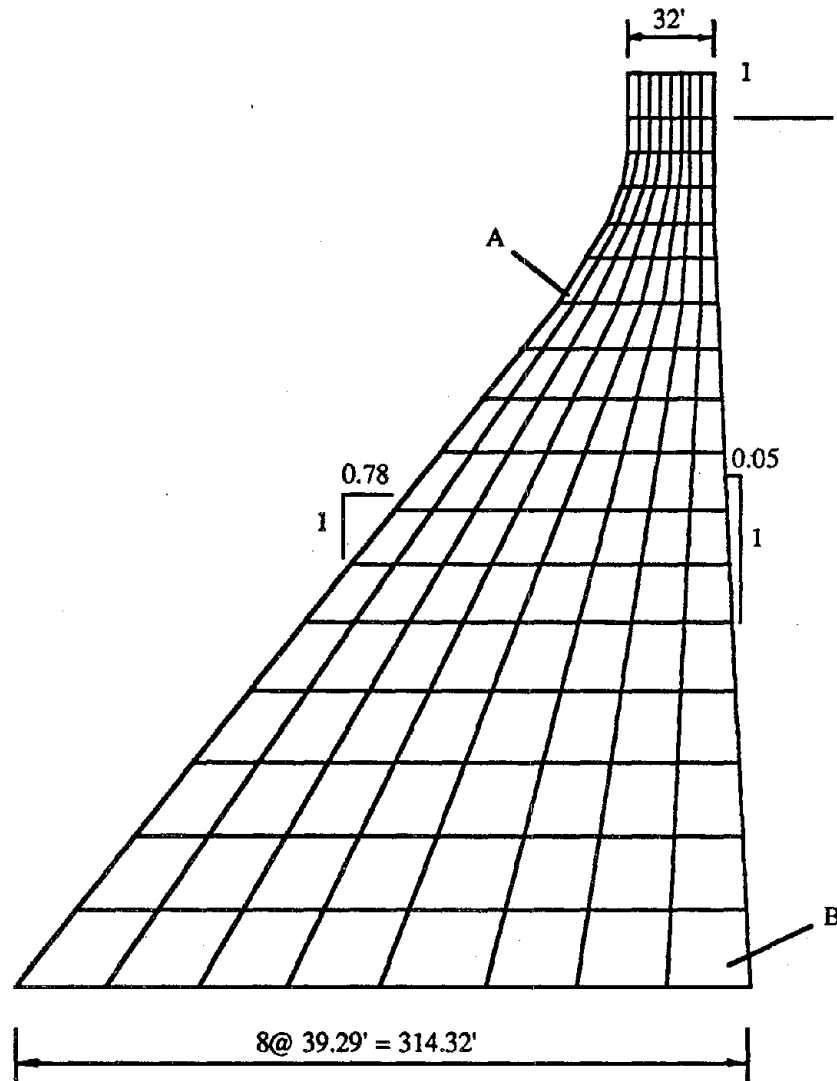
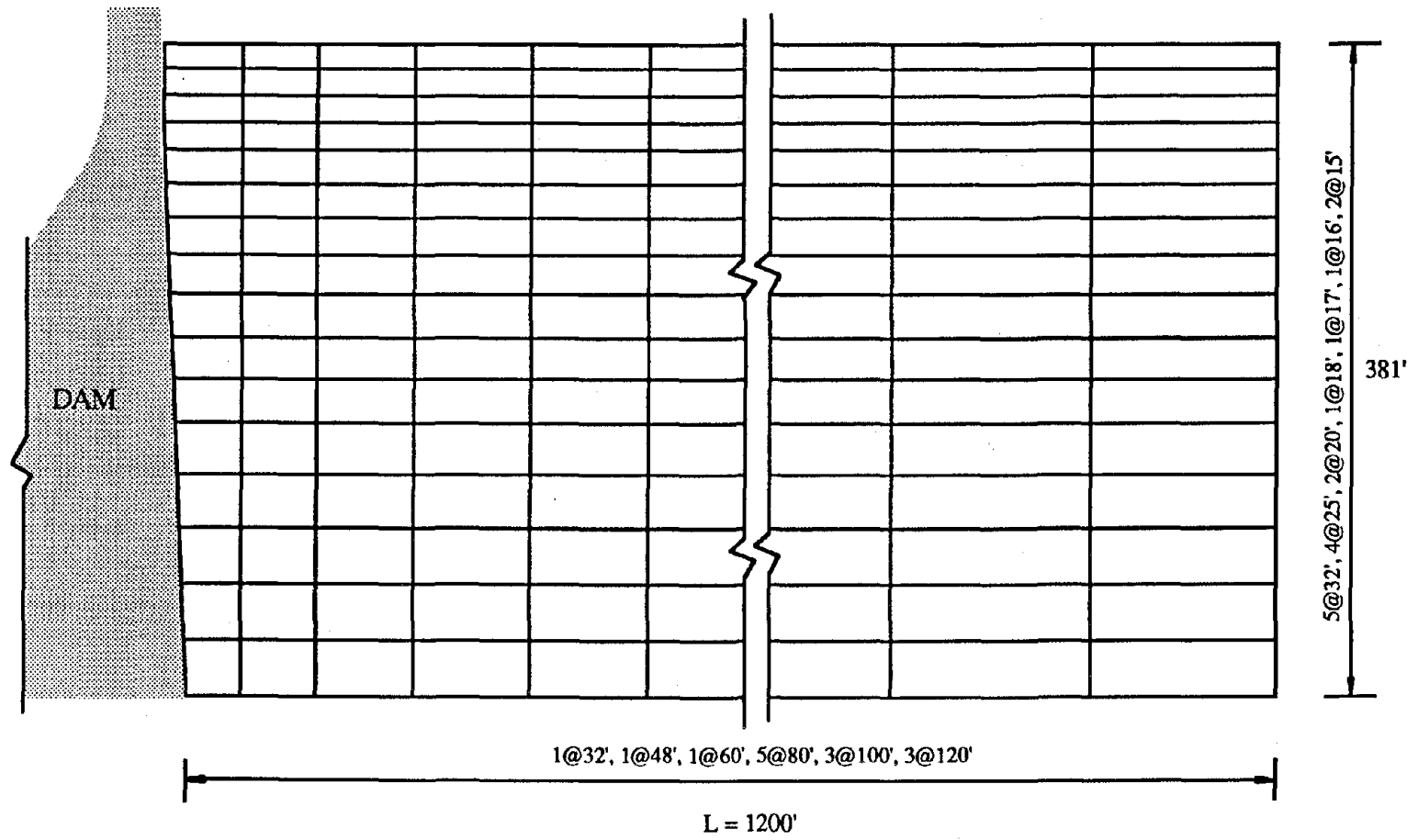Fig. 6.1 Finite element discretization of Pine Flat dam

5@32', 4@25', 2@20', 1@18', 1@17', 1@16', 2@15'

381'

DAM

1@32', 1@48', 1@60', 5@80', 3@100', 3@120'

L = 1200'

Fig. 6.2 Finite element discretization of fluid domain

153
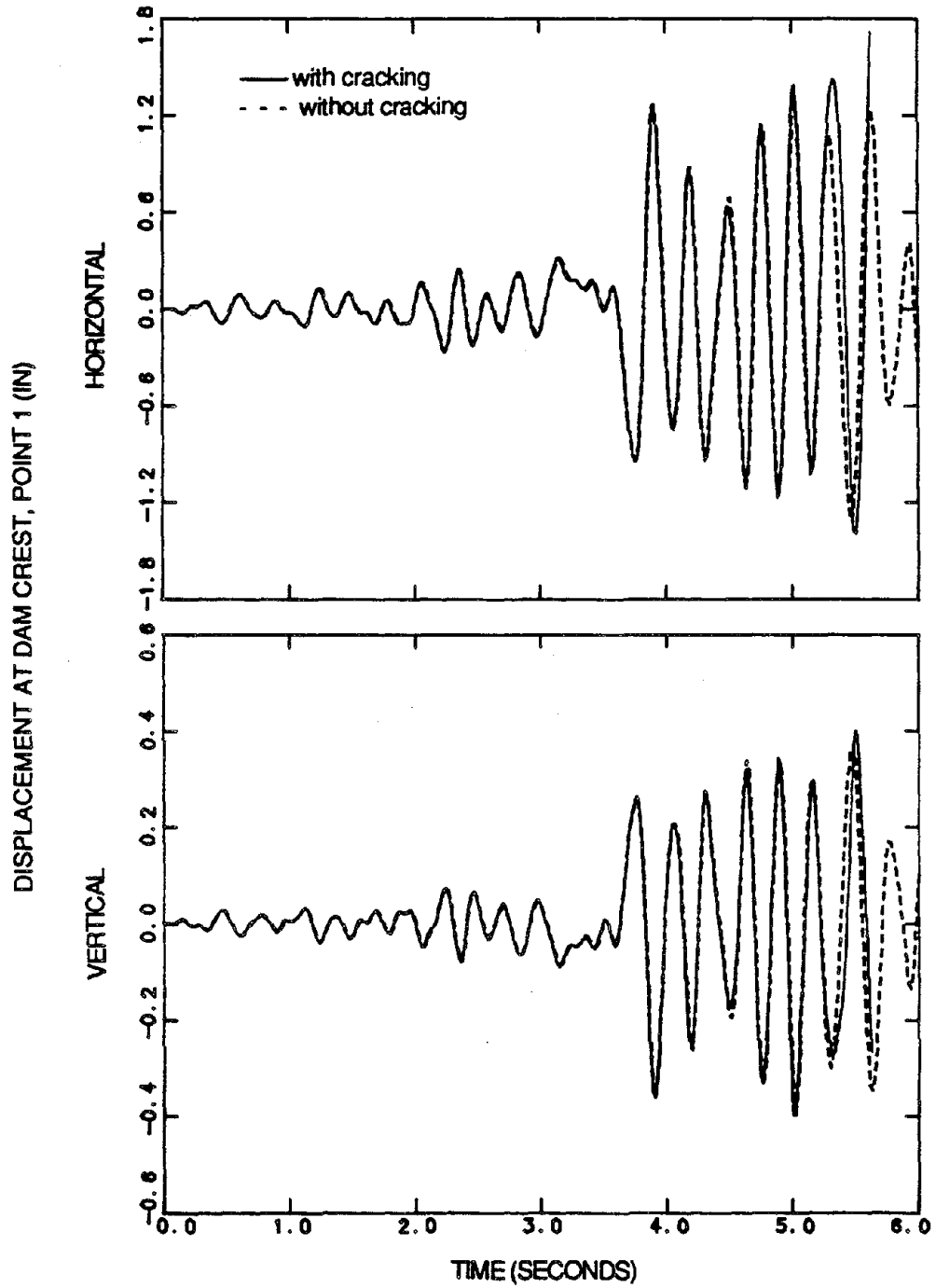
Fig. 6.3 Displacement response of Pine flat dam with empty reservoir due to the S69E component of Taft ground motion; scale factor = 2.5.
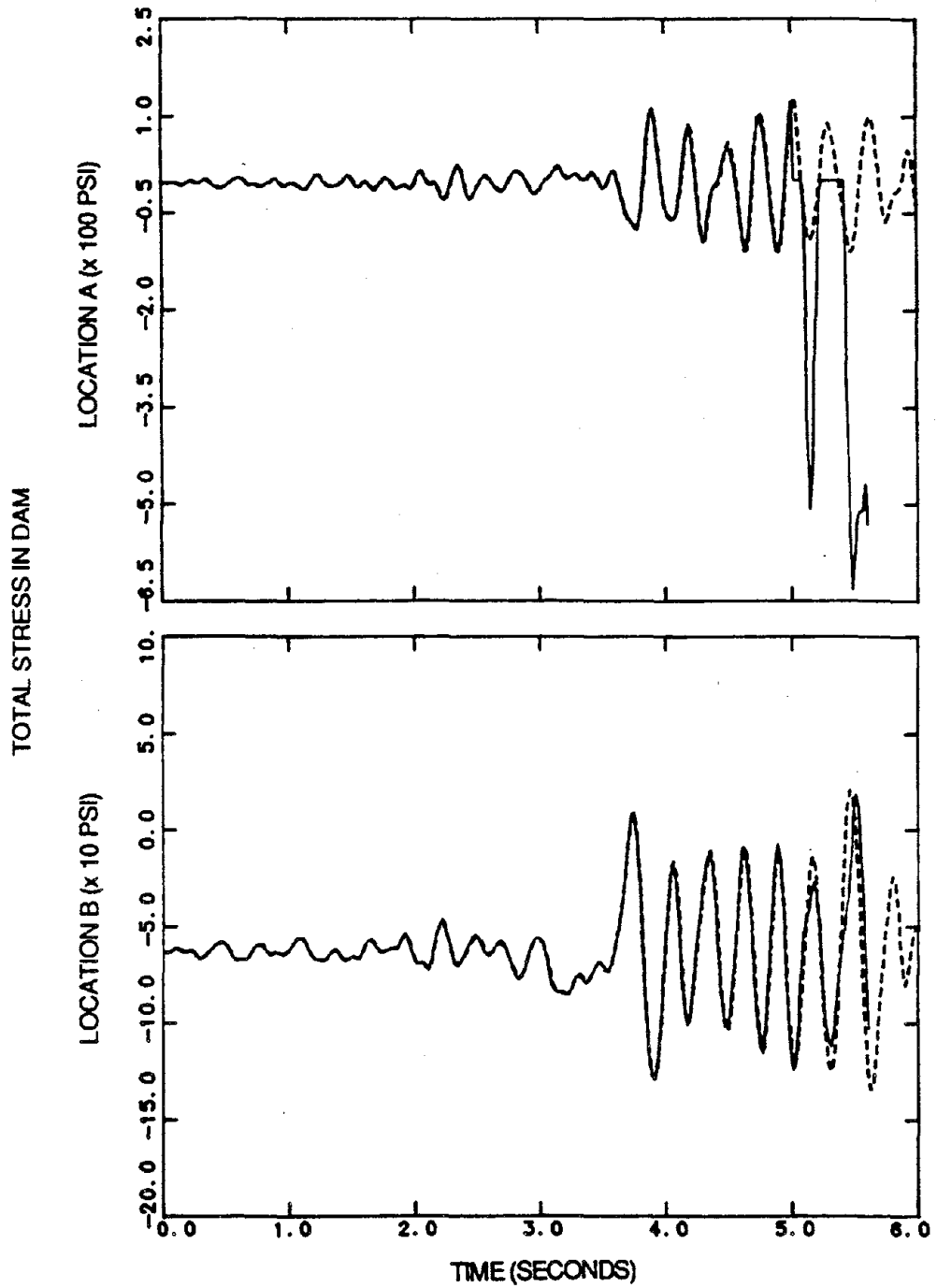
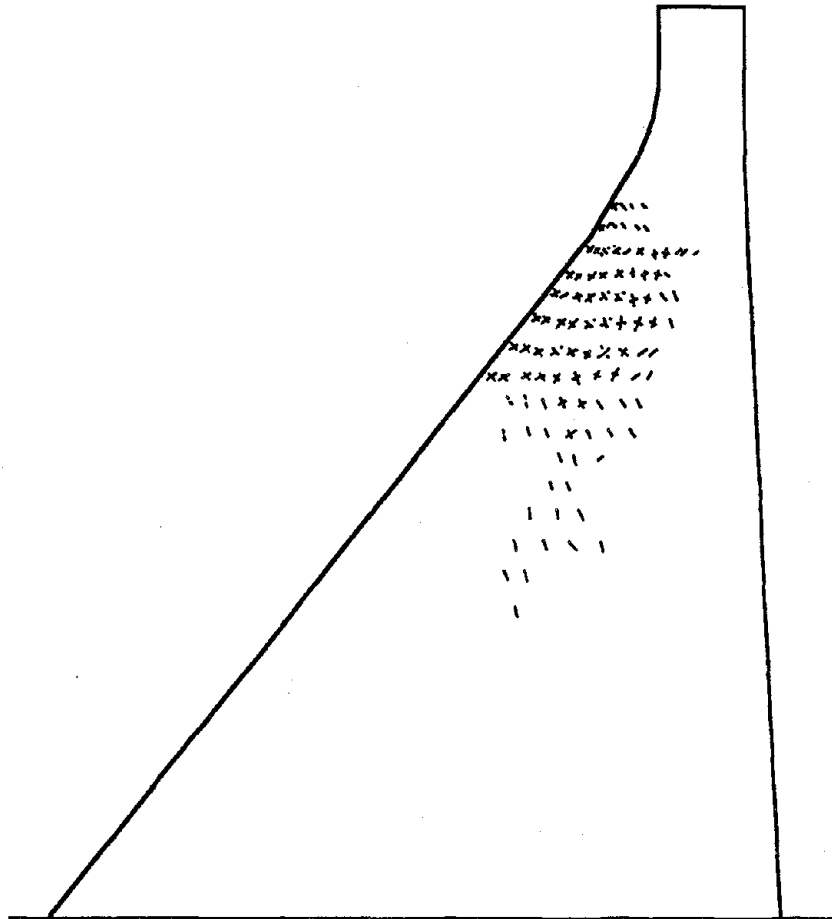Fig. 6.4 Stress response of Pine Flat dam with empty reservoir due to the S69E component of Taft ground motion; scale factor = 2.5.
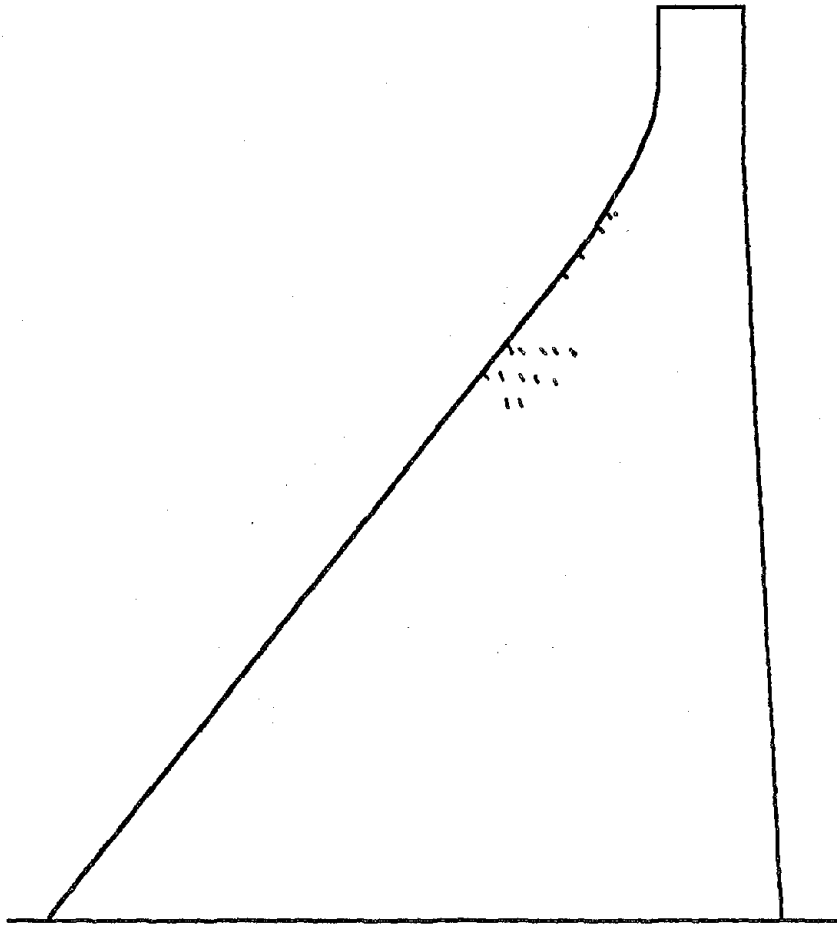
a) time = 5.03 sec

Fig. 6.5 Tensile crack pattern in Pine Flat dam with empty reservoir due to the S69E component of Taft ground motion; scale factor = 2.5.

b) time = 5.63 sec
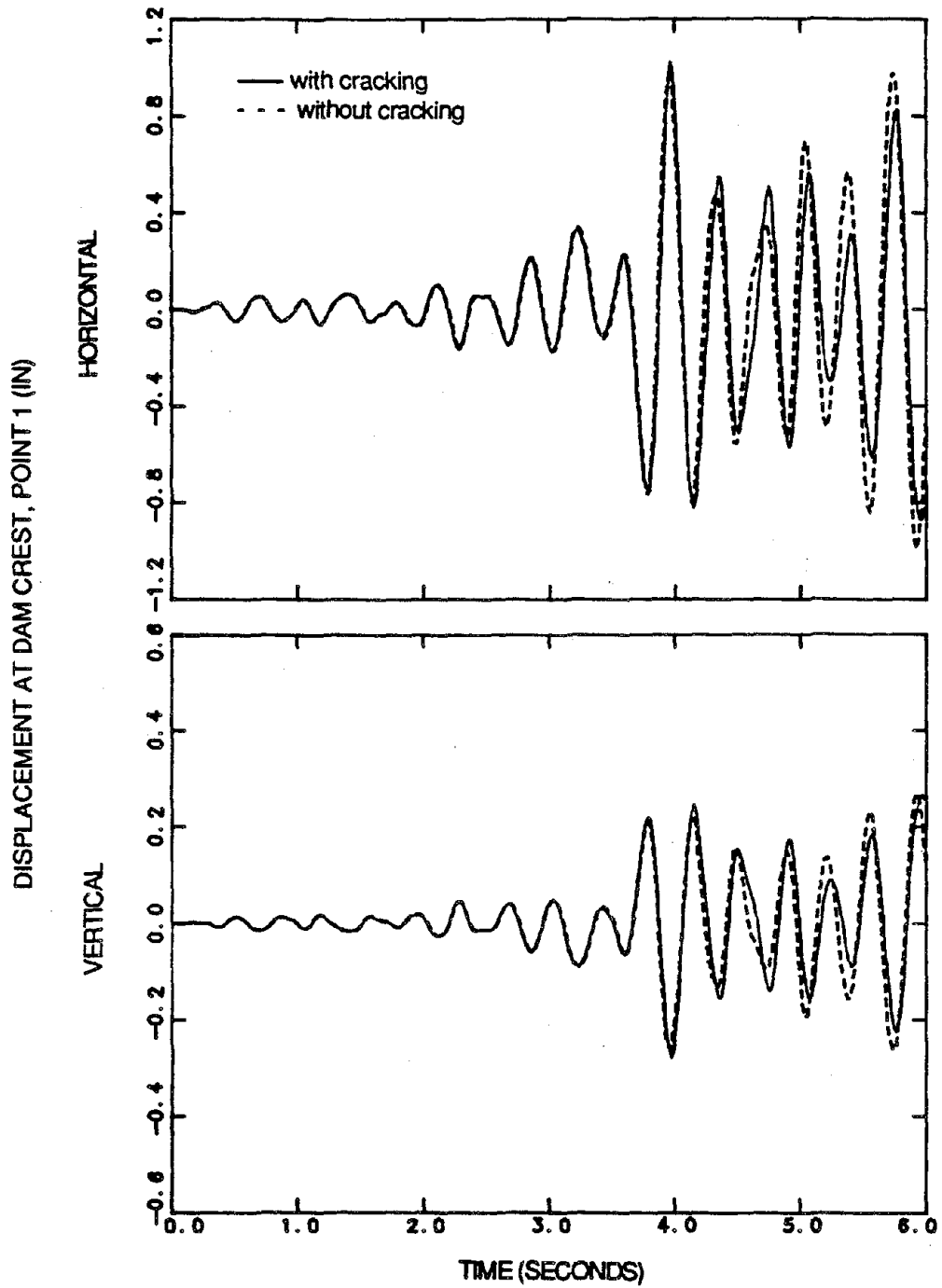
Fig. 6.5 (continued)

Fig. 6.6 Displacement response of Pine flat dam with full reservoir due to the S69E component of Taft ground motion.
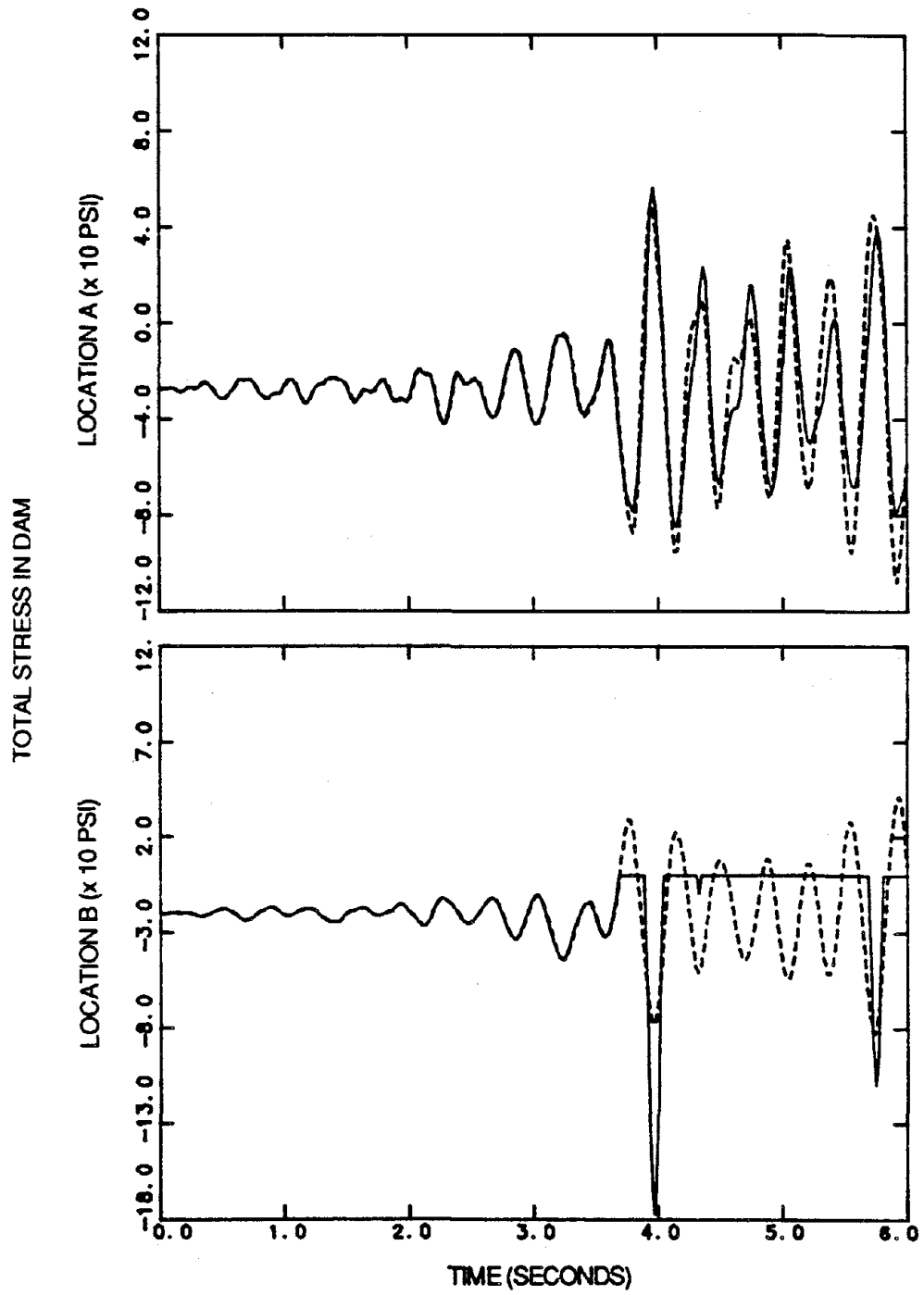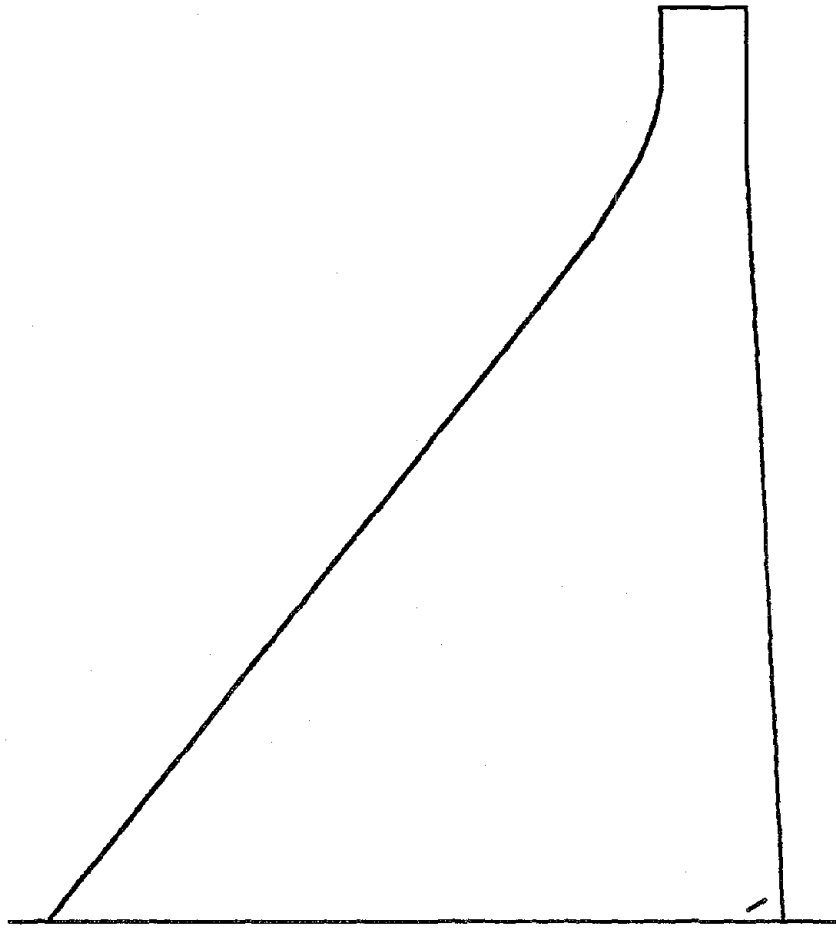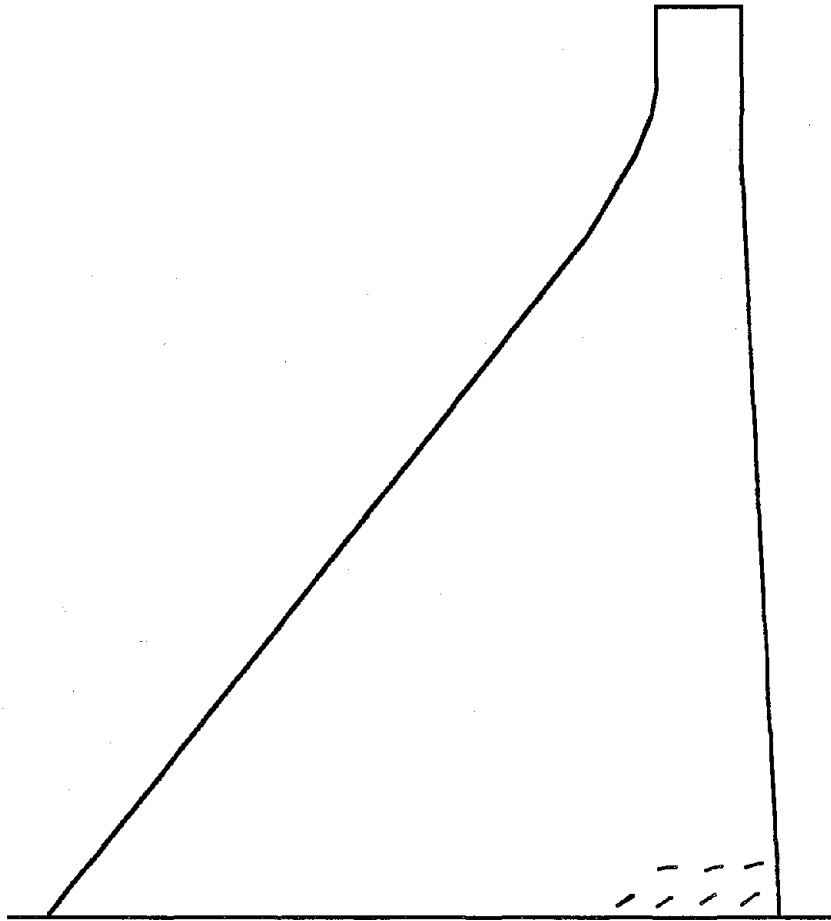
Fig. 6.7 Stress response of Pine Flat dam with full reservoir
due to the S69E component of Taft ground motion.

a) time = 3.71 sec

Fig. 6.8 Tensile crack pattern in Pine Flat dam with full reservoir
due to the S69E component of Taft ground motion.
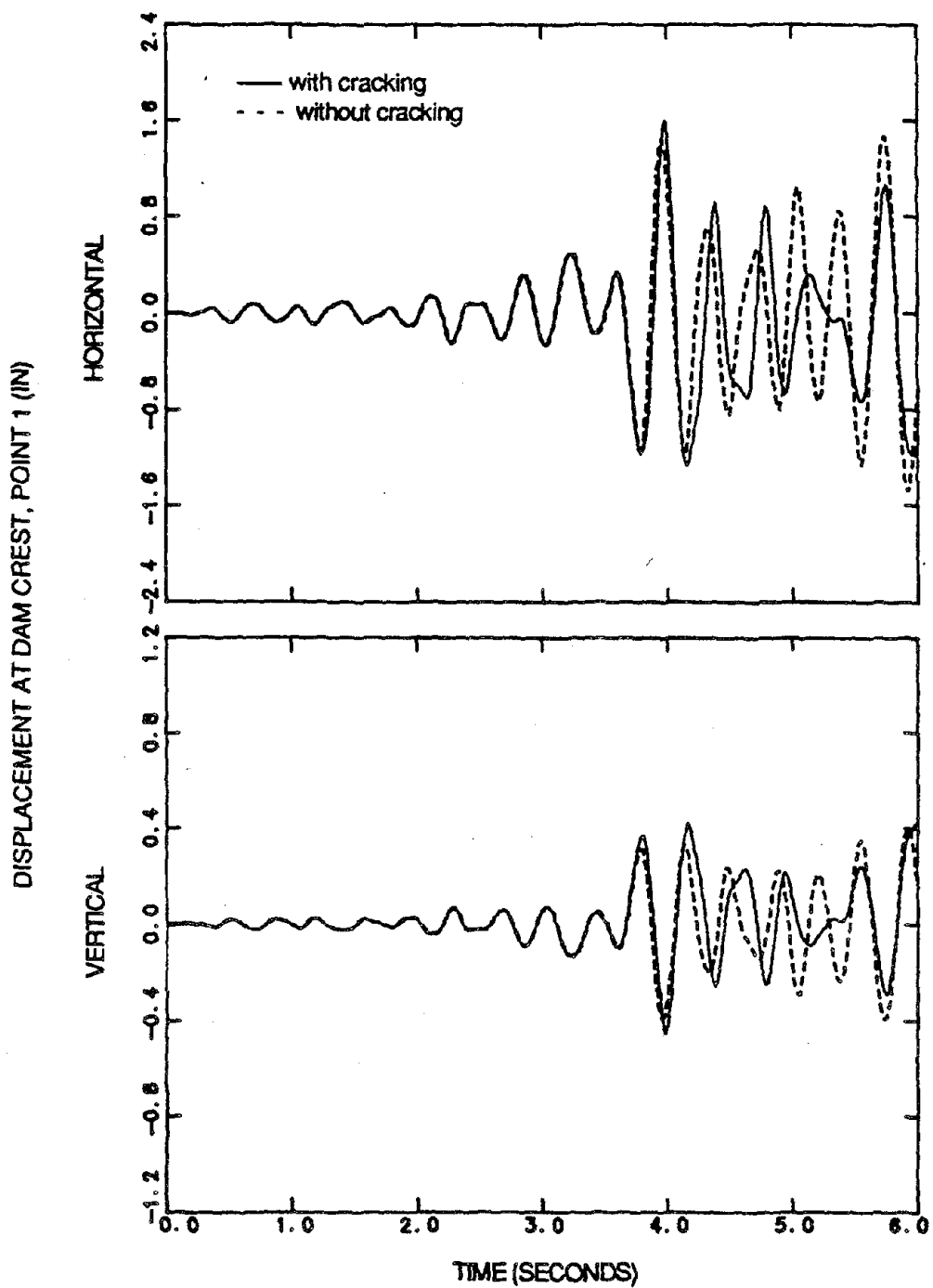
b) time = 5.94 sec

Fig. 6.8 (continued)

Fig. 6.9 Displacement response of Pine flat dam with full reservoir due to the S69E component of Taft ground motion; scale factor = 1.5.

Fig. 6.10 Stress response of Pine Flat dam with full reservoir due to
the S69E component of Taft ground motion; scale factor = 1.5.

a) time = 3.71 sec

Fig. 6.11 Tensile crack pattern in Pine Flat dam with full reservoir due to
the S69E component of Taft ground motion; scale factor = 1.5.

b) time = 5.94 sec

Fig. 6.11 (continued)

Fig. 6.12 Displacement response of Pine flat dam with full reservoir due to the S69E component of Taft ground motion; scale factor = 2.
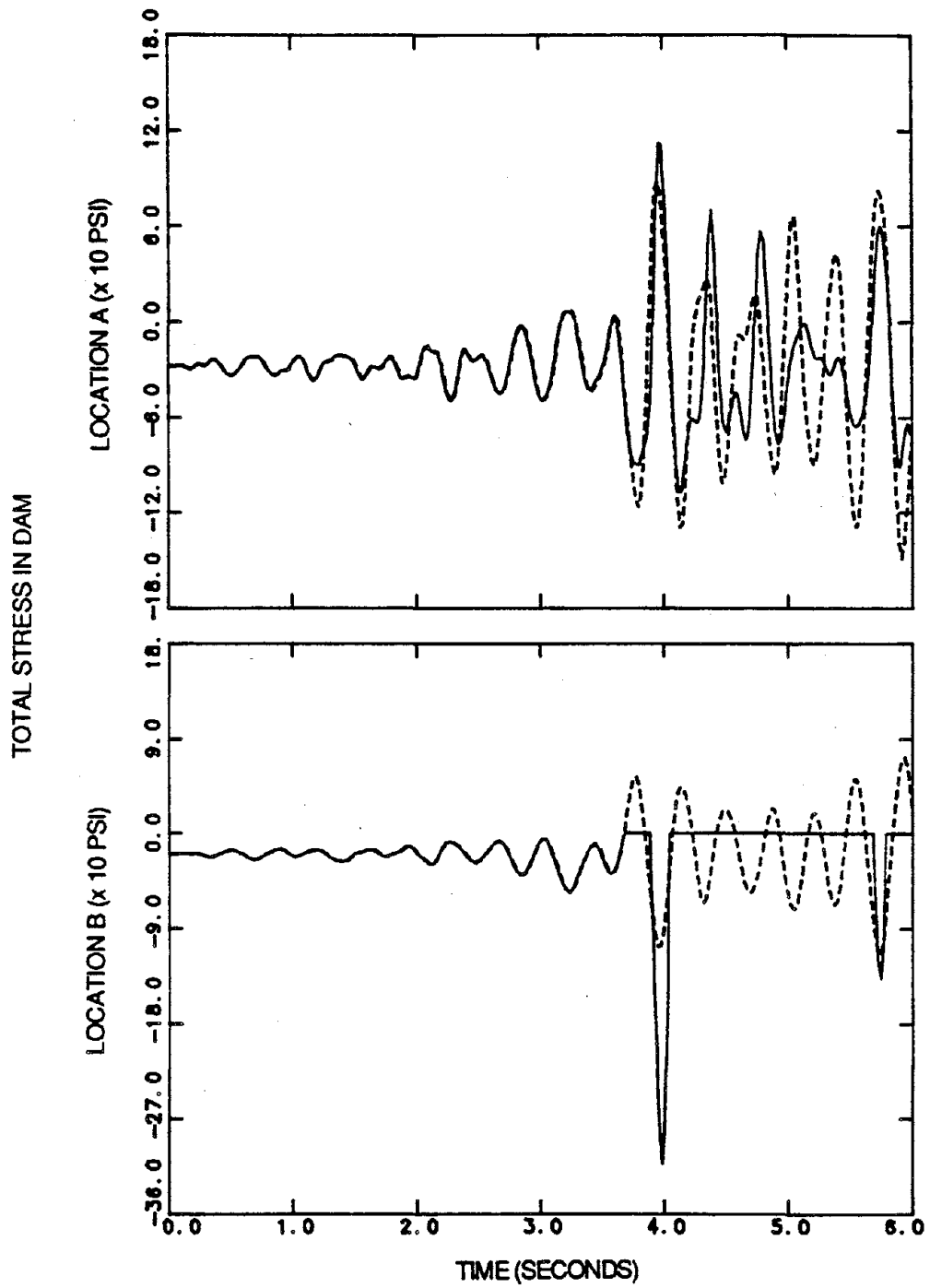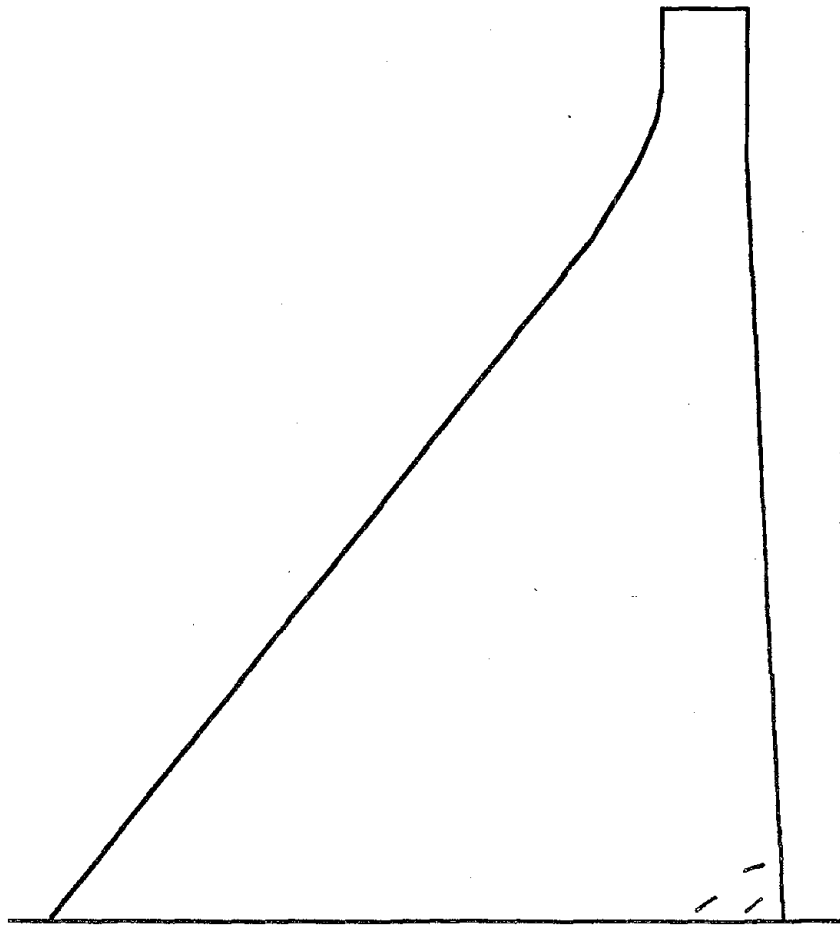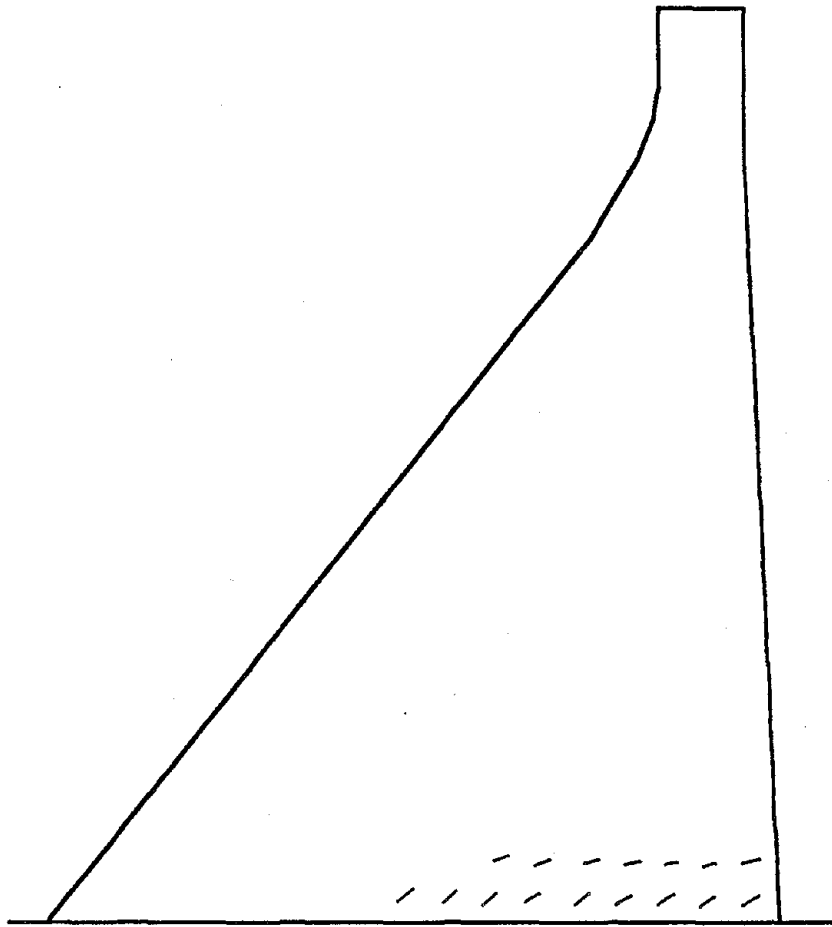
Fig. 6.13 Stress response of Pine Flat dam with full reservoir due to
the S69E component of Taft ground motion; scale factor = 2.

a) time = 3.71 sec

Fig. 6.14 Tensile crack pattern in Pine Flat dam with full reservoir due to
the S69E component of Taft ground motion; scale factor = 2.
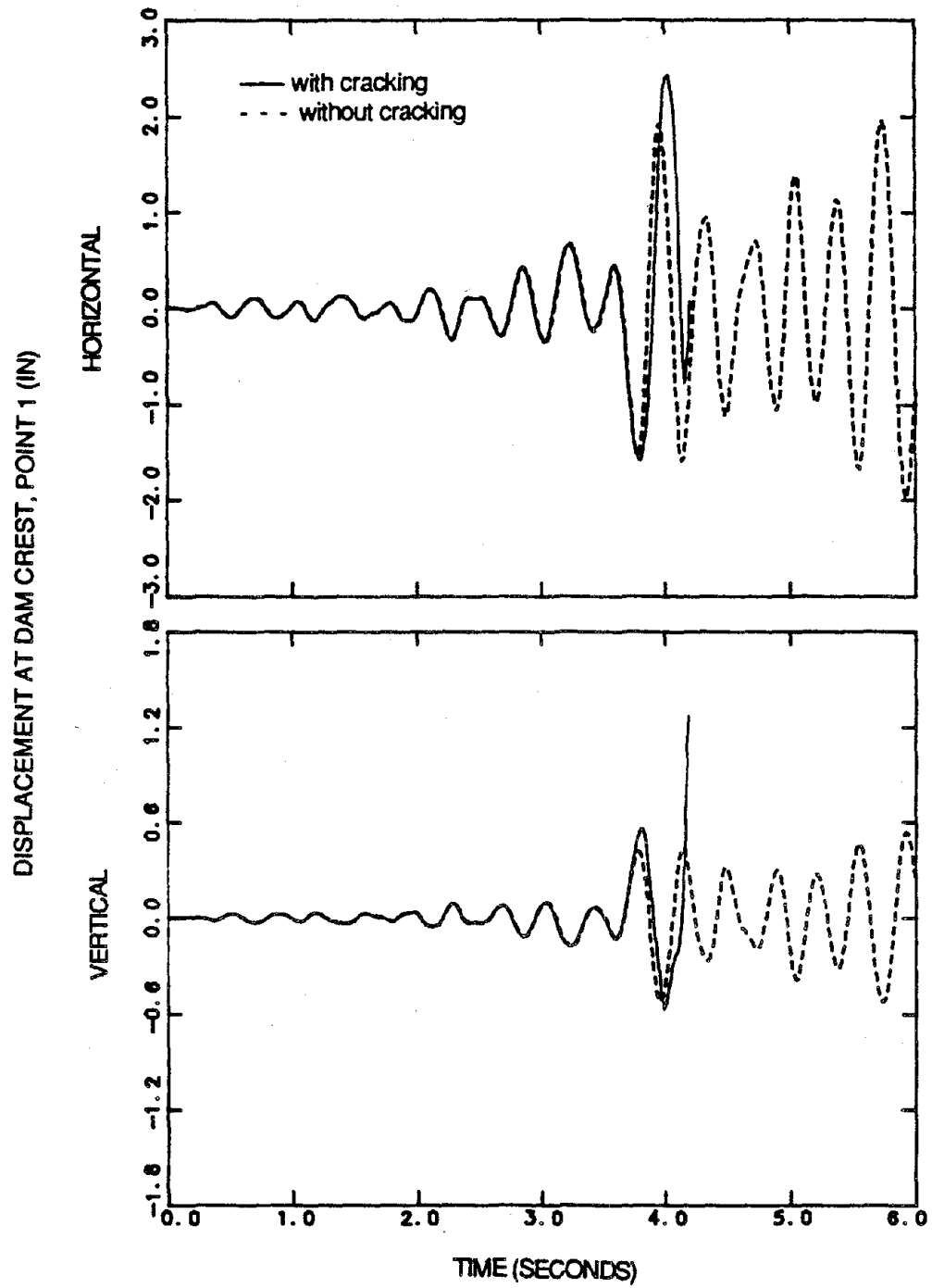
b) time = 4.01 sec

Fig. 6.14 (continued)

c) time = 4.13 sec

Fig. 6.14 (continued)

d) time = 4.19 sec

Fig. 6.14 (continued)

Fig. 6.15 Displacement response of Pine flat dam with full reservoir
due to the S16E component of Pacoima ground motion.
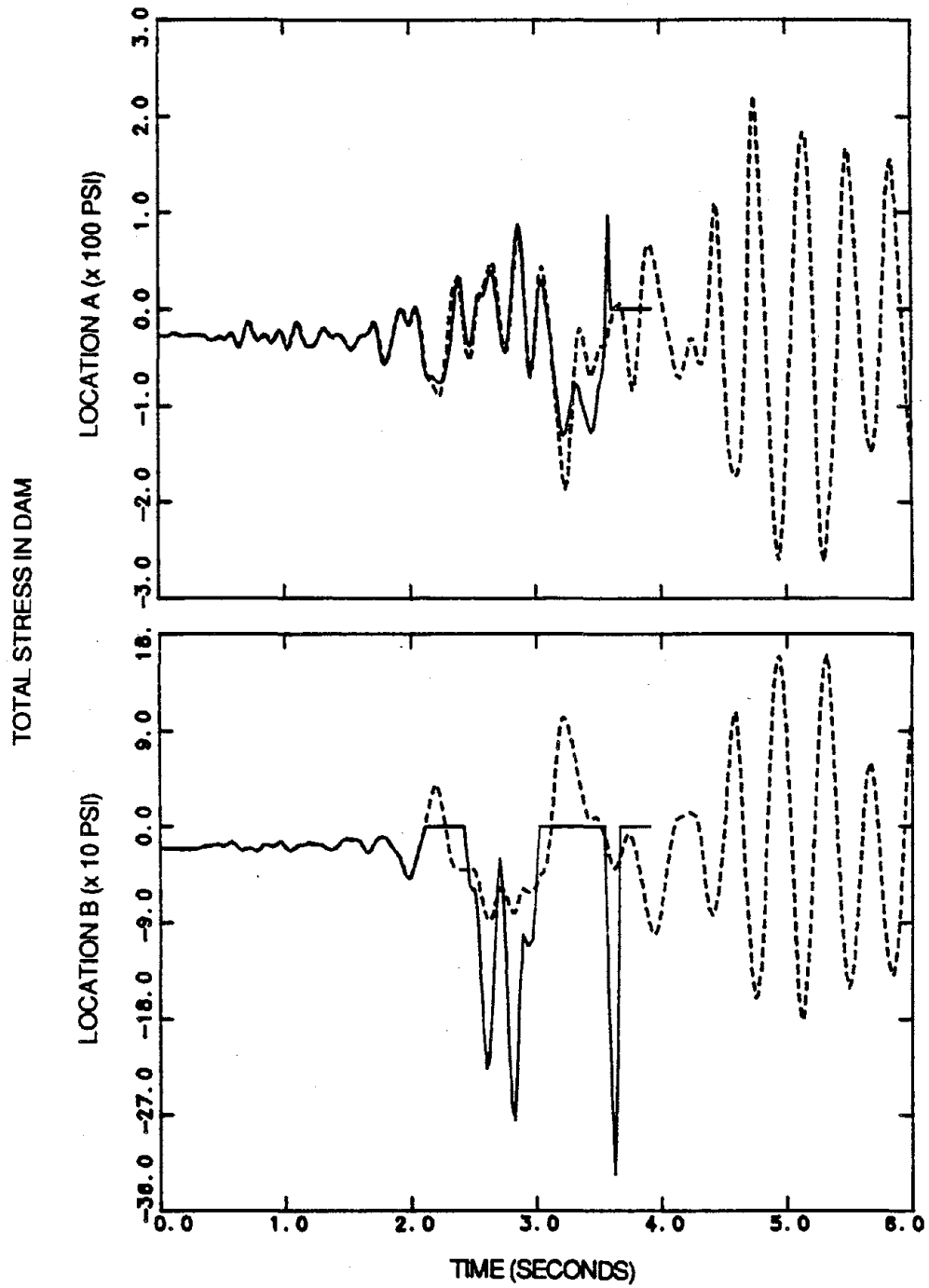
Fig. 6.16 Stress response of Pine Flat dam with full reservoir
due to the S16E component of Pacoima ground motion.
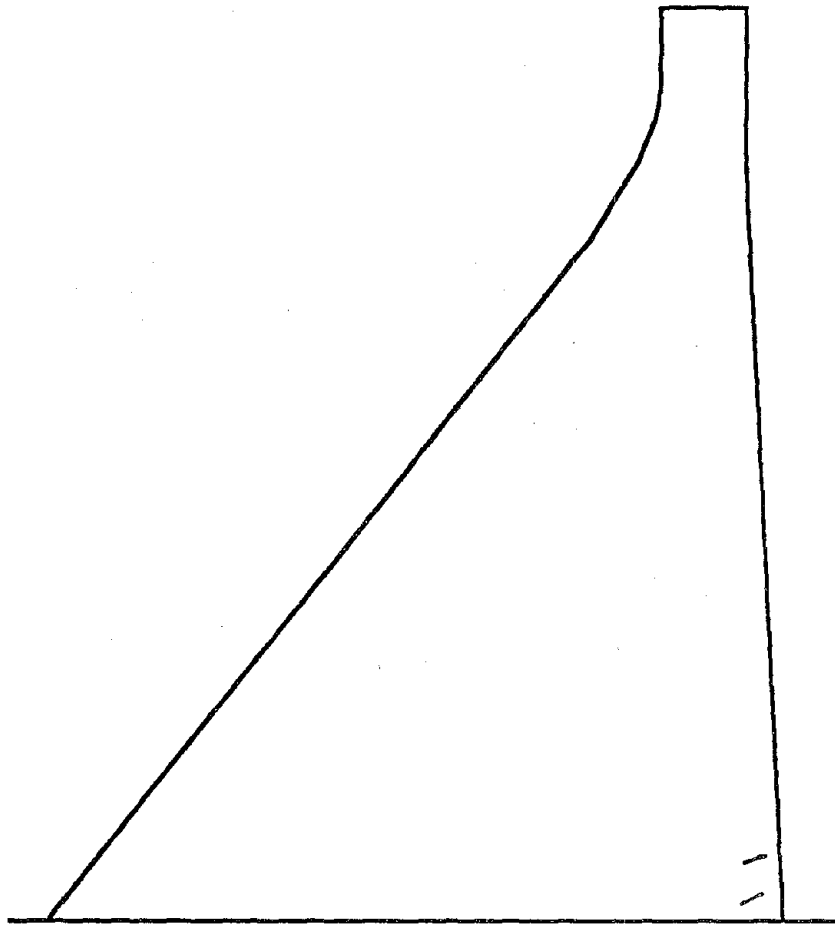
a) time = 2.15 sec

Fig. 6.17 Tensile crack pattern in Pine Flat dam with full reservoir
due to the S16E component of Pacoima ground motion.
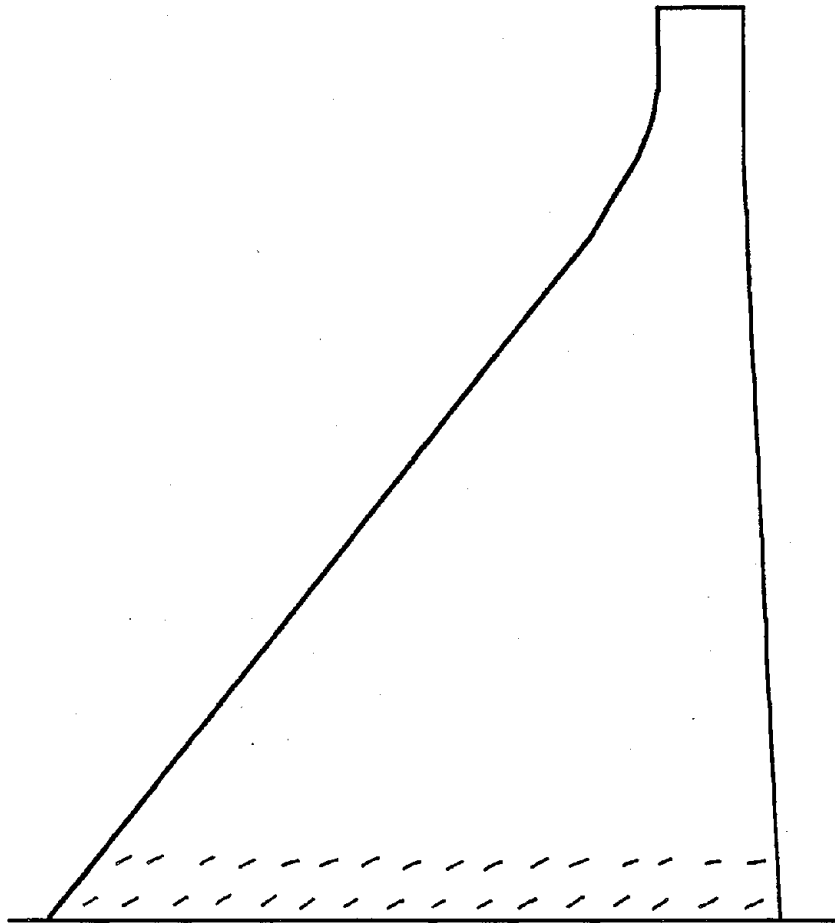
b) time = 3.41 sec

Fig. 6.17 (continued)
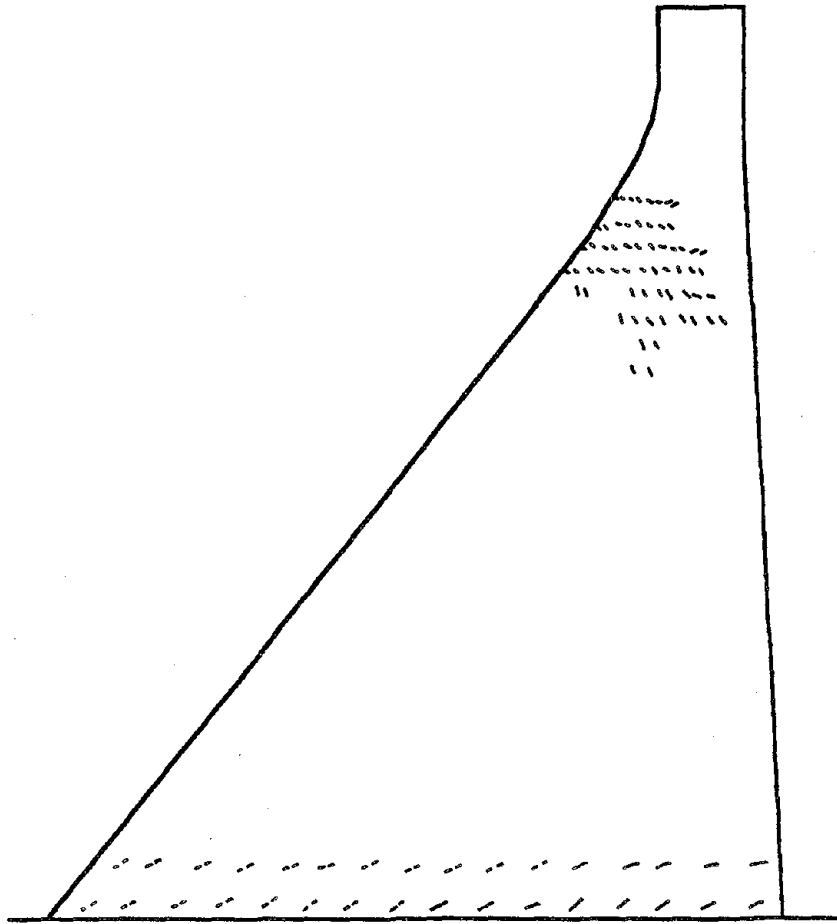
c) time = 3.71 sec

Fig. 6.17 (continued)
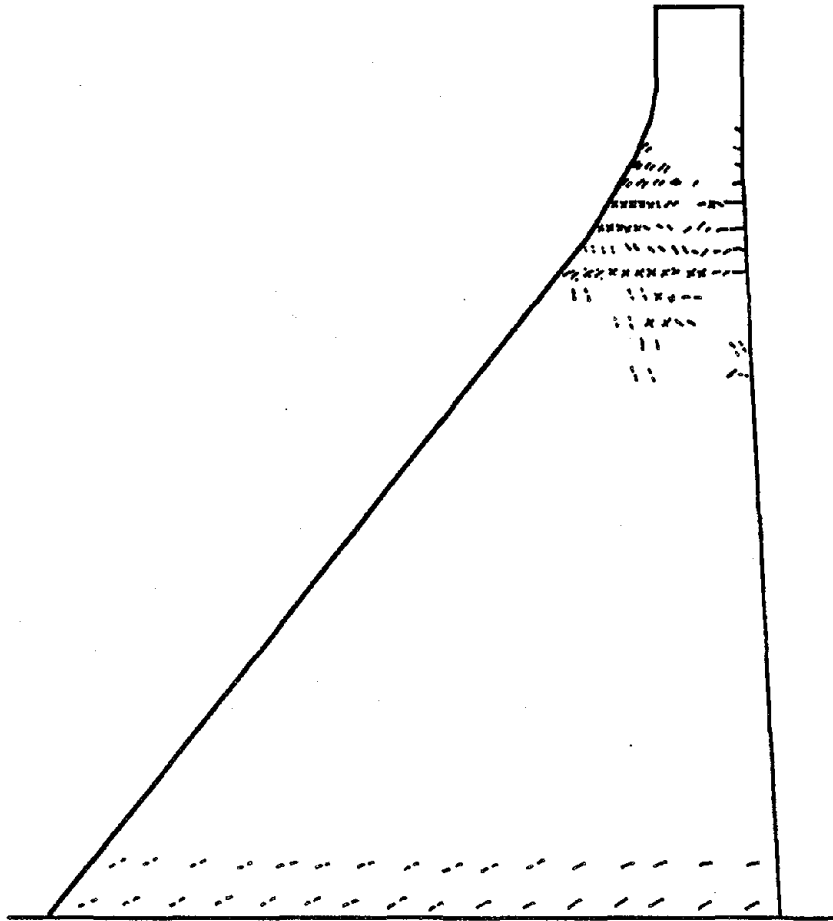
d) time = 3.83 sec

Fig. 6.17 (continued)
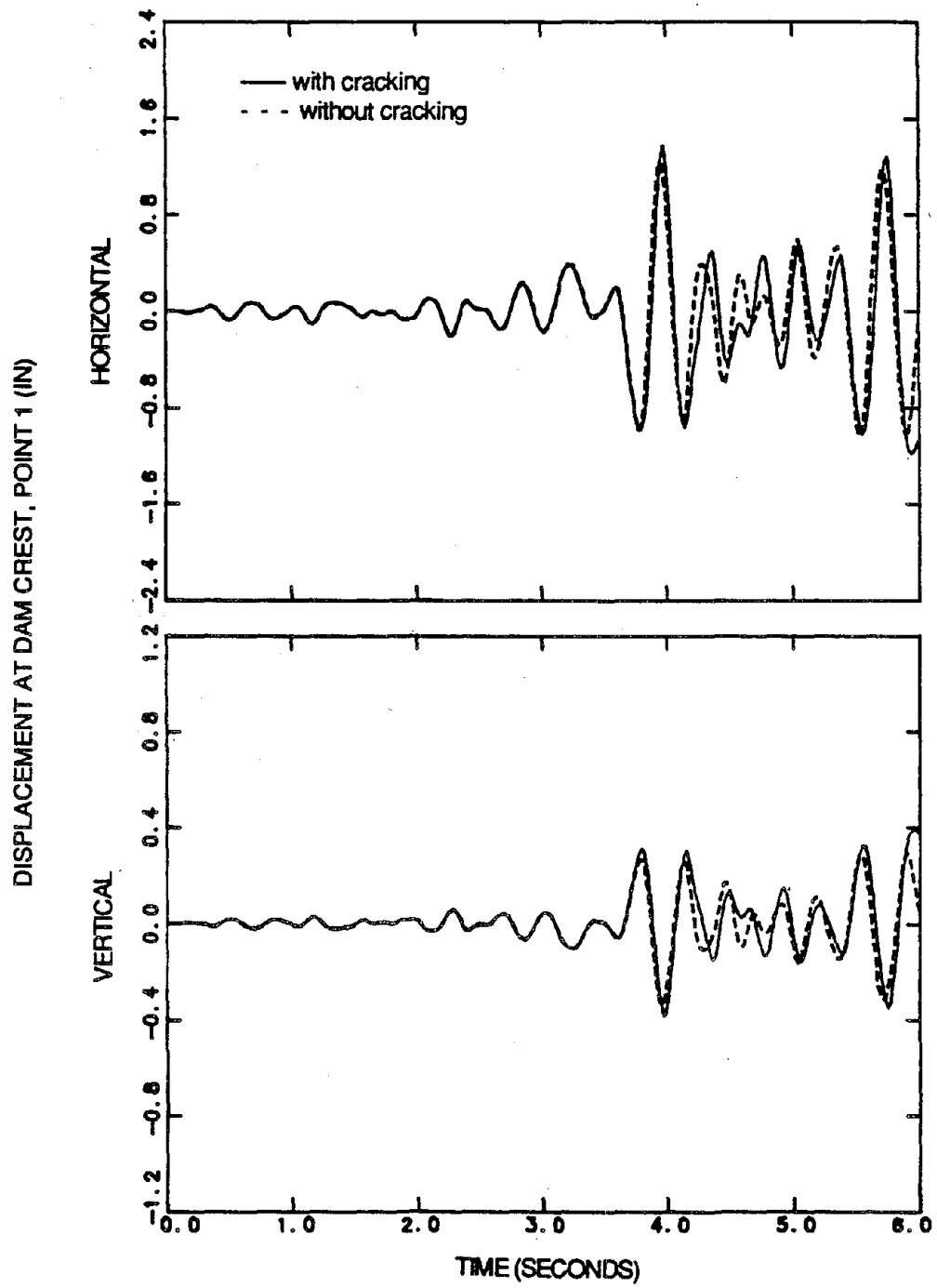
Fig. 6.18 Displacement response of Pine flat dam with full reservoir due to the S69E component of Taft ground motion; scale factor = 1.5; $\alpha_r = 0.5$.
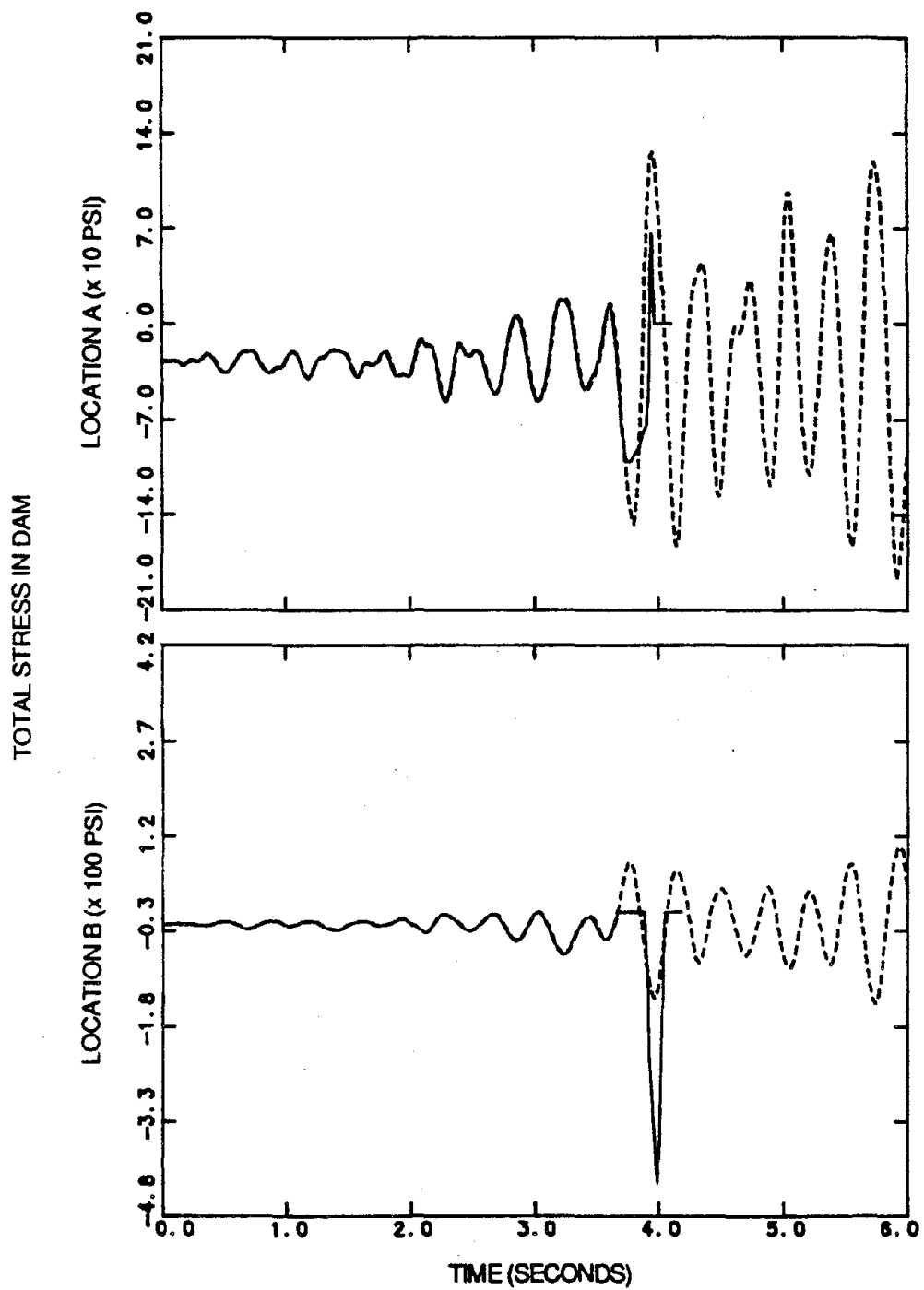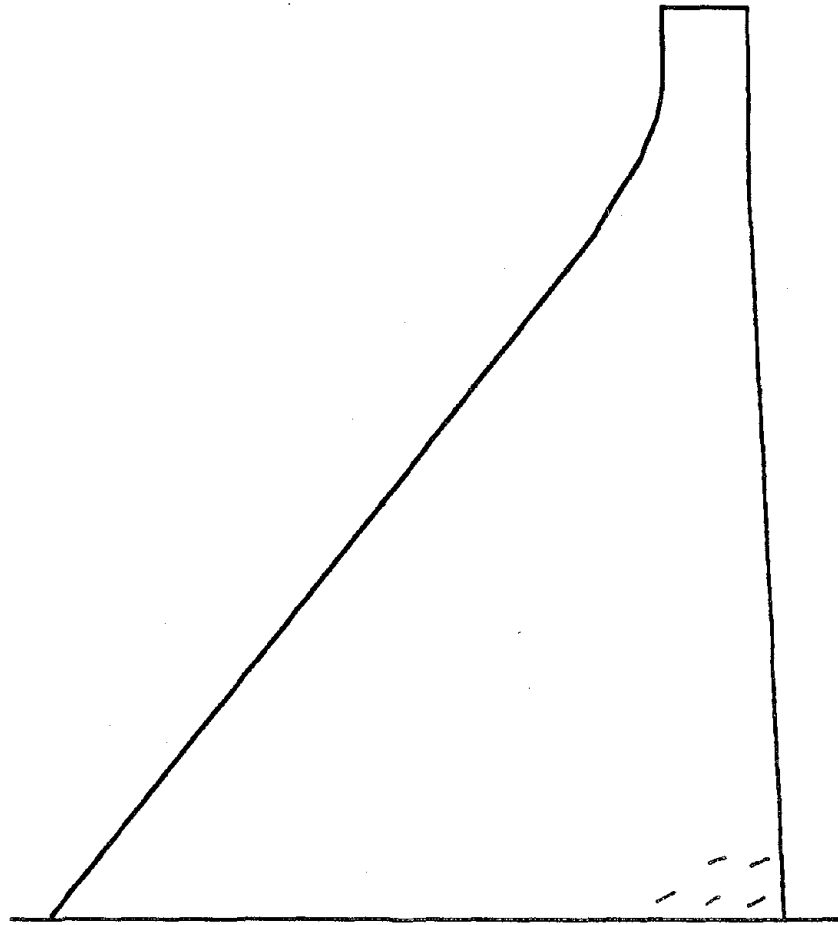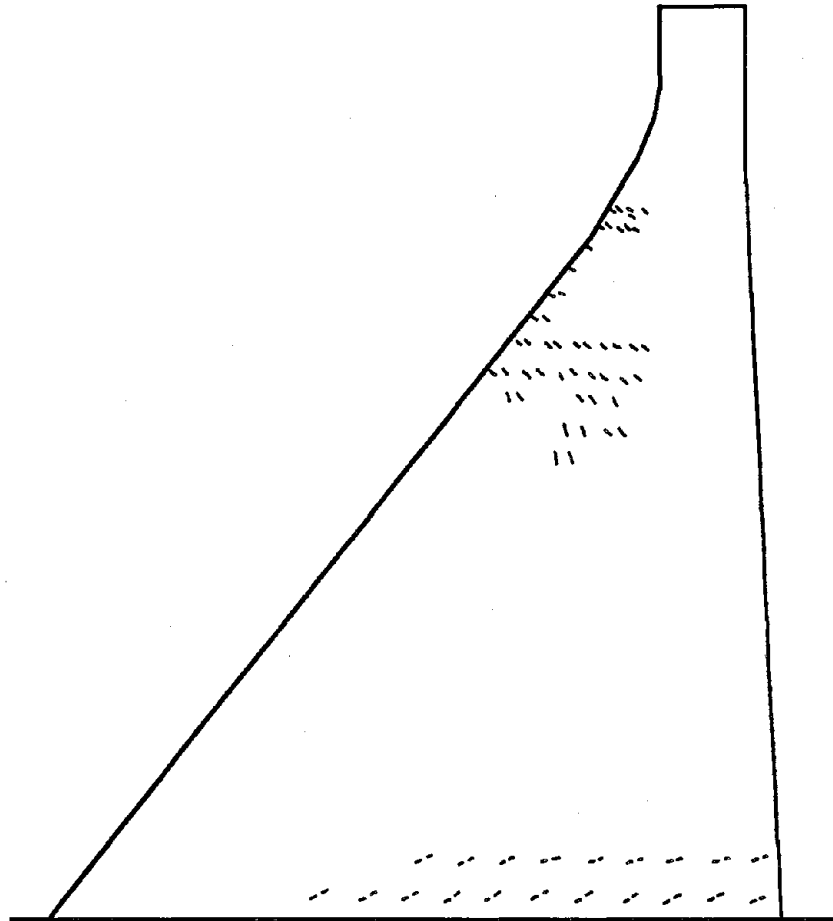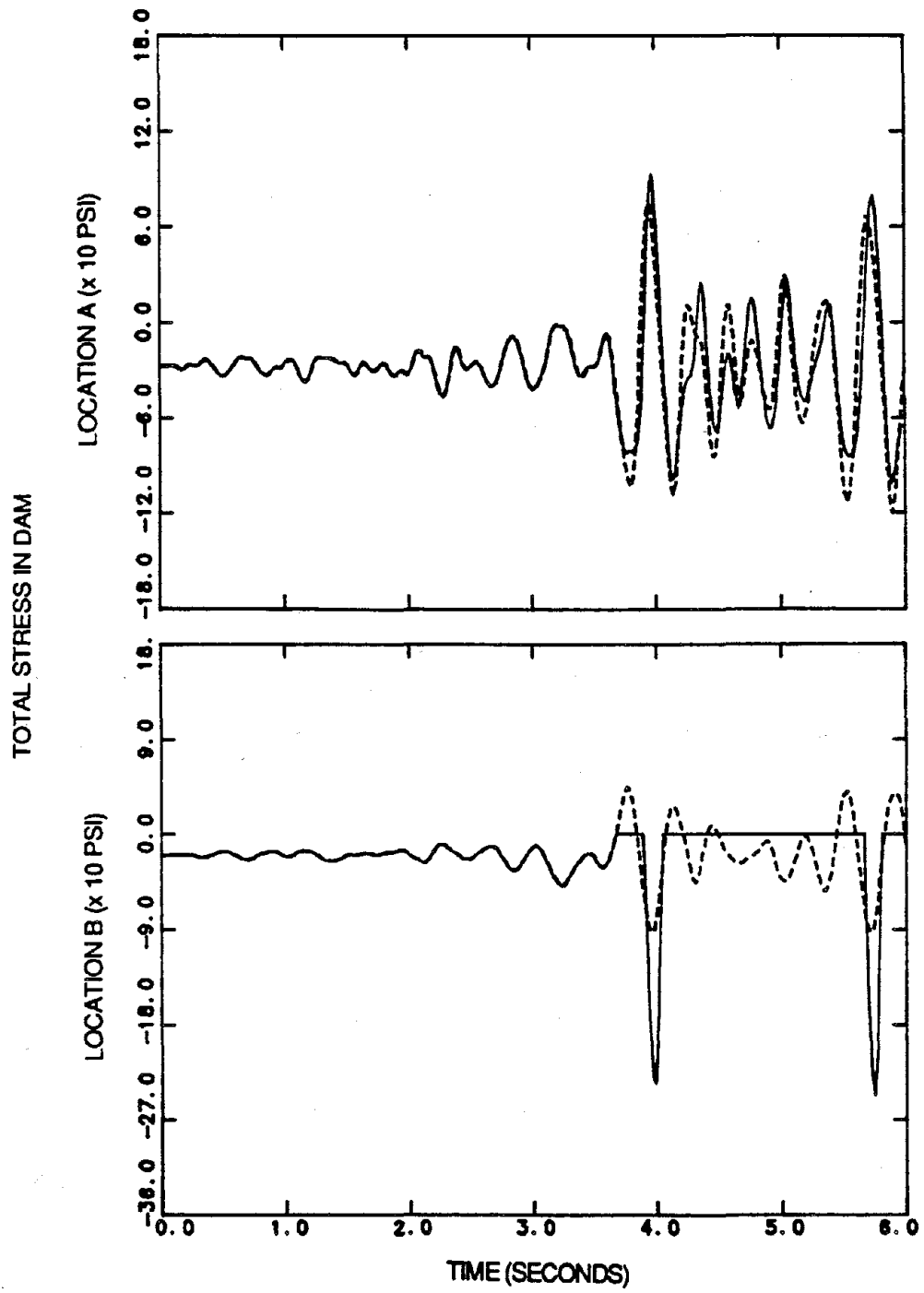
Fig. 6.19 Stress response of Pine flat dam with full reservoir
due to the S69E component of Taft ground motion;
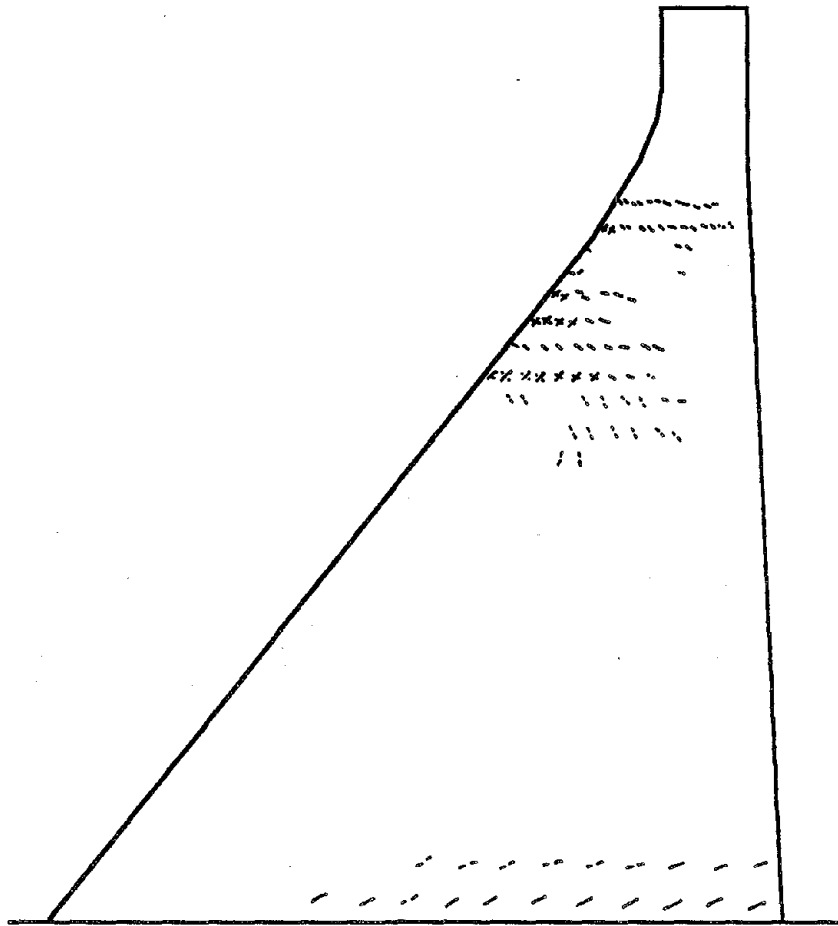scale factor = 1.5; $\alpha_r = 0.5$.
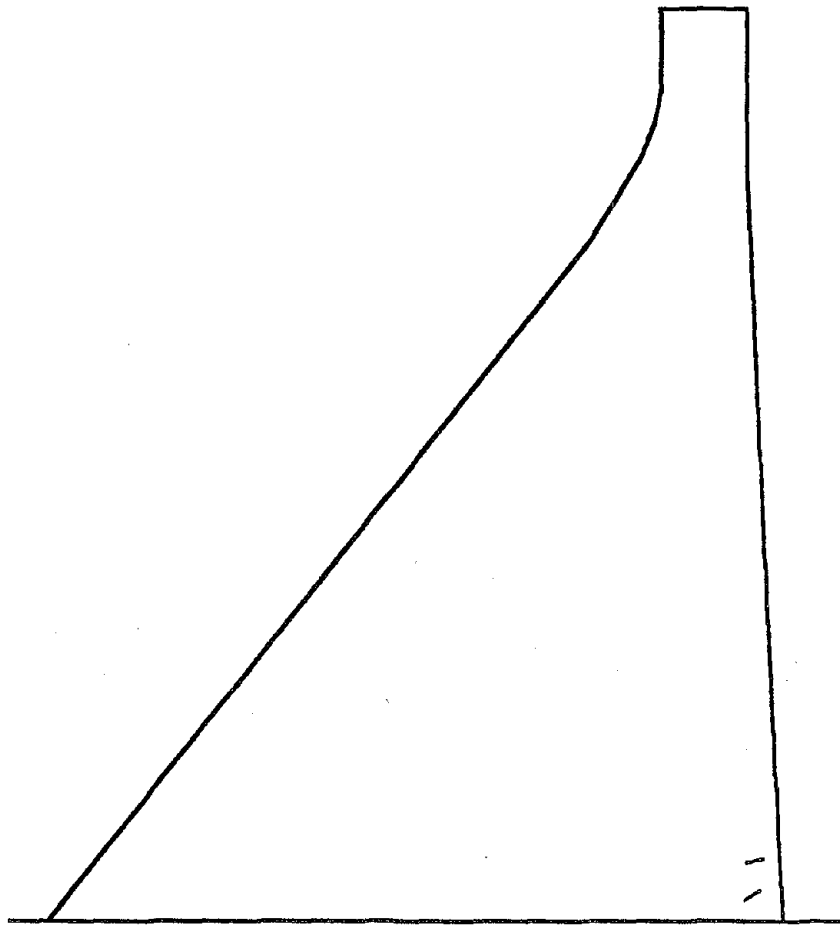
a) time = 3.71 sec

Fig. 6.20 Tensile crack pattern in Pine Flat dam with full reservoir
due to the S69E component of Taft ground motion;
scale factor = 1.5; α_r = 0.5.
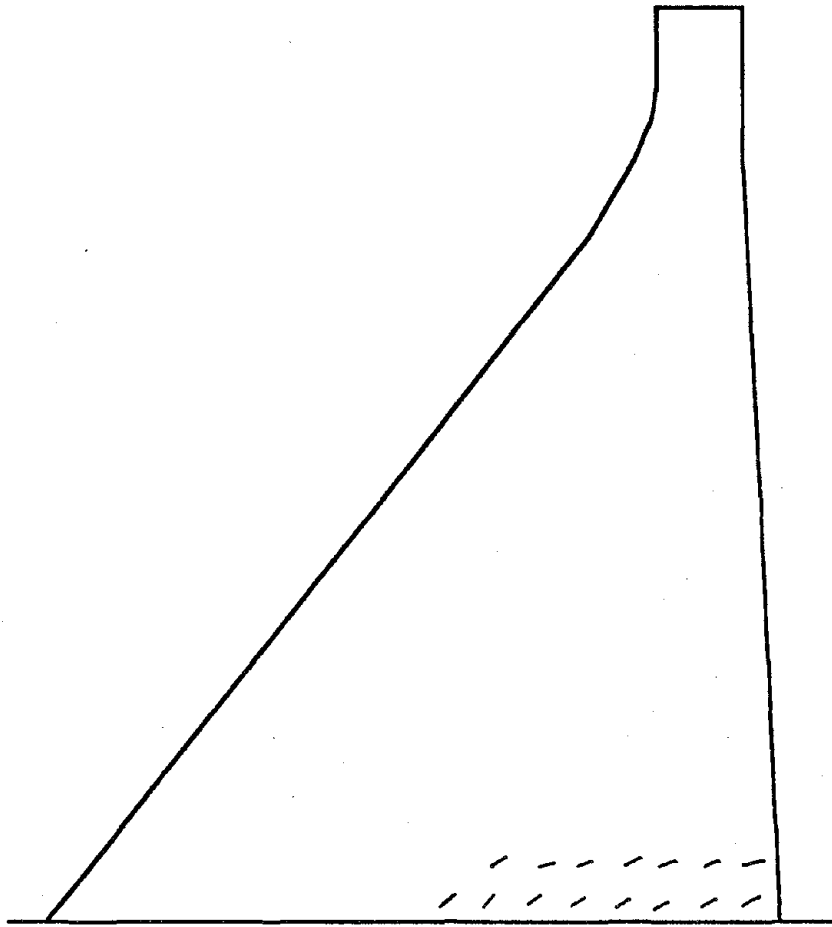
b) time = 5.94 sec

Fig. 6.20 (continued)

Fig. 6.21 Displacement response of Pine flat dam with full reservoir
due to the S69E component of Taft ground motion;
scale factor = 2; $\alpha_r = 0.5$.
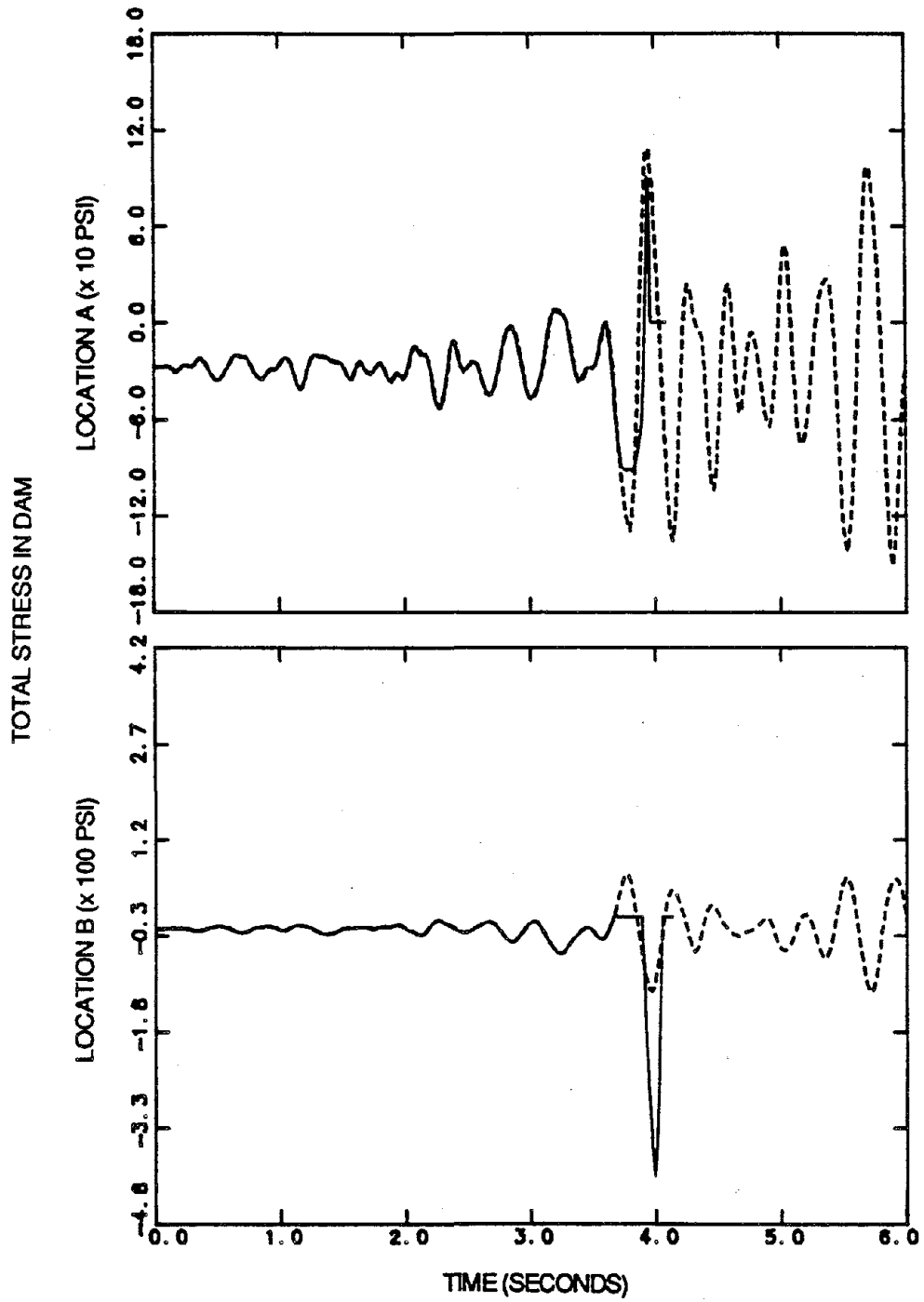
Fig. 6.22 Stress response of Pine flat dam with full reservoir
due to the S69E component of Taft ground motion;
scale factor = 2; α_r = 0.5.
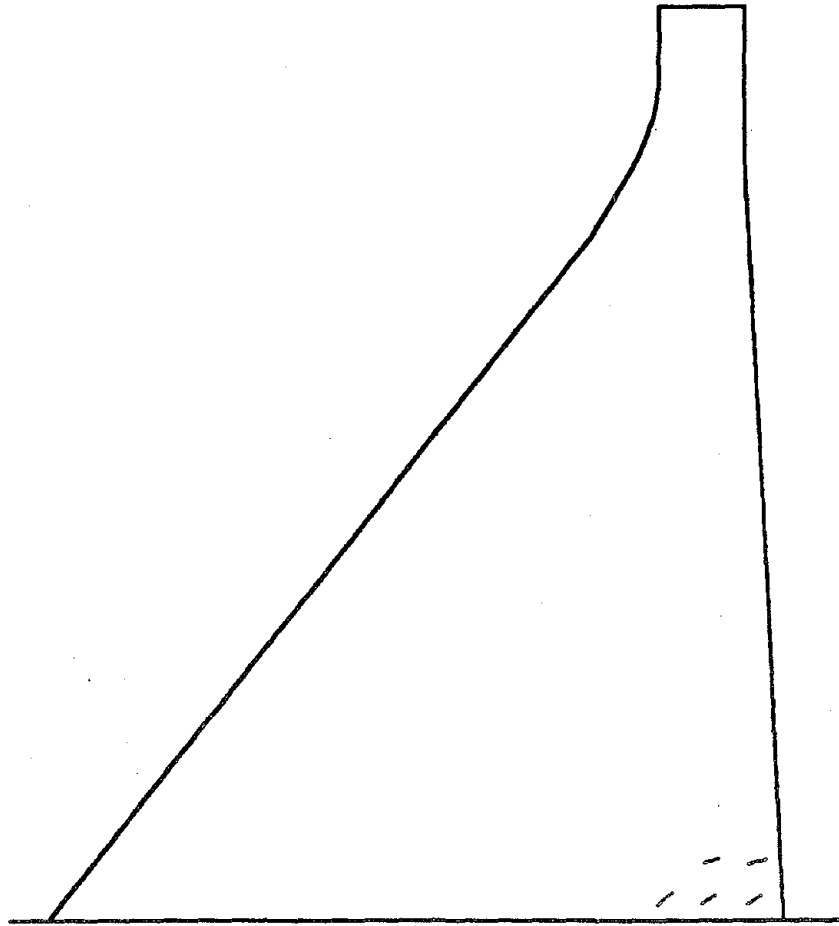
a) time = 3.71 sec

Fig. 6.23 Tensile crack pattern in Pine Flat dam with full reservoir
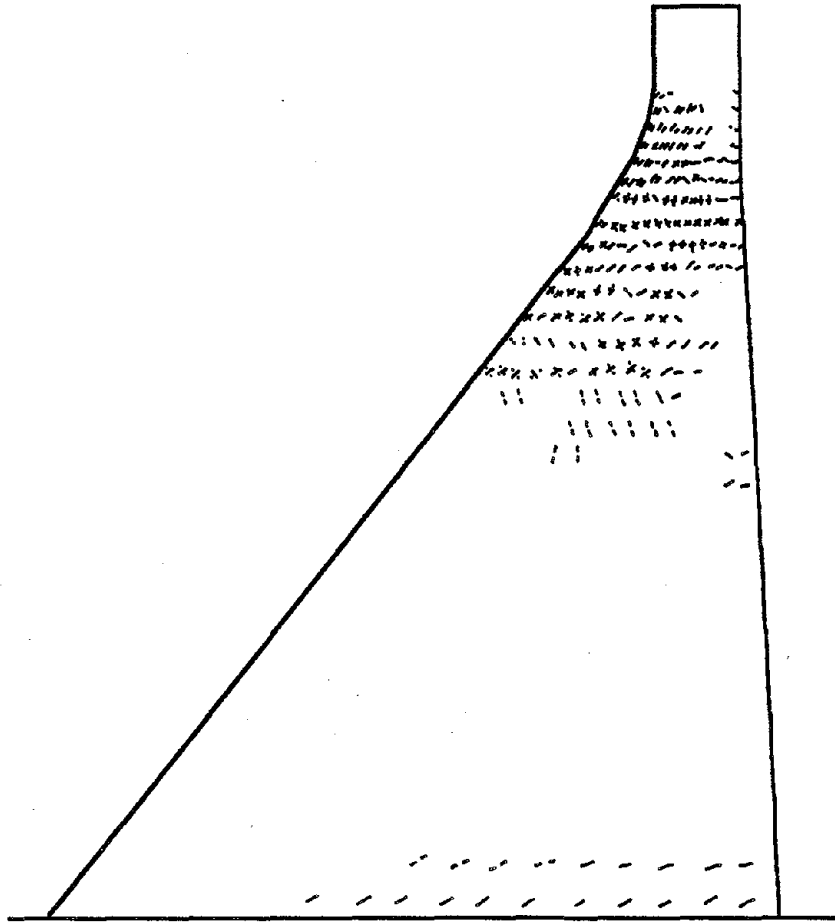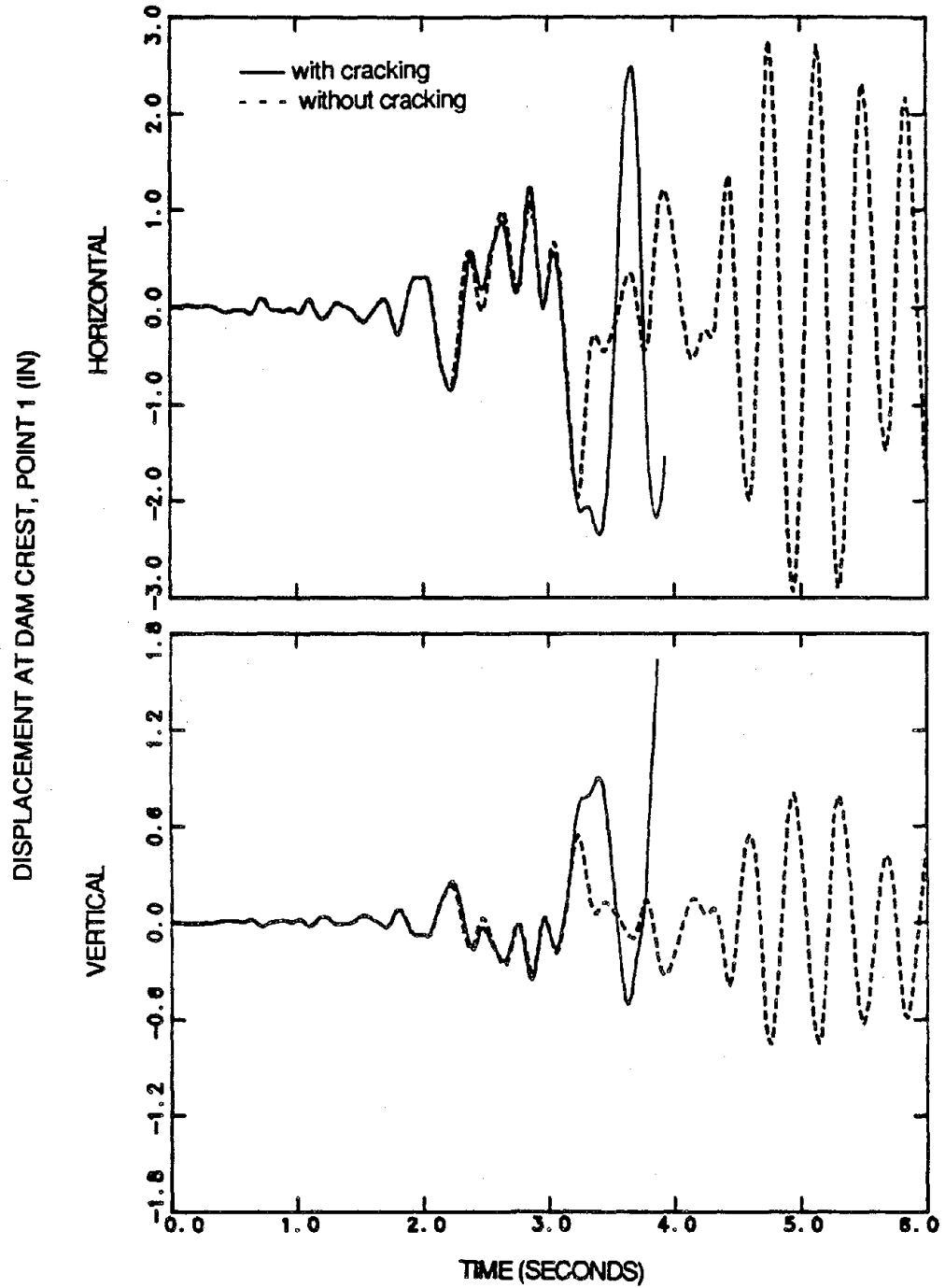due to the S69E component of Taft ground motion;
scale factor = 2; $\alpha_r = 0.5$.
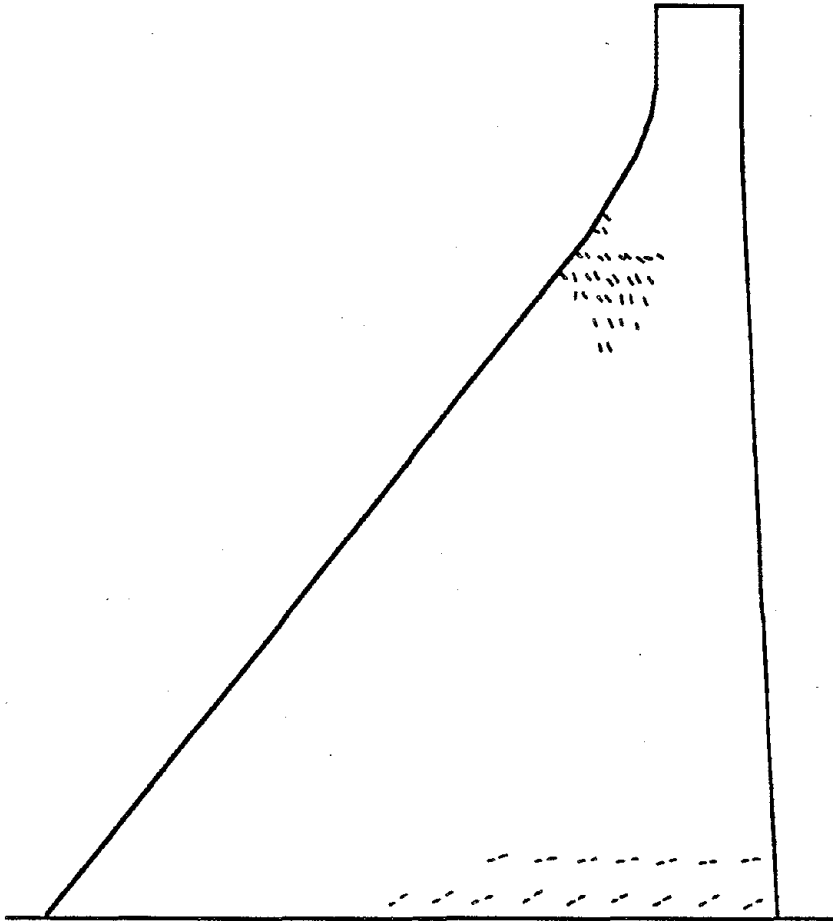
b) time = 4.01 sec

Fig. 6.23 (continued)
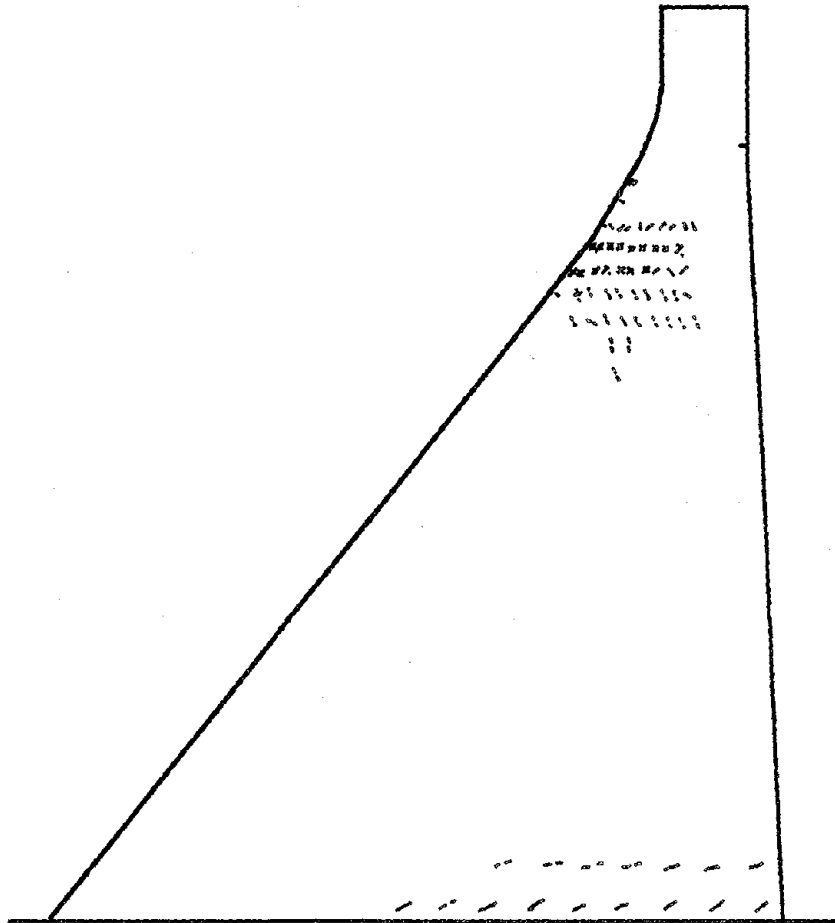
c) time = 4.13 sec

Fig. 6.23 (continued)
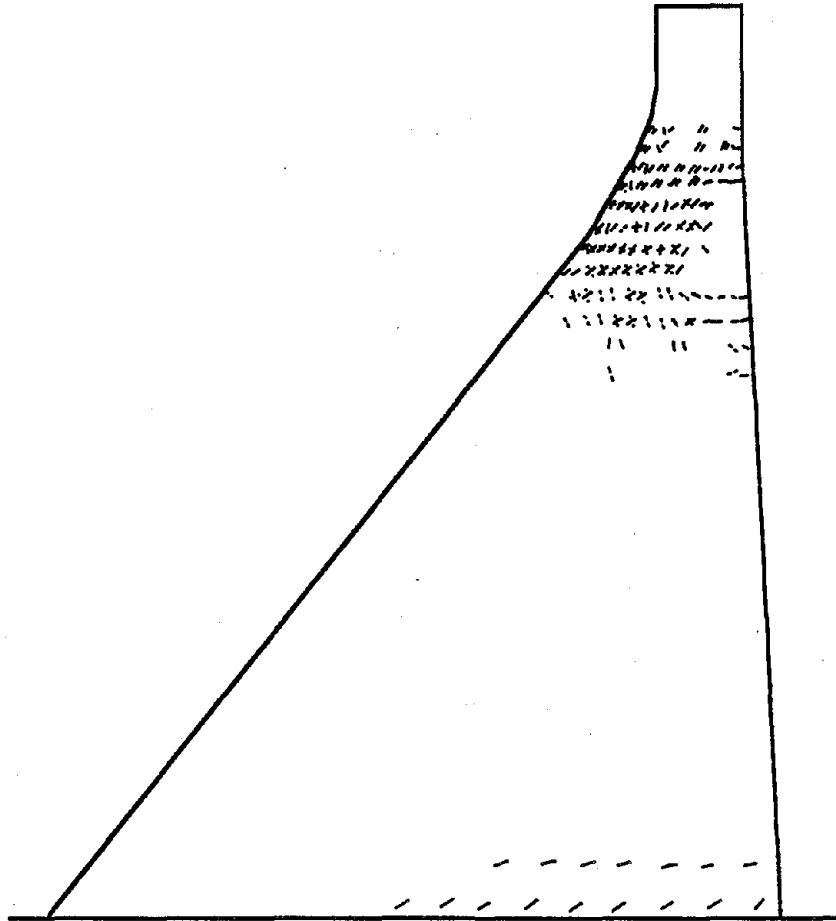
d) time = 4.19 sec

Fig. 6.23 (continued)
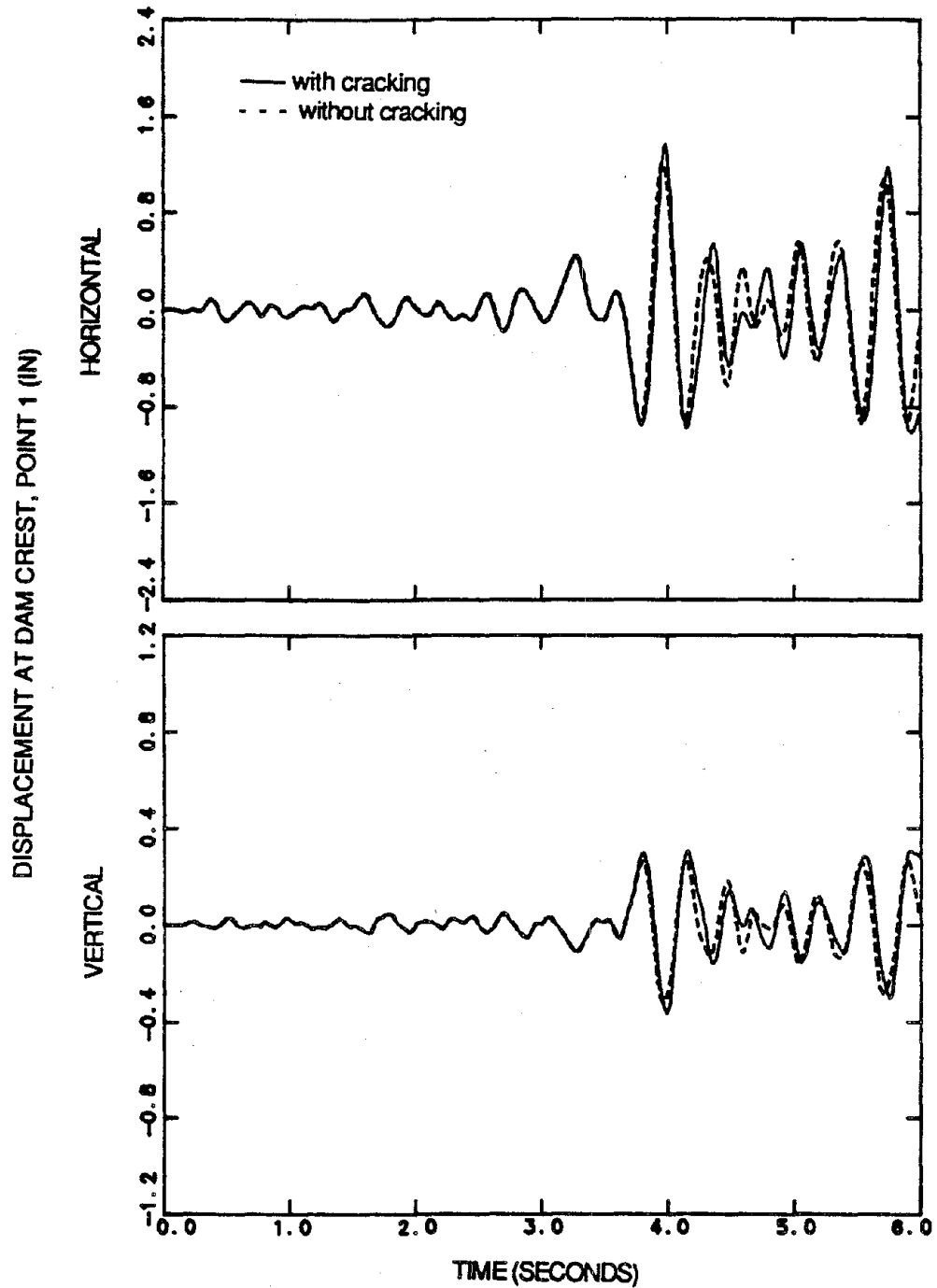
Fig. 6.24 Displacement response of Pine flat dam with full reservoir
due to both the S69E and vertical components of Taft ground
motion; scale factor = 1.5; α_r = 0.5.
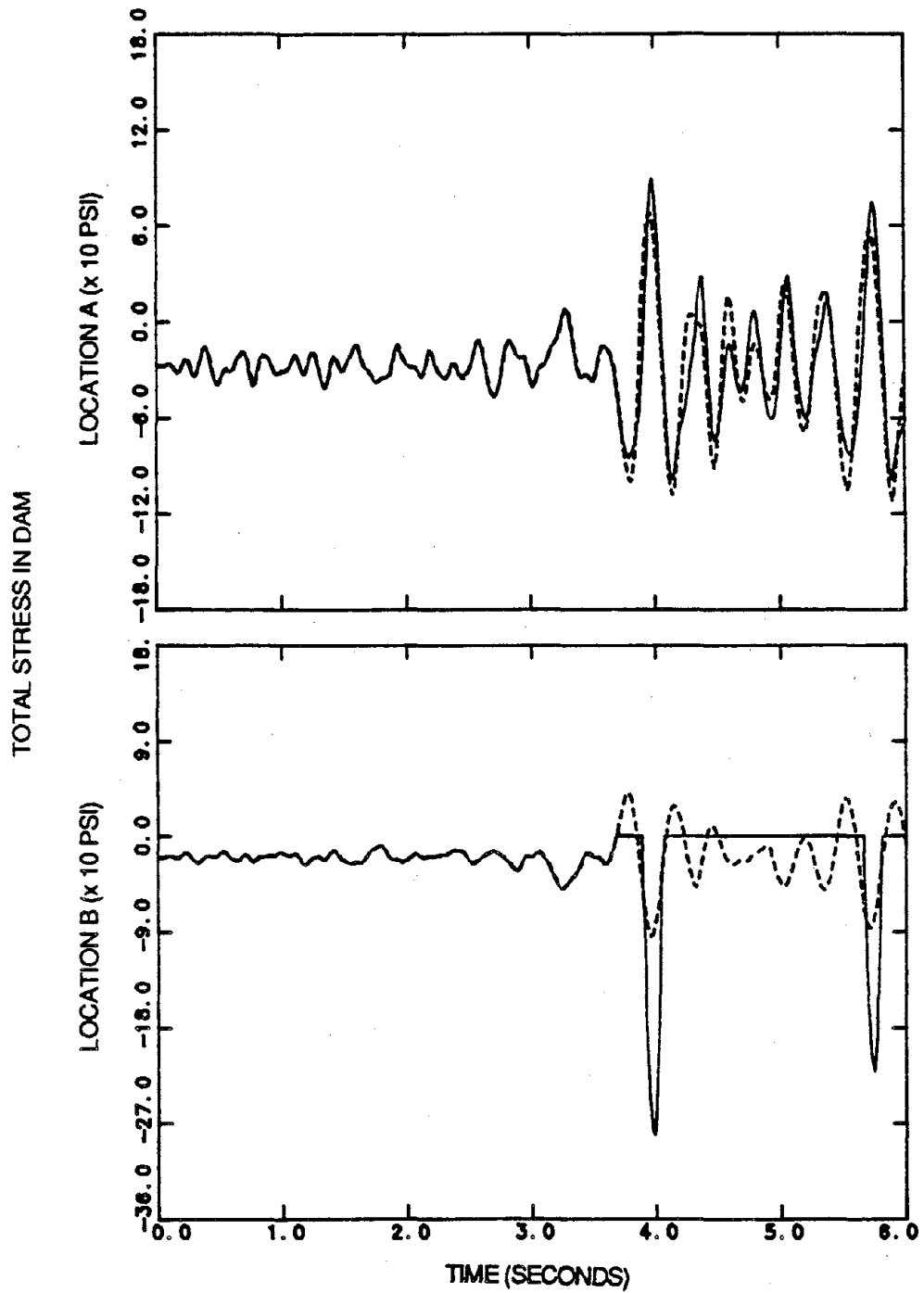
Fig. 6.25 Stress response of Pine flat dam with full reservoir due to both
the S69E and vertical components of Taft ground motion;
scale factor = 1.5; $\alpha_I = 0.5$.
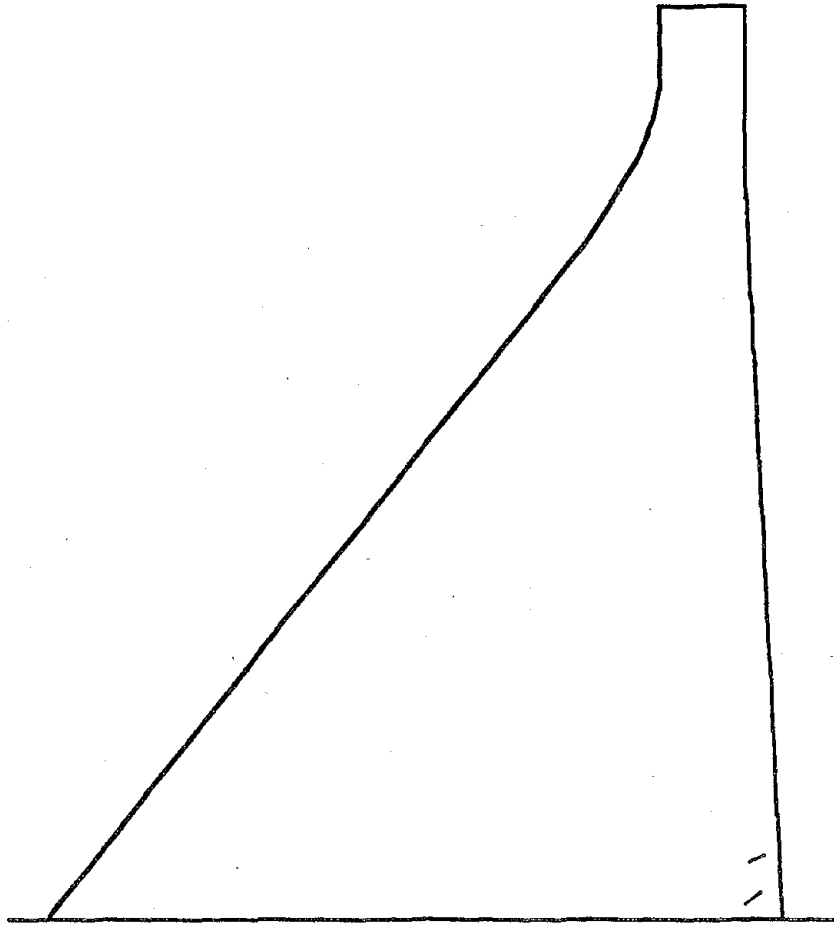
a) time = 3.71 sec

Fig. 6.26 Tensile crack pattern in Pine Flat dam with full reservoir due
to both the S69E and vertical components of Taft ground
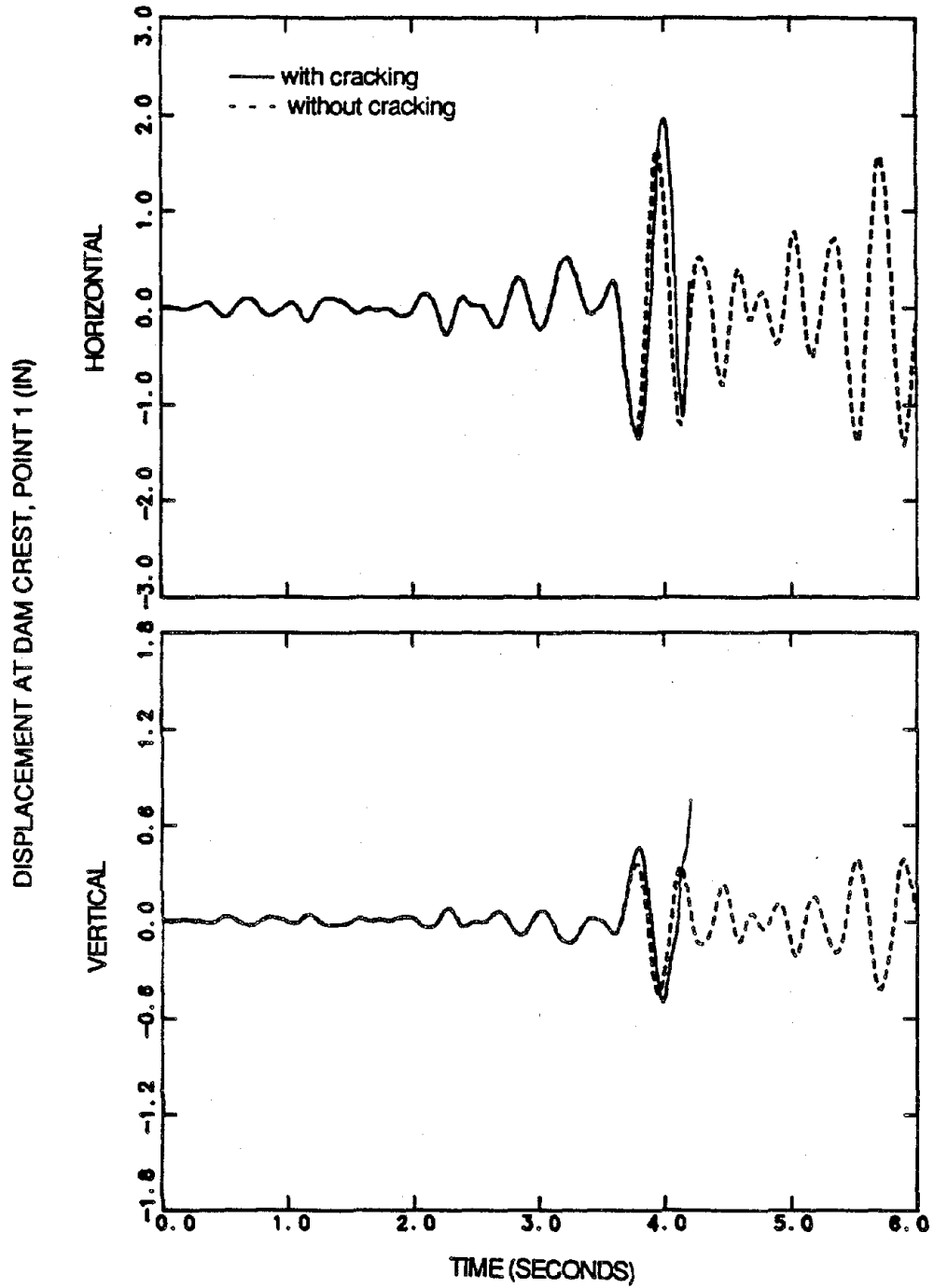motion; scale factor = 1.5; $\alpha_r = 0.5$.
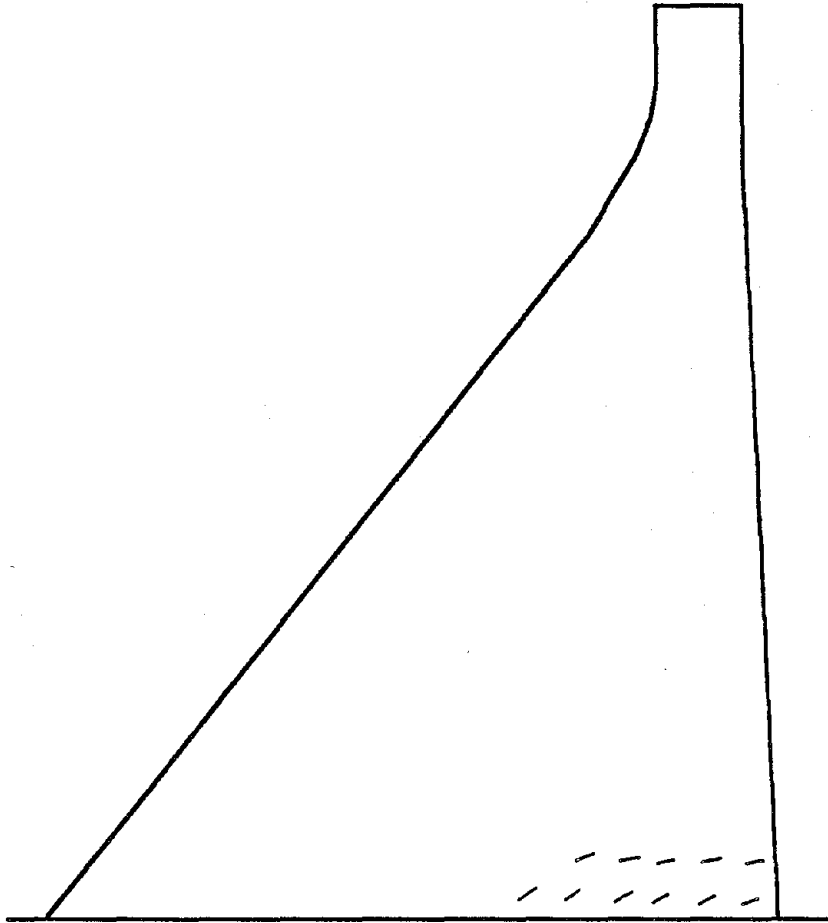
b) time = 5.94 sec

Fig. 6.26 (continued)

Page Intentionally Left Blank

Chapter 7

Conclusions and Recommendations

A numerical procedure for computing the nonlinear transient response of coupled fluid-structure systems has been developed. The primary motivation for developing the analysis procedure is to compute the earthquake response of concrete gravity dam-water systems. The analytical model includes dam-water interaction effects, cavitation of the water, tensile cracking of concrete in the dam, and the approximate effects of the materials at the reservoir bottom.

The fluid is considered compressible, irrotational and inviscid, undergoing small amplitude motion. The computational procedure employs a mixed pressure-displacement finite element formulation for the fluid, where the fluid pressure and displacement are approximated independently. It is shown that reduced integration of the fluid element stiffness matrix is not required, and the inclusion of surface wave effects and a constraint on irrotational motion increases the rank of the element stiffness matrix, eliminating singularities in the global fluid stiffness matrix. The mixed formulation for the fluid allows easy incorporation of the bilinear fluid model to include the effects of cavitation. Unlike the displacement formulation, in which the equation of state is satisfied point-by-point throughout the element, the equation of state in the mixed formulation is satisfied in the average sense over the element. This results in faster convergence, mainly when computing the nonlinear restoring forces due to cavitation. A standard displacement finite element formulation is used to discretize the structure. The coupled nonlinear equations of motion for the fluid and the structure are symmetric and solved by a fully implicit time integration method.

The eigenvalue analysis of several two-dimensional fluid finite elements has shown that the 4 and 9-node elements with one and four pressure functions, respectively, represent well the vibrational characteristics of inviscid fluid and are convergent. A parametric study using the 4 and 9-node elements has found that a penalty parameter of fifty times the fluid bulk modulus suffices to enforce the constraint on irrotational motion.

In application to the earthquake response of concrete gravity dam-water systems, a series of studies have been conducted assuming linear elastic behavior of the concrete in the dam and cavitating water in the reservoir. Response results show that significant water cavitation occurs for dam heights greater than 400 ft. and peak ground accelerations around $1g$. The influence of water cavitation on displacements and maximum principal stresses in the dam is very small, increasing peak response about 3%. However, cavitation has a large effect on peak accelerations at the dam crest. This may have an important consequence by amplifying the response of stiff appurtenant equipment attached to the dam crest. The large stresses produced by the ground motions required to induce cavitation, exceed the concrete tensile strength, indicating the potential importance of tensile cracking on the earthquake response. The effect of reservoir bottom materials, modeled by an approximate absorbing boundary, reduces the large hydrodynamic pressure pulses on the dam produced by cavitation; hence reducing the magnitude of displacements and stresses. The reduction of hydrodynamic pressure due to cavitation is more significant for vertical ground motion than for horizontal motion.

The earthquake response of concrete gravity dams including the tensile cracking of the mass concrete has also been investigated. The crack band theory with a smeared crack representation is used to model mass concrete. Microcrack initiation is determined by a strain criterion, and strain-softening behavior defines

the formation of a crack surface in conjunction with a release of fracture energy. The cracking model is incorporated into the finite element procedure with a displacement formulation using the smeared crack approach. The criteria for crack propagation, closure and reopening of cracks have been established based on experimental results.

The response of a typical concrete dam with empty and full reservoir subjected to various earthquake ground motion records has been examined. The response results demonstrate that concrete tensile cracking has an important effect in the displacement and stress responses. The vibrational period increases as the dam becomes more flexible due to the formation of tensile cracks. Compressive stresses normal to the cracked surfaces increase, although they are still small compared with the concrete compressive strength. With empty reservoir, cracking in the dam starts at the downstream face at the upper part of the dam, and propagates towards the upstream face. With full reservoir, cracking in the dam initiates at an earlier time compared to the case of empty reservoir. Cracks initiate at the heel and extend along the base of the dam and, depending upon the intensity of the ground motion, produce a large rotation of the dam about the toe. At a later time in the response history the cracking at the base stabilizes, but then extensive cracking develops in the upper part of the dam propagating completely across the cross section. When the effects of reservoir bottom materials are included, cracking initiation and propagation do not differ much from the case of rigid reservoir bottom materials. The extensive cracking indicated in the response would result in severe damage of the dam and possible release of water in the reservoir. This behavior, however, does not necessarily imply that the dam has failed since rocking and sliding motions of the separated upper portion of the dam are possible.

Tensile cracking in the concrete appears as the dominant nonlinear effect in the earthquake response of concrete gravity dams. It greatly affects the displacement

and stress responses, and occurs at levels of ground motion insufficient to produce cavitation in the water. The extensive cracking observed is likely to take place in concrete gravity dams under severe earthquakes, since the ground motions used in this study, with peaks accelerations of $0.36g$ and $1.17g$, are not unrealistic for design earthquakes. This should call the attention on the current design practice in which dams are analyzed and designed to withstand high levels of ground motion without significant tensile stresses in the concrete. The general conclusions from this investigation are valid for similar gravity dams and earthquakes, however, the response depends on a particular dam and ground motion.

Because of the limitations on element size in the crack band theory with a smeared crack representation, future research is necessary to improve the modeling of tensile cracking in very large structures, such as concrete dams, under dynamic loads. Experimental testing of mass concrete under dynamic loads will provide useful information in regards to the formation, propagation, closure and reopening of tensile cracks. Future investigations should also focus on the dynamic stability of the upper part of a dam which may separate because of the extensive tensile cracking.

Appendix A

Boundary Conditions for Fluid Domain

This appendix presents the derivations of the boundary conditions used in the equations of motion of the fluid domain.

A.1 Free Surface Boundary Condition

Under the presence of a gravity field, a vertical displacement, $\eta(x)$, of the free surface, where positive x opposes gravity, produces a pressure in the fluid of $p = \rho_0 g\ \eta(x)$. The acceleration of gravity, g, can be expressed in vector notation as $g = -\mathbf{n}^T \mathbf{g}$, therefore

$$p = -\rho_0(\mathbf{n}^T \mathbf{g})\ \eta(x) \tag{A.1}$$

For small amplitude motion, $\eta(x)$ is small. Consequently, it can be assumed [23] that the velocity $\dot{\eta}(x)$ equals the fluid particle velocity normal to the free surface, thus

$$\dot{\eta}(x) = \mathbf{n}^T \mathbf{v}^t \tag{A.2}$$

Differentiating Eq. A.1 with respect to time and using Eq. A.2 yields the free surface boundary condition in Eq. 2.6,

$$\dot{p} = -\rho_0(\mathbf{n}^T \mathbf{g})\mathbf{n}^T \mathbf{v}^t \tag{A.3}$$

A.2 Radiation Boundary Conditions

A.2.1 Reservoir Bottom Boundary

Pressure waves on the reservoir bottom are assumed to excite only vertically propagating dilatational waves in the reservoir bottom elastic materials [15,38].

197

This approximation allows to consider the interaction fluid-reservoir bottom by the solution of the one-dimensional wave equation. In Ref. [15], it was shown that

$$\mathbf{n}^T \nabla p + q\dot{p} = -\rho_0(\mathbf{n}^T \dot{\mathbf{v}}_g) \tag{A.4}$$

where $q = \rho_0/\rho_r c_r$, is the admittance or damping coefficient for the reservoir bottom materials and $\mathbf{v}_g$ is the ground velocity. Substituting ∇p from Eq. 2.1 (momentum balance) into Eq. A.4, and integrating with respect to time yields

$$p = \frac{\rho_0}{q} \mathbf{n}^T(\mathbf{v}^t - \mathbf{v}_g) \tag{A.5}$$

Combining Eq. 2.4 and Eq. A.5, gives the boundary condition at the reservoir bottom, Eq. 2.7

$$p = \rho_r c_r \mathbf{n}^T \mathbf{v} \tag{A.6}$$

A.2.2 Truncated Boundary

The boundary condition in Eq. 2.8, which represents a viscous damper, approximately provides for radiation of pressure waves at the truncated boundary, $\Gamma_{FP'}$, of a large, or infinite, fluid domain. It is essentially expressed from Eq. A.4, in which the ground acceleration at the truncated boundary is zero. That is

$$\mathbf{n}^T \nabla p + q\dot{p} = 0 \tag{A.7}$$

Since there is no change of the fluid accross the truncated boundary, $q = 1/c_0$. Following the same steps as in Section A.2.1, the truncated boundary condition in Eq. 2.8 is

$$p = \rho_0 c_0 \mathbf{n}^T \mathbf{v}^t \tag{A.8}$$

Appendix B

Coordinate Transformations for Rotated Degrees-of-Freedom

A transformation of degrees-of-freedom is required when their orientation does not coincide with the global coordinate system. This is the case at the fluid-structure interface, Γ_{SF}, and the fluid-reservoir bottom boundary, Γ_{FU}, (Fig. 2.3), in which compatibility of displacements normal to the interface must be enforced. Considering that the global coordinate system in two dimensions is oriented with the $x - y$ axes, the relationship of displacements between the global and the rotated $x' - y'$ system is given by [4]

$$\mathbf{U}' = \mathbf{R}\mathbf{U} \qquad (B.1)$$

where $\mathbf{R}$ is an orthogonal matrix defined as

$$\mathbf{R} = \begin{bmatrix} cos\theta & sin\theta \\ -sin\theta & cos\theta \end{bmatrix} \qquad (B.2)$$

in which θ is the angle of rotation, and the prime in Eq. B.1 refers to the $x' - y'$ coordinate system. It can be shown [4], that the submatrix $\mathbf{k}_{IJ}$, corresponding to the degrees-of-freedom associated with the global coordinate system $x - y$, can be transformed into the rotated coordinate system $x' - y'$, as

$$\mathbf{k}'_{IJ} = \mathbf{R}\mathbf{k}_{IJ}\mathbf{R}^T \qquad (B.3)$$

The same tramsformations are required for the velocity and acceleration components, so the mass and damping submatrices in the rotated coordinate system

are given by

$$m'_{IJ} = \mathbf{R} m_{IJ} \mathbf{R}^T \tag{B.4}$$

$$c'_{IJ} = \mathbf{R} c_{IJ} \mathbf{R}^T \tag{B.5}$$

In the fluid-reservoir bottom boundary, the groung motion components must also be transformed accordingly; that is $\mathbf{u}'_g = \mathbf{R}\mathbf{u}_g$, $\dot{\mathbf{u}}'_g = \mathbf{R}\dot{\mathbf{u}}_g$ and $\ddot{\mathbf{u}}'_g = \mathbf{R}\ddot{\mathbf{u}}_g$. In the computer implementation these transformations are performed at the element level, so only the non-prescribed degrees of freedom are considered in the global matrices.

Appendix C

Strain-Softening Characteristics

Considering a system of continuously distributed microcracks with coordinate axes representation as shown in Fig. 5.2(b), the stress-strain relationship including softening is given by [8]

$$
\left\{ \begin{array}{c} \epsilon_1 \\ \epsilon_2 \\ \gamma_{12} \end{array} \right\} = \left[\begin{array}{ccc} E^{-1} & -\nu E^{-1} & 0 \\ -\nu E^{-1} & E^{-1} & 0 \\ 0 & 0 & (\beta_g G)^{-1} \end{array} \right] \left\{ \begin{array}{c} \sigma_1 \\ \sigma_2 \\ \tau_{12} \end{array} \right\} + \left\{ \begin{array}{c} \epsilon_f \\ 0 \\ 0 \end{array} \right\} \tag{C.1}
$$

where ϵ_1, ϵ_2, and γ_{12} are the components of the strain tensor while softening takes place. σ_1 and σ_2 are the normal components of stress and $d\tau_{12}$ is shearing stress. ϵ_f is the fracture strain and is a function of σ_1 only. For linear softening, Fig. 5.1(b), the fracture strain can be derived as

$$
\epsilon_f = \frac{1}{C_f} (f_t' - \sigma_1) \tag{C.2}
$$

C_f, is the slope of the $\sigma - \epsilon_f$ diagram. Upon substitution of Eq. C.2 into Eq. C.1 yields

$$
\left\{ \begin{array}{c} \epsilon_1 \\ \epsilon_2 \\ \gamma_{12} \end{array} \right\} = \left[\begin{array}{ccc} E_t^{-1} & -\nu E^{-1} & 0 \\ -\nu E^{-1} & E^{-1} & 0 \\ 0 & 0 & (\beta_g G)^{-1} \end{array} \right] \left\{ \begin{array}{c} \sigma_1 \\ \sigma_2 \\ \tau_{12} \end{array} \right\} + \left\{ \begin{array}{c} f_t'/C_f \\ 0 \\ 0 \end{array} \right\} \tag{C.3}
$$

in which

$$
\frac{1}{E_t} = \frac{1}{E} - \frac{1}{C_f} \tag{C.4}
$$

The incremental stress-strain relationship corresponding to Eq. C.3 is then given by

$$
\left\{ \begin{array}{c} d\epsilon_1 \\ d\epsilon_2 \\ d\gamma_{12} \end{array} \right\} = \left[\begin{array}{ccc} E_t^{-1} & -\nu E^{-1} & 0 \\ -\nu E^{-1} & E^{-1} & 0 \\ 0 & 0 & (\beta_g G)^{-1} \end{array} \right] \left\{ \begin{array}{c} d\sigma_1 \\ d\sigma_2 \\ d\tau_{12} \end{array} \right\} \tag{C.5}
$$

201

where $d\epsilon_1$, $d\epsilon_2$, and $d\gamma_{12}$ are the increments of strain while softening takes place. $d\sigma_1$ and $d\sigma_2$ are the increments of normal components of stress and $d\tau_{12}$ is the increment of shearing stress. Inverting the compliance matrix, Eq. C.5, the cracked material stiffness matrix is obtained from

$$\left\{ \begin{array}{c} d\sigma_1 \\ d\sigma_2 \\ d\tau_{12} \end{array} \right\} = \left[\begin{array}{ccc} E'_t & \nu E'_t & 0 \\ \nu E'_t & E + \nu^2 E'_t & 0 \\ 0 & 0 & \beta_g G \end{array} \right] \left\{ \begin{array}{c} d\epsilon_1 \\ d\epsilon_2 \\ d\gamma_{12} \end{array} \right\} \tag{C.6}$$

where $E'_t = E_t E / (E - \nu^2 E_t)$; $E_t = E_t(\epsilon_1)$. When two cracks develop, the behavior of both cracks is considered independently, which is equivalent to setting the Poisson's ratio in Eq. C.6 equal to zero. Then

$$\left\{ \begin{array}{c} d\sigma_1 \\ d\sigma_2 \\ d\tau_{12} \end{array} \right\} = \left[\begin{array}{ccc} E_{t_1} & 0 & 0 \\ 0 & E_{t_2} & 0 \\ 0 & 0 & \beta_g G \end{array} \right] \left\{ \begin{array}{c} d\epsilon_1 \\ d\epsilon_2 \\ d\gamma_{12} \end{array} \right\} \tag{C.7}$$

in which $E_{t_1} = E_t(\epsilon_1)$ and $E_{t_2} = E_t(\epsilon_2)$. The material stiffness matrix for the vertical stress drop behavior follows from Eq. C.6, for one crack, and from Eq. C.7 for two cracks, with $E'_t = 0$ and $E_{t_1} = E_{t_2} = 0$, respectively.

For linear softening, Fig. 5.1(b), the fracture energy, Eq. 5.3, is obtained as

$$G_f = w_c \frac{f'^2_t}{2C_f} \tag{C.8}$$

Using C_f from Eq. C.4, G_f can be expressed as

$$G_f = w_c \frac{1}{2} \left[\frac{1}{E} - \frac{1}{E_t} \right] f'^2_t = w_c W \tag{C.9}$$

Notice that the fracture energy, G_f, and the area under the complete uniaxial stress-strain diagram for linear softening behavior, W (Fig. 5.4), are related through the crack band width, w_c.

BIBLIOGRAPHY

[1] American Concrete Institute, Building Code Requirements for Reinforced Concrete, ACI Committee 318, Detroit, MI., 1983.

[2] ASCE Special Publication. *Finite Element Analysis of Reinforced Concrete*, 1982.

[3] Batchelor, G.K., *An Introduction to Fluid Dynamics*, Cambridge University Press, Cambridge, 1967.

[4] Bathe, K.J., *Finite Element Procedures in Engineering Analysis*. Englewood Cliffs, N.J., Prentice-Hall, 1982.

[5] Bathe, K.J., and Hahn, W.F., "On Transient Analysis of Fluid-Structure Systems," *Computers and Structures*, Vol. 10, No. 1/2, April, 1979, pp. 383-391.

[6] Bažant, Z.P., "Instability, Ductility, and Size Effect in Strain-Softening Concrete," *Journal of the Engineering Mechanics Division*, ASCE, Vol. 102, No. EM2, April, 1976, pp. 331-344.

[7] Bažant, Z.P., and Cedolin, L., "Blunt Crack Band Propagation in Finite Element Analysis," *Journal of the Engineering Mechanics Division*, ASCE, Vol. 105, No. EM2, April, 1979, pp. 297-315.

[8] Bažant, Z.P., and Oh, B.H., "Crack Band Theory for Fracture of Concrete," *Matériaux et Constructions*, Vol. 16, No. 93, 1983, pp. 155-177.

[9] Bažant, Z.P., "Fracture Mechanics and Strain-Softening of Concrete," *Finite Element of Reinforced Concrete Structures*, C. Mayer and H. Okamura, Eds., ASCE Special Publication, 1986.

[10] Bleich, H.H, and Sandler, I.S., " Interaction Between Structures and Bilinear Fluids," *International Journal of Solids and Structures,* Vol. 6, No. 5, May, 1970, pp. 617-639.

[11] Carey, G.F., and Oden, J.T., *Finite Elements: A Second Course,* Vol. II, Englewood Cliffs, N.J., Prentice-Hall, 1983.

[12] Chapuis, J., Rebora, B., and Zimmermann, Th., "Numerical Approach of Crack Propagation Analysis in Gravity Dams During Earthquakes," *Proceedings,* 15th Congress, International Congress on Large Dams, Lausanne, 1985.

[13] Chopra, A.K, Wilson, E.L., and Farhoomad, I., "Earthquake Analysis of Reservoir-Dam Systems," *Proceedings,* Fourth World Conference on Earthquake Engineering, Santiago, Chile, 1969.

[14] Clough, R.W., and Chang, C.-H., "Seismic Cavitation Effects on Gravity Dam Reservoirs," *Numerical Methods in Coupled Systems,* R.W. Lewis, P. Bettess, E. Hinton, eds., John Wiley and Sons, Chichester, 1984.

[15] Fenves, G.L., and Chopra, A.K., "Earthquake Analysis and Response of Concrete Gravity Dams," *Report No. UBC/EERC-84/10,* Earthquake Engineering Research Center, University of California, Berkeley, California, Aug., 1984.

[16] Fok, K.-L., and Chopra, A.K., "Hydrodynamic and Foundation Flexibility Effects in Earthquake Response of Arch Dams," *Journal of Structural Engineering,* ASCE, Vol. 112, No. 8, Aug., 1986, pp. 1810-1828.

[17] Greenberg, M.D., *Foundations of Applied Mathematics,* Englewood Cliffs, N.J., Prentice-Hall, 1978.

[18] Hall, J.F., "Study of the Earthquake Response of Pine Flat Dam," *Earthquake Engineering and Structural Dynamics,* Vol. 14, No. 2, March-April, 1986, pp. 281-295.

[19] Hamdi, M.A., Ousset, Y., and Verchery, G., "A Displacement Method for Analysis of Vibrations of Coupled Fluid-Structure Systems," *International Journal for Numerical Methods in Engineering,* Vol. 13, No. 1, 1978, pp 139-150.

[20] Hughes, T.J.R., *The Finite Element Method,* Englewood Cliffs, N.J., Prentice-Hall, 1987.

[21] Hughes, T.J.R, Pister, K.S., and Taylor, R.L, "Implicit-Explicit Finite Elements in Nonlinear Transient Analysis," *Computer Methods in Applied Mechanics and Engineering,* Vol. 17/18, Part 1, Jan., 1979, pp. 159-182.

[22] Kupfer, H., Hilsdorf, H., and Rüsch, H., "Behavior of Concrete Under Biaxial Stresses," ACI Journal, *Proceedings,* Vol. 66, No. 8, Aug., 1969, pp. 656-666.

[23] Landau, L.D., and Lifshitz, E.M., *Fluid Mechanics,* Pergamon Press, Oxford, 1959.

[24] Liu, W.K., and Chang, H.G., "A Method for Computation for Fluid Structure Interaction," *Computers and Structures,* Vol. 20, No. 1-3, 1985, pp.311-320.

[25] Malkus, D.S., and Hughes, T.J.R., "Mixed Finite Elements- Reduced and Selective Integration Techniques: A Unification of Concepts," *Computer Methods in Applied Mechanics and Engineering,* Vol. 15, 1978, pp. 63-81.

[26] Mlakar, P.F., "Nonlinear Response of Concrete Gravity Dams to Strong Earthquake-Induced Ground Motion," *Computer and Structures,* Vol. 26, No. 1/2, 1987, pp. 165-173.

[27] Newton, R.E., "Effects of Cavitation on Underwater Shock Loading - Part I," *Report NPS-69-78-013,* Naval Postgraduate School, Monterey, California, July, 1978.

[28] Ngo, D., and Scordelis, A.C., "Finite Element Analysis of Reinforced Concrete Beams," *Journal of the American Concrete Institute,* Vol. 64, No. 3, 1967, pp. 152-163.

[29] Nilson, A.H., "Nonlinear Analysis of Reinforced Concrete by the Finite Element Method," *Journal of the American Concrete Institute,* Vol. 65, No. 9, 1967, pp. 757-766.

[30] Niwa, A., and Clough, R.W., "Shaking Table Research on Concrete Dam Models," *Report No. UCB/EERC-80/05,* Earthquake Engineering Research Center, University of California, Berkeley, California, Sept., 1980.

[31] Norman, C.D., and Anderson, F.A., "Reanalysis of Cracking in Large Concrete Dams in the US Army Corps of Engineers," *Proceedings,* 15th Congress, International Congress on Large Dams, Lausanne, 1985.

[32] Olson, L.G., and Bathe, K.-J., "A Study of Displacement-Based Fluid Finite Elements for Calculating Frequencies of Fluid and Fluid-Structure Systems," *Nuclear Engineering and Design,* Vol. 76, No. 2, Nov., 1983, pp. 137-151.

[33] Olson, L.G., and Bathe, K.-J., "Analysis of Fluid-Structure Interactions. A Direct Symmetric Coupled Formulation Based on Fluid Velocity Potential," *Computers and Structures,* Vol. 21, No. 1/2, 1985, pp. 21-32.

[34] Pal, N., "Seismic Cracking of Concrete Gravity Dams," *Journal of the Structural Division,* ASCE, Vol. 102, No. ST9, 1976, pp. 1827-1844.

[35] Park, K.C., and Felippa, C.A., "Recent Developments in Coupled Field Analysis Methods," *Numerical Methods in Coupled Systems,* R.W. Lewis, P. Bettess, E. Hinton, eds., John Wiley and Sons, Chichester, 1984.

[36] Raphael, J.M., "Tensile Strength of Concrete," ACI Journal, *Proceedings,* Vol. 81, Mar-Apr. 1984, pp. 158-165.

[37] Rashid, Y.R., "Analysis of Prestressed Concrete Pressure Vessels," *Nuclear Engineering and Design,* Vol. 7, No. 4, 1968, pp. 334-344.

[38] Rosenbluth, E., "Presión Hidrodinámica en Presas Debida a la Acceleración Vertical con Refracción en el Fondo," presented at the 1968, 2do Congreso Nacional de Ingeniería Sísmica, held at Veracruz, Mexico.

[39] Rots, J.G., Nauta, P., Kusters, G.M.A., and Blaauwendraad, J., "Smeared Crack Approach and Fracture Localization in Concrete," *HERON,* Vol. 30, No. 1, 1985.

[40] Saini, S.S., Bettess, P., and Zienkiewicz, O.C., "Coupled Hydrodynamic Response of Concrete Dams Using Finite and Infinite Elements," *Earthquake Engineering and Structural Dynamics,* Vol. 6, No. 4, July-Aug., 1978, pp. 363-374.

[41] Skrikerud, P.E., and Bachmann, H., "Discrete Crack Modelling for Dynamically Loaded, Unreinforced Concrete Structures," *Earthquake Engineering and Structural Dynamics,* Vol. 14, No. 2, 1986, pp. 297-315.

[42] Strang, G., *Linear Algebra and Its Applications,* 2nd Edition, Academic Press, 1980.

[43] Taylor, R.L., Beresford, P.J., and Wilson, E.L., "A Non-Conforming Element for Stress Analysis," *International Journal for Numerical Methods in Engineering,* Vol. 10, No. 6, 1976, pp. 1211-1219.

[44] Taylor, R.L., and Zienkiewicz, O.C., "Mixed Finite Element Solution of Fluid Flow Problems," in *Finite Elements in Fluids,* Vol. 4, R.H. Gallagher, R.H. Norrie, J.T. Oden, and O.C. Zienkiewicz, eds., John Wiley and Sons, Chichester, 1984.

[45] Willam, K., Hurlbut, B., and Sture, S., "Experimental and Constitutive Aspects of Concrete Failure," *Finite Element of Reinforced Concrete Structures,*

C. Mayer and H. Okamura, Eds., ASCE Special Publication, 1986.

[46] Wilson, E.L., and Khalvati, M., "Finite Elements for the Dynamic Analysis of Fluid-Solid Systems," *International Journal for Numerical Methods in Engineering,* Vol. 19, No. 11, Nov., 1983, pp. 1657-1668.

[47] Zienkiewicz, O.C., and Bettess, P., "Fluid-Structure Dynamic Interaction and Wave Forces. An Introduction to Numerical Treatment," *International Journal for Numerical Methods in Engineering,* Vol. 13, No. 1, 1978, pp. 1-16.

[48] Zienkiewicz, O.C., Paul, D.K., and Hinton, E., "Cavitation in Fluid-Structure Response (with Particular Reference to Dams Under Earthquake Loading)," *Earthquake Engineering and Structural Dynamics,* Vol. 11, No. 4, July-Aug., 1983, pp. 463-481.

[49] Zienkiewicz, O.C., and Taylor, R.L., "Coupled Problems – a Simple Time-Stepping Procedure," *Communications in Applied Numerical Methods,* Vol. 1, No. 5, Sept., 1985, pp. 233-239.

[50] Zienkiewicz, O.,C., Taylor, R.L., and Baynham, J.M.W., "Mixed and Irreducible Formulation in the Finite Element Analysis, *Proceedings,* International Symposium on Mixed and Hybrid Finite Element Methods, Atlanta, Georgia, April, 1981.

[51] Zienkiewicz, O.C., *The Finite Element Method,* 3rd Edition, McGraw Hill, London, 1977.